Modelling of hybrid plasma accelerators

A thesis submitted to The Department of Physics
University of Strathclyde /University of Princess Nourah Bint AbdUlrahman
for the degree of Doctor of Philosophy

Reem Altuijri
2022

Supervisors:
Prof. Bernhard Hidding
Dr. Brian McNeil

Abstract

A promising scheme for plasma wakefield acceleration is the hybrid plasma acceleration mechanism, which is experimentally connected to worldwide programs at various accelerator facilities. This scheme may lead to extremely high-quality electron bunches, that can be used to drive ultrabright light sources such as free-electron lasers. The big challenge for plasma acceleration is to produce electron bunches with high quality in terms of low emittance, energy spread, and high brightness. To overcome this challenge, the Trojan Horse "plasma photocathode" scheme is used to produce designer electron beams.

This thesis explores the Trojan Horse mechanism in a systematic simulation-based parametric study. Different interaction regimes are explored by variation of the injector laser pulse by normalised vector potential a_0, spot size w_0 and relative spatiotemporal synchronisation and alignment in the plasma wave at various densities. These parameters define the plasma photocathode process.

The general motivation of this work is to investigate the generation of high-quality electron beams for light source applications. Several factors and mechanisms impact the witness bunch, affect its beam emittance, and drive its growth. The main driver for emittance growth, particularly at increased witness beam charge levels, is space charge and intra-beam Coulomb repulsion. Although the laser-released electrons from the plasma photocathode are rapidly accelerated and focused by the plasma wakefields, increasing the charge, e.g., by means of increasing the background plasma density from which the plasma photocathode electrons are liberated, produced very strong electric fields inside the bunch and thus triggered and driven rapid emittance growth. The effect of evolving space charge in the formative phase of the witness beam production and acceleration is investigated using tailored particle-in-cell simulations, for example, by scanning the evolution of transverse phase space across different plasma densities, and the illumination of the process by analysis is not available to the experiment but only to high-resolution and high-fidelity simulations.

These computational studies provide insight into the sensitivities and robustness of the scheme, which is important for upcoming experiments, e.g., at SLAC, FACET-II, and may allow pushing the emittance and brightness barrier of electron beams produced by the Trojan Horse process. This could dramatically impact applications such as ultrabright, hard x-ray free-electron lasers, particle and strong-field physics.

Acknowledgement

During my research processes, there are many people who have supported me in many ways. I would like to thank my supervisor Bernhard for his continuous constructive support during my research process and for his kindness and continuous support to his students. I thank his support in facilitating the procedures for using the VSim code.

I also thank Dr. Sherif Khalil for his support at the initial stages of my research, and I thank Dr. Ahmed Hala for his valuable suggestions and continued support, and for facilitating the procedures for using Shaheen supercomputer in KAUST. I also thank Dr. Brain McNeil for his presence and support in vivas. And I thank Princess Nora University for their scholarship to complete my doctoral studies. I also thank KAUST for providing the facilities for the use of Shaheen.

And special thanks to Dr. Paul Scherkl for his continued and constructive support in using the VSim code with kindness and high morals, as I highly benefited from my discussions with him throughout my studies.

I thank Thomas for his courteous dealing and his constructive scholarly discussions, also I thank Dr.Fahim Habib for his valuable discussions. I thank my colleague Badriah for her continued support.

And special thanks to my family who supported me in many ways. Thank you to my mother, my husband, and my brother Homoud for all what they did for me.

Finally, I thank everyone who supported me, and I could not write their names.

List of Publications

1. G. G. Manahan, A. F. Habib, P. Scherkl, D. Ullmann, A. Beaton, A. Sutherland, G. Kirwan, P. Delinikolas, T. Heinemann, **R. Altuijri**, A. Knetsch, O. Karger, D. L. Bruhwiler, Z-M Sheng, J. B. Rosenzweig and B. Hidding, "Advanced schemes for underdense plasma photocathode wakefield accelerators: pathways towards ultrahigh brightness electron beams'', Philosophical Transactions of the Royal Society A: Mathematical, Physical and Engineering Sciences **377**, 0182 (2019).

2. **R. Altuijri**, P. Scherkl, T. Heinemann, A.F. Habib, A.J. Nutter,A. Hala and B. Hidding, "Parametric Tolerance Study of Trojan Horse plasma wakefield acceleration scheme", in EPS2019 conference (2019).

3. B. M. Alotaibi, **R. Altuijri**, A. F. Habib, A. Hala, B. Hidding, Sh. M. Khalil, B. W. J. McNeil, P. Traczykowski, "Plasma wakefield accelerator driven coherent spontaneous emission from an energy chirped electron pulse", New Journal of Physics **20**, 013037 (2019).

4. B. M. Alotaibi, **R. Altuijri** et al., "Plasma Accelerator Driven Coherent Spontaneous Emission" in 39th Free Electron Laser conference, TUP051 (2019).

5. A. F. Habib, G. G. Manahan, P. Scherkl, T. Heinemann, A. Sutherland, **R. Altuijri** et al., "Attosecond-Angstrom free-electron-laser at the cold beam Limit", submitted.

Contents

List of Figures

Chapter 1

1 Introduction

Over the last decades, we have seen a remarkable development in plasma-based accelerators. The structures of plasma acceleration are formed using ultrashort laser pulses or charged particle beams to produce relativistic particle beams of electrons or positrons for energy gain. Plasma-based techniques can build a wide range of applications from high energy physics to low energy physics. T. Tajima and J.M. Dawson conceived the basic idea of plasma accelerators were conceived by T. Tajima and J.M. Dawson of UCLA in 1979 [1]. They suggested exciting the plasma waves by an intense laser to produce wakefields. Since then, there has been intense research on plasma accelerators, light sources, and many other applications developing, with enormous advances in recent years.

Before discussing the plasma-based accelerators, we will review some accelerator fundamentals. Firstly, they use either elementary particles or light pulses as drivers. Secondly, they can be used to accelerate particles on a circular ring path or linearly along straight trajectories. Presently, the largest accelerator is the Large Hadron Collider (LHC) at CERN, with a circumference of 27 km and a budget of approximately €7.5 billion [2]. The purpose of the LHC is to validate existing particle physics theories and perhaps discover novel, surprising fundamental physics. A prominent conventional linear accelerator (linac) is the SLAC National Accelerator Laboratory with a length of 3.2km [3], where seminal discoveries in particle physics, free-electron-lasers and plasma wakefield accelerators have been obtained. These conventional accelerators are technically mature. Despite their enormous successes, they have limitations, such as high construction, maintenance costs, and the connected large spatial footprint due to the long distances required to accelerate the particles to high energies. The fundamental reason for this is that the accelerating fields are limited due to breakdown at the accelerator cavity walls due to high accelerating fields that occur at 100 MV/m. Therefore, high-gradient accelerators with reduced size and cost would be highly desirable. Plasma-based wakefield accelerators promise to provide compact machines at reduced financial and spatial footprint because of their ability to afford huge acceleration gradients [4] of the order of hundreds of GV/m in compact setups compared with conventional accelerators [5]. The accelerating structure in this state is the plasma, which plays the enabling role instead of being the limiting factor during the electrical breakdown of a metallic cavity structure through an ionised gas, as in conventional accelerators. In addition, an external feed of injected particle beams is not necessarily needed, because the plasma itself can be exploited as a suitable source of electrons. The power source in the plasma accelerator is a charged particle beam or an intense laser pulse [6] driver, that transfers energy into plasma oscillations

and from the resulting co-moving plasma wake into the particle beam to be accelerated.

The long-term goal of the work presented in this thesis is the development of compact highest quality plasma-based accelerators, which could be realised in the Middle East without requiring an extensive accelerator infrastructure. We aimed to design and create electron beams having unprecedented emittance and brightness, so that advanced light sources like free-electron x-ray lasers (FEL) can be powered. This work can be pursued via particle-in-cell computer codes (such as VORPAL/VSim) [7]. One especially promising scheme is a hybrid plasma acceleration mechanism with novel plasma photocathodes. It is experimentally associated with global projects at a variety of accelerator sites. Subsequently, this system could result in electron bunches of exceedingly high quality and brightness. This, in turn, is being used to generate x-ray flashes of extraordinary brightness in light sources, such as FEL. In theory, research and development, computational modelling and experimental achievements are interconnected and are driven forward in a wider international collaboration led by the University of Strathclyde. The present work is centred on the Trojan Horse mechanism, computational modelling, and exploration, mutually aligned with experimental plans and target applications.

In this chapter, the first section presents an overview of basic plasma properties, including Debye shielding, plasma frequency and dispersion relation, and a description of (laser-based) ionisation processes, including a classification of ionisation according to the Keldysh parameter. The interaction of lasers, plasma and electron beams is the underlying principle of any plasma-based accelerator, and is particularly important for the plasma photocathode scheme.

1.1 Plasma properties

In physics, plasma is an ionised gas, representing the fourth state of matter. Irving Langmuir and his colleague Lewi Tonks were the first who described the plasma in 1920 and introduced the name plasma for an ionised gas [8,9].

Plasma is distinguished and unique due to collective behaviour where the charged particles interact with each other, and the plasma responds to external forces, which determines them collectively [10,11]. Some plasma parameters and characteristics will be briefly described in the subsequent sections.

1.1.1 Debye Shielding

The Debye shielding length is one of the most frequently utilised parameters to characterise plasma. It determines the typical distance D where particles of the opposite sign can shield the electrostatic field from a charged test particle. It may be

described by imagining two charged spherical entities inside the plasma connecting to a battery. Spherical bodies begin to attract particles with opposite charges, creating a cloud of electrons around a positive spherical body and even a cloud of ions surrounding the negative spherical body, while a dielectric layer prevents the recombination process on the plasma surface. Plasma is considered to be cold, implying that there are no thermal activities. At the edge of these two clouds, the potential and thermal energies of particles are in equilibrium. Subsequently, the thickness of the charged cloud is estimated. Assume that a plane grid is placed in a plasma that is maintained at a specific potential ∅.

Furthermore, a potential ∅ that develops due to these two clouds is thought to have a distribution similar to that depicted in figure 1.1, with a maximum value of $\emptyset_0$ at $x = 0$. The mass ratio of electrons to ions is thought to be very small, $\frac{m_e}{m_i} \ll 1$, indicating that the ions are stationary and form a homogeneous positive background.

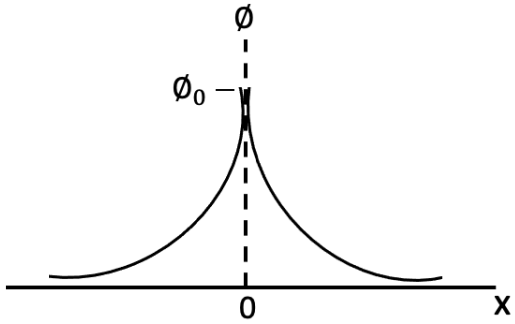

Figure 1.1: Potential distribution near a grid in a plasma, [10].

The disturbance to the potential then tends to fall off quickly into the plasma, unlike in the vacuum scenario. This may be demonstrated with the following key equations [10], Poisson's equation as:

$$\varepsilon_0 \nabla^2 \emptyset = \varepsilon_0 \frac{\partial^2 \emptyset}{\partial x^2} = -e(n_i - n_e) \qquad (1.1)$$

where ε_0 is the permittivity of free space, e is the electron charge, n_i and n_e are ion and electron densities, respectively. These densities can be written according to Boltzmann distribution as:

$$n_i = n_0 e^{-\frac{e\emptyset}{KT}} \quad , \quad n_e = n_0 e^{\frac{e\emptyset}{KT}} \qquad (1.2)$$

Where T and K are gas temperature and Boltzmann constant, respectively, substituting for n_i and n_e, in equation (1.1), then we get:

$$\frac{\partial^2 \emptyset}{\partial x^2} = \frac{2n_0 e}{\varepsilon_0} \sinh(e\emptyset/KT) \qquad (1.3)$$

Where $\sinh(e\emptyset/KT) = \frac{1}{2}(e^{e\emptyset/KT} - e^{-e\emptyset/KT})$. By assuming that $e\emptyset$ is less than KT for electrons and inserting in equation (1.3), we can get the following result:

$$\frac{\partial^2 \emptyset}{\partial x^2} = \frac{n_0 e^2}{\varepsilon_0 KT} \emptyset = \frac{1}{\lambda_D^2} \emptyset \qquad (1.4)$$

$$\text{where } \lambda_D = \sqrt{\frac{\varepsilon_0 KT}{n_\circ e^2}} \qquad (1.5)$$

λ_D stands for the Debye length [12,13], measures shielding distance. As a fundamental but also evident prerequisite for such existence of plasma, the physical dimensions of a system must surpass Debye length (λ_D). Otherwise, the charged particle collection would not behave like plasma unless there is enough zone for such a collective shielding effect to take place.

Another parameter to specify, is the number of electrons inside a Debye sphere N_D, which is provided by [10]:

$$N_D = \frac{4}{3}\pi\lambda_D^3 n_0 \qquad (1.6)$$

Plasma with $N_D >> 1$ is referred to as a weakly-coupled plasma, whereas plasma with $N_D << 1$ is considered as a strongly-coupled plasma [10]. In this thesis, the plasma is considered to be weakly coupled.

1.1.2 Plasma Frequency

Plasma has collective behaviour in the manner of oscillations that occur at a specific frequency, assuming a cold plasma with a uniform charge distribution. If electrons are shifted from an equilibrium state with vanishingly small ions mobility, an electric field is created in the direction of electron movement. This field acts as a restoring force on the electrons, causing them to return to their start point and fluctuate their equilibrium position.

In the simplest scenario, the electron plasma frequency is computed using the following equations in 1D (x-coordinate) for charged particles exposed to the electric field force[10].

Equation of motion:

$$m\left[\frac{\partial \boldsymbol{v_e}}{\partial t} + (\boldsymbol{v_e}.\boldsymbol{\nabla})\boldsymbol{v_e}\right] = -e\boldsymbol{E} \qquad (1.7)$$

Continuity equation:

$$\frac{\partial n_e}{\partial t} + \boldsymbol{\nabla}.(n_e\boldsymbol{v_e}) = 0 \qquad (1.8)$$

Poisson's equation:

$$\varepsilon_0\, \boldsymbol{\nabla}.\boldsymbol{E} = \varepsilon_0 \frac{\partial \boldsymbol{E}}{\partial x} = e\,(n_i - n_e) \qquad (1.9)$$

The variable parameters in the final three equations are linearised before being separated into two parts: equilibrium, and perturbation, as follows:

$$\left.\begin{aligned} n_e &= n_0 + n_1 \\ v_e &= v_0 + v_1 \\ E_e &= E_0 + E_1 \end{aligned}\right] \qquad (1.10)$$

When there is no oscillation in the plasma, the equilibrium components appear. Plasma electrons are thought to remain in a homogeneous and neutral state at rest until being displaced, resulting in:

$$\frac{\partial n_0}{\partial t} = \frac{\partial \vartheta_0}{\partial t} = \frac{\partial E_0}{\partial t} = 0 \qquad (1.11)$$

When an equilibrium state ($n_{i,0} = n_{e,0}$) is assumed, and the ions are at rest and therefore do not move in the turbulent state (n_{i1} =0), Poisson's equation (1.9) can be rewritten as:

$$\varepsilon_0\, \boldsymbol{\nabla}.\boldsymbol{E} = -e\, n_{e1} \qquad (1.12)$$

Then, if the oscillating sections are assumed to be sinusoidal waves, we get:

$$\left.\begin{aligned} n_1 &= n_1 e^{i(kx-wt)} \\ \boldsymbol{v_1} &= v_1 e^{i(kx-wt)}\boldsymbol{e_x} \\ \boldsymbol{E_1} &= E_1 e^{i(kx-wt)}\boldsymbol{e_x} \end{aligned}\right] \qquad (1.13)$$

As a result, the equation of motion (1.7), and continuity equation (1.8) neglecting the nonlinear terms can be rewritten as:

$$m\frac{\partial \boldsymbol{v_1}}{\partial t} = -e\boldsymbol{E_1} \qquad (1.14)$$

$$\frac{\partial n_1}{\partial t} + n_0 \boldsymbol{\nabla}.\boldsymbol{v_1} = 0 \qquad (1.15)$$

As a consequence, the following can be derived by substituting equation (1.13) into equations (1.12), (1.14), and (1.15):

$$-i\, m_e w v_1 = -eE_1 \qquad (1.16)$$

$$-i\, w n_1 = -n_0\, ik\, v_1 \qquad (1.17)$$

$$i\, k\varepsilon_0\, E_1 = -e\, n_1 \qquad (1.18)$$

Inserting equation (1.17) and (1.18) on (1.16) gives:

$$w^2 = \frac{n_0\, e^2}{m\, \varepsilon_0} \qquad (1.19)$$

As a result, the plasma frequency is expressed as:

$$w_{pe} = \sqrt{\frac{n_0\, e^2}{m\, \varepsilon_0}} \qquad \text{(in rad/sec)} \quad (1.20)$$

The plasma frequency determines the duration of harmonic oscillation after electron displacement. The last equation reflects the dependence of the plasma frequency on plasma density [10,14].

1.1.3. Dispersion Relation

Whenever electrons gain thermal energy, the plasma frequency propagates like a wave. Maxwell's equations for such a plasma with external magnetic field $B_0 = 0$ take the form[10] :

$$\boldsymbol{\nabla} \times \boldsymbol{E_1} = -\frac{\partial \boldsymbol{B_1}}{\partial t} \qquad (1.21)$$

$$c^2 \boldsymbol{\nabla} \times \boldsymbol{B_1} = \frac{\partial \boldsymbol{E_1}}{\partial t} + 4\pi \boldsymbol{J_1} \qquad (1.22)$$

By taking the curl of equation (1.21), and applying the time derivative to both sides of equation (1.22), we get:

$$c^2 \boldsymbol{\nabla} \times \frac{\partial \boldsymbol{B_1}}{\partial t} = 4\pi \frac{\partial \boldsymbol{J_1}}{\partial t} + \frac{\partial^2 \boldsymbol{E_1}}{\partial t^2} \qquad (1.23)$$

$$\boldsymbol{\nabla}(\boldsymbol{\nabla}.\boldsymbol{E_1}) - \boldsymbol{\nabla}^2\boldsymbol{E_1} = -\boldsymbol{\nabla} \times \frac{\partial \boldsymbol{B_1}}{\partial t} \quad (1.24)$$

Inserting equation (1.23) into equation (1.24), hence:

$$\boldsymbol{\nabla}(\boldsymbol{\nabla}.\boldsymbol{E_1}) - \boldsymbol{\nabla}^2\boldsymbol{E_1} = -\frac{1}{C^2}\left[4\pi \frac{\partial \boldsymbol{J_1}}{\partial t} + \frac{\partial^2 \boldsymbol{E_1}}{\partial t^2}\right] \quad (1.25)$$

If we consider the waves to vary as $e^{i(kx-\omega t)}$, we get:

$$-\boldsymbol{k}(\boldsymbol{k}.\boldsymbol{E_1}) + K^2\boldsymbol{E_1} = \frac{4\pi i w}{C^2}\boldsymbol{J_1} + \frac{w^2}{c^2}\boldsymbol{E_1} \qquad (1.26)$$

Where *k* is the wavenumber from Maxwell's equations $\boldsymbol{\nabla}.\boldsymbol{E_1} = 0 \ \ or \ \ \boldsymbol{k}.\boldsymbol{E_1} = 0$, so equation (1.26) can be rewritten as:

$$(w^2 - k^2c^2)\boldsymbol{E_1} = -4\pi i w \boldsymbol{J_1} \qquad (1.27)$$

In this state, considering ions are in reset and do not move because they have a large mass, the current density $\boldsymbol{J_1}$ is obtained as:

$$\boldsymbol{J_1} = -n_0 e \boldsymbol{v_1} \qquad (1.28)$$

$\boldsymbol{v_1}$ can be estimated throughout linearising equation of motion, as:

$$\boldsymbol{v_1} = \frac{e}{iwm}\boldsymbol{E_1} \qquad (1.29)$$

Substituting equation (1.29) into (1.28), then:

$$\boldsymbol{J_1} = -((e^2 n_0)/(iwm))\ \boldsymbol{E_1} \qquad (1.30)$$

By inserting equation (1.30) into equation (1.27), we get:

$$(w^2 - k^2c^2)\boldsymbol{E_1} = \frac{4\pi e^2 n_0}{m}\boldsymbol{E_1} \qquad (1.31)$$

with:

$$w^2 = w_{pe}^2 + k^2c^2 \qquad (1.32)$$

Where $w_{pe}^2 = \frac{4\pi e^2 n_0}{m}$, equation (1.32) is known as the dispersion relation [15], for electromagnetic waves in plasma with $B_0 = 0$. It can be observed from this dispersion relation that the frequency is dependent on the wavenumber [10], therefore:

$$k = \frac{w}{c}\sqrt{1 - \frac{w_{pe}^2}{w^2}} \qquad (1.33)$$

This implies that if the frequency of the electromagnetic wave exceeds the plasma frequency, the wavenumber becomes real, allowing for the propagation of an electromagnetic wave within the plasma. In this case, the plasma is considered as underdense. In contrast, the wavenumber becomes imaginary if the electromagnetic wave frequency is less than the plasma frequency. The electromagnetic wave cannot propagate inside the plasma in this condition and therefore is reflected from the plasma. Hence, the plasma is considered as overdense.

1.2 Ionisation

Electrons are bound to the atomic core by their electrostatic potential. A certain energy is needed to break this binding force. This energy is referred to the ionisation energy ζ_i.

There are several ways to create plasma. For example, It can be created as an "electrical discharge" by ionising gas with high voltage applied to electrodes surrounding the gas. In addition, a laser field is another tool to create plasma. In the Keldysh parameter, γ_k, is one approach to distinguish various kinds of ionisation based on laser fields [16-19]. It can be defined as:

$$\gamma_k = \sqrt{\frac{\zeta_i}{2U_p}} \qquad (1.34)$$

Where ζ_i , *and* U_p are considered as ionisation energy of an atom, and the ponderomotive energy of the incident laser, respectively. U_p can be rewritten as:

$$U_P = \frac{e^2 E_0^2}{4\, m_e\, w_l^2} \qquad (1.35)$$

Where E_0, w_l, e, m_e are the electric field that amplitude the frequency, electron charge, and mass, respectively. According to the Keldysh parameters, there are two different regimes:

- Photoionisation regime when $\gamma_k \gg 1$ and
- Field ionisation regime when $\gamma_k \ll 1$ [20].

1.2.1 Photoionisation

If $\zeta_i \gg U_p$ this leads to $\gamma_k \gg 1$, meaning that the incident light has a low intensity and short wavelength [20]. If a valence electron interacts with a single photon with energy that equals the electron's binding energy, the photon's energy is transferred to the electron. In this case, the electron is liberated from the atom's orbit, the atom is ionised, and the photon vanishes. This is known as "single-photon ionisation", as shown in Figure 1.2.

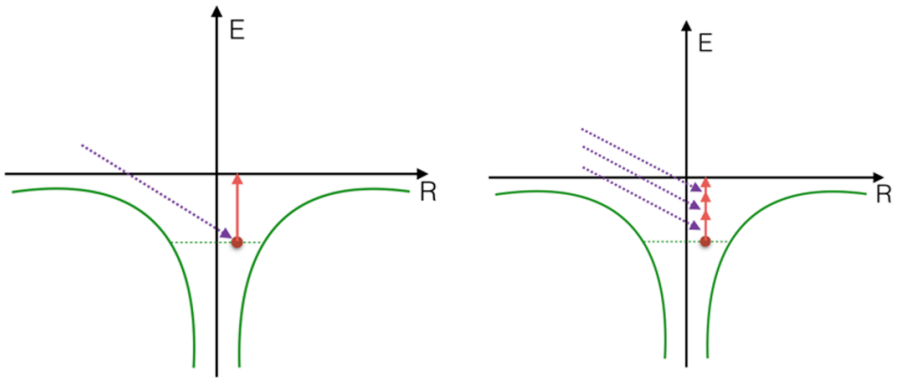

I) Single photon ionisation II) Multi-photon ionisation

Figure 1.2: Photoionisation process illustration. (I) Single photon ionisation: a single photon (purple) interacts with a valence electron (red), causing an electron to be released from the atom's binding potential (green). (II) Multi-photon ionisation: an electron is released by several photons.

On the other hand, when the incident radiation energy is less than the ionisation energy, the ionisation can be induced by absorbing a large number of low-energy photons, and this process is called "multi-photon ionisation". This mechanism requires a high photon intensity I and high photon flux. The probability for liberating one electron with the required number N of photons can be written as [22,21]:

$$P_N \propto I_N$$

1.2.2 Field Ionisation

If the pondermotive energy is greater than the ionisation potential, then Keldysh's parameter $\gamma_k \ll 1$, indicating a high intensity and long-wavelength for the incident light. This implies strong electric fields interacting with the atom [20]. This process leads to tunnel ionisation and barrier suppression ionisation, which are commonly utilised for plasma-wakefield and laser-field interactions.

1.2.2.1 Tunnel Ionisation

Tunnel ionisation is a mechanism in which an incident laser with a strong electric field, and long-wavelength causes an atom potential to drop, allowing the electron to tunnel through the remaining Coulomb Barrier (see Figure 1.3) [23]. Ammosov, Delone, and Krainov presented the ADK model for tunnel ionisation in 1986 [24,25]. To compute the tunnelling ionisation rate for complex (nonhydrogen) atoms under the influence of a constant electric field, the ADK model is utilised. This is performed by averaging the rate over one period of a laser field oscillation, and it is valid when the ionisation potential is smaller than the incident photons energy [26].

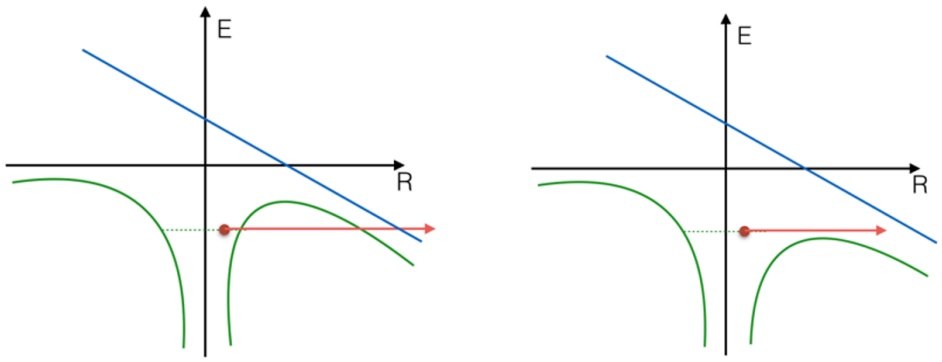

I) Tunnel ionisation II) Barrier suppression ionisation

Figure 1.3: Illustration of field ionisation scheme: (I) Tunnel ionisation: when the length of the potential barrier reduces as a consequence of an intense electric field (blue), the electron (red) can pass through. (II) Barrier suppression ionisation: increasing the intensity causes the electron to be liberated directly from the atom.

The popular formula for ADK ionisation rate, W_{ADK} was adapted for PIC simulation as [27]:

$$W_{ADK} \approx 1.52 \times 10^{15} \left(\frac{4^{n^*} \zeta_i(eV)}{n^* \Gamma(2n^*)} \right) (20.5 \times \frac{\zeta_i^{\frac{3}{2}}(eV)}{E(GVm^{-1})})^{2n^*-1} \times exp\,(-6.83 \frac{\zeta_i^{\frac{3}{2}}(eV)}{E(GVm^{-1})}) \quad (1.36)$$

Where E is the strength of the electric field, Γ is the gamma function, and $n^* \approx 3.69 \frac{z}{\sqrt{\zeta_i(eV)}}$, z is the atomic number. This approximation is valid for electric fields that do not exceed:

$$E_{crit.} = \left(\sqrt{2} - 1\right) 5.14 \times 10^{11} (V/m) \left(\frac{\zeta_i \, eV}{27.2 \, eV}\right)^{3/2} \qquad (1.37)$$

1.2.2.2 Barrier Suppression Ionisation

If the intensity is increased even more, the electron can directly release the atom, as illustrated in Figure 1.4, by lowering the potential barrier without tunnelling. This is known as "barrier suppression ionisation" [26]. It represents a special case of tunnel ionisation.

When the electron may leave the atomic bond freely, the laser's minimum intensity, I_{BSI} follows the relation[26]:

$$I_{BSI}(W/cm^2) = 4 \times 10^9 \, |\zeta_i(ev)|^4 / \, Z^2 \qquad (1.38)$$

Where Z is the ionic charge, for example, the lowest laser intensity is required to ionise a helium atom is in the range [26]:

$$I_{He,BSI} \approx \; 10^{14} \, \mathrm{W/cm^2} \qquad (1.39),$$

which can simply be carried out by focused short laser pulses from modern pulses systems with typical wavelengths.

1.3 Summary

This chapter provides an overview of plasma accelerators, including their basic concept, fundamentals, and features of several of the world's plasma accelerators. In addition, the thesis's objective and goals are provided.
A brief description of the basic plasma parameters, such as Debye shielding, plasma frequency, and dispersion relation, is also introduced. An explanation of (laser-based) ionisation mechanisms is also presented, and a classification of ionisation according to the Keldysh parameter focuses on field ionisation techniques. Any plasma-based accelerator's basic premise is the interaction of lasers, plasma, and electron beams, which is especially critical for the plasma photocathode scheme.

Chapter 2

Plasma-based Accelerator Physics

This chapter provides an overview of the plasma wave excitation techniques and the injection methods of an electron bunch into the plasma cavity. Furthermore, the Trojan Horse scheme concept is described in this chapter. Finally, the particle-in-cell simulation method used by the VSim code is presented.

2.1 Methods of Plasma Wave Excitation

In general, there are different techniques to use whcih involve using plasma for particle acceleration, which are categorised according to how the plasma wave is set up, for example [1,28-30]:

2.1.1 Plasma Wakefield Acceleration (PWFA)

Particle bunches are employed in this approach, such as electrons, which have unidirectional electric fields flowing through the plasma to produce a wakefield by expelling plasma electrons away from positive ions, resulting in a blowout, as shown in Figure 2.1. It consists of a positive charge region surrounded by a negative charge, which produces a strong electric field capable of accelerating any charged particles passing through it [29-31].

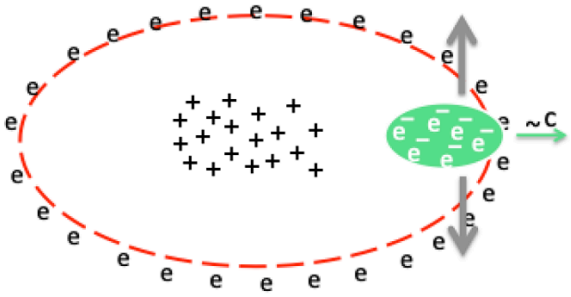

Figure 2.1: PWFA approach: excitation of a plasma wave and the elliptical plasma electron blowout (red) in the wake of an intense electron bunch (green), propagating to the right at approximately the speed of light *c*, [31].

2.1.2 Laser Wakefield Acceleration (LWFA)

A single short laser pulse with high intensity creates a bubble and drives a plasma wave accordingly. When the plasma wavelength is on the order of the laser pulse length $L \sim \lambda_p$, the wakefield is driven more efficiently [1,30]. Laser pulses consist of electromagnetic waves with fields that oscillate in the transverse directions, making them less effective in expelling electrons than electron bunches, known as Laser WakeField Acceleration (LWFA), as illustrated in Figure 2.2 [31].

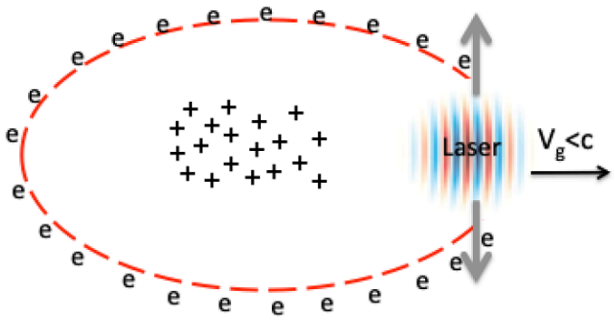

Figure 2.2: LWFA approach: excitation of a plasma wave by an intense laser pulse, propagating at significantly smaller velocities than the speed of light *c* in plasma [31].

2.1.3 Laser Beat-Wave Acceleration (LBWA)

In this approach, two long laser pulses are employed with frequencies w_1 and w_2 to resonantly excite a plasma wave and generate a large amplitude of these waves. This is achieved by adjusting the plasma density and laser frequency to obtain the resonance condition, $\Delta w = w_1 - w_2 \simeq w_p$ where w_p is the plasma frequency, each of these pulses had a role in forming the plasma wave [1,28].

2.1.4 Self-Modulated Laser Wakefield Accelerator (SMLWFA)

SMLWFA concept employs a single long ultra-high intensity laser pulse with a duration longer than the plasma wavelength. Because it has a wavelength longer than

the plasma, the single long-laser pulse is split into a series of short pulses [32-34], resulting in a large-amplitude plasma wave under specific conditions.

Many early studies employed the LBWA and SMLWFA techniques; however, the most recent studies have used PWFA and LWFA techniques. When comparing PWFA and LWFA techniques, researchers discovered that the PWFA approach is significantly superior at expelling plasma electrons than the LWFA technique because it employs unidirectional electric fields rather than a laser pulse. LWFA employs the ponderomotive force for expelling plasma electrons. The electromagnetic fields for laser pulses that oscillate in transverse directions affect plasma electrons [31]. Nevertheless, the required field strength to ionise the plasma region in the case of PWFA is smaller than that in the LWFA case. For example, for an electron bunch with charge, $Q = Ne = 100$ pC, bunch radius $\sigma_r \approx 2\ \mu m$ and bunch length $\sigma_z \approx 4\ \mu m$, the peak electric field for this bunch is about [31]:

$$E_r \approx \frac{Q \times 0.025}{\sigma_r \varepsilon_0 \sigma_z} \qquad (2.1)$$

Where ε_0 is the absolute permittivity in free space. The electric field is approximately equal to $E_r \approx 35\ GV/m$ with the values mentioned above. This field can ionise a medium like hydrogen, which has an ionisation potential of 13.6 eV, but it is more challenging to ionise a medium like helium, which has 24.6 eV. In contrast, the peak electric field for Ti: sapphire lasers with wavelength $\lambda = 800\ nm$ and connected to a normalised vector potential $a_o = 1$ is [31]:

$$E_0 = \frac{2\pi\ m_e c^2}{e\ \lambda} a_\circ \qquad (2.2)$$

Where $a_\circ$ is the normalised amplitude of the laser pulse. This quantity of electric field, which equals 4 TV/m, can ionise a medium such as He. In addition, the particle bunch (as a driver) provides a long distance of acceleration to gain energy compared to a laser pulse by defining the length of beta function, which represents the length of the transverse envelope of the electron beam in plasma accelerators. It can be expressed as [31]:

$$\beta^* = \frac{\gamma}{\epsilon_n} \sigma_{r0}^2 \qquad (2.3)$$

It is clear from this relation that the square of the electron bunch diameter at focus, σ_{r0}, as well as the Lorentz factor $\gamma = (1 - v^2/c^2)^{-1/2}$ and normalised transverse emittance ϵ_n, have a significant impact on the value of the beta function. For example, for σ_{r0} =10μm, $\epsilon_n = 10^{-6}\ mrad$ and energy equal to 1 GeV, the beta function length β^* is equal to 20 cm. Consequently, the Rayleigh length, Z_R of the laser pulse is presented as [31]:

$$Z_R = \pi w_0^2/\lambda \qquad (2.4)$$

Where w_0, and λ are the spot size and wavelength of the laser pulse, respectively. For a Ti: sapphire laser pulse with a wavelength $\lambda = 0.8\ \mu m$, intensities in the range of $I = 10^{18} - 10^{19}\ W/cm^2$ with spot size $w_0 = 10\ \mu m$, and the Rayleigh length for this laser pulse is about $Z_R \approx 400\ \mu$m. This value is much shorter than that of the electron bunch case due to some phenomena occurring in the LWFA cases, such as dephasing, where the speed of the formed beam within the cavity exceeds the laser pulse then enters the deaccelerating region and that limits the acceleration length.

2.2 Electron Bunch Injection into Plasma Cavity

The significance of forming a plasma wakefield in a plasma cavity with a powerful accelerating field is explored. Because of the impact of the injection technique on the bunch's performance, injecting electrons into the plasma cavity is an important aspect of producing a high-quality witness bunch. Moreover, the trapping criterion states that electrons must move through the plasma wakefield at a velocity comparable to the phase velocity of the wakefield to inject electrons into the plasma cavity. It can be expressed as [35]:

$$(1 - \frac{1}{\gamma_p}) \leq \frac{e}{m_e c^2} \Delta\psi \qquad (2.5)$$

Where ψ denotes the electrostatic potential, and γ_p represents the Lorentz factor of the wakefield. The electric potential produced by the longitudinal electric field of the plasma cavity can trap electrons under this condition.
Different methods of electron bunch injection into the plasma cavity have been reported (Esarey [30] and Malka [36]), as well as how they impact the quality of the witness beam. The following is a brief overview of most of these techniques:

2.2.1 Self-Injection

Self-injection occurs when a strong laser intensity or relativistic electron bunch with high electric fields creates a plasma cavity, which expels plasma electrons away from positive ions. The expelled electrons travel and collide at the end of the plasma cavity. It induces the statistical scattering for the electrons within the plasma cavity by trapping some of them. Such a process is known as transverse wave breaking [37].
The latter process continues injecting until the space charge for the trapped electrons deforms the topology of the plasma electric field, which is known as beam loading [40,41].

This injection, however, is unstable for the witness bunch. Consequently, a wide electron spectrum is produced due to its random injection behaviour. Due to the electrons trapped early, this spectrum is accelerated for a longer distance than the electrons trapped later. As a result, the total amount of distributed energy and the emittance of the witness beam is increased. That is recognised as dark current [38,39], and it impacts the features of the witness bunch.

2.2.2 Density Downramp Injection

Density downramp injection [42] is a controllable plasma electron injection method that is more efficient than transverse wave breaking. In this approach, stretching the length of the plasma cavity due to the increasing plasma wavelength reduces the plasma density and produces a drop in the wake phase velocity. Consequently, the proportion of trapped electrons rises since a potential trapping area is large due to the reduced trapping momentum.
Moreover, downramp injection can give better control during injection procedures than self-injection. As a result, it can be applied in both PWFA [43] and LWFA [42] techniques. More recent attention has focused on the provision of density downramp injection to produce high-quality bunches [44,45].

2.2.3 Ionisation Injection

The ionisation injection technique is utilised to control electron trapping better, since it can inject electrons directly into the plasma cavity rather than injecting them at the cavity rear in a plasma accelerator. Consequently, these approaches are typically based on the employment of two types of gas mixtures with various ionisation levels separated by a significant ionisation gap or a single gas with multiple ionisation levels [46, 47]. The low ionisation threshold (LIT) is the first ionisation level, and it is utilised to drive the plasma wake. The second level, known as the high ionisation threshold (HIT), is utilised to generate free electrons at a specified place within the plasma cavity by the laser field when the trapping requirement (equation 2.5) is met, at which point the electrons can be trapped and accelerated [48]. The laser pulse characteristics allow us to manipulate the place and time at which electrons are released.

This approach is effective for trapping the electrons in the LWFA technique. Otherwise, it has certain drawbacks, like decreasing the laser intensity for a driver to control electron trapping to avoid ionising HIT medium by the driving pulse. In addition, a precision synchronisation between the laser pulse and the wakefield is

required. Furthermore, the quality of the electron bunch is influenced by many of the laser characteristics (described in section 2.1).

2.3 Trojan Horse Schem

Based on the characteristics mentioned in section 2.1, an electron bunch is excellent for creating plasma waves, but a laser pulse is ideal for ionising the plasma medium. Accordingly, Hidding *et al.,* 2012 [49], created a novel hybrid system to combine the benefits of the two approaches of LWFA and PWFA. This scheme is known as Trojan Horse (TH) (underdense photocathode process) [31, 49-51]. It emits electron bunches with ultra-low emittance values in the range of $\epsilon =$ 100 to 10 nm rad with high brightness in the order of $B = 10^{17}$ to 10^{19} $\mathrm{A/m^2.rad^2}$. The concept of underdense plasma asserts that electron beam density should be higher than that of plasma, which is critical for creating a plasma cavity.
Moreover, the requirements for this technique are the availability of LIT and HIT media, electron beam propagation through an underdense plasma, and a synchronising co-propagating laser pulse. In this technique, a compact electron bunch is used as a driver to travel through an underdense plasma to set up the plasma blowout at a LIT medium like hydrogen. Additionally, a synchronised laser pulse is focused onto a HIT medium, like that of helium, to liberate He electrons inside the blowout directly. After that, these electrons are subsequently trapped and compressed, resulting in a compact beam defined as "witness beam or witness bunch". The bunch is accelerated to gain highly-tunable energy. Using numerical simulations, we observed the Trojan Horse injection process in these circumstances, as illustrated in Figure 2.3.

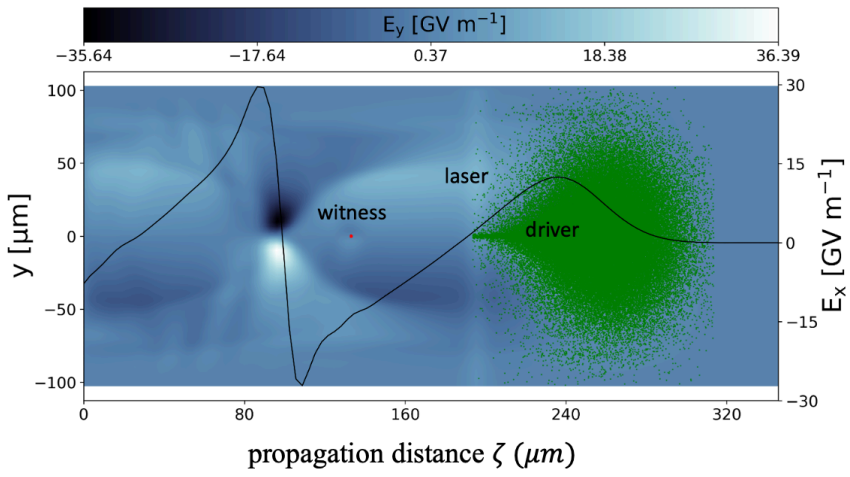

Figure 2.3: PIC simulation snapshot of the Trojan Horse technique, in which the driver (electron beam) sets up the plasma blowout in the LIT medium (H), while a moderately intense focused laser pulse ionises HIT medium (He), and thus, releases He electrons to form the witness bunch.

The quality of the witness bunch is typically controlled by altering the properties of the laser pulse, such as the spot size w_0 of the laser pulse and the laser intensity a_0. The challenge in this process is to compromise among the bunch's parameters.

Moreover, the Trojan Horse hybrid scheme is a useful tool for producing electron bunches having low emittance and high brightness while reducing energy spread through beam loading [31]. Therefore, it can be used for many applications such as Free Electron Lasers (FEL).

This project aims to develop an efficient compact plasma accelerator that could be established in the Middle East without a large infrastructure. To implement a powerful FEL, we want to create electron beams with unprecedented emittance and brightness.

2.4 Particle-in-cell Simulation for VSim Code

In a plasma system, a nonlinear state creates a high density of particles with strong interactions between them and with the fields. It results in extremely complex behaviour. As a result, finding an analytical solution in 3D without reducing the computations is extremely challenging. The particle-in-cell (PIC) technique is utilised to solve this problem, since it can provide useful tools to simplify the complex behaviour of plasmas.

PIC methods were first implemented in the late 1950s [52]. As a result of its ability to simulate the experimental results, the PIC simulation has evolved substantially in recent years. VSim is a 3D PIC code used to simulate for Trojan Horse configurations. In particular, the VSim code is provided by Tech-X has been used in this thesis to perform such simulation [53]. The VSim code uses a mix of PIC and finite-difference time-domain (FDTD) concepts to obtain reliable results. Likewise, the FDTD technique in the leapfrog type of the time advancement formulas assumes the estimation of the Electric and magnetic field at half – and one- integer of the time steps, respectively.

In this study, the whole 3D laser- and beam-driven PWFA scenarios were computed using the high-performance multi-physics cross-platform VSim. All operations in VSim are internal, allowing for local communication through the Message Passing Interface (MPI) for scalability to over 30000 processing units. The particles are organised consistently with this closeness on the nodes. B-splines of second order are employed to form the macro-particles [54]. Moreover, the VSim concept reduces the number of particles in a macroscopic calculation to make plasma simulation easier.

Additionally, to decrease self-forces and analytical heating, higher-order field interpolation is required for the Lorentz force. The currents are also regulated to

minimise analytical heating. The ADK tunnels ionised concept (equation 1.36) is used to establish the ionising approach. This field-ionisation approach is used for ionisation processes generated from lasers, and the space-charge fields of charged particles are used to ionise matter. Furthermore, perfectly matched layers (PML) are installed around the simulation box's edges to collect any incoming wave energy and avoid reflection back towards the simulation domain. The simulated box was shifted at the light speed along with the plasma wave to save processing costs and exclude areas of no physical significance. The ionising laser is not completely resolved in the TH simulation, but its surround minimises the computational load and makes the simulation run quicker [55].

It preserves plasma's fundamental behaviour, in which each macro particle is composed of a large number of smaller particles [56]. We wish to simulate an arbitrary physical volume made up of particles as well as electric and magnetic fields. We assume that a mesh covers this volume with a specific number of cells. In one simulation time, Figure (2.4) depicts the PIC process. The initial locations and velocities of particles are weighted based on their distance from the mesh point at the start of the numerical simulation. Calculating the densities of charged particles and current is the next step. Then, by Maxwell equations, the electric and magnetic fields are derived. Finally, the new locations and velocities of particles are calculated using Lorentz force. The simulation is tested on the FACET II Trojan Horse experiment (E210) [50]. In 2011, FACET consented to the "E210: Trojan Horse PWFA" project, which began as a multi-institutional partnership of international research teams (Strathclyde-UK, UCLA and Austin -USA, Hamburg- Germany, and Oslo- Norway), research facilities (SLAC- USA and DESY-Germany), incorporation with some companies (RadiaBeam, Tech-X, and RadiaSoft - USA) in 2012. Accordingly, E-210 at SLAC was significant cooperation to demonstrate the plasma photocathode technology for the first time [57], which is regarded as a promising experiment for the Trojan Horse.

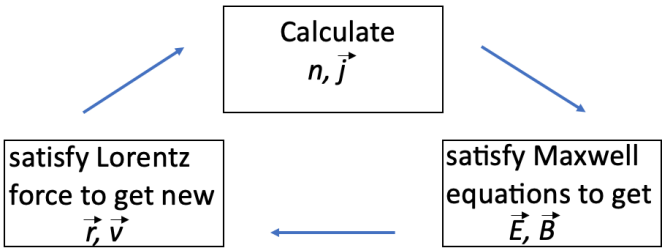

Figure 2.4: PIC simulation cycle used for Trojan Horse configurations.

2.5 Summary

The excitation techniques for plasma waves, such as plasma wakefield acceleration (PWFA), laser Wakefield acceleration (LWFA), laser beat-wave acceleration (LBWA), and self-modulated laser wakefield accelerator (SMLWFA), are briefly explained in this chapter. Because particle bunches, particularly electrons, are used to generate a wakefield in PWFA. The injection mechanism (using LWFA) have a significant influence on the performance of the bunch. Therefore, an overview of electron bunch injection techniques into the plasma cavity is described, including self, density downramp, and ionisation injections.
The excitation methods and ionisation techniques have been given as a prologue since the Trojan Horse regime combines PWFA and LWFA excitations. Moreover, a basic overview of the Trojan Horse concept was presented. Finally, a description of the PIC simulation and VSim code, as well as the simulation cycle used to model the FACET II Trojan Horse experiment (E210), are provided.

Chapter 3

The Properties of the Witness Bunch and its Applications in Free Electron Laser

Chapter 3 describes the quality of witness bunch in FEL, which is impacted by many parameters, including emittance, brightness, and space charge. Free electron lasers were also investigated for potential use on the ultrabright light sources.

3.1 The Quality of the Witness Bunch

Each laboratory accelerator facility should be able to produce extremely small electron bunches with a high quality of emittance, energy spread, and beam current. Subsequently, the quality of such electron beam played a key role in developing the FEL light source. During the undulator, this was adequate to attain the saturation of FEL amplification inside a single path of the bunch. Finally, this is offered up the potential of expanding the wavelength range from the VUV to the X-ray zone.

3.1.1 The Emittance

Normalised emittance is the most important parameter for assessing the quality of electron bunch, since it describes the distribution of momentum and the transverse form of the electron beam. Therefore, the ability to achieve low emittance of witness bunch is essential for developing a new generation of light sources, such as FELs. Although the concept of the emittance is established for such an ideal distribution of elliptical phase space, not all electron bunches provide the same shape practically, especially the plasma accelerator witness bunch, which has a complicated transverse phase space shape. Lapostolle and Sacherer [58,59] introduced the concept of the equivalent beam. When the first X and second X^2 moments are the same in that beam, two bunches with distinct phase-space distributions have the same charge density and energy. As a result, we can explain these bunches using their RMS values, and we can write the RMS emittance as [60]:

$$\varepsilon_x = (\langle X^2 \rangle \langle (X')^2 \rangle - \langle XX' \rangle^2)^{1/2} \qquad (3.1)$$

Where X is the transverse position, X' is the divergence of the particle, and the $\langle XX' \rangle^2$ represents the correlation between two quantities, X and X'. Equation (3.1) estimates the particle spread; therefore, the ε_x determines the quality of the bunch [61].

Additionally, because the emittance is usually conserved by acceleration, the initial situation of the trapped electron bunch has a significant impact on the quality of the electron bunch. Therefore, it is helpful to provide another definition of emittance to remain constant during acceleration, which is called "normalised emittance", it is given by:

$$\varepsilon_n = \beta\gamma\varepsilon_x \quad , \beta = {}^{v}/_{c} \sim 1 \qquad (3.2)$$

Where v is the charged particle speed, c is the light speed, and γ represents Lorentz factor which equals to $[1 / (1 - \beta^2)^{1/2}]$. This normalised emittance is an essential feature of electron bunch to measure their transverse size and their attempt to diverge, which is crucial in accelerators and for many bunch applications like FELs.

3.1.2 The Brightness

Another essential factor to take into consideration when evaluating bunch quality is the total current of the bunches. This current is expressed as:

$$I = {}^{\partial Q}/_{\partial t} \approx {}^{Q}/_{\tau} \qquad (3.3)$$

It exhibits the longitudinal charge, and Q distribution over the bunch duration τ. As a result, high-current bunches are preferable over low-current bunches in most applications because they can establish more electron beam interactions per unit of time. The normalised brightness [62] is a parameter that links the normalised emittance and the current of an electron bunch, which is given by:

$$B = \frac{2\,I}{\varepsilon_{n,(x,y)}} \qquad (3.4)$$

3.1.3 Space charge

Owing to Coulomb forces, it is difficult to compress charged particles. In particular, space charge forces are one of these forces that are formed directly by the distribution of charge. Therefore, these forces are responsible for undesired beam dynamics, including instability, beam emittance growth, and energy loss processes. Hence, the space charge force F_{sc} is considered as inversely proportional to electron energy [63]:

$$F_{sc} \propto \frac{1}{\gamma^2} \quad \sim \frac{1}{(2E)^2} \qquad (3.5)$$

This means that the focusing force and defocusing force balance are out, as the electron energy increases. As a result, the contribution of the space charge is reduced. Figure 3.1 shows the radial Coulomb force for an electron in a stationary mode. The field lines contract towards being perpendicular to the direction of motion for relativistic electrons. The radial Lorentz force of particles inside the bunch is expressed as [64,65]:

$$F_r = q\,(E + v \times B) \qquad (3.6)$$

Where q is the electron charge, and the electric field is predicted using Gauss law for such a long bunch having uniform density represented as:

$$E = \frac{e\,r\,n_b}{2\,\varepsilon_0} \qquad (3.7)$$

In Faraday's law, the magnetic field is equal to:

$$B = \frac{e\,r\,\mu_0 n_b}{2} \qquad (3.8)$$

Inserting equations (3.7) and (3.8) on equation (3.6), we get:

$$F_r = qE\,(1 - \frac{v^2}{c^2}) = \frac{qE}{\gamma^2} \qquad (3.9)$$

Where $c^2 = (\varepsilon_0\,\mu_0)^{-1}$. In the early stages of producing the witness bunch at low energies, the space charge forces rise and become dominant.

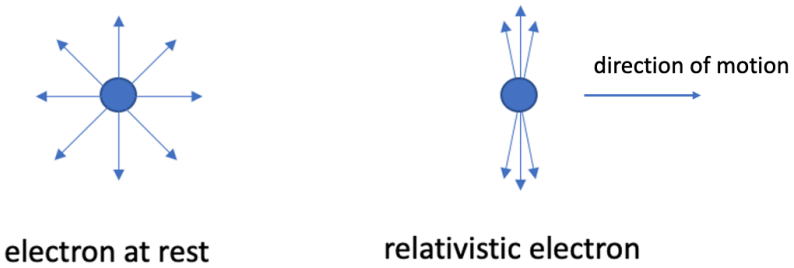

Figure 3.1: Electron field lines at stationary-state (left) and in motion with relative speed (right), [65].

It is vital to understand the effect of the space charge to avoid any impacts on the quality of the witness bunch. As a result, the envelope formulas specify the relationship between space charge and emittance, which can be used to anticipate whether space charge effects are significant. With concerns to the assumption of a symmetric distribution transversely $(\sigma_x = \sigma_y = \sigma_o)$, we compute the space charge to emittance ratio as follows [66]:

$$R_0 = \frac{I_p\, \sigma_o^2}{2\, I_0\, \gamma\, \varepsilon_n^2} \qquad (3.10)$$

Where Ip is the peak current of the bunch, $I_0 = \frac{ec}{r_e}$, and r_e are the electron radius. When $R_0 < 1$, the bunch is emittance dominated; hence space charge forces are neglected, otherwise, whenever $R_0 > 1$, space charge forces are dominated.

3.2 Free Electron Laser (FEL) as an Application

A plasma accelerator is a useful source for witness bunches with a high current, low emittance, and high energy created over short distances [30]. As a consequence, a plasma accelerator driven FEL is an attractive potential coherent light sources that operate in the x-ray zone [67]. In addition, compared to traditional RF accelerators, the underdense plasma photocathode technology [49] has improved the transverse emittance, current, and brightness of the witness bunch. Furthermore, massive energy spread and associated energy spread (energy chirp), which have the potential to be obstacles to FEL processes [68], are by far the most serious challenges.

3.2.1 FEL Concept

The FEL is a high-energy coherent radiation source that operates at wavelengths ranging from infrared to hard x-ray, making it a one-of-a-kind source. Accordingly, two major advancements could contribute significantly to the high-quality production of FEL radiation [69]. To begin with, advanced plasma-based accelerators have been developed to produce high energy, high current, and low normalised emittance electron bunches, resulting in a tighter concentration of the bunch. In this study, we employed TH as an electron bunch source (as indicated in section 2.3) while considering that energy dispersion, as previously stated (section 3.2), has an adverse impact on the FEL. Furthermore, the criterion of resonant wavelength is the best approach to fully understand this adverse impact:

$$\lambda_0 = {\lambda_u}/{2\gamma^2} \quad (1 + a_u^2) \qquad (3.11)$$

Where λ_0 is the radiation wavelength, λ_u is the length of undulator period, γ represents the Lorentz factor of such the electron, and a_u is undulator parameter [67]. Considering resonant wavelength conditions, a large energy spread causes spread in resonant conditions, which reduces FEL gain. Likewise, another TH-generated obstacle is related to an energy chirp in the electron bunch. This signifies that the energy of the tail of the electron bunch is higher than that of the head, and this is a natural result of such an accelerated bunch in an electric field within blowout. As a result of the energy chirp, the lasing process on the FEL is disrupted, resulting in Coherent Spontaneous Emission (CSE) [70,71]. Moreover, electron bunch dispersion prevents the FEL from bunching since electron bunches generate radiation at different wavelengths.

The second advancement contributes to the production of high-quality of FEL radiation. Likewise, the undulator is a special device with linear alternating magnets having a period of λ_u. As the relativistic electrons propagate through the undulator, this type of alternation tries to deflect them [72]. A schematic diagram of the undulator employed in this section, as shown in Figure 3.2.

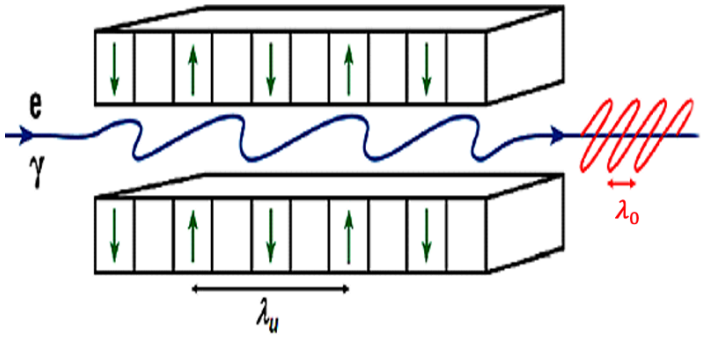

Figure 3.2: Electron bunch propagates along a planar undulator with periodic magnet arrangement, thereby emitting resonant radiation [73].

3.2.2 Electron Bunch Production for driving FEL

An electron bunch generated from the Trojan Horse technique in collaboration with a colleague [68] is proposed, using the identical procedure and settings that will be described in detail in section 4.2.1. However, the duration of the PIC simulation was changed to the t_{sim}=4.6 ps with propagation distance z_{sim}=14 mm and using driver beam charge Q_d = 800pC. The outputs of the witness bunch generated from the simulation are summarised in table 3.1.

Name	Symbol	Values
Energy	Ww	247.3 MeV
Lorentz factor	γ	483.9
Slice energy spread	σ_γ/γ	0.3%
Normalised emittance	ε_n	21nm rad
RMS bunch length	σ_W	0.26 μm
Bunch charge	Q_w	3.6 pC
Peak current	I	1.5 kA
5D Brightness	B_{5D}	6.8 x10^{18} A/m^2/rad^2

Table 3.1: Projected witness bunch parameters at the end of acceleration z of 14 mm [68].

This section focuses on the 3D simulation of a plasma accelerator-driven FEL. In particular, the Puffin code is used to perform FEL modelling [74]. It can simulate the effects of the macroscopic electron beam change by the effects of energy chirp, any CSE, and Self Amplified Coherent Spontaneous Emission (SACSE). The VSim code's output files (.h5 files) have been analysed, and several parameters for the electron bunch have been depicted in Figure 3.3. It is clear from this Figure that the original bunch of macroparticles, their characteristics, and the witness bunch propagate in the z-axis are along with the undulator. These characteristics include normalised emittance ε_n, Lorentz factor γ, RMS energy spread σ_γ as well as the current I.

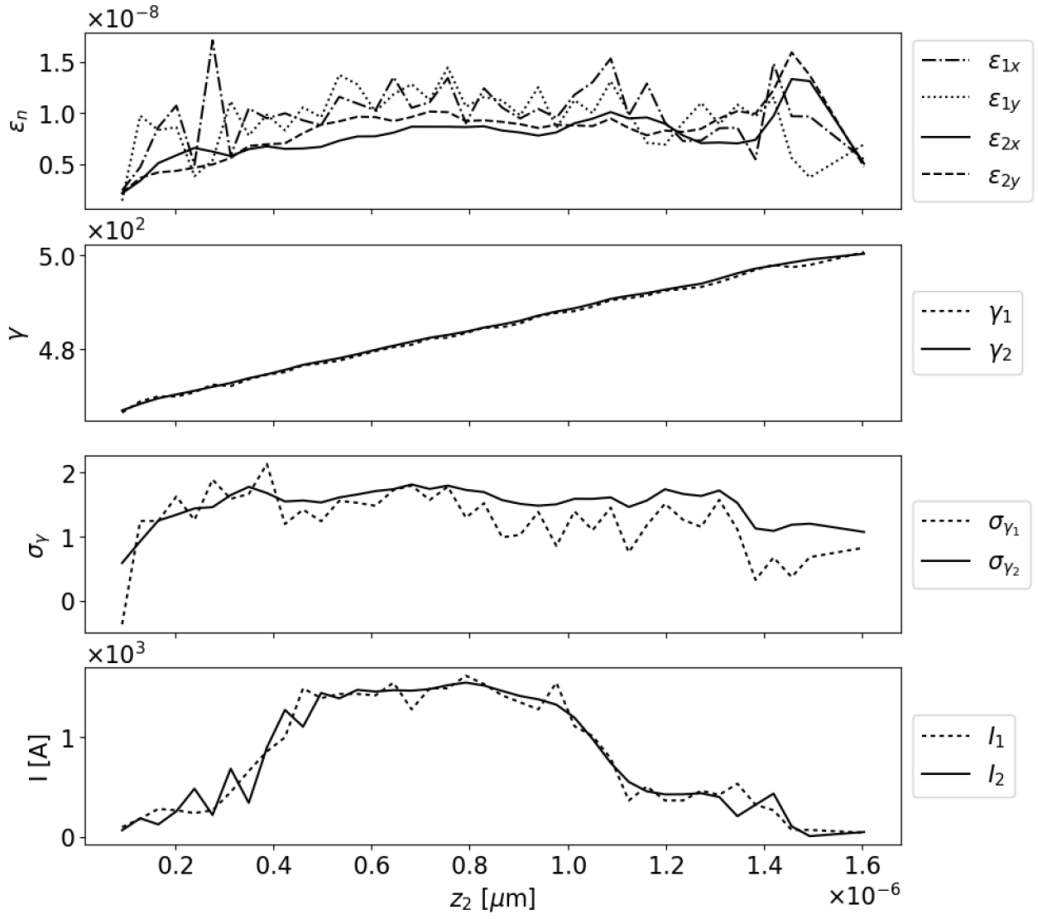

Figure 3.3: From top to bottom, ε_n is the normalised emittance of the witness bunch, γ represents Lorentz factor, σ_γ is RMS energy spread, and I represents the current as a function of z [68].

Consequently, the resulting bunch has a low normalised emittance of approximately 21 nm. rad, a current exceeds 1 kA with a slice energy width σ_γ of 1.5 on average with relatively-slice energy spreading σ_γ/γ of 0.3% [68,75]. Additionally, the generated .h5 files from the VSim code have been organised to implement the Puffin code. Then, the study procedure [76] was used to match the microparticles bunch with a natural focusing channel for the undulator. After that, the parameters of such an undulator device, a_u = 1.0 and λ_u = 0.015 m, were therefore selected to be suitable for the produced bunch. According to these parameters, the value of radiation wavelength is λ_0 = 67 nm, and it was then executed using the Puffin code.

As a result of energy chirp and emitting considerable CSE power, the electron pulse will shorten when propagated through the undulator. CSE has been observed to be able to drive the bunch's electrons into the weak super-radiant regimes. This is not the effect of FEL, which is in a collective high gain regime. There are various methods

for removing the energy chirp produced in the electron bunch, either within the TH scheme [69,77] or even after its extraction [68]. In this project, we performed a simple geometrical approach to reduce the effect of energy chirp. Figure 3.4 [71] illustrates that this approach involves rotating the bunch in phase space to diminish the microparticle's energy chirp. Consequently, with the unchirped beam, we observed a clear bunching at the resonant radiation wavelength with SASE as compared to the chirped simulation. Finally, this approach may open the way for a promising future in which plasma accelerators are used to drive FEL [71].

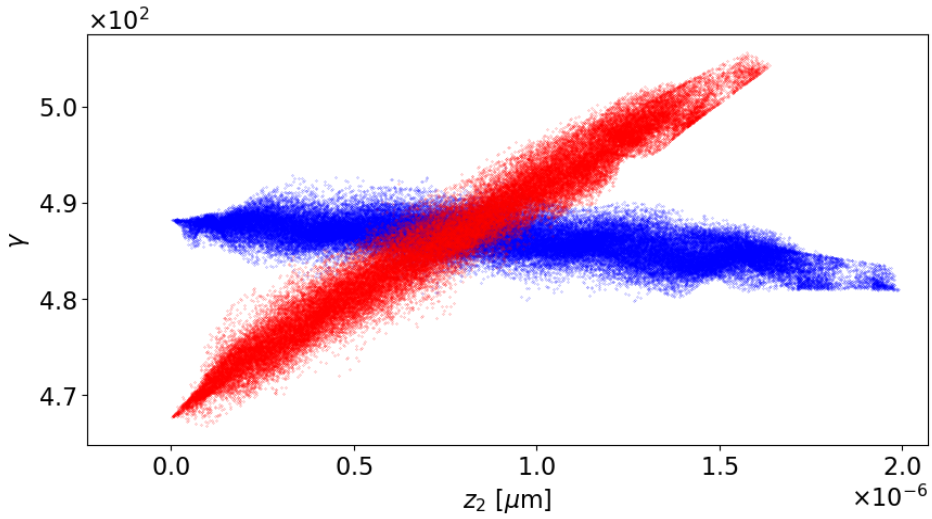

Figure 3.4: The bunch propagates along the positive z-axis; the red bunch represents the output phase space of the accelerator electron bunch, Lorentz factor versus position z_2 inside the bunch. At the same time, the blue bunch shows electron bunch after the energy chirp has been artificially removed [71].

3.3 Summary

This chapter discussed the properties of the witness bunch in a free-electron laser, such as its quality, emittance, brightness, space charge. Additionally, the concept of FEL is described, as well as the electron bunch generation for driving FEL. PIC is used to simulate an electron bunch using the TH method, utilising duration, propagation distance, and beam charge as inputs. Table 3.1 summarises the features of the witness bunch at the end of acceleration (14 mm). The emittance, brightness, and bunch charge of this bunch are 21 nm rad, 6.8×10^{18} A/m^2/rad^2, and 3.6 pC, respectively.

Furthermore, Puffin is used to model the impacts of energy chirp on the macroscopic electron beam and any CSE and SACSE in FEL. Normalised emittance, Lorentz factor,

RMS energy spread, and current as a function of propagation distance are the aspects of the bunch. The VSim code outputs are then incorporated in Puffin code to fit the microparticles bunch to a suitable focusing channel for the modulator. The electron pulses will shrink when carried via the undulator due to energy chirp and producing significant CSE power. According to the findings, CSE was shown to be capable of driving the bunch's electrons into weak super-radiant regimes. This is not the impact of FEL, which is in a high gain collective mode.

The main challenge in this research is to use a simple geometrical strategy to minimise the energy chirp effects. This strategy involves rotating the bunch in phase space to reduce the microparticle's energy chirp. As a result, when comparing the chirped and unchirped simulations, we see a distinct and evident bunching at the resonant radiation wavelength with SASE. Finally, this method might pave the way for a bright future in which plasma accelerators are employed to power FELs.

Chapter 4

Study of Parametric Dependencies of the Injector Laser Pulse

This chapter discusses the impact of various injector laser pulse parameters on the electron beams produced in the collinear Trojan Horse scheme. Exploratory simulations have been used to identify several parameter constellations to be studied to maximise the insight gained at affordable computational costs. As key parameters of interest, the laser pulse spot size w_0, its laser intensity in the form of the dimensionless laser amplitude a_0, and the spatiotemporal position concerning the blowout have been selected. As conventional photocathodes, the variation of the plasma photocathode laser pulse parameters is the crucial parameter that determines the initial fundamental witness bunch properties, such as charge. For example, tight focusing of the laser pulse, and its comparable low intensity produce electrons in a small volume and with small transverse residual momentum, are key to produce ultralow emittance, and ultrahigh brightness electron bunches. However, similarly to conventional photocathodes in linacs, the accelerating and focusing fields, phase mixing, and space charge have a very important influence on the accelerating witness bunch and its parameter evolution. In broad strokes, the injector part of the plasma photocathode – plasma wakefield accelerator system is largely determined by the laser pulse parameters and its spatiotemporal positioning. The high ionisation threshold (HIT) plasma medium type and density, and the accelerator of the plasma photocathode – plasma wakefield accelerator system are largely determined by the driver beam configuration, the low ionisation threshold (LIT) medium type, and density [31,49]. While there is a far-reaching decoupling between the injector and the accelerator – a particular strength of the plasma photocathode mechanism – it is still significant inter-dependence of the injector and accelerator, for example, reflected by the transverse and longitudinal matching relations.

4.1 Low-fidelity Particle-in-cell Simulation

The fully explicit particle-in-cell code VSim/Vorpal has been used for all simulations presented in this thesis. The input deck describing the physics representation, and the associated techniques for computational efficiency and numerical noise management have been developed collaboratively in the group over many years since 2012 [49]. The required resolution and noise management are based on the explored physics and adapted from case to case. The VSim code calculates the

tunnelling ionisation rates by considering the He gas density, spot size and intensity of laser pulse, and ionisation potential to calculate how much charge is released per time step, then, the accumulated charge is the final witness charge. The PWFA stage and the subsequent controlled injection of witness bunches via the Trojan Horse mechanism is modelled in 3D. Here, the moving window simulation box, propagating with the speed of light, contains 109 x 65 x 65 cells with cell size DX=DY=DZ= 3.2 μm to accommodate the plasma blowout structure, and one macroparticle for each cell. This corresponds to nearly 450,000 macroparticles forming the plasma background. The PIC-simulation was run for $t_{sim} \approx 3.3$ ps, corresponding to a propagation distance of $z_{sim} \approx 10$ mm. The charge of the Gaussian electron driver beam is set to $Q_d = 900$ pC with beam energy W_d=10 GeV, energy spread 2%, and its longitudinal $\sigma_{z,d} = 20$ μm (r.m.s), and transverse $\sigma_{(x,y),d} = 3.5$ μm (r.m.s) dimensions are in one scenario matched (4.2.1) with the plasma density. In this study, a combination of two different types of gas was used. For the LIT component, hydrogen gas with density n_H= 4.95 x 10^{16} cm^{-3} and plasma wavelength λ_p=150 μm was used, and for the HIT component, helium gas with density n_{He} =1.5 x 10^{17} cm^{-3}. These parameters have been applied to all cases studied in this chapter. A laser pulse ionises the HIT component inside the plasma wakefield for the Trojan Horse injection. The laser is implemented in the envelope approximation, with an intense laser pulse following up the driver beam at the distance = 100 μm, FWHM pulse duration τ = 30 fs, and at z_i = 2mm reaches its focal position where the intensity of laser pulse is just a little above the threshold of tunnel-ionisation of the neutral helium. This leads to the release of He electrons on-axis directly inside the blowout cavity. The thereby formed witness beam is then accelerated by the plasma wave for 10 mm, which leads to witness beam energies in the range of 90-150 MeV based on the precise laser setting. The generated witness beams are then visualised, post-processed and analysed.

In this thesis, the search was used computational resources of the National Energy Research Scientific Computing Center - KAUST, which is supported by Shaheen Supercomputer (project k1191), and the National Center for Combustion and Plasma Technology – KACST continued support.

4.2 Variation of the Injector Laser Pulse

It is crucial to examine the variation of plasma photocathode laser pulse, since the quality of the witness bunch strongly depends on the properties of the laser pulse, such as spot size of laser $w_{0,}$ and normalised amplitude quantity a_0. On the one hand, the variation is necessary to adjust and optimise the quality of the produced witness bunches [31]. On the contrary, it is also important to understand the impact of the laser pulse parameters.

As mentioned in section (2.3), in the plasma photocathode technique, the driver beam produces a plasma wave, and the co-moving, collinear, spatiotemporally synchronised laser pulse is focused within the blowout. The intensity of the laser pulse is tuned to exceed the helium ionisation threshold (or, more generally, the higher ionisation medium threshold) around its focus, which releases helium electrons confined directly inside blowout with negligible transverse momentum. The compactness of the release volume in combination with the low transverse momentum leads to confinement of the initial transverse phase space. Thus, it produces a witness bunch with low emittance, if the amount of released charge becomes not too high and the emittance becomes space-charge dominated (see chapter 5).

The electron beam driver that is used to excite the LIT plasma wave can come either from a conventional, radiofrequency cavity-based accelerator, or from LWFA [31]. The origin of the driver beam influences many features of the setup, because, for example, while an electron beam from a state-of-the-art linac can be assumed to be stable, have low energy spread, and electron driver beam from LWFA would tend to have a larger energy spread, be shorter, and have higher current. For a suitable setup, one may consider this, which may also impact the choice for the injector laser beam parameters to form the initial phase space for the witness bunch, with high tunability [78].

4.2.1 The Spot Size of the Laser Pulse

The normalised transverse emittance in one dimension has a proportional dependence with the laser pulse spot size and its normalised amplitude that can be expressed as $\varepsilon_n \propto w_0 a_0$. Therefore, the initial 'thermal' emittance due to the residual momentum of the release laser pulse is combined with the laser pulse spot size. It should be noted that the laser pulse spot size during the release process is not the same as the formed electron witness bunch, once trapped. First, the laser intensity may not be large enough to the tunnel that ionises the HIT medium, thus releasing electrons across the full spot size transverse profile. Second, the released electrons and the formed witness bunch formed by them are then subject to the strong focusing forces of the plasma wave. At the same time, the formed witness bunch exhibits transverse forces due to Coulomb expulsion and Lorentz-contracted transverse electric fields. The relation and equilibrium between transverse fields of the witness bunch, and the transverse wakefields at the position of the witness beam are very important for the witness beam evolution.

The witness bunch and the driver electron beam are subjected to the transverse wakefields of the plasma wave. Therefore, the important part of plasma wakefield acceleration is ensuring the stability of the driver beam propagation inside the plasma blowout, which can be optimised by applying the beam matching formula:

$$r^2_{matched} = \varepsilon_n \left(\sqrt{2} / (\omega_p/c) / \sqrt{\gamma}\right) \qquad (4.1)$$

By adjusting the radius r of the driver beam to its normalised emittance ε_n, Lorentz factor γ, and the plasma frequency ω_p [79]. The plasma frequency is dependent on the plasma density and represents the focusing ion forces in the electron-free blowout. This means that the electron driver beam transverse forces (pointing to the outside) are in equilibrium with the transverse forces (pointing inwards) produced by the ion background generated by the electron-ion charge separation in the plasma. Before applying equation (4.1), the drive beam emittance was 2.25×10^{-6} m rad, the radius is 30×10^{-6} m with plasma wavelength 150 μm, and gamma factor 19500. Nevertheless, after applying it, a beam emittance of 50×10^{-6} m rad, and the matched radius would be equal to 3.5×10^{-6} m. Reduced emittance aims to get a smaller matched radius, leading to higher densities, which means higher fields. The plasma photocathode spot size, w_0, and laser pulse intensity, a_0, were varied in one case before applying the matching condition, and in the other case after it was applied. We start by changing w_0 and fixing a_0 to 0.018. The spot size w_0 has been varied from $w_0 = 7$ μm to $w_0 = 19$ μm.

The driver electron beam and laser pulse parameters are summarised in table 4.1. Witness beam charges were calculated on the one hand via VSim, and on the other hand, via an external tunnelling ionisation script developed by D. Ullmann and T. Heinemann. This external script is much faster than a full PIC-simulation with VSim and can be used to estimate approximate charge yields to be obtained in VSim, by considering the laser pulse parameters, gas density, and ionisation potential. In Figure (4.1), the calculated charge yields from the external script and from VSim are compared across the full range of considered spot sizes w_0. The witness beam charge predicted by the external tunnelling ionisation script is slightly higher than those obtained in the simulations. One of the reasons for this difference is the use of lower resolution in the full PIC simulation, which leads to the interpolation of fields and can be responsible for reduced tunnel ionisation rates. The trend is correct, confirming that the underlying calculations and trends are confirmed.

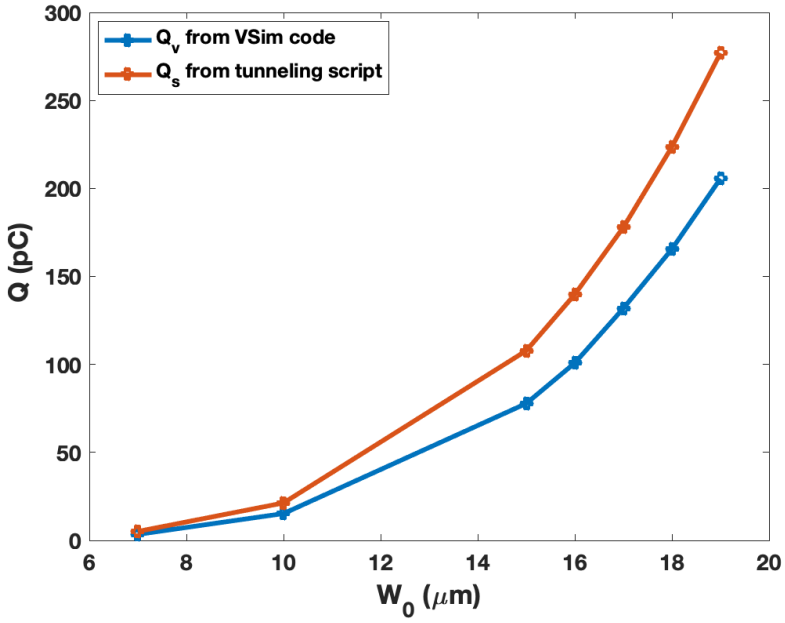

Figure 4.1: Plot of charge Q_v predicted by the VSim code and charge Q_s expected from the tunnelling ionisation script versus spot size of plasma photocathode laser pulse.

Next, Figure 4.2 shows the evolution of the projected transverse emittance, brightness, and mean energy during propagation over a distance of 10 mm for the unmatched case, and the matched case, obtained by VSim.

Without transverse matching

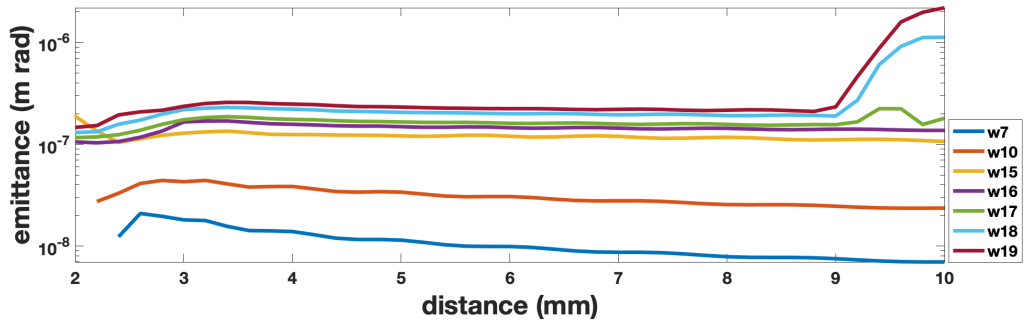

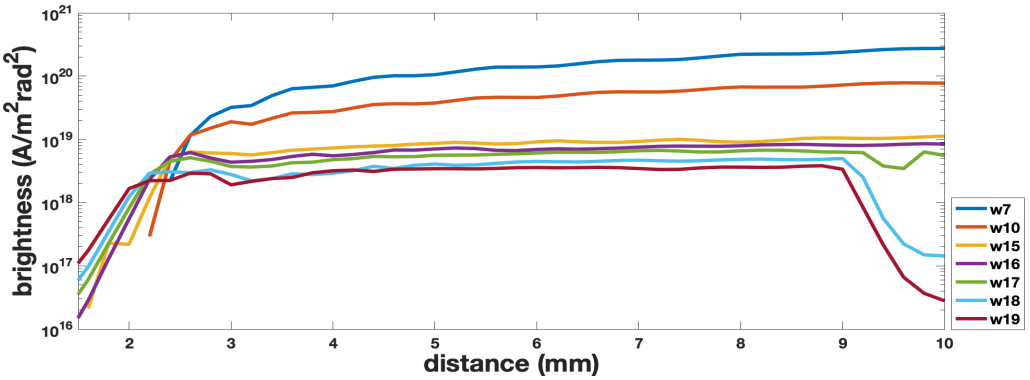

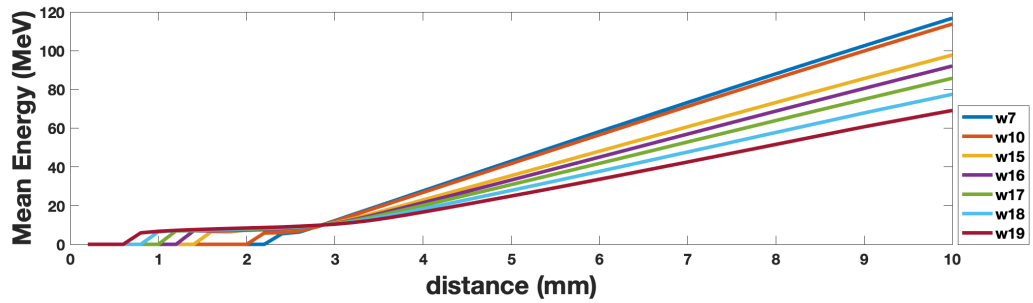

With transverse matching

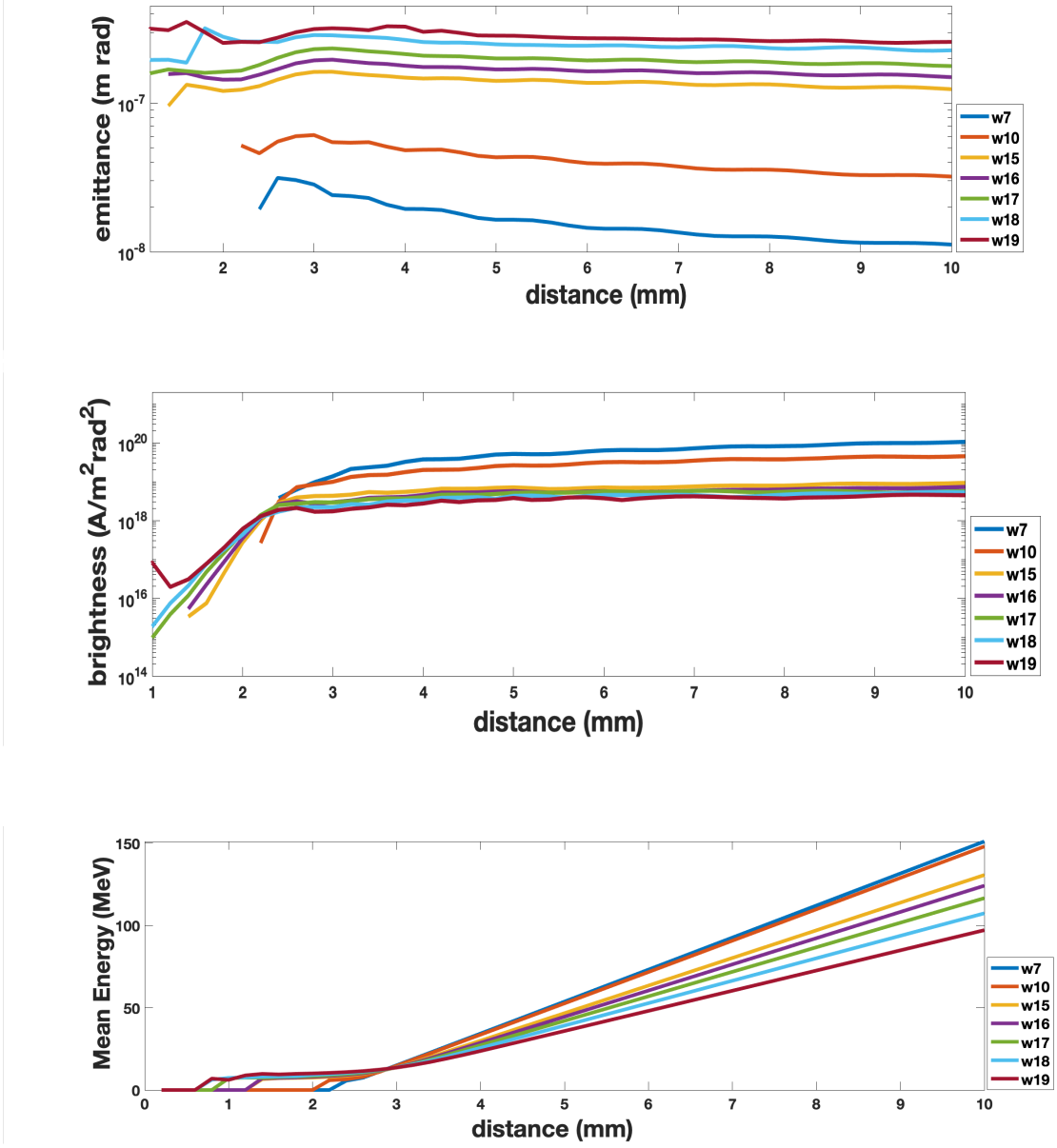

Figure 4.2: Evolution of the witness bunch parameters during propagation, when w_0 is changed, and a_0 is fixed. Shown are transverse emittance, brightness, and mean energy. Both the scans are shown for the unmatched and matched case.

Laser pulse parameters

Name	Values
Laser amplitude a_0	0.018
Pulse duration τ	30 fs
Laser wavelength λ_l	800 nm
Laser pulse position ξ_i	100 μm
Focal position z_i	2 mm

Driver beam parameters

Name	Without matching	With matching
Charge Q	2000 pC	900 pC
RMS bunch length $\sigma_{z,d}$	20 μm	20 μm
RMS bunch width $\sigma_{(x,y),d}$	30 μm	3.5 μm
Normalised emittance ε_n	2.25 m rad	50 m rad
Energy W	10 GeV	10 GeV

Table 4.1: The laser pulse parameters and driver beam (without and with matching).

Regarding emittance, both in the unmatched and the matched case, the emittance is monotonically increased when the spot size is increased from w_0 = 7 μm to w_0 = 19 μm. In the matched case, the emittance values are closer together.
The witness beam obtains higher mean energy after matching concerning mean energy.

Figure 4.3 shows PIC simulation result snapshots after a propagation distance of 10 mm. The electron beam (green macroparticles) propagates to the right and drives a blowout in the medium with LIT (here, hydrogen). The black line is the on-axis accelerating electric field. In the centre of a blowout, a synchronised laser pulse has ionised the HIT medium (here, helium) and has released He electrons (red dots) inside the blowout. These He electrons have then been trapped and are accelerated to energies by the accelerating field of the plasma wave. The colourmap shows the transverse electric plasma wave field, which focuses on the electrons inside the blowout.

Without matching

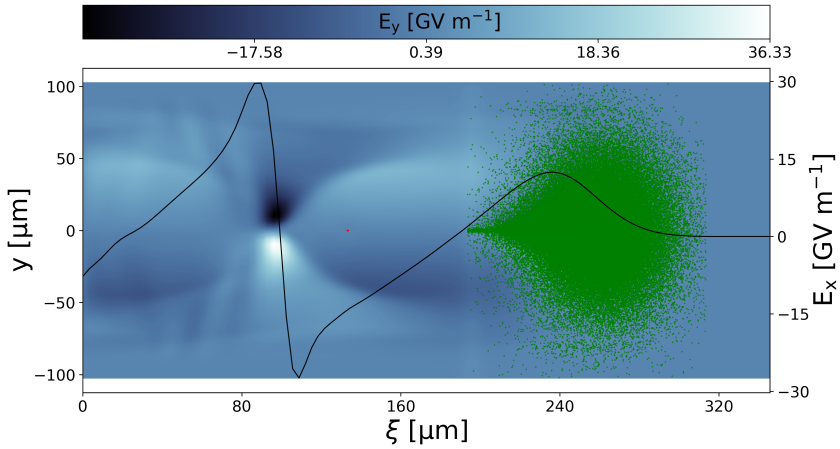

With matching

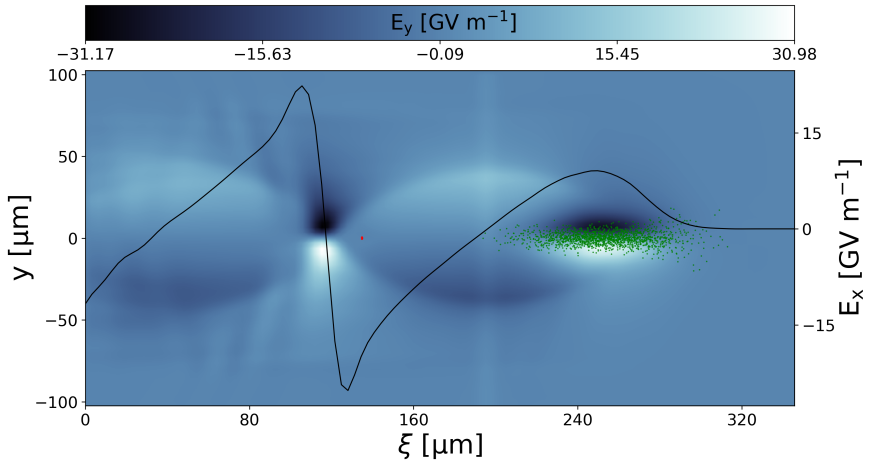

Figure 4.3: Numerical simulation of the TH technique (before and after matching) over a distance of 10 mm. The green dots represent the driver beam, the black line is the accelerating electric field, the middle is the laser pulse, and the red macroparticles represent the witness beam.

The contribution of the laser pulse to the normalised transverse emittance can be reduced using higher frequencies of the laser pulse and a small value of spot size $w_0 \propto \lambda$, which decreases the Rayleigh length $Z_R \propto \frac{w_0^2}{\lambda}$.

4.2.2 Variation of the Normalised Amplitude of the Laser Pulse

For this scan, w_0 was fixed to $w_0 \approx 15\ \mu m$, and the dimensionless normalised light amplitude a_0 was changed, as defined in equation (2.2). As described by equation (1.36), tunnelling ionisation rates have an exponential term, and for a given ionisation potential of gas, the electric field of the laser pulse is decisive for the rate and amount of ionised gas. By changing a_0, as shown in equation (2.2), the corresponding laser pulse electric field is changed linearly, and the tunnelling ionisation rates are changed dramatically.

Another impact of a_0 variation is that the volume over which the ionised gas tunnel is changed because the volume around the laser pulse exceeds the tunnel ionisation threshold field. An increased transverse extent of the ionisation region when increasing the a_0 of the laser pulse, for example, means that the initial betatron oscillation amplitude is larger for some electrons. Therefore, the initial transverse momentum: an electron 'born' further away from the propagation axis will be accelerated towards the axis by the transverse focusing force of the plasma. It hence will accumulate more transverse kinetic energy than an electron born closer to the axis. A larger range of electrons being born farther away from the focus position in the longitudinal direction means enhanced phase mixing for the produced electron beam. Neither of these two volumetric effects can be good for the emittance of the formed witness beams. While increased charge yield due to higher a_0 should increase current and the brightness of the formed beam. The rivalling effects are increased emittance due to large release volume when a_0 increases. The current and emittance influence the composite parameter beam brightness. Hence, it is interesting to see how changes of a_0 will quantitatively affect the emittance, current, and brightness because of these competing effects.

A simulation-based scan of a_0, based on parameter accessibility to tune, has been carried out in the range from $a_0 = 0.016$ to $a_0 = 0.019$ to examine the impact on emittance and brightness, and energy gain, because the expected variation of charge may also have an impact on the mean accelerating field due to beam loading. Figure (4.4) depicts results for the unmatched and matched driver beam cases. Again, the simulations have been run over a simulation distance of 10 mm.

The charge levels obtained for the various a_0-values are an insufficient agreement between tunnelling ionisation estimations and PIC, as we see in Figure (4.5).

First, the emittance increases monotonously with increasing laser intensity. It should be noted that the transverse residual momentum of the released electrons is not correctly modelled because the plasma photocathode laser pulses have been implemented in an envelope approximation by an analytical function. On the one hand,

this simplification is required because the computational demands of a spatially resolved injector laser pulse would require computational cell sizes small enough to cover a single laser wavelength with tens of cells. In other words, it would open a whole new resolution scale and therefore is computationally prohibitive. On the other hand, such a simplification is justified because the residual momentum at the investigated laser intensity levels is small compared to phase mixing, but even more important small compared to space charge based effects on emittance. What is observed in Figure (4.4) in the emittance plot is to be attributed to phase-mixing and space charge effects. It should be noted that the y-axis is plotted logarithmically because of the huge differences in emittance, likely an effect dominated by space charge.

Regarding 5D-brightness, the picture is unclear: the obtained values are more similar, which is the result of the competing effects between increased current due to the increased charge, which increases the brightness, and the increased emittance due to space charge and phase mixing, which decreases the brightness.

Finally, the mean energy obtained is plotted. Again, we observe a monotonous behaviour in obtained mean energies is larger for lower a_0. This is the effect of beam loading of the plasma wake, which manifests itself as reduced electric accelerating field and, consequently, reduced energy gain. This observation indicates that the dominating effect in the scan is indeed a space charge.

Concerning differences between the unmatched and matched case, a more regular behaviour can be observed in the matched than in the unmatched case, even with logarithmic scales for emittance and brightness plots.

Without transverse matching

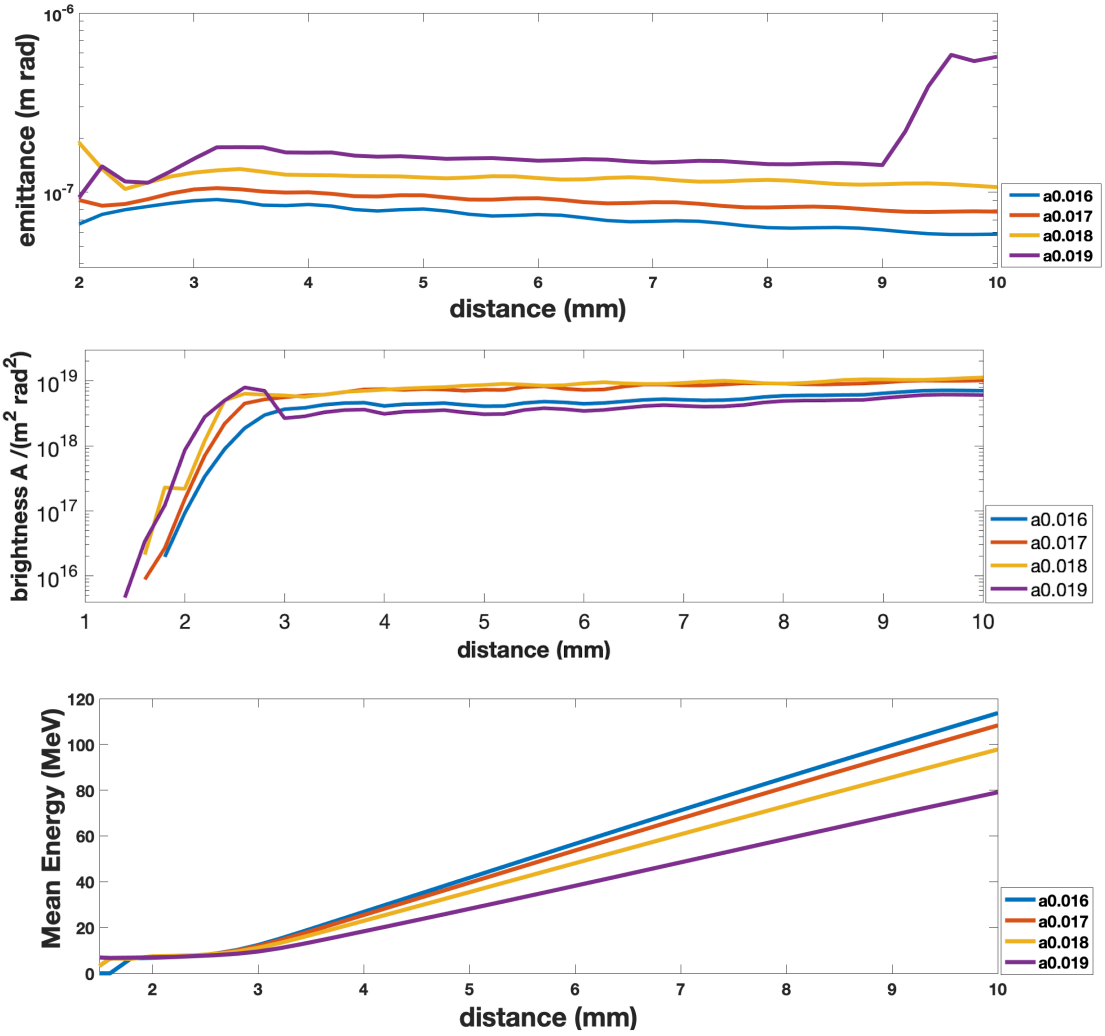

With transverse matching

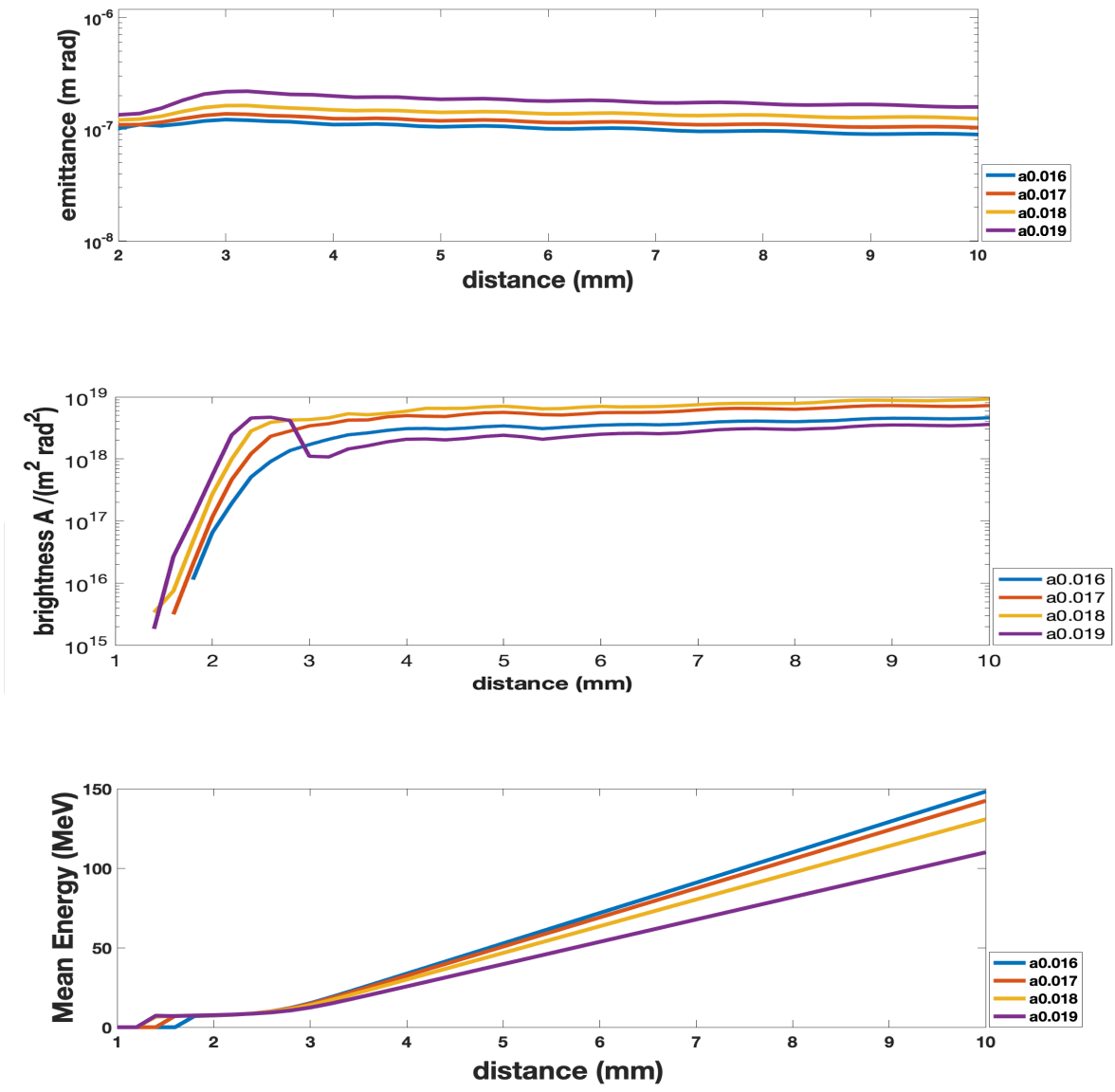

Figure 4.4: Evolution of the witness bunch parameters during propagation when a_0 is changed, and w_0 is fixed for transverse emittance, brightness, and mean energy, the scans before and after matching.

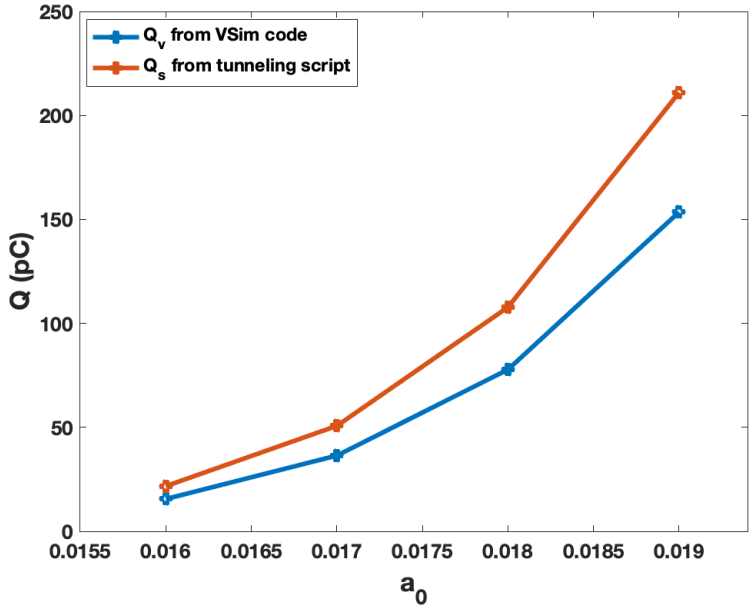

Figure 4.5: Plot of charge Q_v predicted by the VSim code and charge Q_s expected from the tunnelling ionisation script versus plasma photocathode laser pulse intensity.

4.3 Variation of the Laser Pulse Offset

The previous study shows that the properties of the plasma photocathode laser pulse in terms of spot size w_0 and laser intensity, represented by a_0, have a distinct effect on the quality of the witness bunch. Another method to tune the parameters of the witness bunch, and an experimentally very real parameter variation even from shot to shot, is a transversally and horizontally varying position of the laser pulse within the blowout. The following two subsections are studied, such as transverse and longitudinal offset of the release laser pulse and its effects on key witness beam parameters.

4.3.1 Transverse Offset

First, the effect of transverse offset variation is studied. One can straightforwardly inject electrons with a transverse offset at another transverse position inside the blowout, experimentally, by shifting the injector pulse in the corresponding position through a mirror shift. The positively charged ion background inside the

plasma wake blowout provides a restoring force for an electron produced off-axis or overshoots. When injecting any electrons off-axis, they oscillate inside the blowout at a betatron frequency :

$$w_\beta = w_p/(2\gamma)^{1/2} \qquad (4.2)$$

Where $\gamma = (1 - v^2/c^2)^{-1/2}$ is the Lorentz factor of witness bunch, and w_p is the plasma frequency. The oscillations performed by the electrons in the transverse plasma wake are known as betatron oscillations, and the name is derived from the classical Betatron accelerator device, in which the electrons oscillate around stable orbits during the acceleration process. Betatron oscillations are useful for radiation production because electrons in their turning points of the oscillations emit radiation. The plasma photocathode technique offers a unique path to release distinct electron populations off-axis and trigger betatron oscillations, which could be used for radiation production and light source applications. Here, the impact of transverse off-axis released on electron beam quality shall be examined.
In a PIC simulation scan, transverse offsets up to 10 μm were applied and explored. Table 4.2 shows the impact of transverse release laser offsets on charge Q, produced bunch length, peak current I_{max}, emittance and 5D brightness B_{5D}.

Name	**Transverse offset value**	**Charge Q**	**Max current I_{max}**	**Emittance ε**	**5D brightness B_{5D}**	**The max length LenMax**
Unit	**μm**	**pC**	**KA**	**m rad**	**A/(m^{2}rad^2)**	**μm**
	0 (no offset)	77.01	70.74	y=1.24x10^{-7} z=1.23x10^{-7}	9.27 x 10^{18}	2.43
	1	81.16	66.75	y=1.34x10^{-7} z=1.25x10^{-7}	8.01 x 10^{18}	2.52
	3	91.83	51.83	y=1.85x10^{-7} z=1.27x 10^{-7}	4.30 x 10^{18}	2.63
	5	104.33	38.97	y=2.22x10^{-7} z=1.27x10^{-7}	2.54 x 10^{18}	2.68
	10	144.01	43.78	y=5.52x10^{-7} z=1.06x10^{-7}	1.50 x 10^{18}	5.73

Table 4.2: The witness bunch parameters when shifting the release laser pulse transversely for the case of a_0=0.018, and w_0=15μm.

First, because the blowout, in this case, is small, a transverse variation of the laser pulse position will mean that the superposition of the laser pulse electric field with the plasma wakefield is significant [51]. As a result, the charge yield further away from the central propagation axis is significantly increased, doubling from 77 pC on-axis to 144 pC, at a release position 10 μm away from the axis, where the transverse wakefield is large (see Figure 4.6)[80].

At the same time, a larger charge produces increasingly longer formed electron witness beams, this occurs on the one hand, due to an increased release volume because of the superposition of laser and wakefield, but on the other hand, also because of beam loading. Also, this is shown by the calculated current I, thus reflecting the ratio between increasing charge and increasing bunch length. The current I does not show a clear trend but reflects the competing effects and linear impact of charge and bunch length.

The increasing beam loading with increasing charge is also reflected by the mean energy gain, as shown in Figure (4.7): higher charge means stronger beam loading, and the average accelerating field is lower and leads to reduced energy gain.

Regarding transverse emittance, Figure (4.8) shows that the emittance of the witness beams increases strongly (note the logarithmic scaling of the y-axis), when the laser pulse releases electrons further away from the axis. Increased space charge forces cause this due to the larger charges released when further off-axis, but there will also be a contribution of increased phase mixing, and an effect to be attributed to an increased transverse momentum of the released electrons. They accumulate a kick by the electric forces produced by the field of the ions, which accelerates released electrons transversally towards the axis.

Finally, the joint impact of current and emittance is visible in the 5D brightness B_{5D} as a composite parameter (see figure 4.9). As one may expect from the comparable current values obtained for various transverse offsets, the emittance increases for larger offsets, but the brightness is largest for on-axis release smallest for release far from the axis. Again, logarithmic scaling is required to visualize this trend properly.

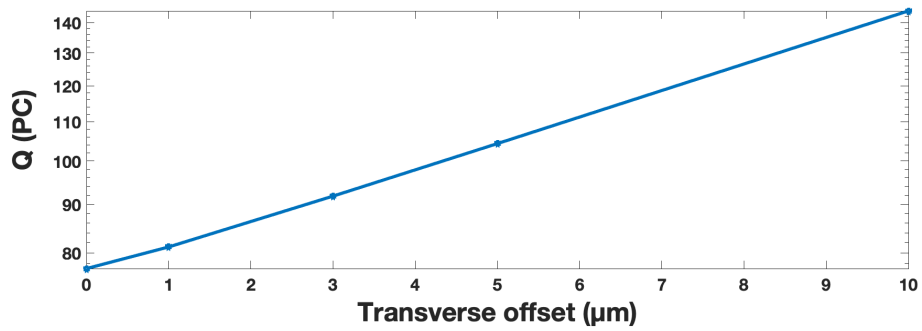

Figure 4.6: The injected charge against the transverse offset of the laser pulse.

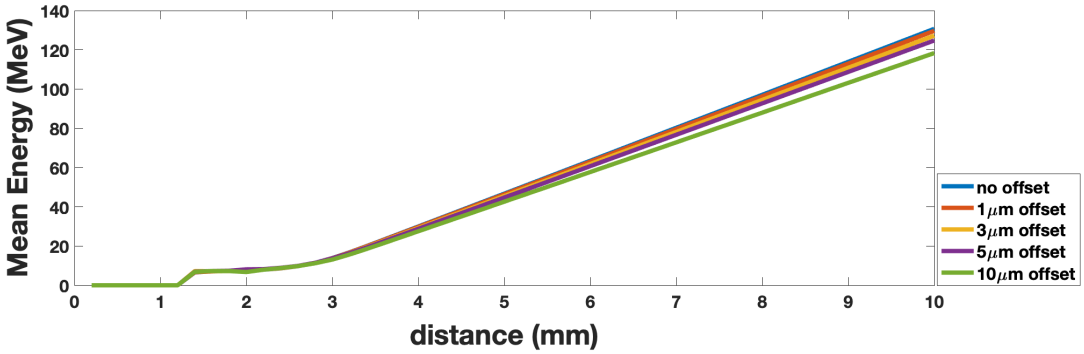

Figure 4.7: Energy scan of the witness bunch at various values of transverse offset of the laser pulse during propagation.

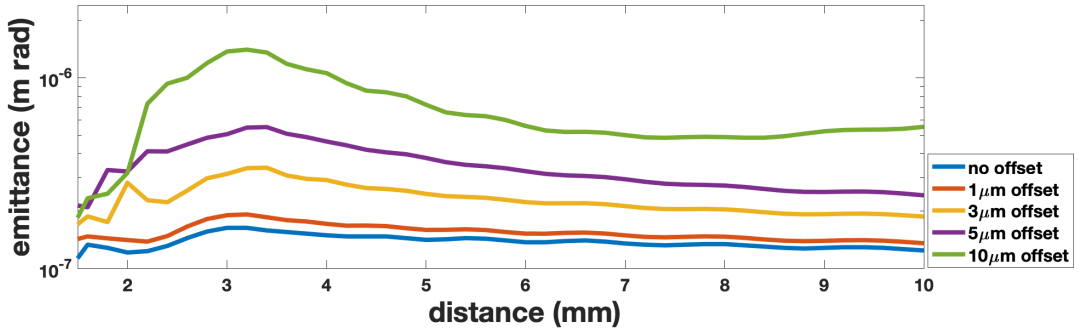

Figure 4.8: Evolution of the transverse emittance of the witness bunch during propagation when the laser pulse is released transversely.

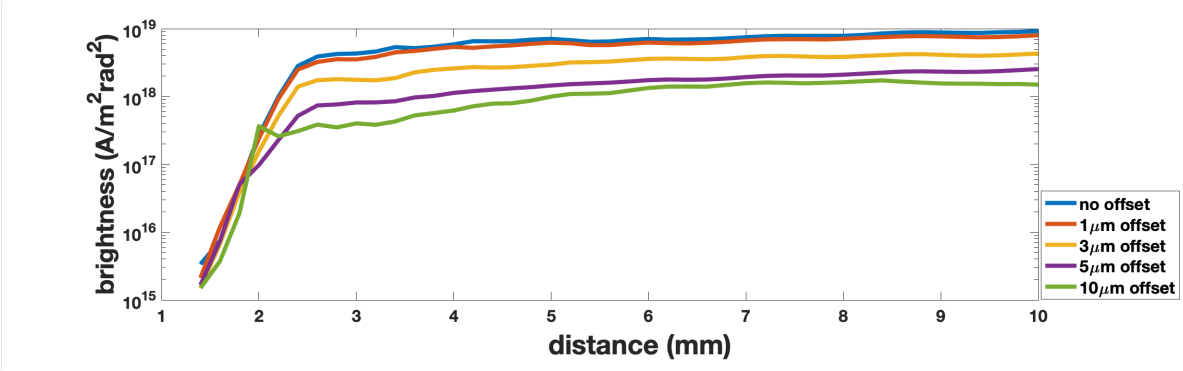

Figure 4.9: Evolution of brightness of the witness bunch during propagation when the laser pulse is released with different transverse offsets.

4.3.2 Longitudinal Offset

The effect of changes in the longitudinal release position has been explored in another simulation scan. This corresponds to a timing variation between the laser pulse and the driver electron beam, which is particularly relevant for linac-driven systems. The default release position is in the centre of the blowout, located at ≈ 100 μm behind the drive beam. As shown in table (4.3), the longitudinal offset increases from the centre of the blowout up to 120 μm to explore the effect on charge Q, bunch length, peak current I_{max}, emittance and 5D brightness B_{5D}.

As a result of these scans, the charge increases gradually, as we move the laser pulse away from the centre of the blowout longitudinally. This can be explained by the fact that the longitudinal wakefield is zero around the centre of the blowout, where the longitudinal field changes from accelerating to decelerating but increases the farther one moves away from the zero-crossing. As for a longitudinal shift, an increasingly larger longitudinal shift means that superposition of laser electric field and plasma wakefield increases the peak electric field amplitude, and the tunnelling ionisation rates. This explains why one sees an increase in charge, as shown in Figure 4.10.

As shown in table (4.3), the current for this scan shows a decreasing trend as the longitudinal offset and, therefore, the amount of released charge increases, reflecting the competing impacts between charge and bunch length.

Concerning the transverse emittance, as shown in Figure (4.11), the emittance shows a decreasing trend when the offset is changed from 100μm to 120μm.

Finally, as shown in Figure (4.12), the 5D brightness decreases because of the ratio between current and emittance, as mentioned earlier in section (4.3.2).

Name	longitudinal offset value	Charge Q	Max current I_{max}	Emittance ε	5D brightness B_{5D}	The max length LenMax
Unit	**µm**	**pC**	**KA**	**m rad**	**A/(m^{2}rad^2)**	**µm**
	100 (no offset)	77.80	69.70	y=1.24x10^{-7} z=1.23 x10^{-7}	9.15 x 10^{18}	2.43
	105	79.38	47	y=1.27x10^{-7} z=1.23 x10^{-7}	5.99 x 10^{18}	2.46
	110	80.73	35.04	y=1.27x10^{-7} z=1.23 x10^{-7}	4.47 x 10^{18}	2.83
	115	81.64	27.88	y=1.23x10^{-7} z=1.21 x10^{-7}	3.75 x 10^{18}	3.54
	120	83.34	23.30	y=1.15x10^{-7} z=1.13 x10^{-7}	3.59 x 10^{18}	3.46

Table 4.3: The witness bunch parameters when shifting the laser pulse release position longitudinally, for the case of a_0=0.018 and w_0=15µm.

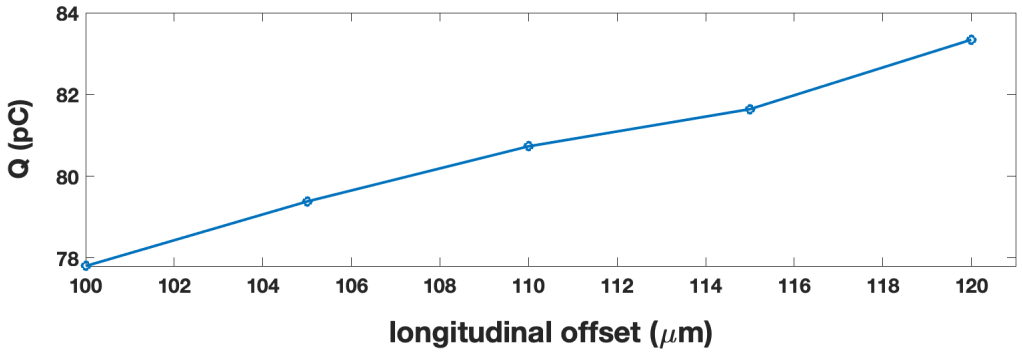

Figure 4.10: The injected charge against the longitudinal offset of the laser pulse.

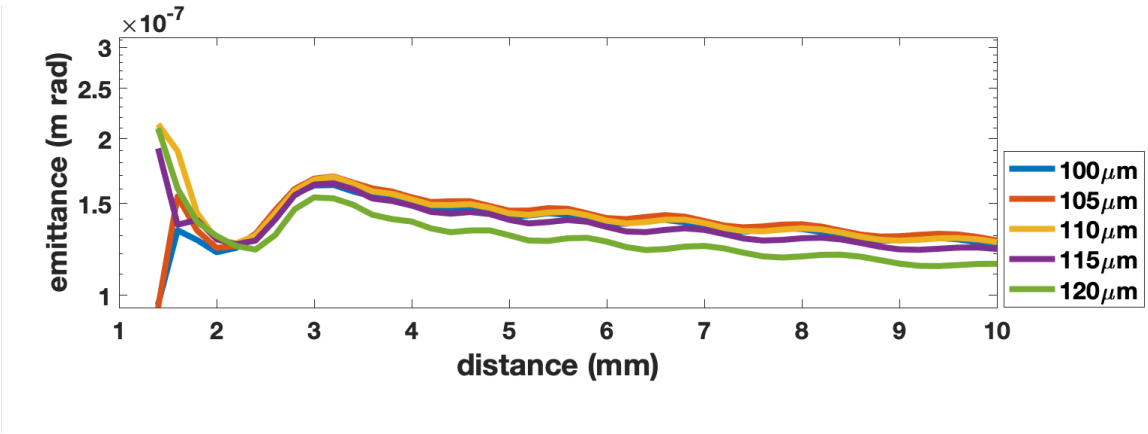

Figure 4.11: The evolution of transverse emittance of the witness bunch during propagation when the laser pulse is released longitudinally.

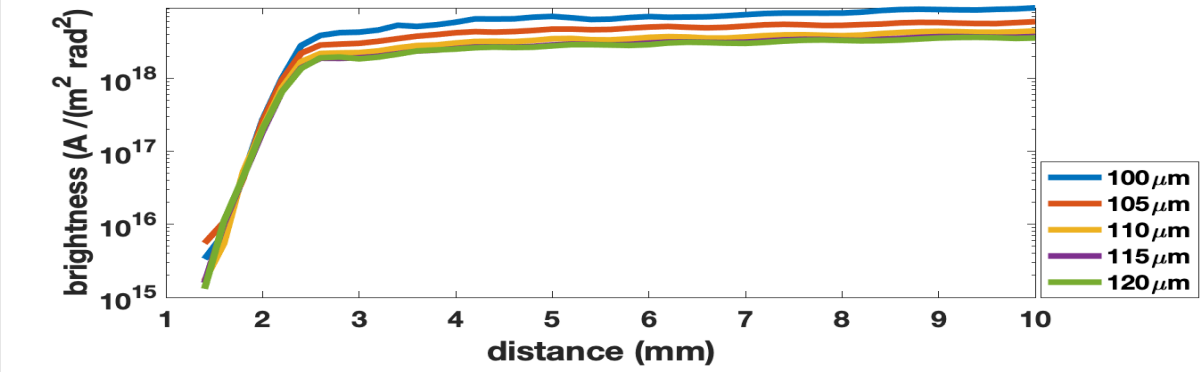

Figure 4.12: Evolution brightness of the witness bunch during propagation when the laser pulse is released longitudinally.

4.4 Summary

The laser pulse must be adjusted accurately to produce a high-quality witness bunch, which strongly depends on the properties of the laser pulse. We saw how increasing the laser spot size affected the quality of the witness bunch by increasing its emittance value and decreasing brightness. Also, this applies to the laser intensity, where increasing its value led to a worse emittance value and brightness growth. Furthermore, beam matching is a critical part of accelerators because it minimizes the instabilities inside the plasma and increases the mean energy of the witness bunch.

About transverse offset, we observed how increasing the offset affected the witness bunch parameters by significantly increasing the emittance value with the increase in the beam length, which affected the current value. Likewise, increasing the longitudinal offset affected the current value by decreasing its value and brightness value and slightly affecting the emittance.

These considerations guide the experimental parameter range which is required to realize future experimental implementations, with major long-term applications such as a plasma-based free-electron laser via ultrahigh brightness beams produced through the Trojan Horse technique.

Chapter 5

Space Charge Effects In a Plasma Photocathode

In the previous section, we have seen that the charge released by the plasma photocathode process plays a dominating role in emittance and brightness when increasing the space charge to higher levels, e.g., in the high 10's to 100's of the pC range. For example, beam-loading leads to increased bunch length due to the interaction with the plasma wave wakefield and electrostatic potential, but more importantly, intra-beam space charge leads to an increase of transverse momentum of the beam electrons. This increases the emittance as the released charge is increased. This is very important because it is desirable to have a high charge (and current) and low emittance for applications.

In [77], the issue of space charge emittance growth was addressed in the context of energy spread. While it is possible to beam-load the wake with a single plasma photocathode to flatten the local accelerating field for optimized energy spread yields, the emittance suffers from that approach. The deleterious effect of space charge on emittance occurs at the beginning of the release and trapping process. This is because the beam stabilizes relativistically, as it accelerates and becomes increasingly immune to space charge effects.

However, the evolution and dynamics of space charge during release, trapping, and acceleration on a single bunch has to be explored. It is crucial to understand this to optimize the process and perhaps to develop novel schemes that can be used to compensate for associated emittance growth.

The approach taken here is to extend the exploration by scanning various densities of HIT components, including very high density, to find links, e.g., between produced charge (density) and emittance growth. We examine this for two different laser spot sizes at three levels of HIT densities at specific, artificially set ionisation potential values to investigate and explain how released charge impacts the formed witness bunch. In this context, we will exploit several options that are not directly accessible to experiments but are possible to exploit in simulations.

5.1 Generating a Witness Bunch by Varying the Background Density with Low-fidelity PIC Simulation

It is expected that increasing the density of helium (or any HIT components, for that matter) will increase the charges of the witness bunch approximately linearly with density, because the quantity of electrons released is proportional to the density of the gas [81]:

$$N_e \cong w_o^2 \, l_i \, f_i \, n_{He} {a_o}^2 \qquad (5.1)$$

Where l_i represents the region length of gas that will be ionized, f_i is the fraction of ionized electrons, n_{He} the gas density, and a_o is the normalised amplitude of the laser field.

By increasing the He density, the witness electrons repel each other much more because they feel the Coulomb field of many surrounding electrons, which is expected to increase the transverse momentum that develops. They also change the collective wakefield structure such that the wakefield is distorted (beam loading effect).

In the context of the various forces occurring inside the plasma accelerator, intra-beam space charge forces are to be seen with the other forces present in the plasma wave. It is important to remember that a beam injected from a Trojan Horse plasma photocathode will have an initial emittance specified by the laser's w_0 and a_0. However, the further evolution is then dependent on the plasma wake characteristics, such as the focusing force of the wake, the relation of intra-beam space-charge forces to the plasma wave focusing, and phase mixing, …etc.

The preliminary laser parameters and the focused wakefield forces are crucial. A beam injected may extend or compress transversally until the balance between both extending and focusing forces is reached naturally, resulting in matching. In that case, the beam may rapidly match, e.g., when the released electrons can not accumulate too large transverse momentum during the trapping process in the transverse fields of the plasma wake, and emittance may then remain constant, ideally at as low level as possible. The space charge force becomes more significant and widens the beam if we liberate further charge by raising the HIT density. Furthermore, when a high charge quantity is released, space charge begins to dominate all other contributions to the emittance, causing the beam emittance to grow.

Therefore, it is crucial to explore the space charge related emittance effects during release, trapping and initial acceleration. This PIC study first plotted the transverse normalised emittance during the plasma photocathode process to understand its evolution. Two cases of laser spot size were examined, namely w_0=7 μm and w_0=15 μm. For these two spot sizes, the helium density was changed.

In this study, the two different initial beam radiation are only in the low charge regime determined largely by laser spot size w_0 and intensity a_0. In both cases, increasing the HIT density; then increases the space charge until it dominates.

The PWFA and the subsequent controlled injection of witness bunches via the Trojan Horse mechanism are modelled by the fully explicit 3D PIC code VSim. As in chapter 4, the produced witness beam charge observed by the tunnelling ionisation implementation in VSim and the one predicted by the external tunnelling ionisation script have been compared. For the simulation runs to be comparable as much as possible, the simulation length and the number of dumps must be the same in both situations. Here, the dump ratio is chosen such that there is 1 dump per 5 μm of simulated propagation. The simulation code then keeps all relevant files (e.g. "dumps" of electric fields, macroparticles etc.) every 5 μm that the moving simulation box propagates. This means, in the case of w_0=7 μm, the number of dumps is 600, and in the case of w_0=15 μm, the dump number=800.

A combination of two different types of gas was used to provide the LIT medium and the HIT medium independently. This is required to be able to vary the HIT medium to vary the released charge linearly. The LIT (hydrogen) gas density is the same as used in the fourth chapter settings. Concerning the HIT medium, we used different helium densities from $1.5\text{x}10^{21}$ m^{-3} up to $1.5\text{x}10^{26}$ m^{-3}. The charge of the driver beam was also changed and initially set to Q_d = 4500 pC, and the ionisation potential used by the simulation has been artificially increased and set to ξ_i = 70 eV. The reason for the driver beam charge increase is to be able to trap and contain a higher witness beam charge. Otherwise, the released charge is not all trapped when operating at elevated HIT densities, and the effects of beam-loading are influential. Both compromise the comparability of the simulations regarding intra-beam space charge force effects. As a result of the increased driver beam charge, however, the peak electric field of the drive beam and the wakefield are increased, beyond the real ionisation potential of helium of ξ_i = 24.6 eV. This means that both the electric field are associated with the driver beams, and the wakefield exceeds the tunnelling ionisation threshold of helium – thus leading to unwanted hot spots and current dark production. Fortunately, the simulation allows one to set the ionisation potential to arbitrary values, thus enabling the study of space charge effects in experimentally inaccessible parameter regimes, which is helpful to gain a proper understanding of the parametric dependencies involved. The driver electron beam and laser pulse parameters are summarized in tables 5.1 and 5.2, respectively.

Name	Unmatched
Charge Q	4500 pC
RMS bunch length $\sigma_{z,d}$	20 μm
RMS bunch width $\sigma_{(x,y),d}$	3.5 μm
Normalised emittance ε_n	50 m rad
Energy W	10 GeV

Table 5.1: The driver beam parameters in the 3D PIC simulation for the broad range witness space charge effect studies.

Name	Values
Laser amplitude a_0	0.081
Pulse duration τ	30 fs
Laser wavelength λ_l	800 nm
Focal position z_i	2 mm

Table 5.2: The laser pulse parameters used in the 3D PIC simulation for these scans.

First, the results of the witness beam charge from PIC and the external tunnelling ionisation script should again broadly agree, as they describe the same physics. Figure (5.1) shows the results from numerical implementation via the tunnelling ionisation script and the VSim code for the two spot sizes of w_0 =7 μm and w_0=15 μm. Here, a linear y-axis scaling is chosen to show that at low to modest "He" densities, the released and trapped charge yield predictions agree (similar to in chapter 4), but that at higher HIT densities, a substantial difference between prediction and VSim code develops. This is less a signature of numerical differences between the external script and the VSim implementation, but the wakefield is no longer strong enough to contain all the witness beam charges. In VSim, the charge is counted after the release process is over: when the wakefield is not strong enough, an increasing amount of charge is not captured and has already left the forward-propagating simulation box is not counted anymore. In any case, to overcome this, one needs a stronger driver beam and associated wakefield. The drive beam charge hence has been increased to 5500 pC. Re-running the simulations with this driver beam shows that all released charge is indeed trapped for the whole range of laser spot sizes and He densities, and the predicted/observed values are in much better agreement, as shown in Figure (5.2).

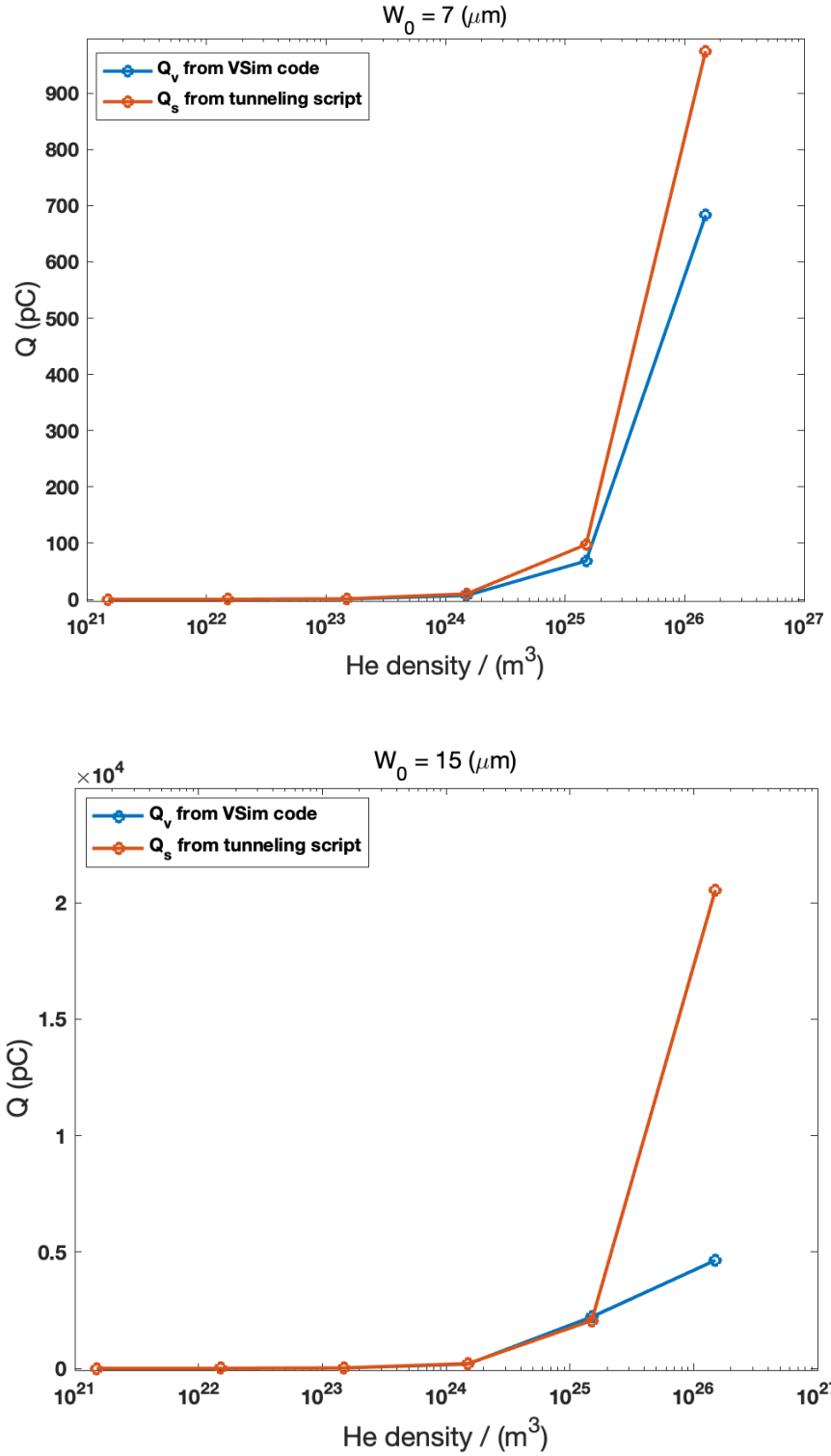

Figure 5.1: The plot of Q_v (VSim) and Q_s (script) versus He density for both cases w_0 =7 μm and w_0 =15 μm when Q_d=4500 pC.

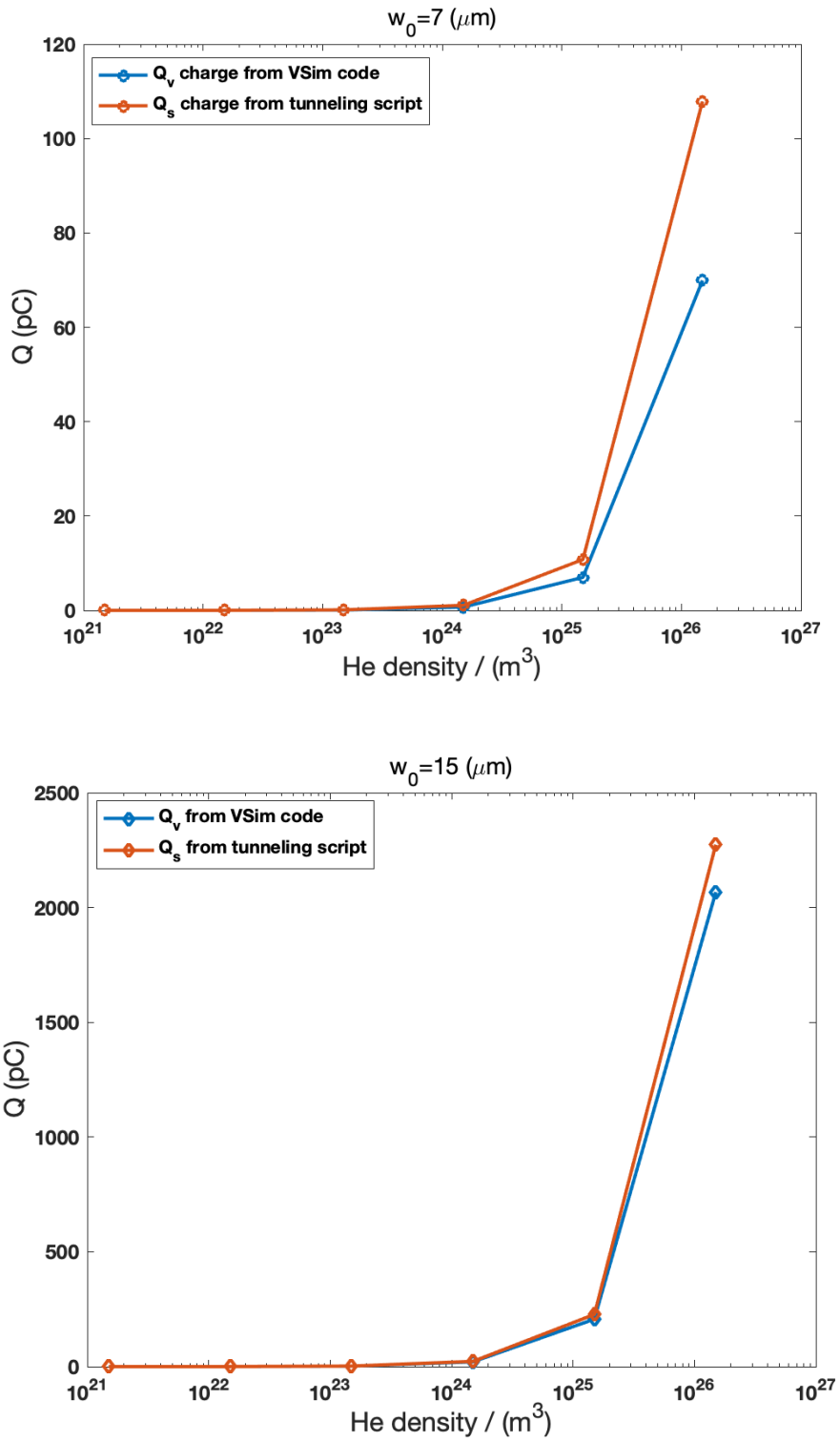

Figure 5.2: Plot of Q_v and Q_s versus He density for both cases w_0 =7 μm and w_0 =15 μm, when Q_d=5500 pC.

Figure (5.3) shows the evolution of the transverse emittance. For the w_0=7 μm case, one obtains transverse normalised emittance values of the order of ε_n < 100 nm rad for HIT densities up to 1.5×10^{21} m^{-3} and correspondingly low total witness charge levels. For higher HIT densities, emittance increases, but then, when the density is increased to 1.5×10^{26} m^{-3}, there is a dramatic jump in emittance up to > 1 μm rad. This corresponds to a jump in witness charge up to the 100 pC level. A first assumption and conclusion are at such charge levels, space charge effects kick in and suddenly increase the obtained emittance by order of magnitude. This observation is useful for the first estimation of the range where space charge effects begin to dominate the emittance levels. For the w_0=15 μm case, due to the much larger charge ionisation volume (remember, the peak laser intensity is kept constant for both cases). As shown in the plot, the space-charge-related emittance growth sets at much lower densities revealed by the corresponding simulations. In the case of w_0=7 μm, if the number of macroparticles is too low in the simulation, we get statistical outliers (e.g., emittance plots would show irregular behaviour) for that we increased a_0 to 0.1 in the case w_0=7 μm with the same parameters to get sufficient witness beam charge to adjust the growth of transverse emittance, see table (5.3). The charge is produced in the simulation increased by a factor of 10, and the growth of transverse emittance looks good for He density=10^{24} up to 10^{26}.

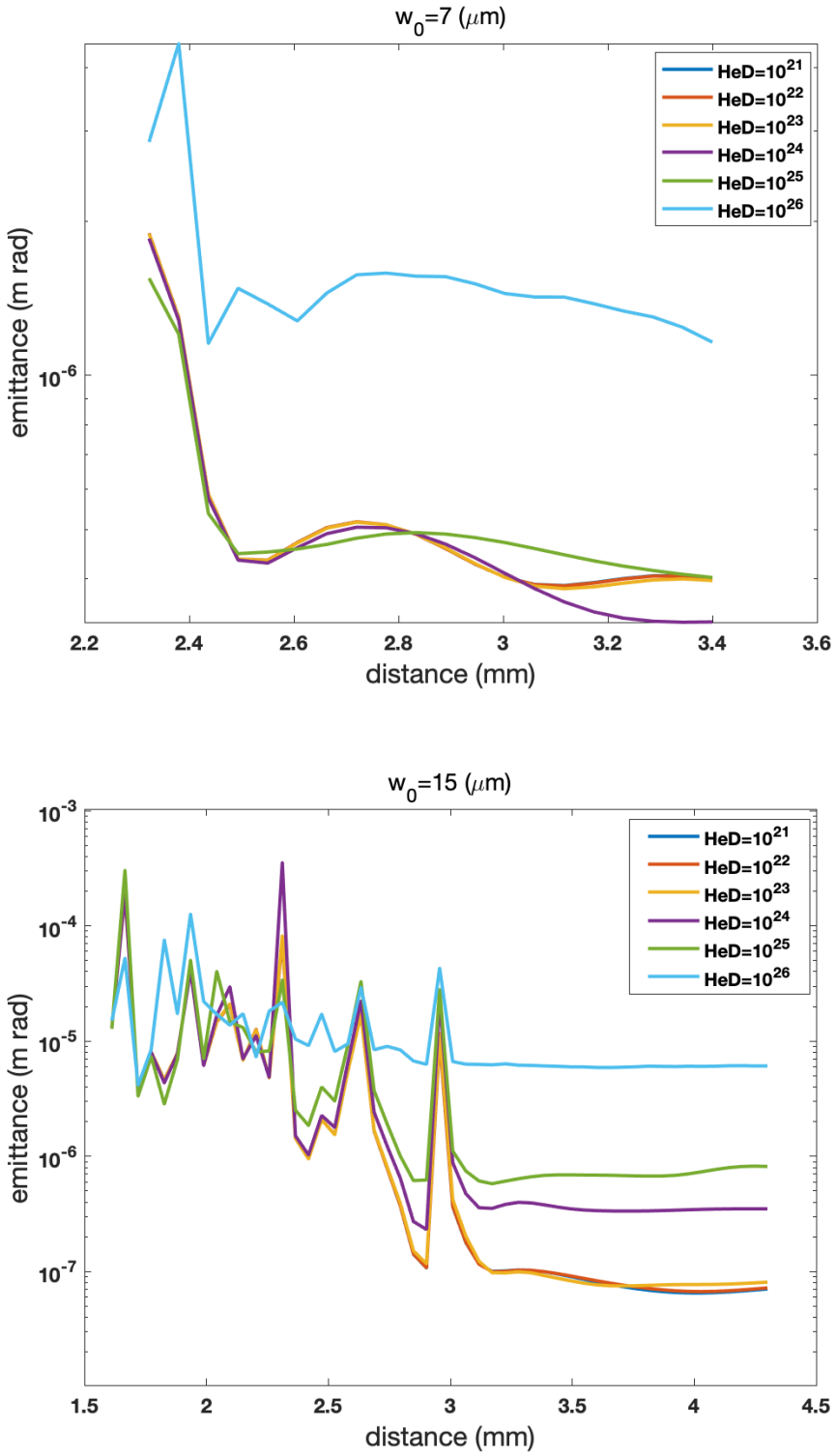

Figure 5.3: Evolution of the transverse emittance for the witness bunch during propagation for w_0=7 μm and w_0=15 μm.

He density (m^{-3})	1.5×10^{21}	1.5×10^{22}	1.5×10^{23}	1.5×10^{24}	1.5×10^{25}	1.5×10^{26}
Charge (pC)	0.013	0.13	1.31	13.18	131.8	1313.45
Transverse emittance (m rad)	6.60×10^{-8}	6.29×10^{-8}	3.22×10^{-8}	1.18×10^{-7}	3.69×10^{-7}	2.81×10^{-6}

Table 5.3: The witness bunch charge and its transverse emittance value when the dimensionless laser pulse intensity is increased to $a_0 = 0.1$ in the case w_0=7 μm.

The last results have shown that the chosen physical parameters yield an appropriate range of witness beam charges for both cases w_0=7 μm and w_0=15 μm across the range of He densities. However, this working point range has to be adjusted from a numerical standpoint in the next step. The grid resolution has to be increased (i.e., the cell size has to be decreased) to achieve a better resolution and get accurate results across the wide range of HIT densities and corresponding witness beam charges.

Before executing high-resolution simulations for study space charge effects during the injection process of trojan horse PWFA simulations, in the previous simulation, a limited number of macroparticles were used where ionized 0.2 percent of the gas background was ionized after the laser passed through. After applying the ADK model, we found out by inserting a_0 and ξi values in equation (1.36). To ensure that we end up with enough macroparticles to evaluate the simulation, we used the ADK model to get a suitable parameter set that leads to ionized 10 percent background by using laser pulse intensity a_0= 0.123 with ξi =75 eV, as shown in Figure (5.4).

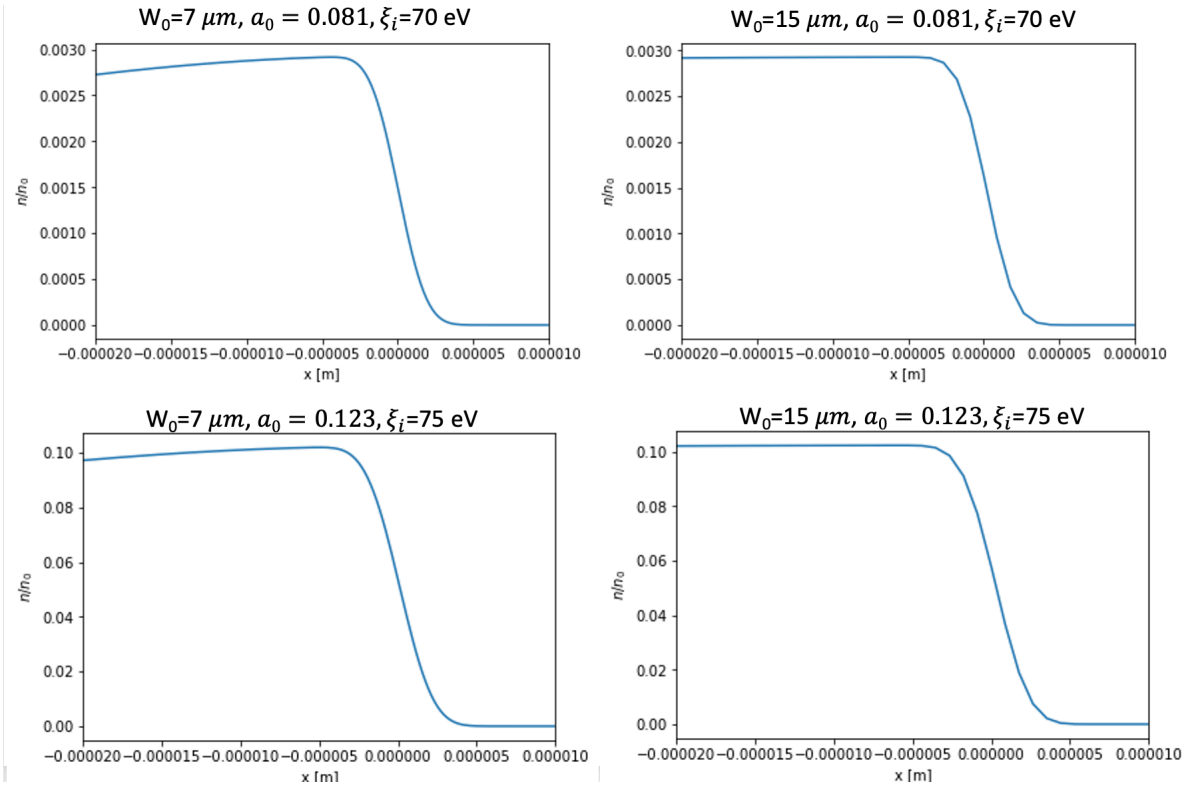

Figure 5.4: Plot of the on-axis ionisation ratio exactly at the time when the laser reaches its focus for both cases w_0=7μm and w_0=15μm. The top panels show the scenario a_0=0.081 and ξ_i =70 eV, and the bottom panels a_0=0.123 and ξ_i =75 eV.

After raising the percentage of ionisation in the background gas density, the previous simulations were repeated with the same parameters that were used for both cases, w_0=7 μm and w_0=15 μm, as presented in tables (5.4) and (5.5).

He density (m^{-3})	1.5 x 10^{21}	1.5 x 10^{22}	1.5 x 10^{23}	1.5 x 10^{24}	1.5 x 10^{25}	1.5 x 10^{26}
Charge (pC)	0.044	0.451	4.516	45.16	451.6	3916.6
Transverse emittance (m rad)	3.33x10^{-8}	2.28x10^{-8}	4.11x10^{-8}	1.18x10^{-7}	4.67x10^{-7}	6.54x10^{-6}

Table 5.4: The witness bunch charge and its transverse emittance value, after increasing the ionisation rate to ξ_i =75 eV with a_0= 0.123 in the case w_0=7 μm.

He density (m^{-3})	$1.5x\ 10^{21}$	$1.5\ x\ 10^{22}$	$1.5\ x\ 10^{23}$	$1.5\ x\ 10^{24}$	$1.5\ x\ 10^{25}$	$1.5\ x\ 10^{26}$
Charge (pC)	1.16	11.60	116.04	1161.10	7799.44	6869.74
Transverse emittance (m rad)	$8.57\ x\ 10^{-8}$	$1.69\ x\ 10^{-7}$	$9.08\ x\ 10^{-7}$	$9.91\ x\ 10^{-7}$	$1.64\ x\ 10^{-5}$	$1.25\ x\ 10^{-5}$

Table 5.5: The witness bunch charge and its transverse emittance value, after increasing the ionisation rate to ξ_i =75 eV with a_0= 0.123 in the case w_0=15 μm.

5.2 Using High-fidelity PIC Simulation

An overarching motivation for this work is to explore the production of high-quality electrons bunches, particularly for FEL applications. As the preliminary simulations have shown, various factors impact the properties of the generated witness bunches and can increase emittance value. Some physical reasons and mechanisms lead to emittance growth (such as a poorly matched witness beam) and numerical mechanisms, and often these mechanisms occur strongly in particle-in-cell simulations. As discussed, one strong factor that dominates witness beam quality at elevated charge levels comes from space charge forces. The matched witness beam size is small, and the charge density is particularly large. Therefore, one needs extremely well-resolved and noise-free simulation methods to resolve the physics, but on the other hand, to suppress numerical emittance growth, e.g., due to numerical Cherenkov radiation. Even if the input deck and simulation setup are optimized, high resolution inevitably means that simulations are very costly. We will examine the impact of space charge on the witness bunch as well as the mechanisms that space charge produces during and immediately after injection in this research, because, at low energies, space charge has a significant impact, the forces of space charge increase with decreases of gamma during acceleration according to equation (3.5).

Three well-defined high-resolution simulations are used in the refined simulations: low-charge, medium-charge, and high-charge witness bunches for two spot sizes of the plasma photocathode, the laser pulse of w_0=7 μm, and w_0=15 μm (see Figure (5.5)). Based on the previous findings, these simulations are physically and numerically well comparable and allow to delve into details of the emittance growth

during release. VSim's average ADK model for ionisation and otherwise identical simulation settings are used.

As indicated previously, a very important and useful trick is available exclusively for simulation-based work, not for the experiment. In addition to the realistic simulations with intra-bunch space charge effects, each high-resolution simulation is repeated by artificially switching off the witness beam self field interaction. This means that the witness beam electron macroparticles will only be subject to the plasma wakefields but not repel each other. This allows one to compare the witness beam parameters for the simulations with space charge (SC) on and off, to explore the substantial differences, isolate, and understand the space charge effects.

The parameters of the driver electron beam, photocathode laser, and gas medium (HIT) are summarized in tables (5.6), (5.7), and (5.8), respectively.

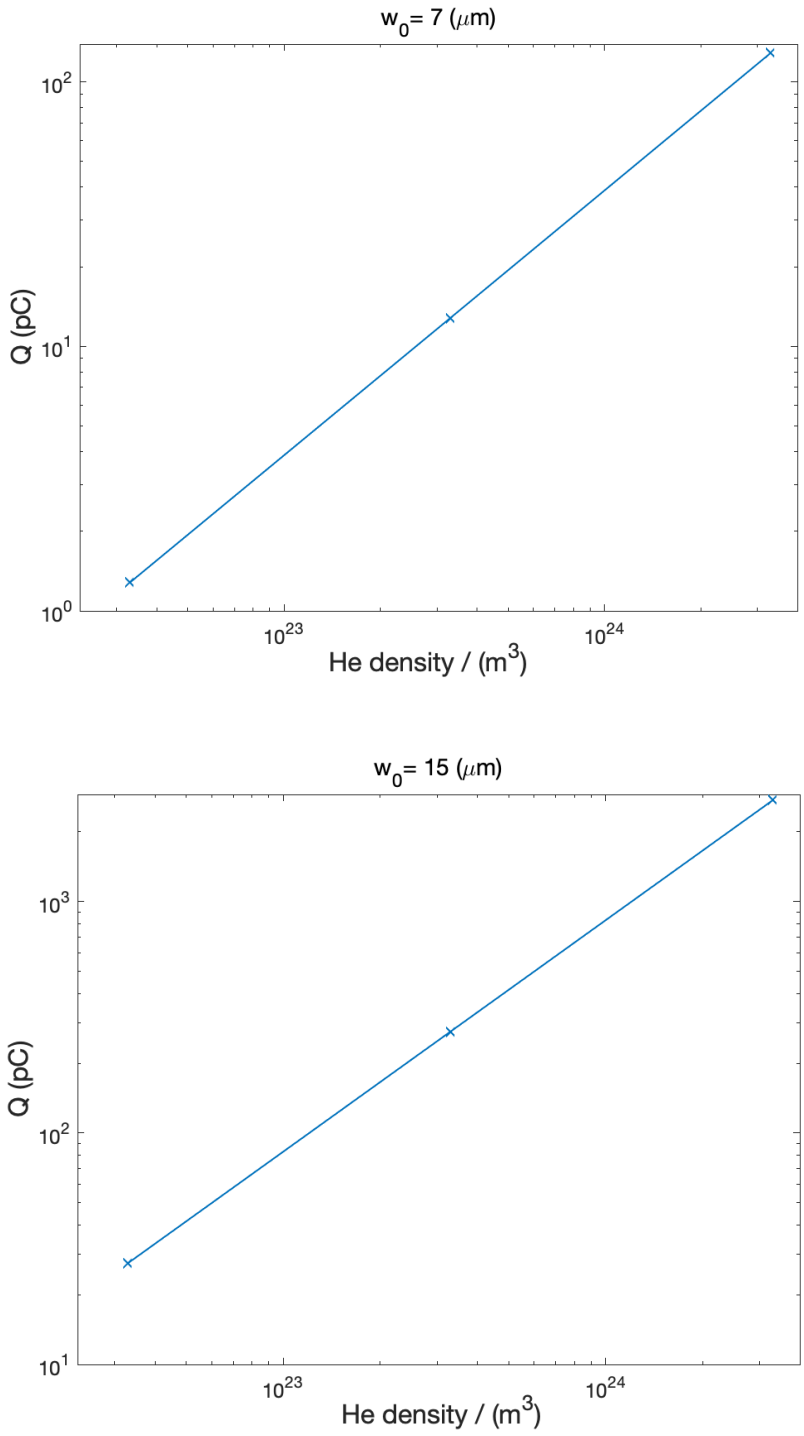

Figure 5.5: Plot of witness charge versus He density for w_0 =7 μm and w_0 =15 μm, respectively.

Name	Values
Charge Q	5500 pC
RMS bunch length $\sigma_{z,d}$	20 μm
RMS bunch width $\sigma_{(x,y),d}$	3.5 μm
Normalised emittance ε_n	50 μm
Energy W	10 GeV
Energy spread	2%
plasma Wavelength λ_p	200 μm

Table 5.6: The driver beam parameters used for the high-resolution 3D PIC simulations.

Name	Values
Laser amplitude a_0	0.123
Pulse duration τ	30 fs
Laser wavelength λ_l	800 nm
Focal position z_i	2 mm
Laser position (behind the drive beam center)	100 μm
RMS spot size w_0	7 μm and 15 μm

Table 5.7: The laser pulse parameters used for the high-resolution 3D PIC simulations.

Name	Values
Ionization potential ξ_i	75 eV
HIT DENS	change value in this study

Table 5.8: The gas medium parameters (HIT) are used for the high-resolution 3D PIC simulations.

Studying the relevance of space charge forces for Trojan Horse injection with physical parameters shown in Tables 5.6-5.8 requires highly optimized simulation decks. Since space charge forces occur within the electron witness beam distribution, the spatial resolution must be improved substantially compared to the simulations, as shown in Chapter 4. Here, the optimized resolution of DX = 0.16 μm longitudinally and DY = DZ = 0.4 μm in transverse direction represents a tremendous improvement and challenge. Combined with an improved Yee solver [82], this setting yields high numerical precision and ultra-low numerical noise so that observed emittance growth can be attributed directly to physical space charge effects. Consequently, these simulations are extremely costly and require ~ 8000 processors for 1281 hours on the Shaheen-II supercomputer.

Furthermore, this simulation deck employs an extremely high dump rate that allows identification of space charge effects already during the dynamics of the ionisation process of the Trojan Horse process. Particle tracking allows the following the 6D phase space trajectory of each electron released by the Trojan Horse process via unique macroparticle identifier tags. Combined with the high resolution, the simulations produce several TB data within a very short time. To realise this demanding simulation, the burst buffer feature of Shaheen-II is used, which speeds up the I/O process by a factor of ~10-100. The high dump rate is maintained until the witness beam is fully formed and has gained relativistic energy, which is defined here as having 10-20 MeV mean energy.

The settings that were made in this simulation are as follows (see Figure (5.6)):

First, the simulation was carried out on the Shaheen super-computer for eight hours and uses 10TB of burst buffer capacity to speed up the production of dump files. The beam is started in a vacuum at the start. Then, the beam penetrates the plasma with a suitable upramp and produces the wakefield. When the wake has formed, the simulation performance is improved by spreading the particle load over all processors as evenly as feasible. Iterative post-processing and visualisation of the produced dumps and simulation results have been used to ensure the numerical and physical evolution of the fields, particles and beams in the simulation box are sound and can be used for analysis. This is important due to the very high computational costs of these simulations.

Second, the simulation is restarted, and the simulation propagates until the blowout is formed and stable. This is also confirmed through postprocessing/visualising of the produced dumps. Because the distance from the first dump until the laser commences ionising is identical for all our simulations. Then, we only have to save the final dump before the ionisation occurs. This is then used as a starting point for all subsequent simulations, whereby the different HIT densities and spot size of the laser pulse are varied, and the space charge effects are turned off for the important artificial reference simulation. This avoids repeating the redundant simulation part before the laser ionisation occurs.

Third, the simulation is restarted with an increased dumps rate for HIT electrons during injection, but the reduced dump rate for all other fields and particles for the injection phase, since keeping the same dump rate for fields would exceed the storage capabilities of the Shaheen-II. The iterative postprocessing/visualizing of the dumps and, in particular, the witness beam macroparticles was crucial to carry out the simulations without exceeding the storage capabilities of the Shaheen-II HPC cluster. In the end, all released HIT electrons were accelerated to approximately 20 MeV, where they are regarded as relativistically stable regarding space charge, and phase-mixing has been completed largely.

It shall be confirmed that the simulations shown here are purposefully not all realistic. The driver beam charge is set particularly high in order to drive a wake that allows systemic investigation of witness beam space charge, the ionisation potential is set to an artificially high value to avoid current dark production by the driver beam, wakefield and witness beam, and the intra-beam space charge effects have been switched off by the split-field method. Only this enables us to isolate the relevant effects to be studied here and compare them to maximize the relevance of the results. In the split field method, the witness electron macroparticles do not only not interact with each other based on their Coulomb forces but also do not interact by magnetic pinching due to the current they collectively (would) produce. They are exclusively subject to the wakefields.

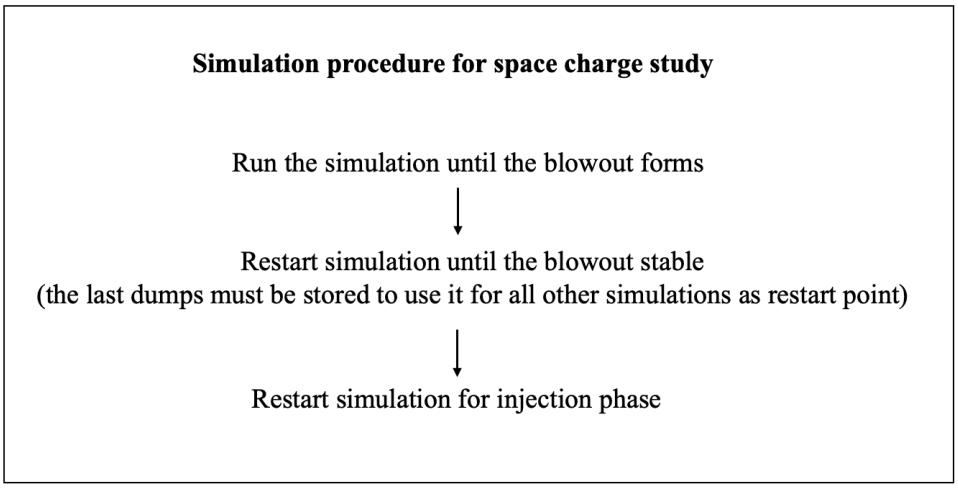

Figure 5.6 : Illustration of the computing steps used for space charge study.

5.3 Examining the Impact of Space Charge on Witness Bunch Quality

With the settings described in the previous section, the case of $w_0 = 7$ μm at a He density equal to 3.3×10^{22} m^{-3} is investigated in detail. This produces a low-charge witness bunch with very low emittance. Now, the normalised emittance evolution in both transverse planes during injection and trapping is plotted in Figure (5.7). At dump 836, the energy of the accelerated electrons corresponds to 15.8 MeV. As shown in (5.6), there are spikes in the plots that make the analysis more difficult. These spikes can result from single electron macroparticles that may appear from non-zero ionisation rates even outside the laser focus spot, dramatically impacting the momentary emittance calculation. Figure (5.8) shows how the macroparticle appeared physically irrelevant, but numerically impactful positions in phase space can distort the emittance calculation. The corresponding spike in emittance is not permanent because either the stray particle is not trapped and hence lost from the simulation box, or it is trapped, and then, legitimately contributes to the formed witness beam. This explains the tail of the spikes, with a typical length of a few dump numbers.

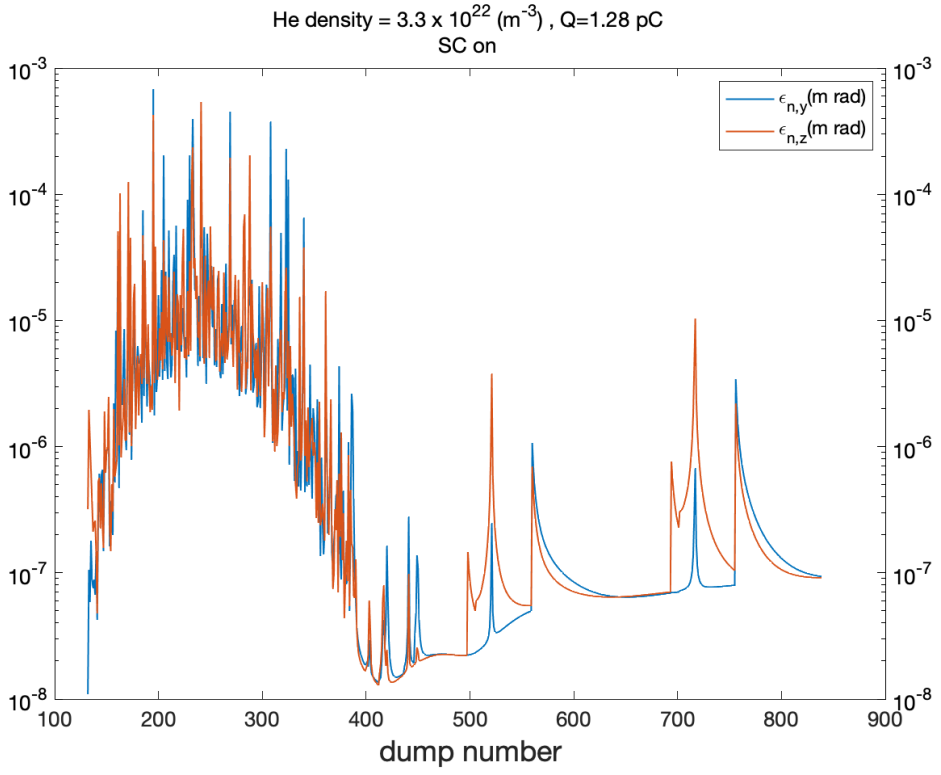

Figure 5.7: Evolution of the transverse emittance in both planes for the witness bunch versus dump numbers, for $w_0 = 7$ μm, with stray particles.

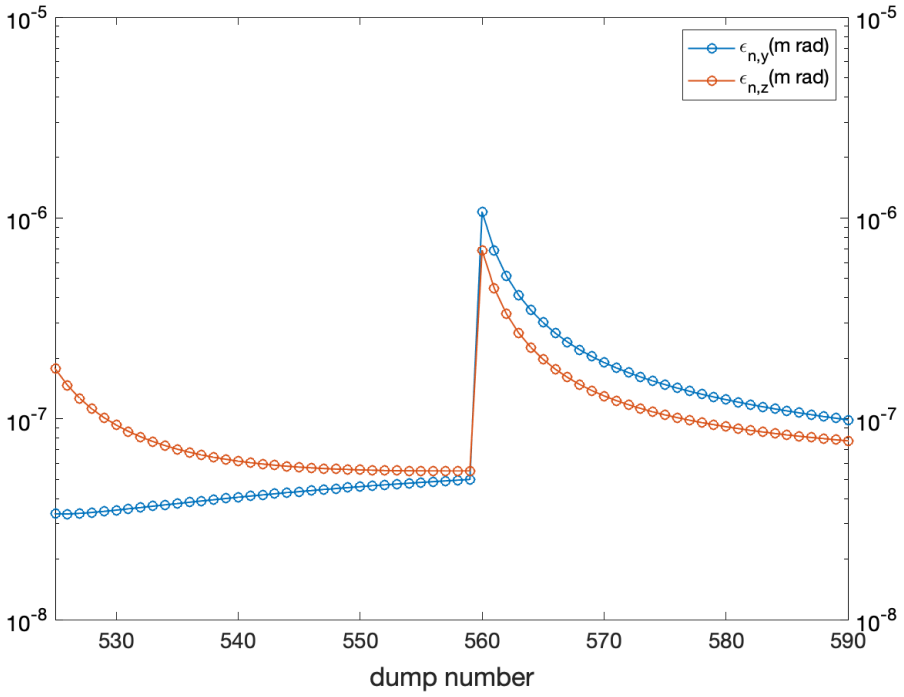

Figure 5.8: A zoom in on the emittance spike shown in Figure 5.7, resulting from a stray particle appearing in the simulation box at dump number 560.

An in-depth analysis by plotting the longitudinal and transverse phase spaces for these dumps, as shown in Figure (5.9), reveals where stray particles that falsify the calculated emittance value are located in longitudinal and transverse phase spaces. Figure (5.10) shows the stray particle in real space. This stray particle does not belong to the formed witness bunch and therefore has to be excluded from the analysis. This identification allows omitting the distorting macroparticles from the analysis, cleaning the plots and focusing on the statistically relevant emittance of the laser-produced witness beam.

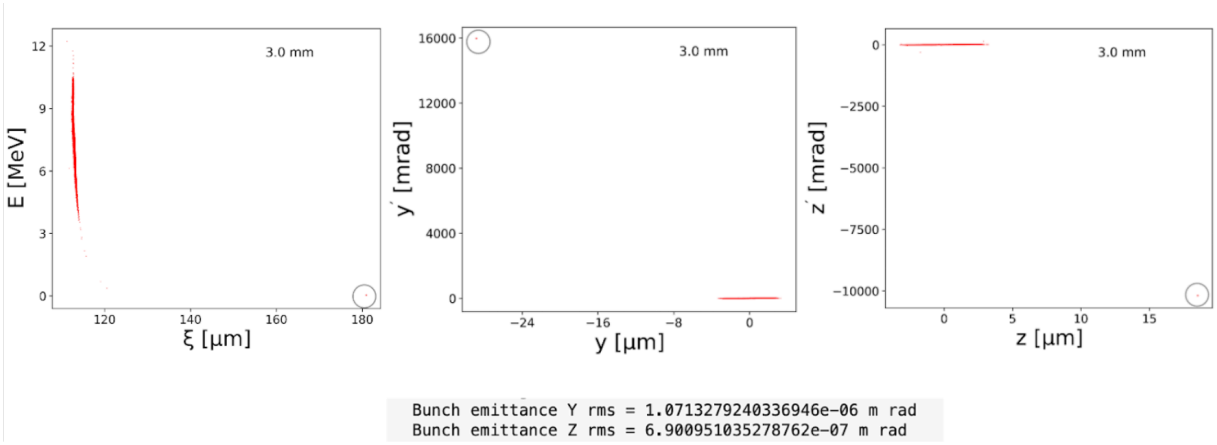

Figure 5.9: Example of identification of stray macroparticles (emphasized by adding the circle) that falsify the calculated emittance value of the beam by plotting the longitudinal phase space and the transverse phase spaces in both planes, shown here for the example of dump number 560 in the simulation shown in Figure 5.8.

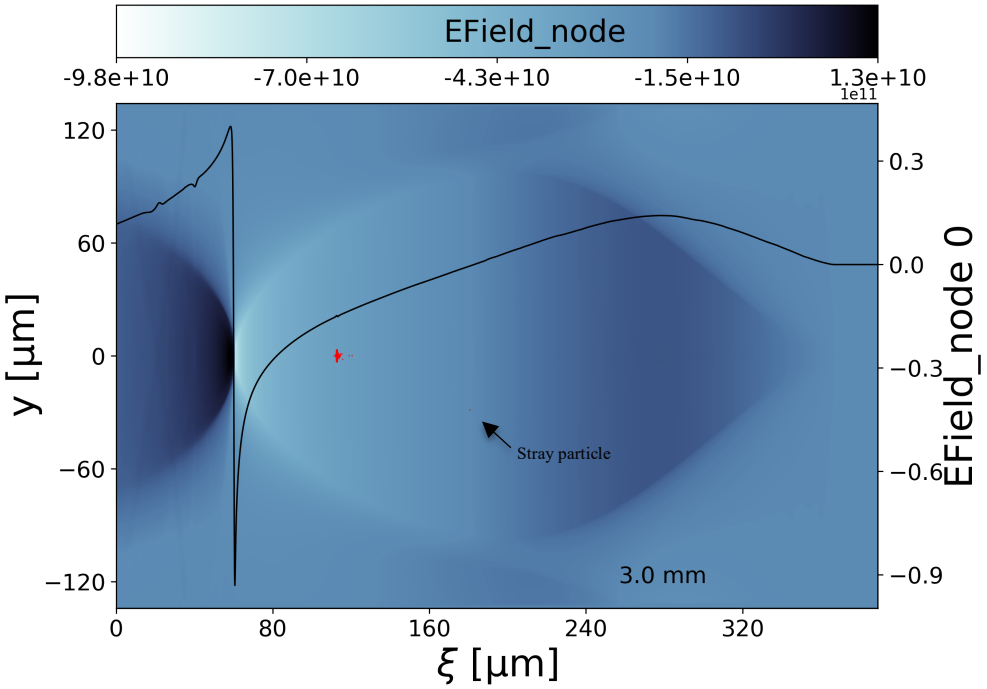

Figure 5.10: Real-space visualization of dump number 560, where the black arrow highlights a red stray particle.

In this example, before cutting, the obtained transverse emittance values are at dump 560 amounts to 1.07×10^{-6} and 6.9×10^{-7} m rad in the y and z directions, respectively. After removing the stray particle, at that dump, the (projected) emittance reaches 5.02 $\times 10^{-8}$ m rad and 5.03×10^{-8} m rad in the y and z directions, respectively,

which is a more realistic value. Now, one can focus on the real witness beam phase (and real) spaces, as shown in Figures 5.11 and 5.12. Interestingly, the transverse phase space plots show how phase is mixed due to the plasma photocathode release procedure causing a broadening of the phase space (i.e., several phase space ellipses of electrons are produced and then mixed).

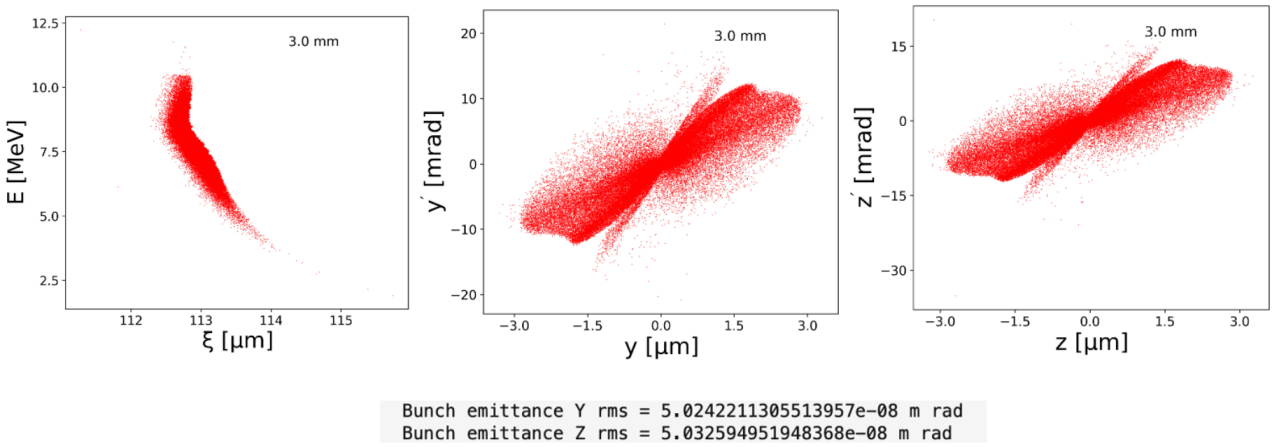

Figure 5.11: Plot of phase spaces in x (longitudinal), y and z directions for dump number 560, after cutting away the stray particles.

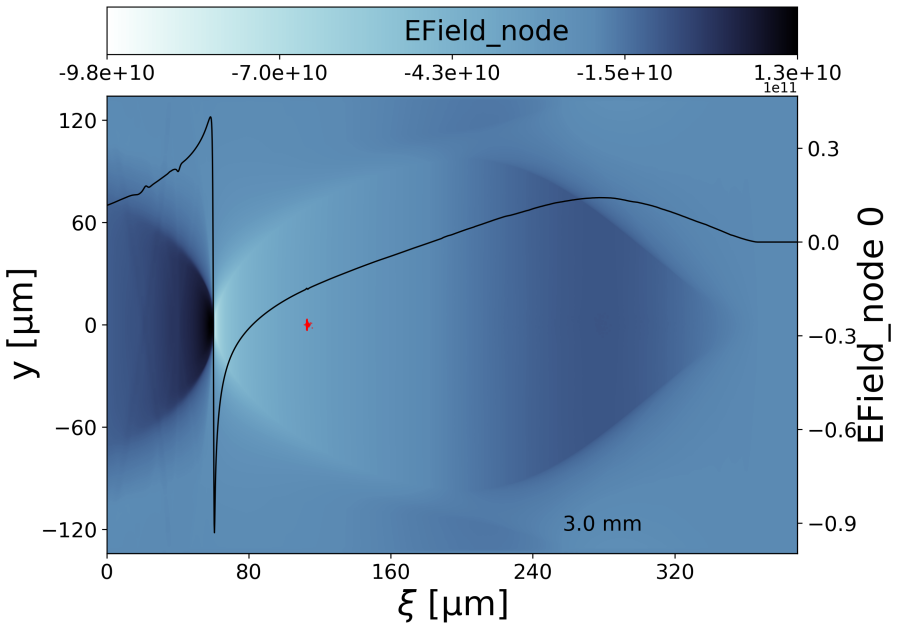

Figure 5.12: The real space of dump number 560 after cutting away the stray particles.

The cleaning procedure can only be partially automatised, and has to be repeated for each dump where stray particles and corresponding dumps in the emittance plots appear. Following this procedure, it was possible to obtain the real emittance curve shown in Figure (5.13). With that, much more meaningful and systematic analysis is possible. Here, one sees that after the initial release process and corresponding high emittance, the emittance reaches a minimum shortly after dump 400, and then increases due to phase mixing. The bunch emittance value rises to ~8.82 x10^{-8} m rad, and while at this stage, it does not yet seem to have reached saturation in this scenario. It allows us to examine the most important phase of release trapping, initial acceleration, and the emittance dynamics are associated with it.

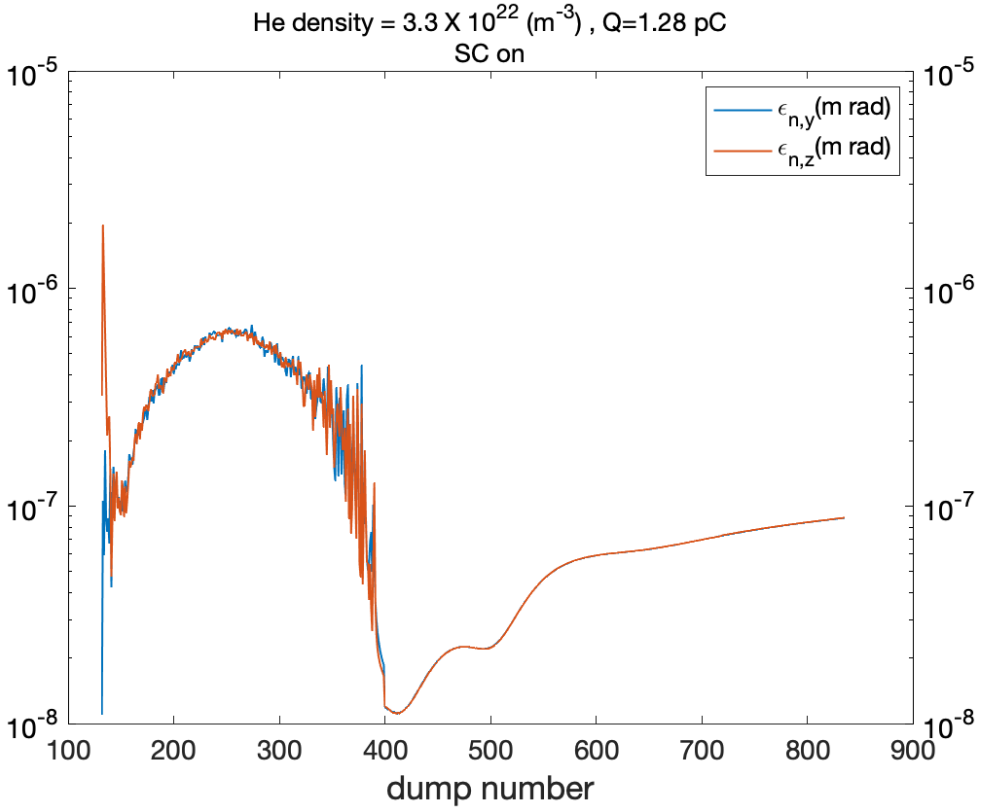

Figure 5.13: Evolution of the transverse emittance for the witness bunch versus dump numbers after cutting the stray particles, for $w_0 = 7$ μm.

The full range of (projected) witness beam parameters is extracted, namely charge Q, r.m.s. bunch length, current, bunch width, transverse momenta, mean

energy, r.m.s. energy spread, and 5D brightness. The evolution of these parameters is displayed in Figure (5.14). Such a comprehensive plot that allows one to correlate trends in one parameter with trends in another, and in particular composite parameters such as emittance and brightness, is crucial to understanding the details of the Trojan Horse beam dynamics.

First, the charge Q curve shows that the release process is finished at a propagation distance of approximately 2300 μm. This is expected because the laser focus is specified to be around 2.2 mm in the simulation. One sees that the laser starts ionising shortly after the wakefield has propagated 2000 μm. The released charge then ramps up in a sinusoidal fashion during focusing. The charge yield (i.e. the time derivative of charge versus time) reaches its maximum at the focus position, and then the charge yield rate decreases until the charge saturate when the ionisation of the laser pulse stops because the laser is diffracting away. The total charge accumulated by this process is $Q \sim 1.28$ pC.

The corresponding evolution of the bunch length σ_x shows that the bunch length is longest during the release process, and reaches a maximum length approximately when some electrons already have reached their final trapping position in the back of the plasma wave. Others are still significantly released by the laser pulse around the centre of the plasma wave. The maximum bunch length is reached at about 2180 μm of propagation distance with $\sigma_x \approx 20$ μm. Generally, when the laser pulse releases in the centre of the plasma wave, and the released electron population is completely trapped, the maximum length the bunch can assume during release is half of the plasma wavelength $\sigma_x \approx \lambda_p/2$, in reality, because the trapping position is earlier. In this case, it is significantly earlier due to the strong plasma wake, and one has $\sigma_x < \lambda_p/2$ for the maximum bunch length. Once the laser-based tunnelling ionisation ceases, the electrons are compressed during the trapping process as they accumulate around the trapping position. Interestingly, while the second panel of Figure (5.14) may appear to indicate that the trapping process is over at a propagation distance of approximately 2.5 mm, a zoom-in (shown in the third panel) shows that the compression process goes on a little while longer until the final, minimum bunch length is assumed. This is important to understand the trend of the current I in the next panel.
The peak current can be expressed as [83]:

$$I_p = dQ/dt|_{max} = \beta cQ/\sqrt{2\pi}\sigma_x \quad (5.2)$$

Where β is the beta function of the electron bunch and c is the speed of light, which clearly shows the dependence of the peak current on bunch length σ_x. Consequently, the current ramps up while charge release is ongoing and the trapping and compression occur. The current monotonically increases (the zigzag spikes in the plot are a

numerical artefact) and asymptotically reaches $I \sim 0.92$ kA at the end of the simulation at 3.3 mm.

Next, the bunch width σ_y is plotted. While the laser pulse is propagating in the centre of the plasma wave also transversally, its waist has a finite size (in this case, w_0 = 7 μm). Therefore, electrons are released in this range around the axis, dependent on the momentary local intensity and the electric field that may cause tunnelling ionisation. Electrons released off-axis are subject to the transverse electric wakefields and, therefore, will gather transverse momentum towards the axis, will overshoot and oscillate back – a phenomenon known as betatron oscillation. Because the release region of the laser pulse is not perfectly localized, electrons will be indifferent betatron oscillation phases. Nevertheless, the average beam size shows that there are trends visible. The r.m.s. The beam size is large at the beginning, approximately of the order of the laser waist size – this simply reflects that the electrons are released over the width of the plasma photocathode laser pulse. Then, transverse forces focus the beam also transversally, which is reflected by a local minimum of the bunch width reached approximately 2.3 mm. Then, however, while the electron beam release ceases due to the diffracting laser pulse, the beam is also compressed in the longitudinal direction, which increases the charge density. The transverse acceleration in the transverse wakefield corresponds to an increase in average transverse momentum (shown in the next panel) – in total, the increasingly complex dynamics then produce a wider beam than initially, with a local maximum, reached approximately 3.1 mm.

The average transverse momentum P of the released electrons has been calculated. This is useful and can relatively directly allow one to gain insights and draw conclusions about the development of space charge forces. As expected, the average transverse momentum is smallest at the beginning of the release process: electrons are released via tunnelling ionisation with negligible transverse momentum – one of the key physics pillars of the Trojan Horse principle. As the witness beam electrons are subject to plasma wakefields during the trapping and acceleration process, and as the witness beam charge density increases due to ongoing release and witness beam compression, the average transverse momentum increases. A local maximum is reached at approximately 2.8 mm. This results from the focusing transverse wakefield, the defocusing transverse space charge forces between individual witness beam electrons, the developing magnetic field, and the self-pinching effect associated with the witness beam current as displayed in panel 4. This is a highly dynamic process, where growing transverse momenta drive the growth of the transverse phase space ellipses and hence emittance. Both the transverse beam size and the average transverse momentum show to some extent, anti-cyclic behaviour: when the transverse momentum is large, the transverse beam size is small and the other way around. There is no perfect match between maximum momentum and minimum beam size, but it is close enough. This is the signature of betatron oscillations, and since both the transverse momentum and the transverse extent of beam electrons

determine the emittance, the transverse emittance develops rather linearly once the beam is completely released.

The emittance is shown in the next two panels. There is an initial peak in emittance at about 2.2 mm during the release, corresponding to the case where some transverse momentum is already developed, but the plasma photocathode release has not yet finished, i.e. the spatial extent of electrons is still large. After reaching a minimum at ~2.6 mm, the emittance increases and at the end of the simulated propagation distance, it has reached a normalised emittance value of ε_n = 88 nm rad. The emittance evolution thus reflects various effects: the increasing transverse momentum, the transversal and longitudinal compression, space charge effects and phase mixing. The latter process can be descriptively described as follows: during the release process, the individual electrons are released at different times, and then added to the bunch at the trapping position until the laser stops to ionize due to diffraction. The first released electrons start gaining energy and rotate in the transverse direction of phase space before the electrons that are released later, and this mixing also leads to the growth of the bunch emittance.

Concerning the 5D brightness, defined as $B_{5D} = 2I/(\varepsilon_{n,x}\,\varepsilon_{n,y})$ as composite parameter featuring the ratio of peak current and emittance in both planes, the resulting trend is shown in the last panel. The brightness scales are linear with current and inversely with the squared emittance, given that in this system, or a plasma photocathode in general, typically, the emittance is the same in both planes. In this case, the competing effect of rising current and slightly rising emittance translates into a rather constant brightness value in the low 10^{18} A/(m^2 rad^2) range over the simulated propagation.

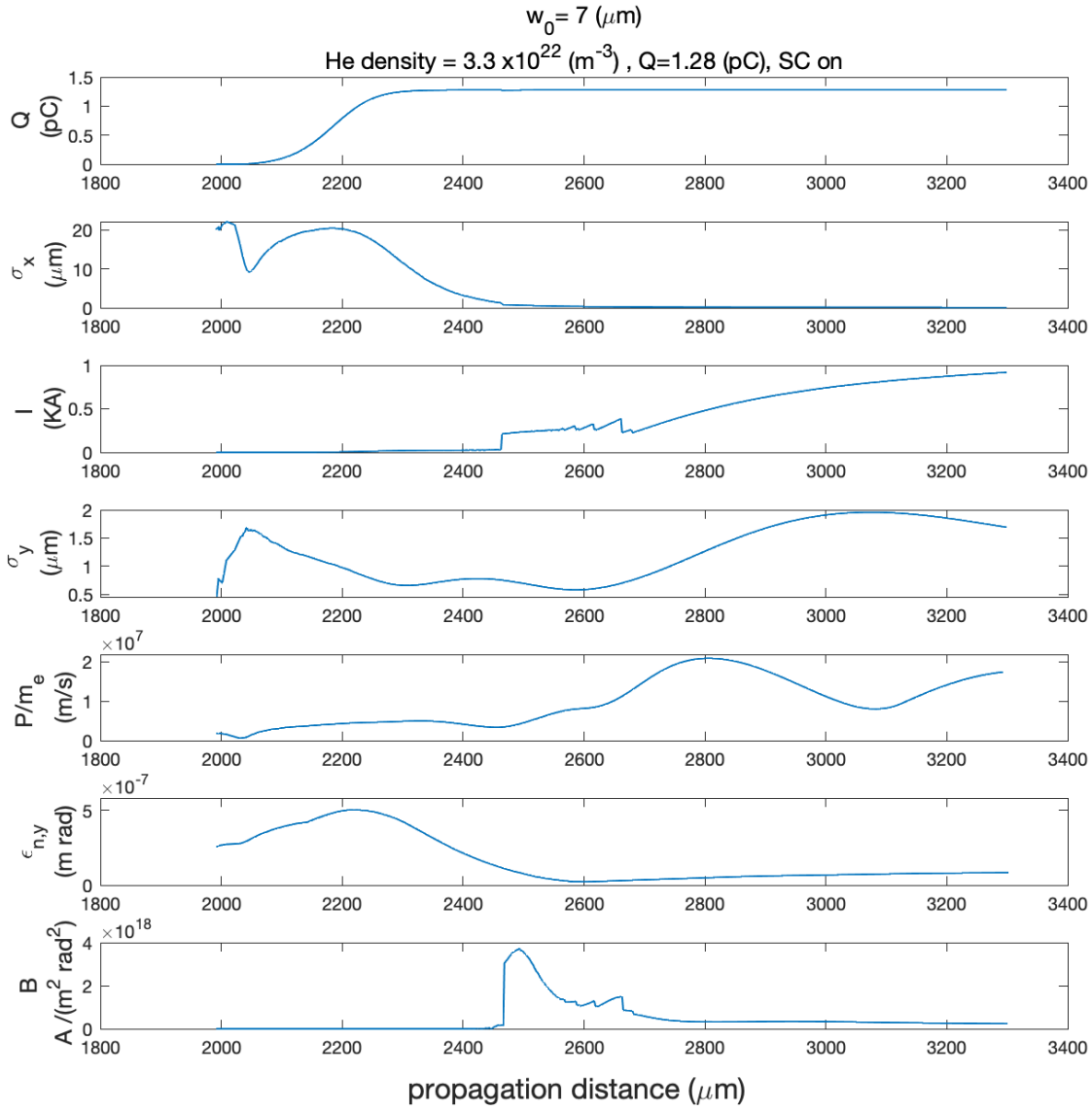

Figure 5.14: The evolution of key witness bunch properties during release trapping and initial acceleration over a propagation distance up to 3.3 mm, for the case of w_0 = 7 μm with He density = 3.3x10^{22} m^{-3}. From top to bottom, the charge Q, r.m.s. bunch length $\sigma_{x,}$, current I, bunch width σ_y, average transverse momenta P, transverse normalised emittance $\epsilon_{n,y}$ and 5D brightness are shown.

Now, we repeat all the previous settings with the same case of w_0 = 7 μm but with He density =3.3 x10^{23} m^{-3} and 3.3 x10^{24} m^{-3}. Then, we plot the witness bunch parameters (see Figures (5.15) and (5.16)). From the scan of the parameters of the witness bunch with He density =3.3 x10^{23} m^{-3} Figure (5.15), it is clear to us that the value of the charge increases to 12.8pC as a result of the increase in the density of helium to 3.3 x10^{23}m^{-3} and this will affect other parameters of the bunch as we shall see. Concerning the length of the bunch, we notice that the length of the bunch increased to 0.47 μm,

where the force of the space charge dominates with the increase in the density and leads to an increase in the length of the beam. As for emittance, the effect of the space charge on its value becomes clear, as it increases to 102 nm rad, and for the 5D brightness, its value increases with the rise in the current value to 3.99×10^{20} A/(m^2 rad^2).

From the Figure (5.16), we increased the He density to 3.3×10^{24} m^{-3}. This will affect increasing the charge to 128.6 pC, followed by a clear influence of the forces of space charge on the other parameters of the bunch and this is evident by increasing the length of the bunch to 2.26 μm., and this is an expected result of the large influence of the forces of space charge on the bunch, which in turn, will also raise the emittance value to 137 nm rad.

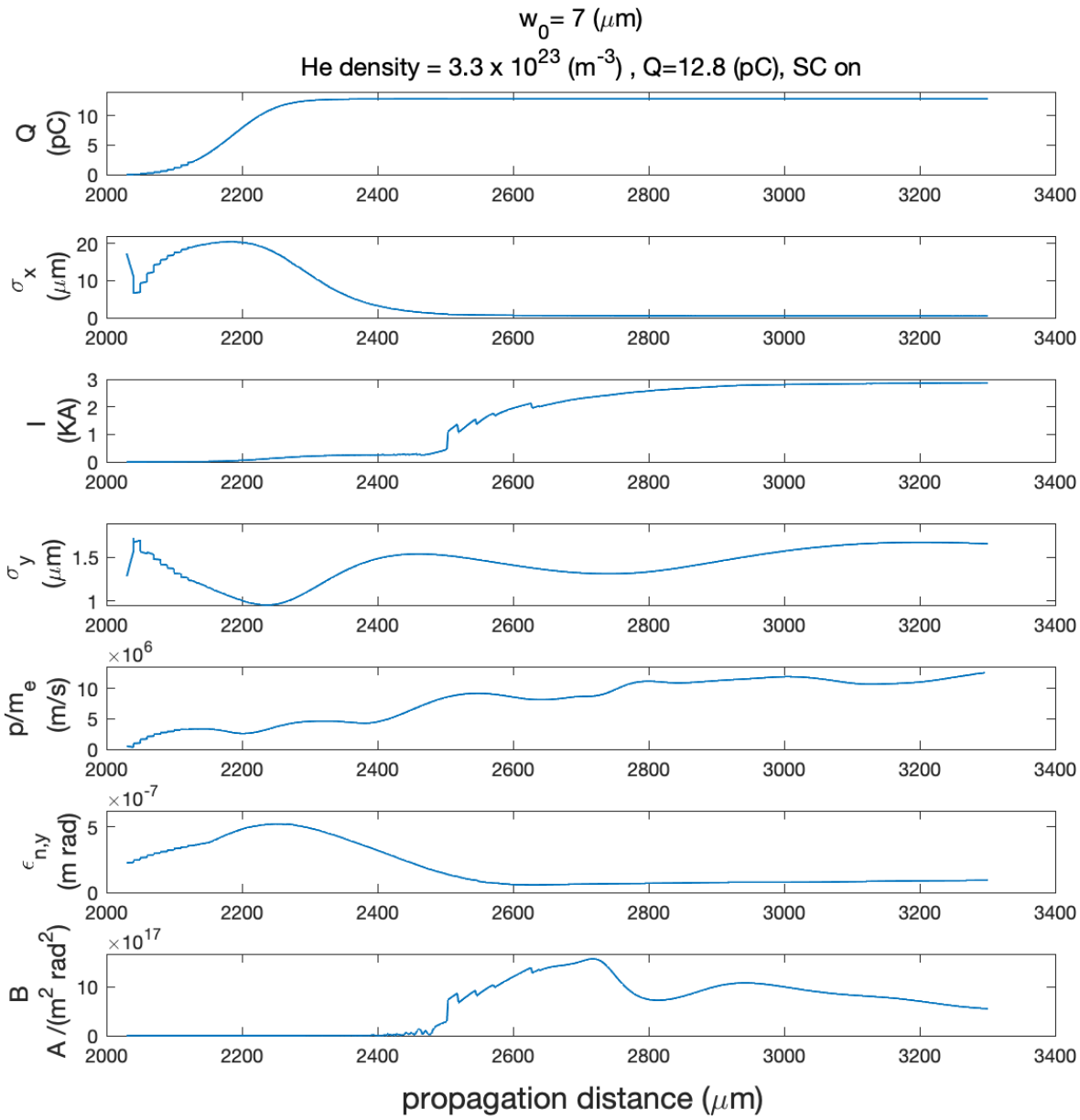

Figure 5.15: The evolution of key witness bunch properties during release trapping and initial acceleration over a propagation distance up to 3.3 mm, for the case of w_0 = 7 μm with He density = 3.3x10^{23} m^{-3}. From top to bottom, the charge Q, r.m.s. bunch length $\sigma_{x,}$, current I, bunch width σ_y, average transverse momenta P, transverse normalised emittance $\epsilon_{n,y}$ and 5D brightness are shown.

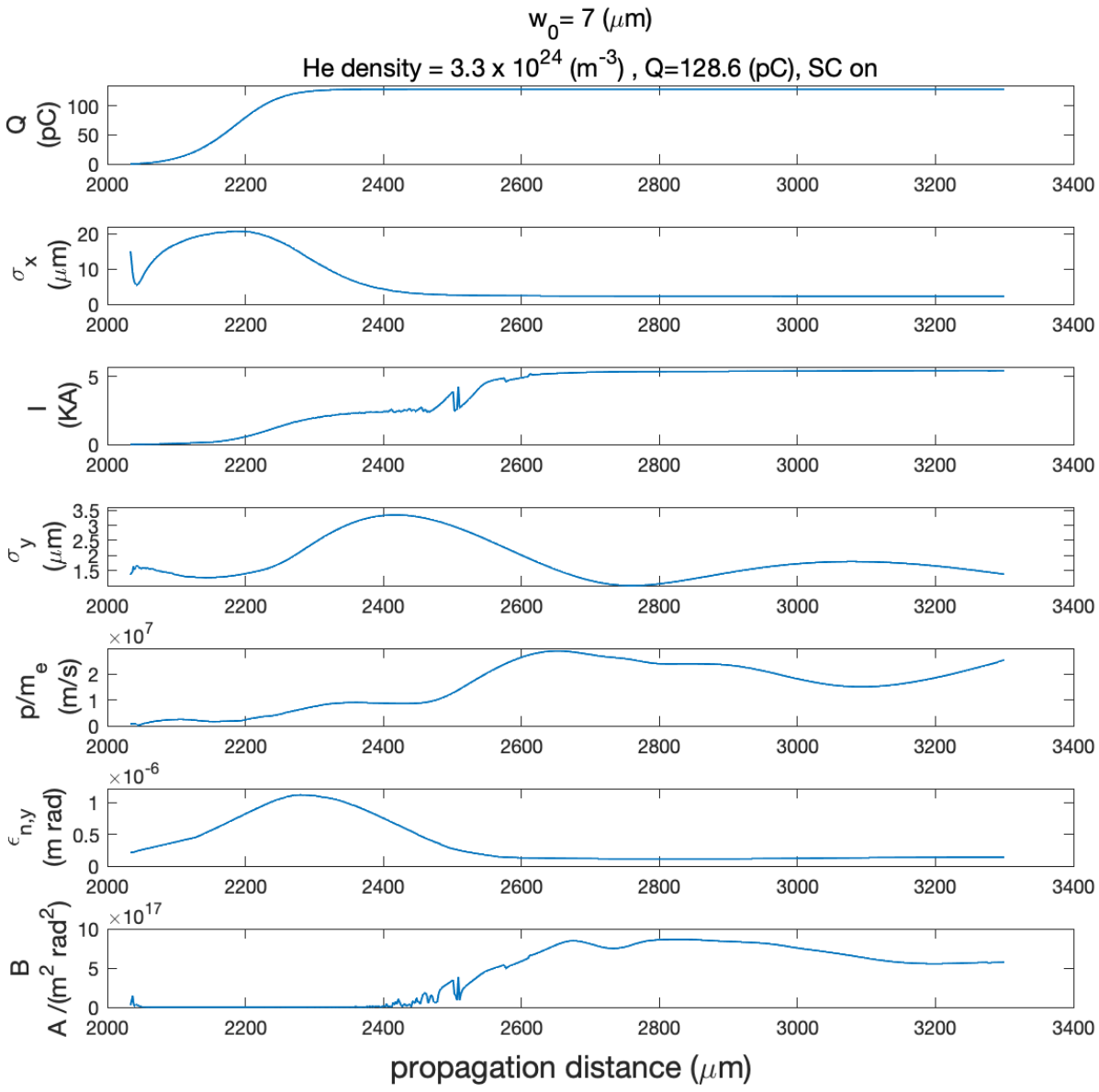

Figure 5.16: The evolution of key witness bunch properties during release trapping and initial acceleration over a propagation distance up to 3.3 mm, for the case of w_0 = 7 μm with He density = 3.3x10^{24} m^{-3}. From top to bottom, the charge Q, r.m.s. bunch length $\sigma_{x,}$, current I, bunch width σ_y, average transverse momenta P, transverse normalised emittance $\epsilon_{n,y}$ and 5D brightness are shown.

Likewise, we also produced three levels of charges of witness bunch for the case of w_0=15 μm with He density 3.3x10^{22} m^{-3}, 3.3x10^{23} m^{-3}, and 3.3x10^{24} m^{-3} respectively and scanned the properties of the witness bunch for all three cases, see Figure (5.17)-(5.19). In this case, we increased the laser spot size, and this is followed

by obvious effects on the produced bunch parameters with increasing helium density. From the Figure (5.17), with a density of helium $3.3x10^{22}$ m^{-3}, the value of the bunch charge reaches 27.4 pC, which is higher than the value of the charge that we obtained in the first scan in Figure (5.14) when we used a spot size of laser pulse w_0=7 μm. In addition, the current value reaches 4.89 KA with a bunch length of up to 0.24 μm. The width of the bunch is 4.6 μm, with an average transverse momentum reach $3.2x10^7$. As for the emittance value, it is estimated at 756 nm rad. In the Figure (5.18), we observe the charge yield is ramped up to 273.98 pC with a bunch length reach to 1.04 μm as a result of increased the density of helium to $3.3x\ 10^{23}m^{-3}$. In contrast, the emittance value increases with increased He density to reach around 4013 nm rad. Regarding the 5D brightness, Its value decreases to $3.05x10^{15}$ $A/(m^2\ rad^2)$, and the reason is due to the large increase in the emittance value according to the equation (3.5). From Figure (5.19), the value of the bunch charge increases to 2739.1 pC followed by a noticeable increase in bunch length of up to 7.78 μm, due to the increase in the strength of the effect of space charging in this case. As for the current, it is a natural result; with an increase in the charge, its value reaches 41.17 kA. The emittance value reaches a maximum value of 8177 nm rad, which is the upper limit in this scan. It is expected of the higher helium density and the laser spot size. In the last, the 5D brightness decreases to reach $1.23x10^{15}$ $A/(m^2\ rad^2)$ due to the large increase in the emittance value with the increase of the bunch charge.

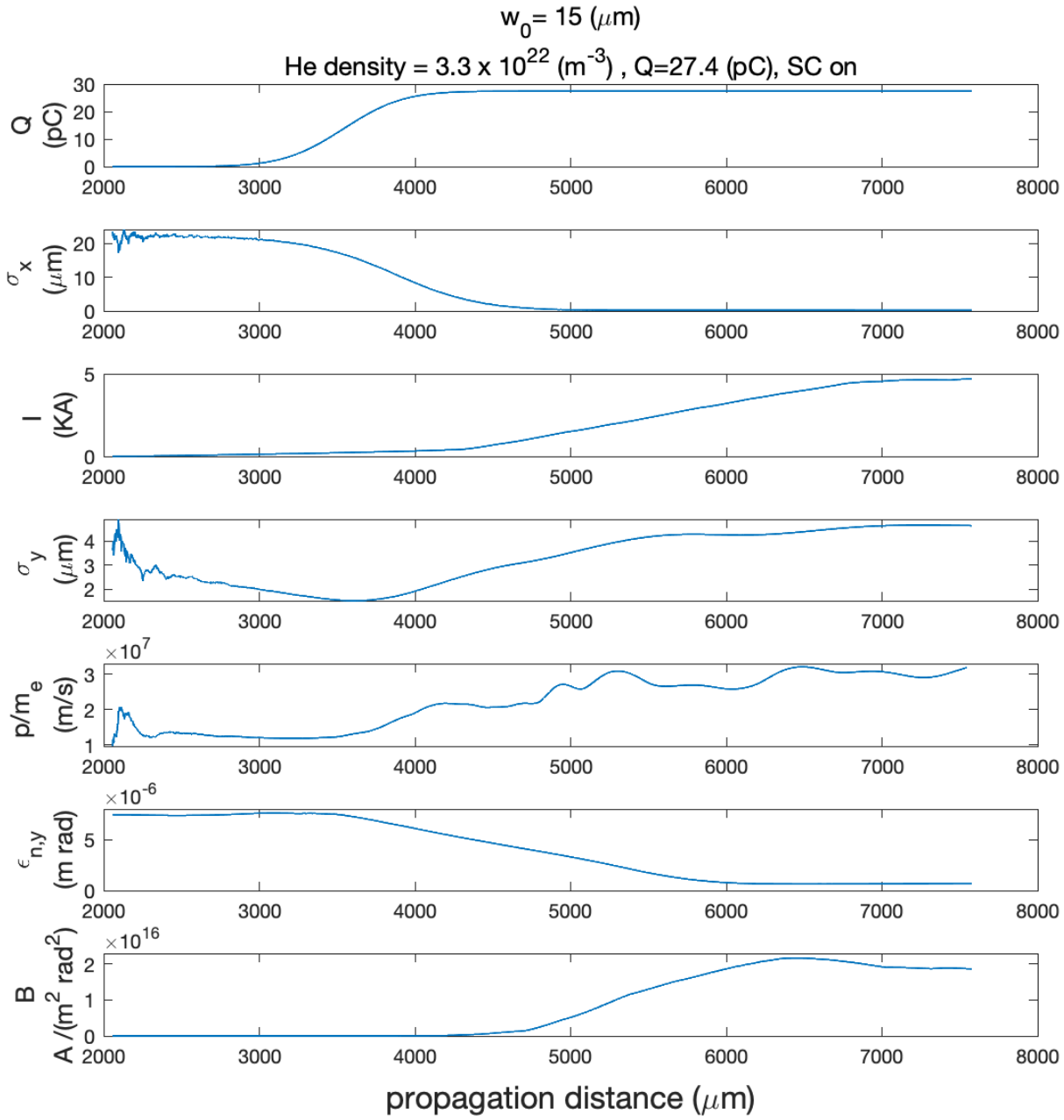

Figure 5.17: The evolution of key witness bunch properties during release trapping and initial acceleration over a propagation distance up to 3.3 mm, for the case of w_0 = 15 μm with He density =3.3x10^{22} m^{-3}.From top to bottom, the charge Q, r.m.s. bunch length $\sigma_{x,}$, current I, bunch width σ_y, average transverse momenta P, transverse normalised emittance $\epsilon_{n,y}$ and 5D brightness are shown.

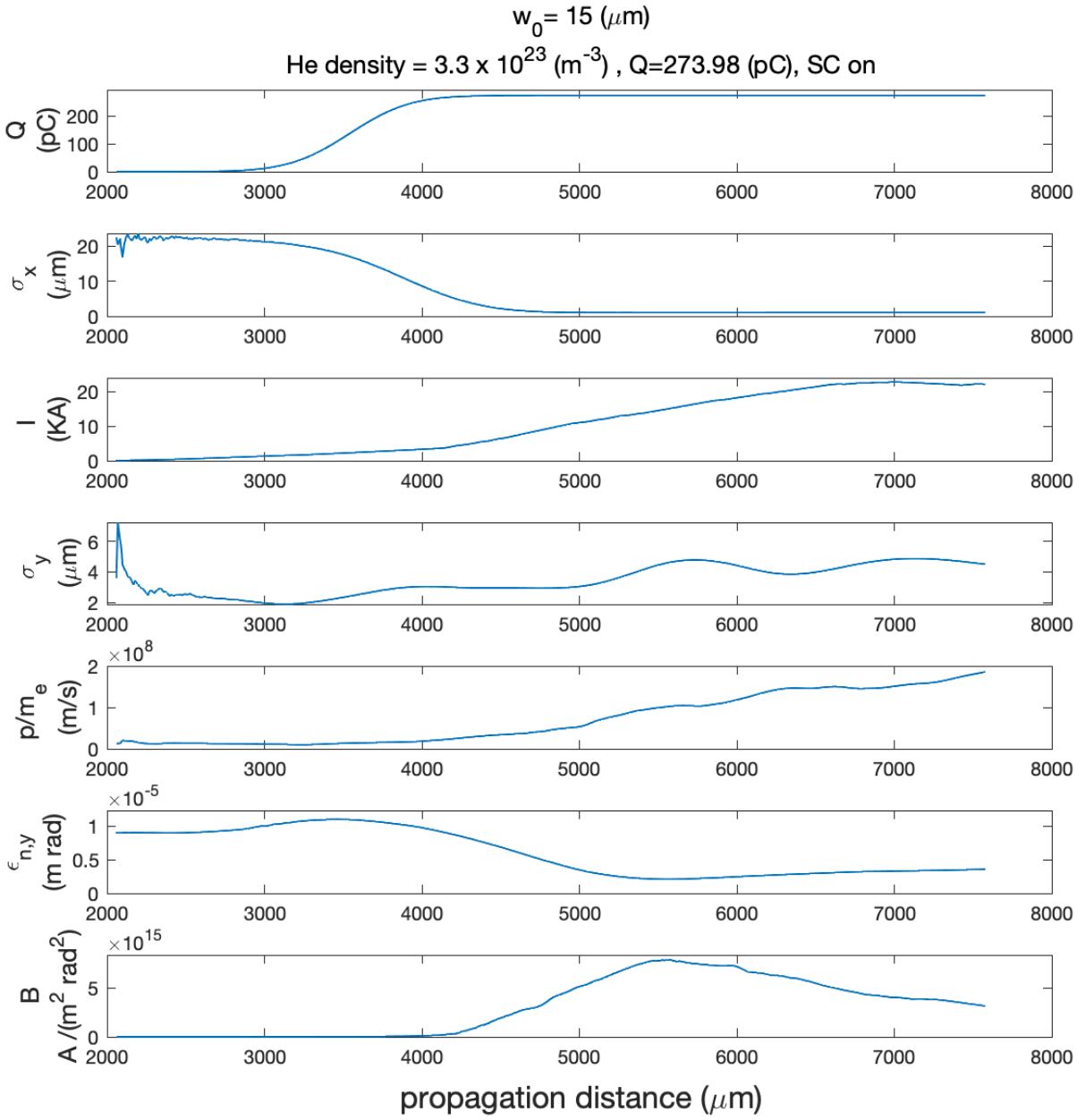

Figure 5.18: The evolution of key witness bunch properties during release trapping and initial acceleration over a propagation distance up to 3.3 mm, for the case of w_0 = 15 μm with He density =3.3x10^{23} m^{-3}.From top to bottom, the charge Q, r.m.s. bunch length $\sigma_{x,}$, current I, bunch width σ_y, average transverse momenta P, transverse normalised emittance $\epsilon_{n,y}$ and 5D brightness are shown.

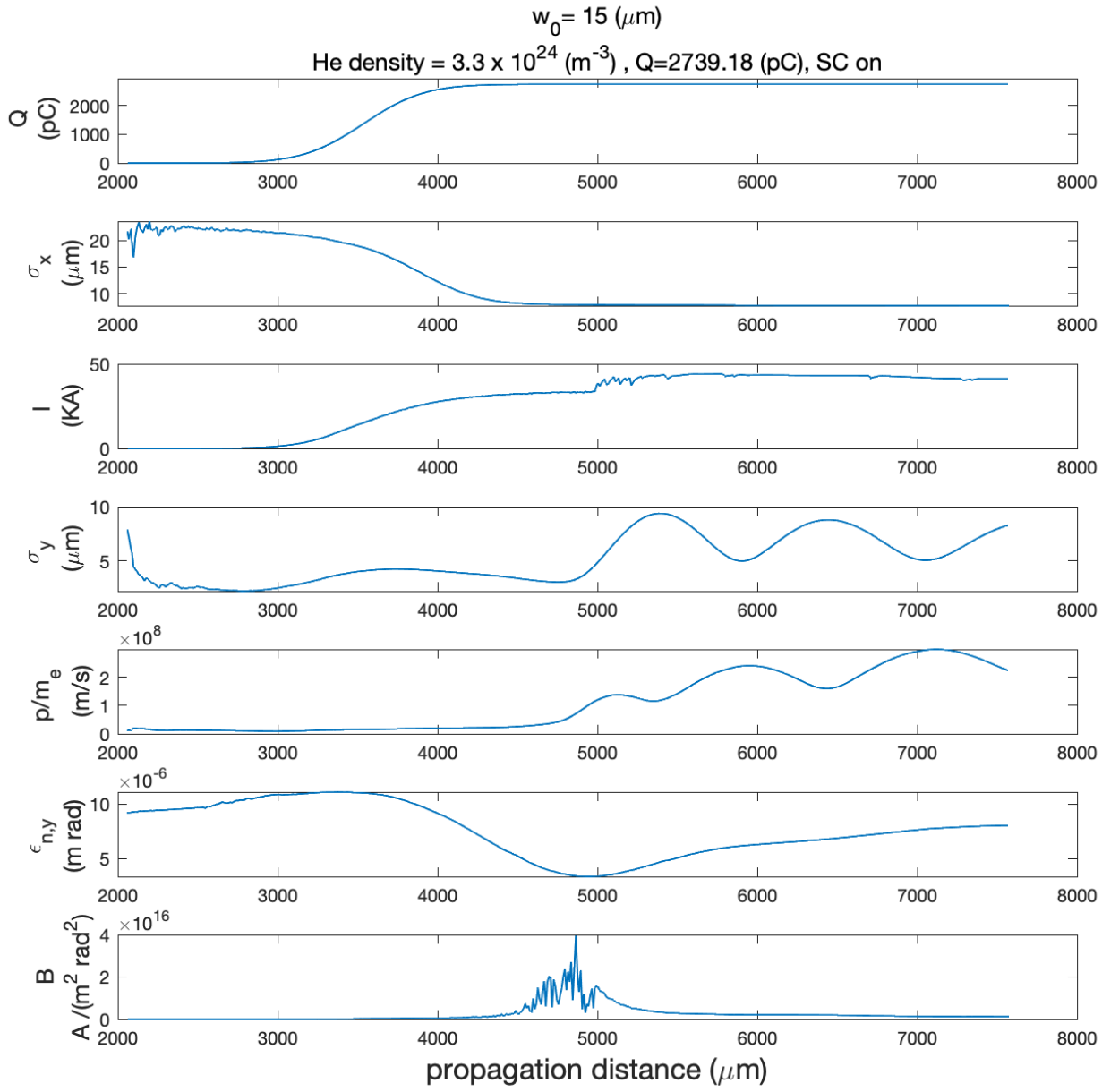

Figure 5.19: The evolution of key witness bunch properties during release trapping and initial acceleration over a propagation distance up to 3.3 mm, for the case of w_0 = 15 μm with He density =3.3x10^{24} m^{-3}.From top to bottom, the charge Q, r.m.s. bunch length σ_x,, current I, bunch width σ_y, average transverse momenta P, transverse normalised emittance $\epsilon_{n,y}$ and 5D brightness are shown.

5.4 Isolation of the Space Charge Effect

The previous scans, which reflect the real physics, including space charge, have shown the dramatic effects on the space charge when the witness beam charge increases substantially. Now, the effect of intra-bunch space charge forces is switched off. This can be performed in the simulation by having the witness beam interact only with the plasma wakefields. The focus is now on the transverse emittance, and the evolution of the emittance is plotted for w_0 = 7 μm with He density $3.3\text{x}10^{22}$ m^{-3}, $3.3\text{x}10^{23}$ m^{-3}, and $3.3\text{x}10^{24}$ m^{-3}, respectively, and is contrasted with these cases when the space charge is switched off. Figure (5.20) shows the emittance in the y-direction, and (5.21) z-direction. At the same time, the emittance increases when He density is increased for the simulations that take space-charge into account when the space charge effects are switched off. The resulting emittance is the same, independent of the assumed He density. Since the release laser pulse has the same parameters in each case, the same volume is ionized. The only difference is that orders of magnitude more charge is released when orders of magnitude ramp up the He density. Therefore, it is not required to run simulations with space charge artificially switched off for multiple He densities; one is enough.

In the case of spot size w_0 = 15 μm, the space charge-off case was applied to only one case (with a nominal helium density equal to $3.3\text{x}10^{22}$ m^{-3}). Figures (5.22) and (5.23) show the transverse normalised emittance in the y-and z-directions. The dashed line shows the space charge-off simulation case. These plots are immensely instructive since they reflect the minimum emittance obtained in these cases, only considering the effects of phase mixing.

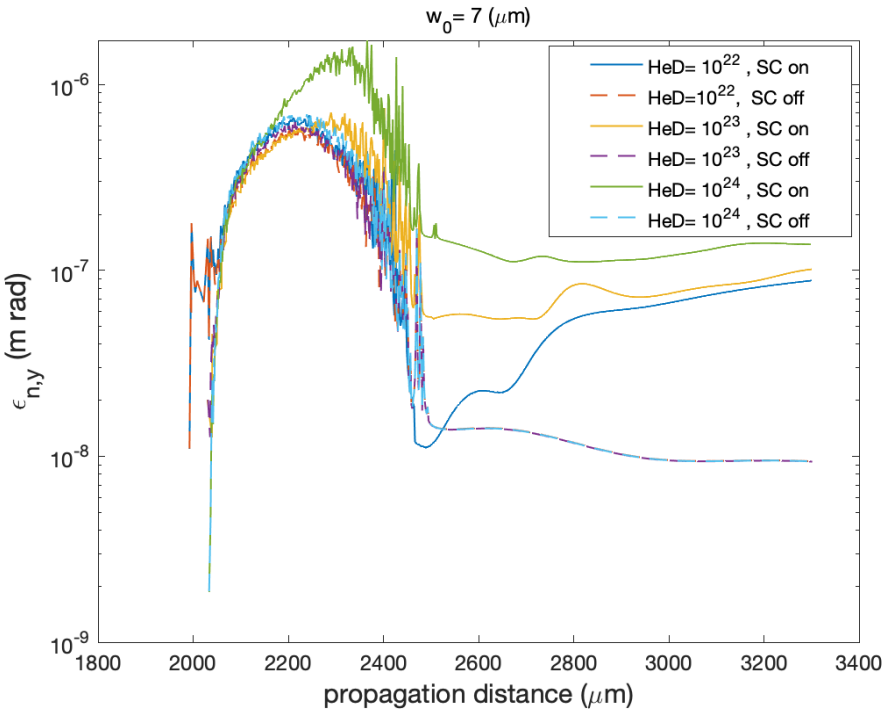

Figure 5.20: Evolution of the transverse emittance in y-direction for the witness bunch versus dump numbers, for $w_0 = 7$ µm with He density =$3.3x10^{22}$ m^{-3},$3.3x10^{23}$ $m^3$and $3.3x10^{24}$ m^{-3}, respectively.

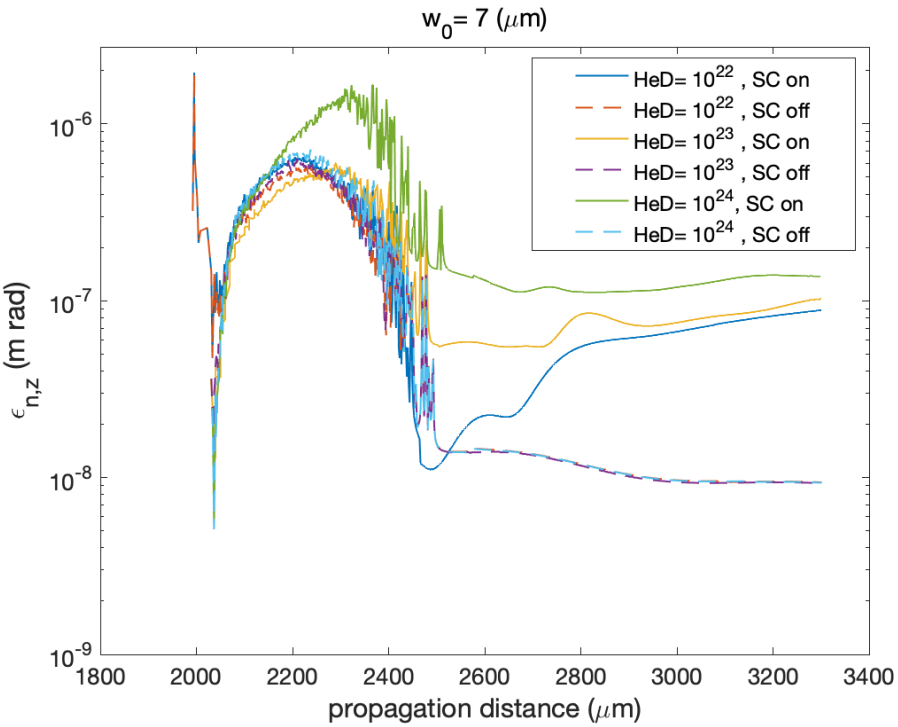

Figure 5.21: Evolution of the transverse emittance in z-direction for the witness bunch versus dump numbers, for $w_0 = 7$ µm with He density =$3.3x10^{22}$ m^{-3},$3.3x10^{23}$ $m^3$and $3.3x10^{24}$ m^{-3}, respectively.

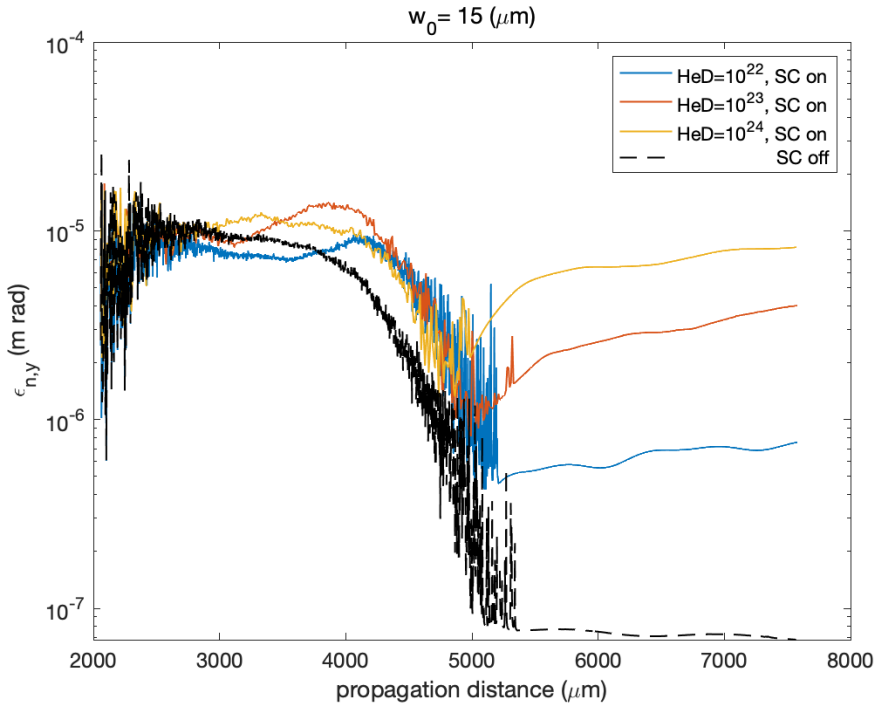

Figure 5.22: Evolution of the transverse emittance in y-direction for the witness bunch versus propagation distance, for $w_0 = 15$ µm with He density=$3.3\text{x}10^{22}\text{m}^{-3}$, $3.3\text{x}10^{23}$ $\text{m}^3$and $3.3\text{x}10^{24}$ m^{-3}, respectively.

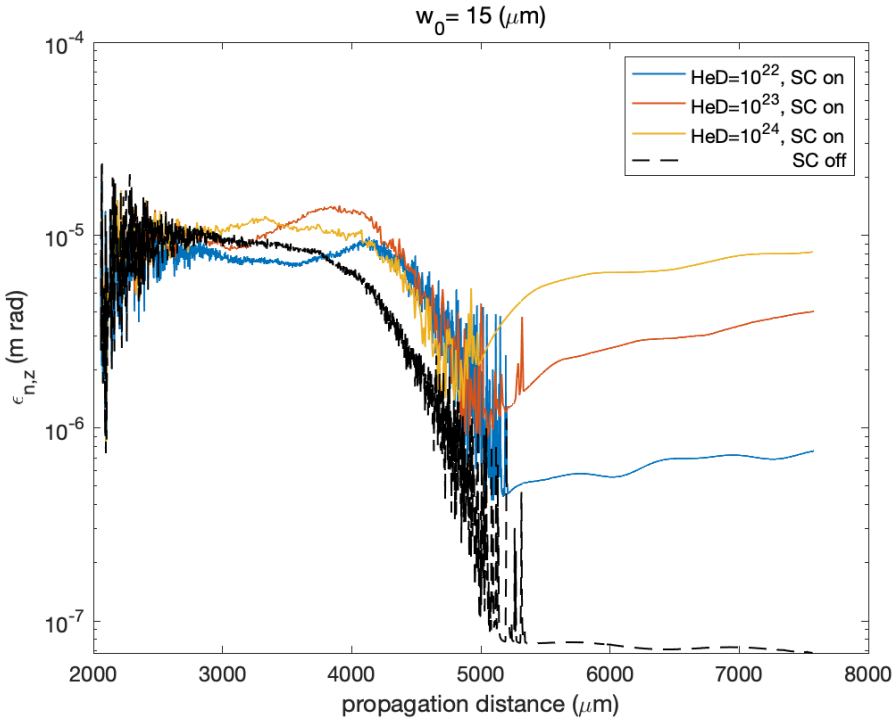

Figure 5.23: Evolution of the transverse emittance in z-direction for the witness bunch versus propagation distance, for $w_0 = 15$ µm with He density=$3.3\text{x}10^{22}\text{m}^{-3}$, $3.3\text{x}10^{23}$ $\text{m}^3$and $3.3\text{x}10^{24}$ m^{-3}, respectively.

Another way of exploring the influence of space charge is to investigate the evolution of transverse momenta. Then, the transverse positions increase as the transverse momenta let the electrons move farther outside. So, it is a dynamic process where growing transverse momenta drive the growth of the transverse phase space ellipse and emittance. One would expect that at the very beginning of the release, the average absolute transverse momenta are close to zero, and then the transverse wakefields and the transverse space-charge forces increase the momentum. In Figures (5.24) and (5.25), the average of absolute transverse momenta is plotted for the case of w_0=7 μm and w_0=15 μm for different He densities. As expected and seen before in Figure (5.14) ff., at the very beginning of the release, the average absolute transverse momentum is small, and then, the transverse wakefields and the transverse space-charge forces increase the momentum. In fact, if one looks at Figure (5.24), the plot without space charge looks most regularly. The transverse momentum oscillates between local minima and local maxima. This is the signature of betatron oscillation of the bunch in the plasma wakefield, where collectively a low average transverse momentum P corresponds to a large beam size (many of the individual electron trajectories reach the largest transverse amplitude and a turning point at the same time, have low transverse momenta). The other way around, the maximum transverse momentum is reached when electrons cross the propagation axis, which corresponds to the smallest beam size. While this oscillatory behaviour is also present for the other plots with switched space charge effects, it is less systematic and regular. The space charge disturbs the pure oscillation in the wakefield, leading to the more peculiar transverse momentum evolution patterns. For example, it may be a little counter-intuitive to see that the plot for the He density of 10^{23} m^{-3} exhibits a much reduced oscillatory momentum evolution than for the lower density of 10^{22} m^{-3}, and in particular larger peak average momenta P at the higher density. This indicates that beam loading may result, and this expectation is confirmed later in section 5.5.

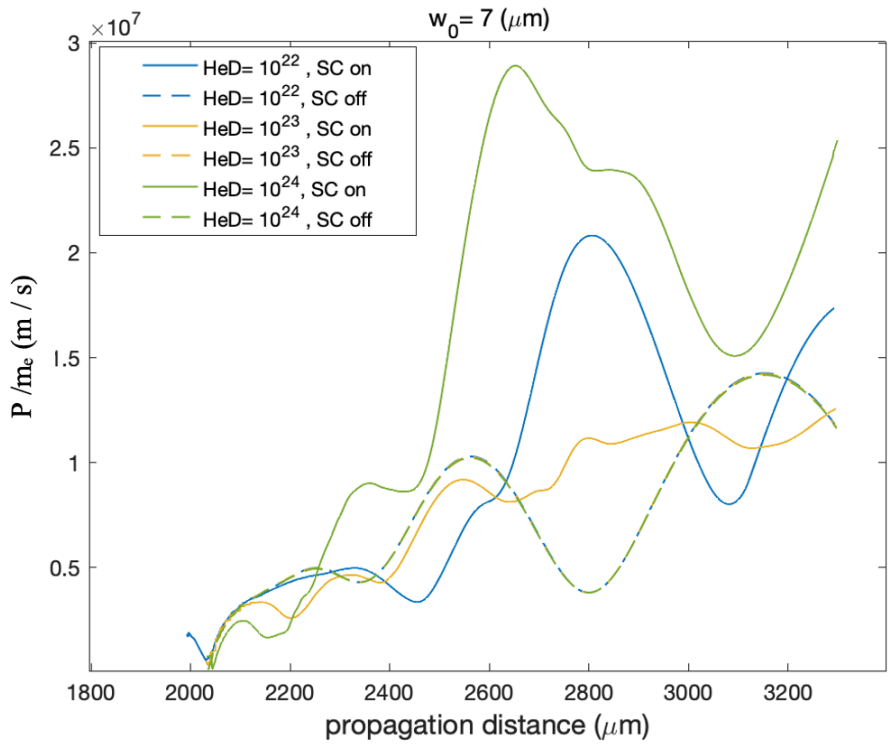

Figure 5.24: The average of absolute transverse momenta during versus propagation distance, for w_0 = 7 μm with He density =3.3x10^{22} m^{-3}, 3.3x10^{23} m^{3} and 3.3x10^{24} m^{-3}, respectively.

In Figure (5.25), the average transverse momentum P evolution for the laser spot size of w_0 = 15 μm across the He densities and the space charge off. As a reminder, the case of He density of 3.3x10^{24} m^{-3} produces a charge of Q » 2739 pC. Therefore, one expects a much different evolution when contrasted to lower charge values or even the case where space charge is neglected. Indeed, the Figure shows that the local minima and maxima of the average transverse momentum are completely shifted. Interestingly, in this case, P exhibits a maximum for n_{He} = 3.3x10^{24} m^{-3}, whereas the case of space charge off exhibits a minimum. This shows that the effect of space charge can turn the bunch evolution completely upside down.

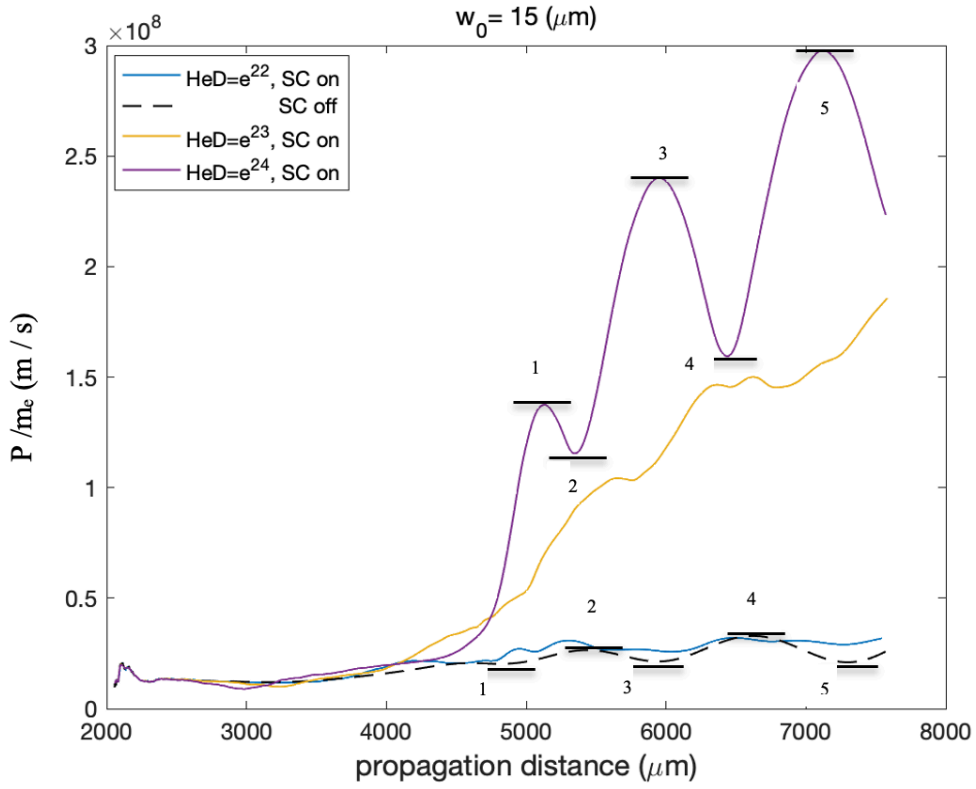

Figure 5.25: The average of absolute transverse momenta during versus propagation distance, for w_0 = 15 μm with He density =3.3x10^{22} m^{-3},3.3x10^{23} m^{3}and 3.3x10^{24} m^{-3}, respectively.

This behaviour can be explored in further detail by looking at the transverse phase space situations, e.g., at these prominent positions highlighted in Figure (5.25). We plot the transverse phase spaces for n_{He} = 3.3x10^{24} m^{-3} in Figure (5.26), and the corresponding transverse phase spaces for the case of space charge off in Figure (5.27). For example, at point 2 (a local minimum of average transverse momentum), Figure (5.26) reveals that the transverse shape of macroparticles is 'horizontal', i.e., there is low angular momentum (y-axis) and a large extent of macroparticles in the transverse direction (x-axis). There is a dense central core of macroparticles, but significant fractions of the electron population have oscillation amplitudes substantially larger than the core. This is a clear sign of the space charge transverse kick. In contrast, at point 3, many particles have large transverse momentum but are compressed to a small transverse size.

On the contrary, in Figure (5.27), no such wings exist around the central core. Note that the scaling of the axes is very different from Figure (5.26). The much higher phase space density of the core, together with the absence of 'space-charge wings', is the reason for the dramatically smaller emittance in this hypothetical case, which is accessible only to simulations.

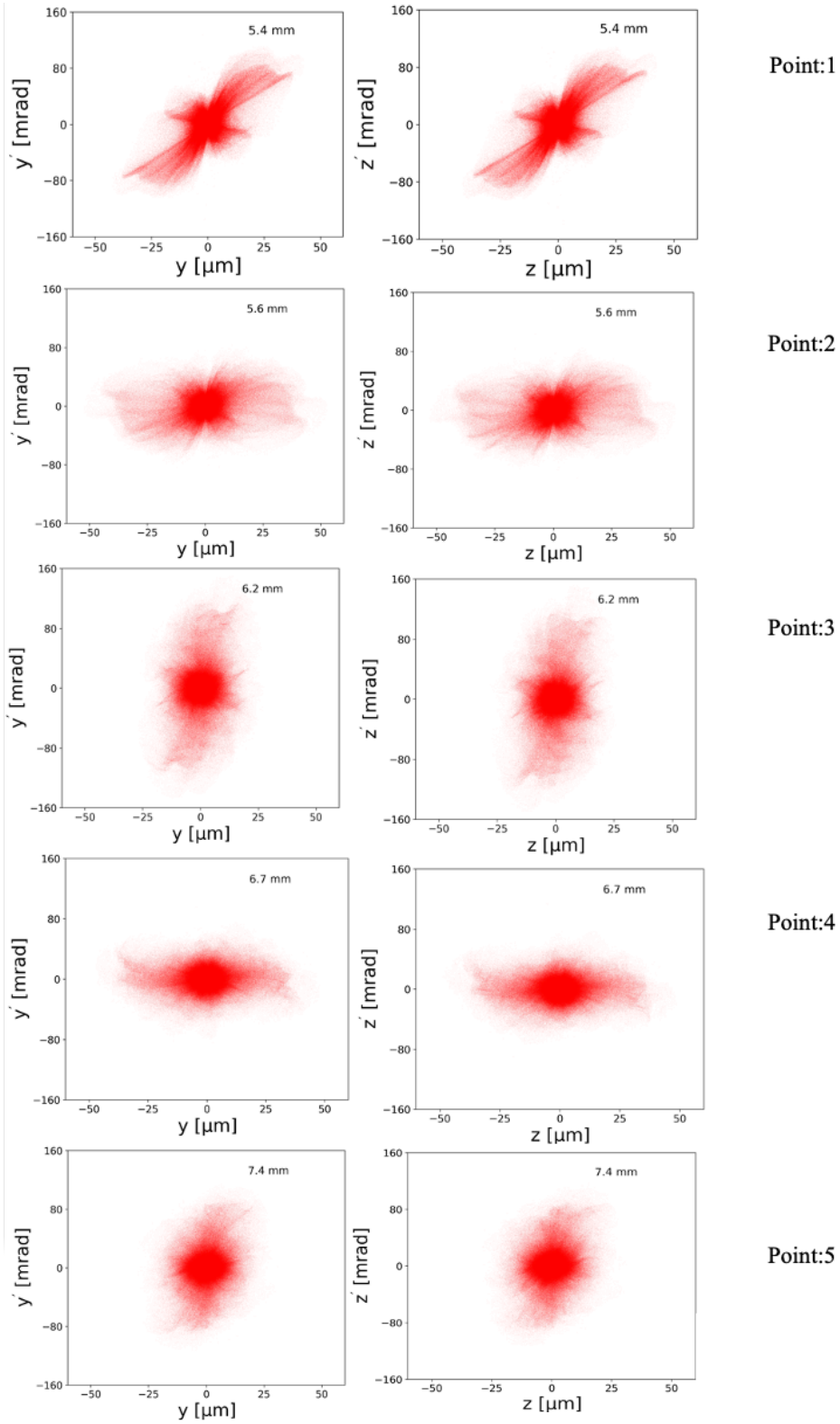

Figure 5.26: Plot of the transverse phase spaces at local minima and maxima points for the density curve = 3.3×10^{24} m^{-3} at the Figure (5.25).

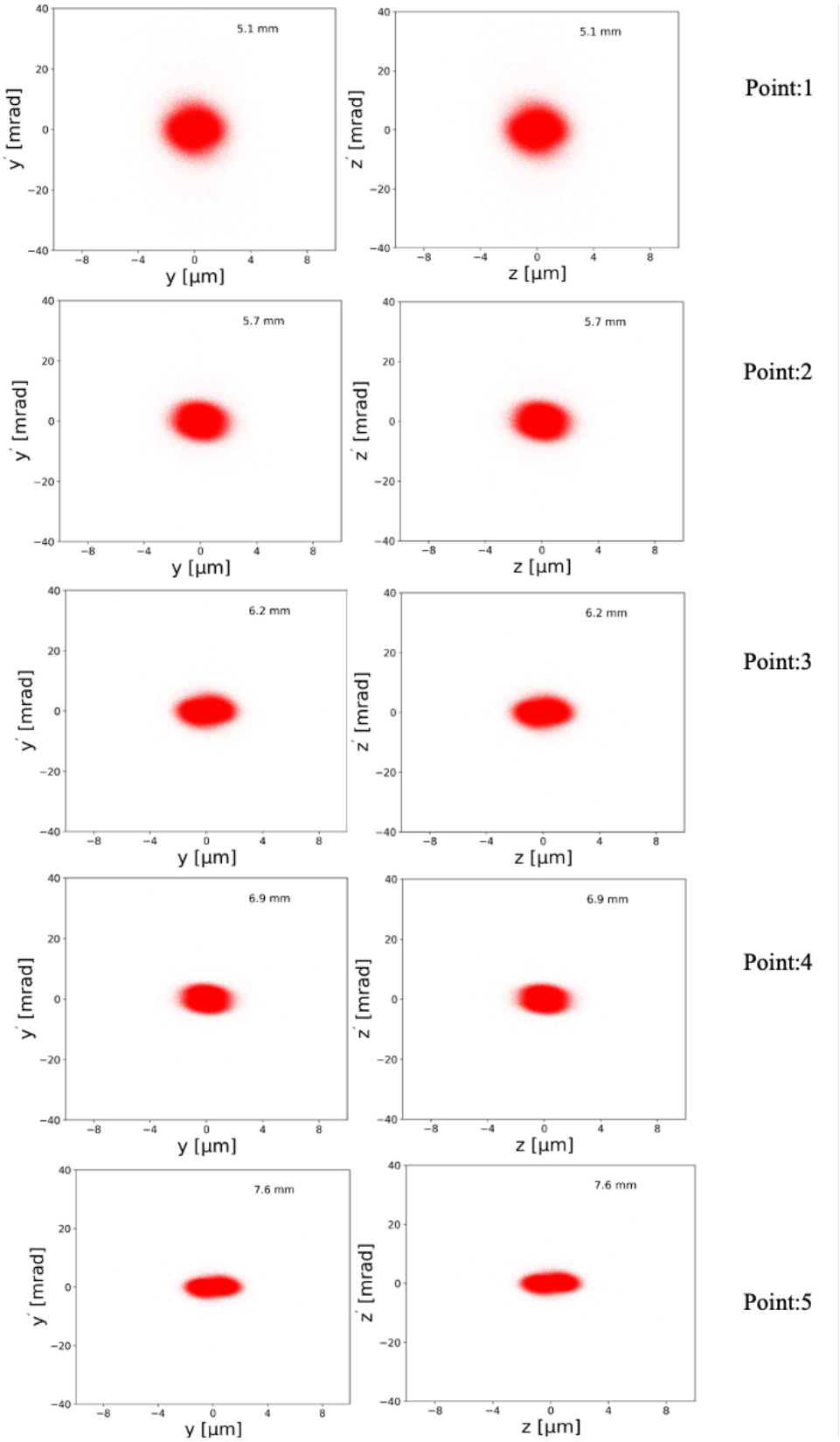

Figure 5.27: Plot of transverse phase spaces at local minima and maxima point for the curve when space charge is off, Figure (5.25).

5.5 Comparison of Witness Bunch Parameters at Different He Densities with and without Space Charge Effects

In this section, first, the evolution of key parameters is plotted as a function of different He densities, including the case of space charge off. This comparison helps to understand the evolution of parameters, taking into account the insights offered by previous observations. Figure (5.28) and (5.29) contrast the charge Q, bunch length σ_x, current I, transverse beam width σ_x, mean energy E, and 5D brightness B_{5D} for the two spot sizes w_0=7 μm and w_0=15 μm, respectively.

Regarding the charge Q, we simply observe the linear relation in charge yield when the He density is ramped up. The bunch length σ_x, on the other hand, shows a more complex behaviour. The bunch length is based on beam loading and intra-bunch effects in a complex way. In any case, the shortest bunch length is obtained for the case of no space charge, is very similar to very low bunch charge, and is largest for the highest He density run, rather suddenly jumping to a bunch length of the order of $\sigma_x \approx 3$ μm when setting the He density to $n_{He} = 3.3\text{x}10^{24}$ m^{-3}. In all cases, the bunch length reaches a local maximum when all charge is released by the laser pulse, consistent with previous observations.

The corresponding current I, plotted with the logarithmic y-axis, provides further insight. There is a sudden jump in current in the runs where the space charge was switched on. This sudden jump is largest for the low-charge case, suggesting it is numerical. On the other hand, strong beam loading is associated with strong deformation of the longitudinal field, which may lead to local current spikes in the simulation, but perhaps also in reality. This phenomenon will be investigated in future works.

The comparison of bunch width evolution σ_y again shows the oscillatory behaviour and shows that the bunch width is minimal when the space charge is off. This is consistent with the much reduced average transverse momentum, and the much higher phase space density in the hypothetical case of no space charge effects.

The mean gained energy reflects the effect of beam loading, leading to reduced energy gradients in case of larger charge values, and the strongest energy gains in low charge cases or when beam loading is completely absent in the case of space charge off.

Finally, the 5D brightness is calculated. This reveals that the brightness of space charge-off cases strongly diverges from the end of the release process. The brightest beams of the space charge on cases here are produced by the two highest He densities used, $n_{He} = 3.3\text{x}10^{24}$ m^{-3} and $n_{He} = 3.3\text{x}10^{23}$ m^{-3}, thus reflecting the balance between competing the impact of current and emittances.

Similar behaviour in all aspects is exhibited by the scans for the laser spot size w_0=15 μm (shown in Figure 5.29), partially even more pronounced due to the released larger charge.

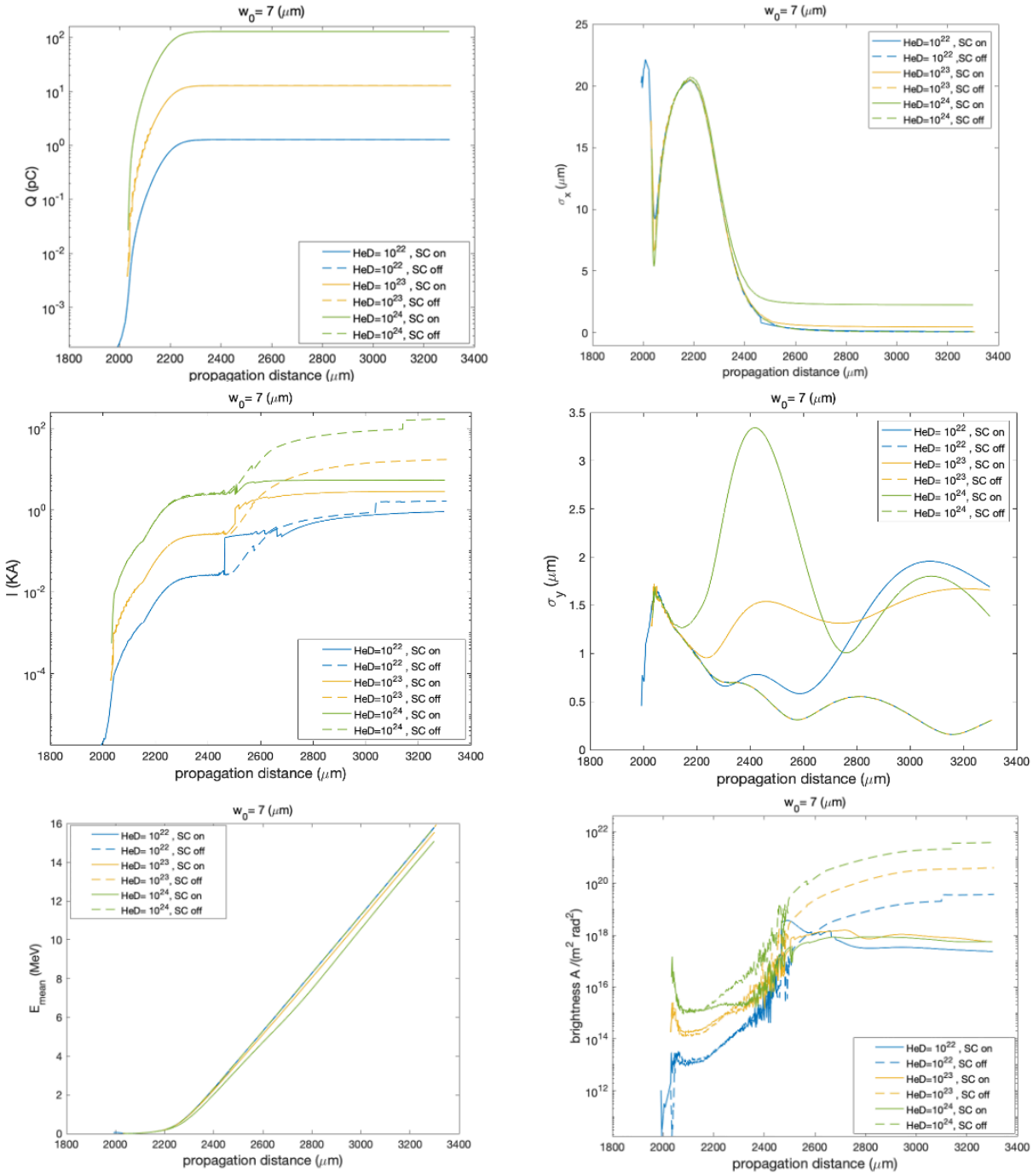

Figure 5.28: The evolution of the charge Q, r.m.s. bunch length σ_x, current I, bunch width σ_y, mean energy Emean and *5D* brightness versus propagation distance at different He densities, when SC is on and off for w_0=7μm.

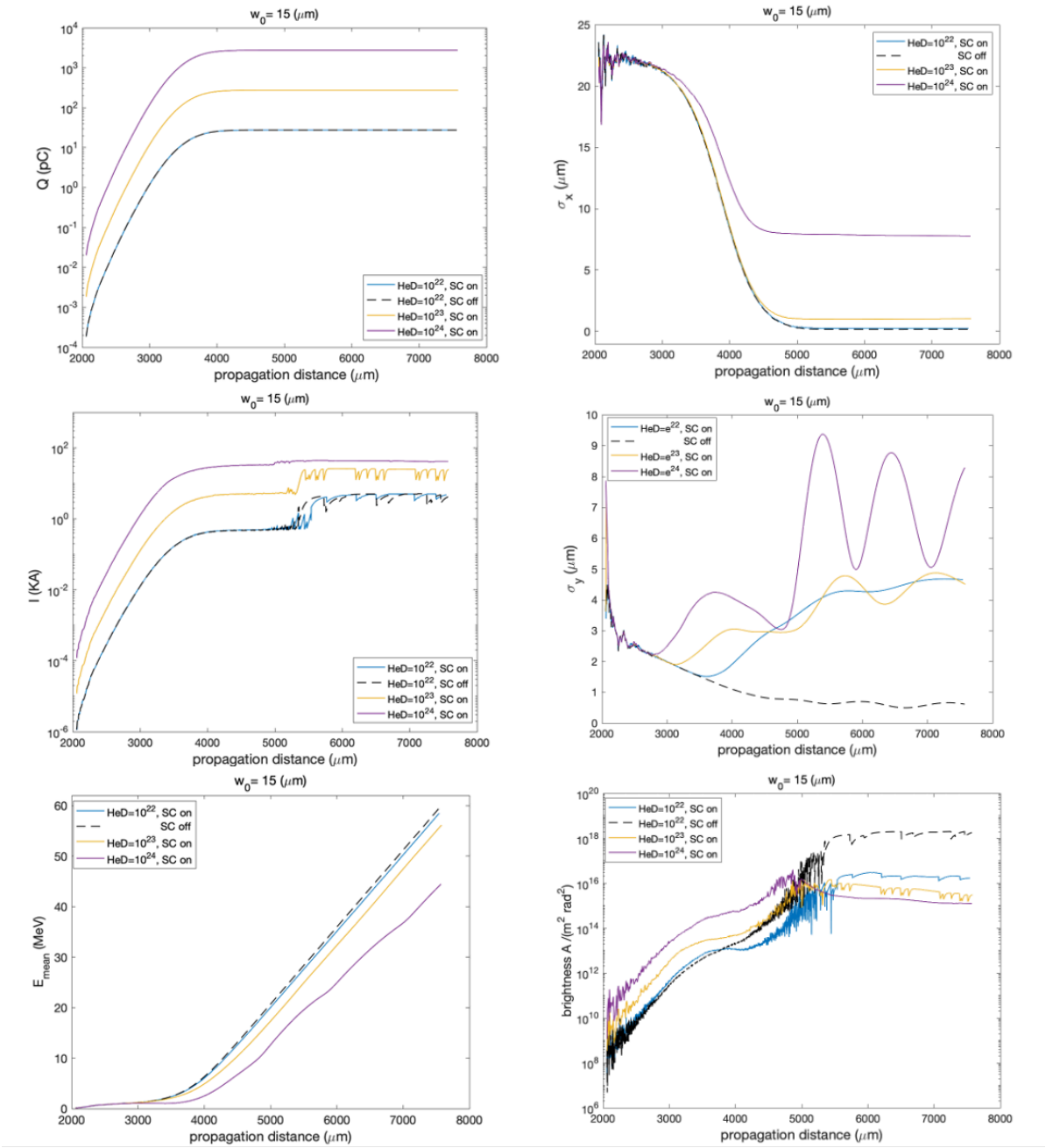

Figure 5.29: The evolution of the charge Q, r.m.s. bunch length σ_x, current I, bunch width σ_y, mean energy Emean and *5D* brightness versus propagation distance at different He densities, when SC is on and off for w_0=15μm.

While the focus was on projected global beam parameters, further detail can be investigated by resolving the slice parameters of the produced beams. The slice emittance and current at the end of the simulation are shown in Figures (5.30) and (5.31) for both cases, w_0 =7 μm and w_0 =15 μm across the He densities tested, including the space charge off cases.

The first observation that becomes very clear from plotting the slice details is that the $n_e = 3.3\times10^{24}$ m^{-3} case (pink lines) produces Q = 128.6 pC of charge. The formed bunch is much longer than in all other cases. Note that both emittance and current are plotted with a logarithmic scale. The $n_e = 3.3\times10^{23}$ m^{-3} case (green lines) already produces much shorter beams, and the $n_e = 3.3\times10^{22}$ m^{-3} case (blue lines) already has a very comparable beam duration compared to the space charge off cases. The clear reason for the longer bunch at higher densities is beam loading. In contrast to beam loading via external injection, a relativistically stable beam injected with a pre-defined length and its fields are simply overlayed on the wakefield, beam loading in status nascendi. This highly dynamic process leads to bunch lengthening, which can be seen very well.

Such lengthening can also be understood in a single-particle picture, where an electron released later would be kicked out transversally by the existing charge that had been released earlier and is already trapped and has gained energy. A transverse kick (i.e. momentum growth) is then reflected by increased (slice) emittance. Therefore, (slice) emittance, current, and bunch length are coupled. When more charge is released, such as in the $n_e = 3.3\times10^{24}$ m^{-3} case, the current and emittance are larger, and the bunch is longer than in the cases where less charge is produced.

Dynamics beam loading also affects the bunch shape, e.g., in the form of the current longitudinal profile. The zoom-in in Figure (5.30) shows the space charge-off cases. The current longitudinal profile is nearly Gaussian and symmetric. This is produced from a laser pulse that symmetrically is focused, reaches the focus and then diffracts again. The peak of the current profile then reflects the longitudinal position within the laser pulse, where the most charge is released on aggregate. This may not necessarily be the longitudinal centre of the laser pulse, and things may be complicated by a situation where the laser pulse is not exactly centred in the middle of the wakefield but is slightly shifted and/or by the movement of the ionisation front of the laser pulse, which will be regarded later.

In any case, when space charge is on and at elevated He densities, the current longitudinal profile deviates from its simple, more or less symmetric shape. This is another result of beam-loading and can be seen, e.g., by local dips in current and emittance.

An interesting trend can be observed in the simulation for w_0 = 15 μm, as shown in Figure (5.31). The current peak in the low charge and space charge off cases is located at the head of the bunch. Such a profile can be expected when the ionisation front is mostly located in the front of the release laser pulse. In such scenarios, more charge is released at the front of the laser pulse than at the end, leading to such

asymmetric current profiles. Another possibility for such a shape may be an imperfect centring of the laser pulse in the centre of the wake at the wakefield zero-crossing.

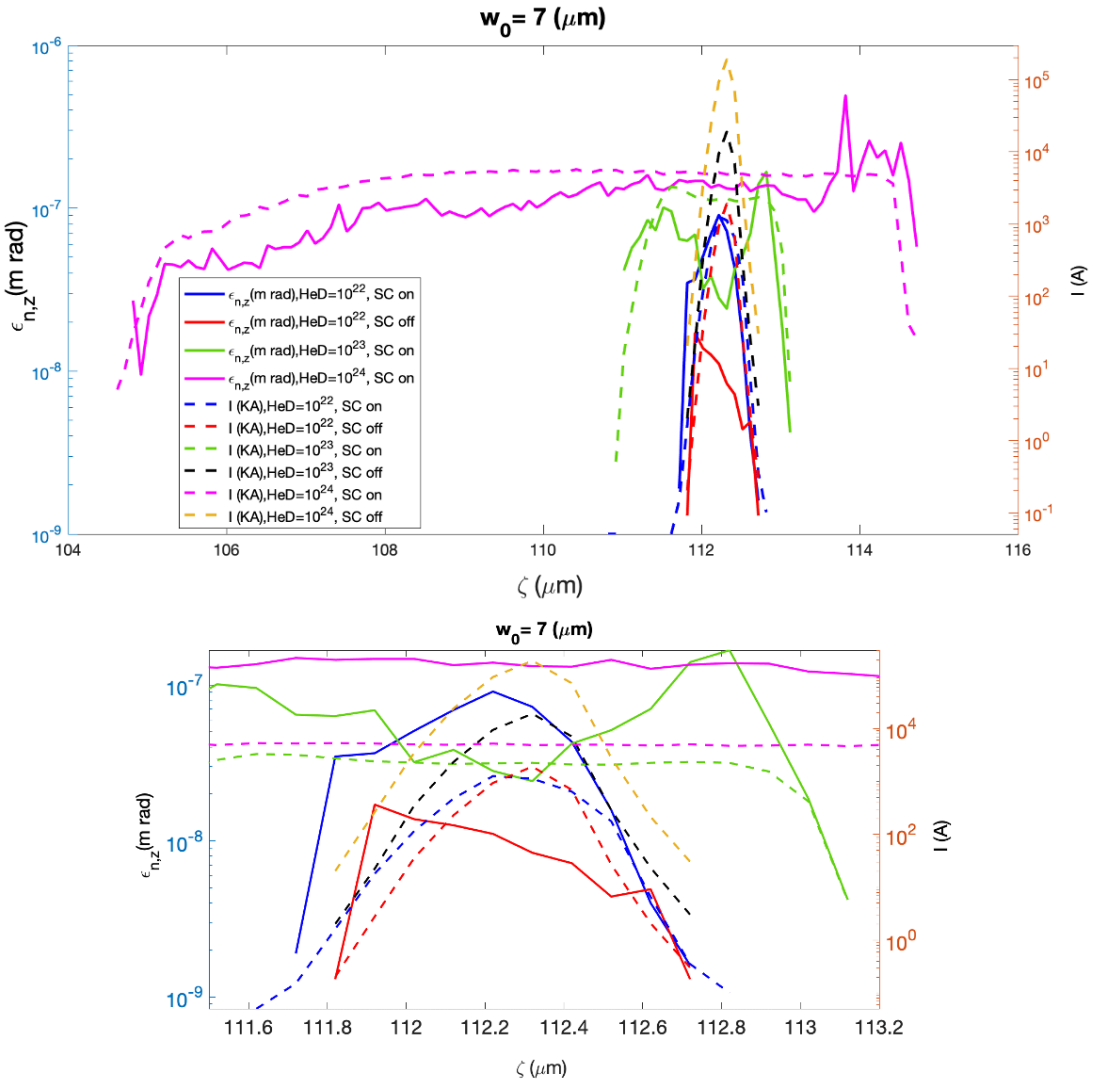

Figure 5.30: Plot of slice emittance and current for w_0=7μm at different He densities, when SC is on and off. The solid lines represent emittance, and the dashed lines represent the current. The second panel is zooming in on the region of the cases with low or non-existing space charges.

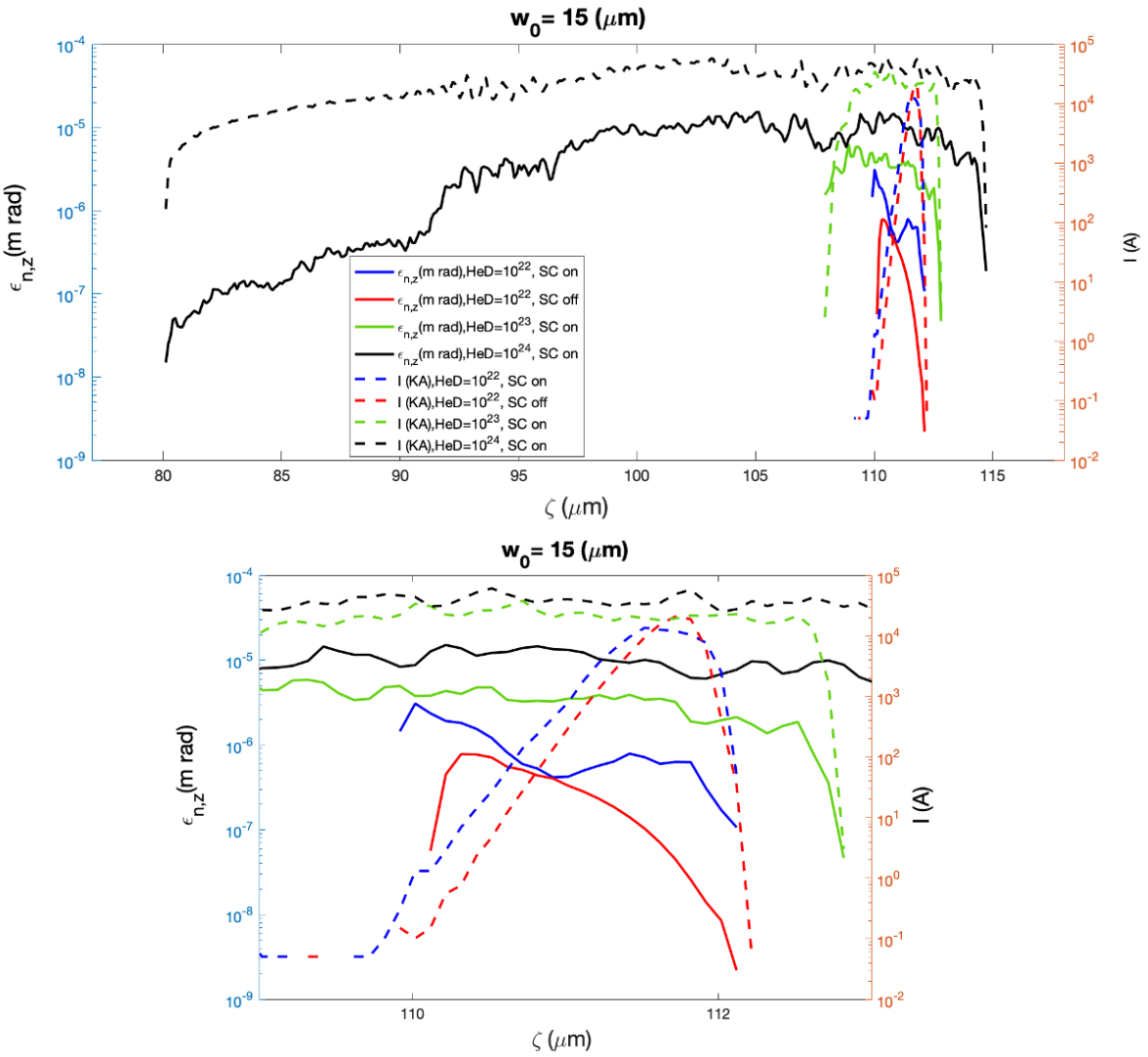

Figure 5.31: Plot of the slice emittance and current for w_0=15μm at different He densities when SC on and off. The solid lines represent emittance and dashed lines for current. In the second plot, we zoom the region on cases 10^{22} m^{-3} to 10^{23} $m^{-3}$to be clear.

Next, the slice energy spread is plotted in Figure (5.32). Interestingly, the largest projected energy spreads are assumed for the cases where space charge is off or low, while the energy spread is lower for higher He densities and charge and current values. This is an impressive result of dynamic beam loading and shows that it can be exploited to tailor the energy spread of the whole beam or at least more or less large slices of it. A particularly interesting case is $n_e = 3.3\times10^{23}$ m^{-3}, where the formed witness beam exhibits a dip in energy spread right in the centre of the beam.
Also, in Figures (5.30) and (5.31), the slice current follows the same behaviour when we plot the current evaluation for the whole witness bunch which the slice current

grows with the increase of He density, and it grows larger when turning off the space charge. We see them in two cases of the spot size. The bunch is so much longer in case of the high "He" density due to the increased charge that is released in the very high "He" density case leads to bunch loading of the wakefield, so that the released charge is trapped less locally in the wake, but more spread out. This leads to a much longer witness bunch, and the associated current is not a factor 10 higher for the 10^{24} case than for the 10^{23} case.

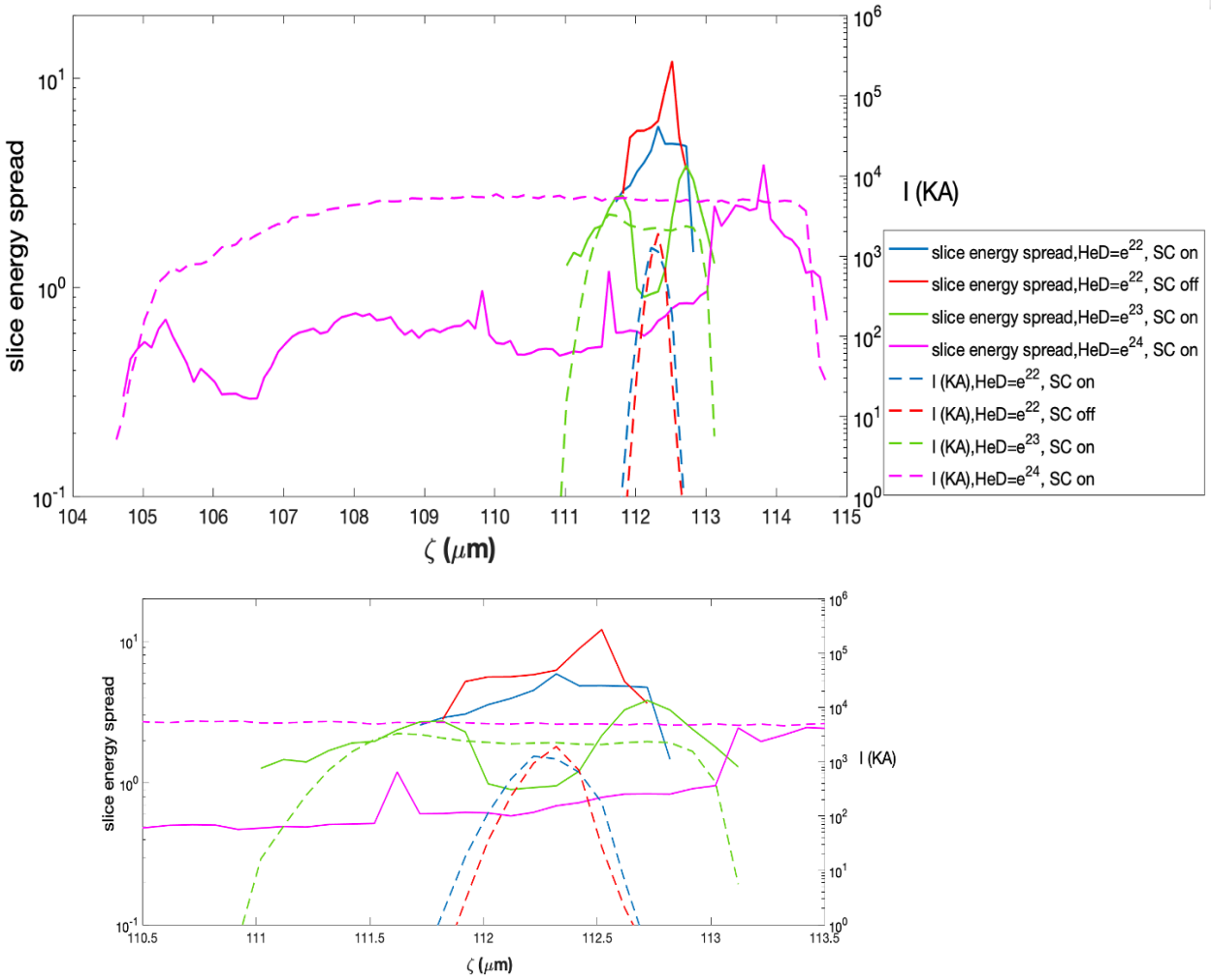

Figure 5.32: Plot of the slice energy spread for w_0=7μm at different He densities when SC is on and off.

Ultimately, the local longitudinal electric field in the plasma wake is responsible for the energy spread and chirp that the witness bunches assume, as shown in Figure (5.30). The green curve (10^{23} density) shows both better energy spread and emittance in the middle part than the blue curve (10^{22} density). The reason for the He

density=10^{23} has a low energy spread than the He density=10^{22} case. The accelerating field of the case of He density=10^{23} is altered as a result of producing more charge, and the field becomes flattered, which does not show a steep gradient but shows a more constant accelerating field compared with the He density =10^{22}case. Therefore, with little charges, such as the case of He density =10^{22}, the unloaded wakefield leads to higher energy spread which the front of the witness bunch has lower energy than the back, and with He density =10^{23}, the front and back of the witness bunch have the same energy due to flattening the accelerating field (see Figure (5.33).

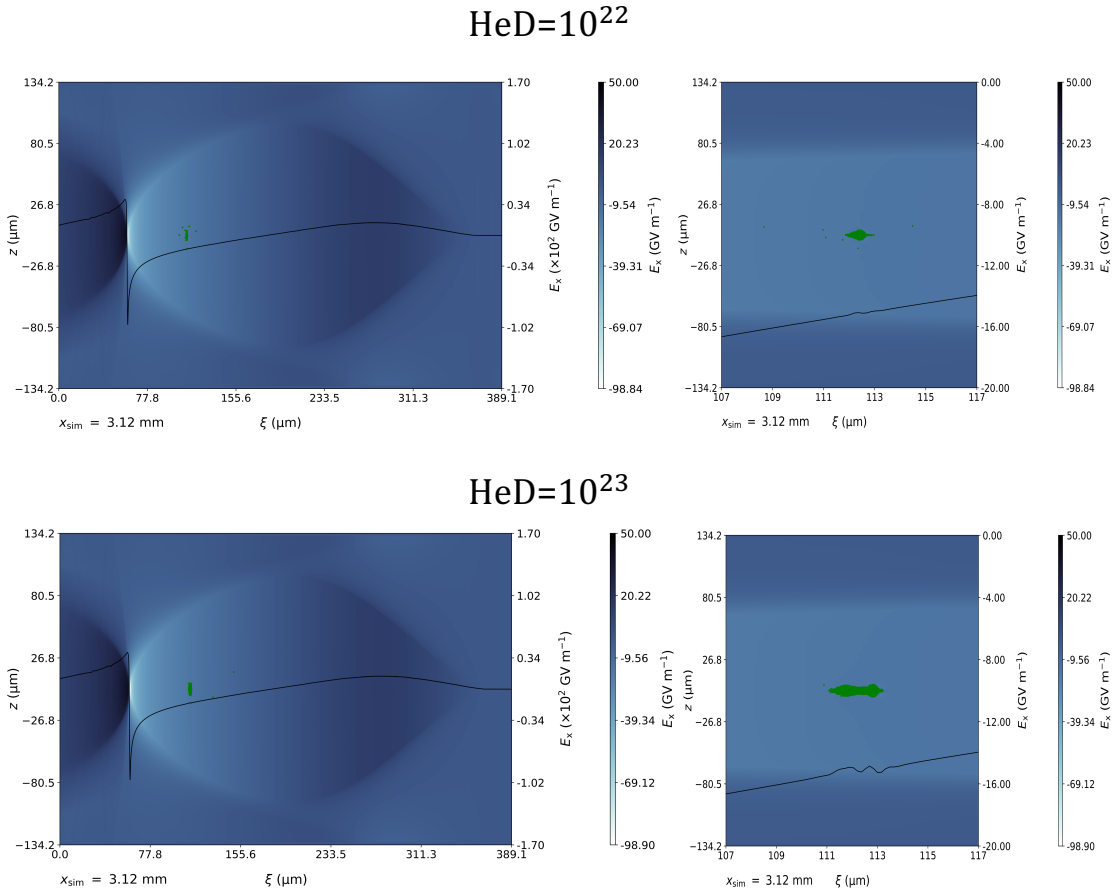

Figure 5.33: Plot of the accelerating longitudinal field in real space for $w_0 = 7$ µm, when $n_e = 3.3\times10^{23}$ m^{-3}, and $n_e = 3.3\times10^{22}$ m^{-3}. The zoom-in focuses on the beam loading, which is prominent in the $n_e = 3.3\times10^{23}$ m^{-3} case and hence can facilitate locally very low slice energy spreads.

In addition, from Figures (5.34) and (5.35), we plot the accelerating wakefield when w_0=7μm and w_0=15μm for the He density = 10^{22} until 10^{24} when SC is on and off. The goal is to see how locally the witness bunch distorts the accelerating wakefield through-beam loading. For the case when w_0=7μm for all He densities (Figure (5.34)), the beam loading shows surprisingly moderate when the space charge switch is on. On the other hand, beam loading does not affect the wakefield when the space charge is switched off, which is an expected result. While from Figure (5.35) at a larger laser spot size w_0=15μm and with an increase in helium density, the effect of beam loading becomes clearer and stronger when the He density=10^{24} m^{-3}. This explains the behaviour of the slice energy spread in Figure (5.32), where it appears that the energy spread decreases with increasing witness charge, and its highest value is when the bunch with low charge and when the space charge is switched off.

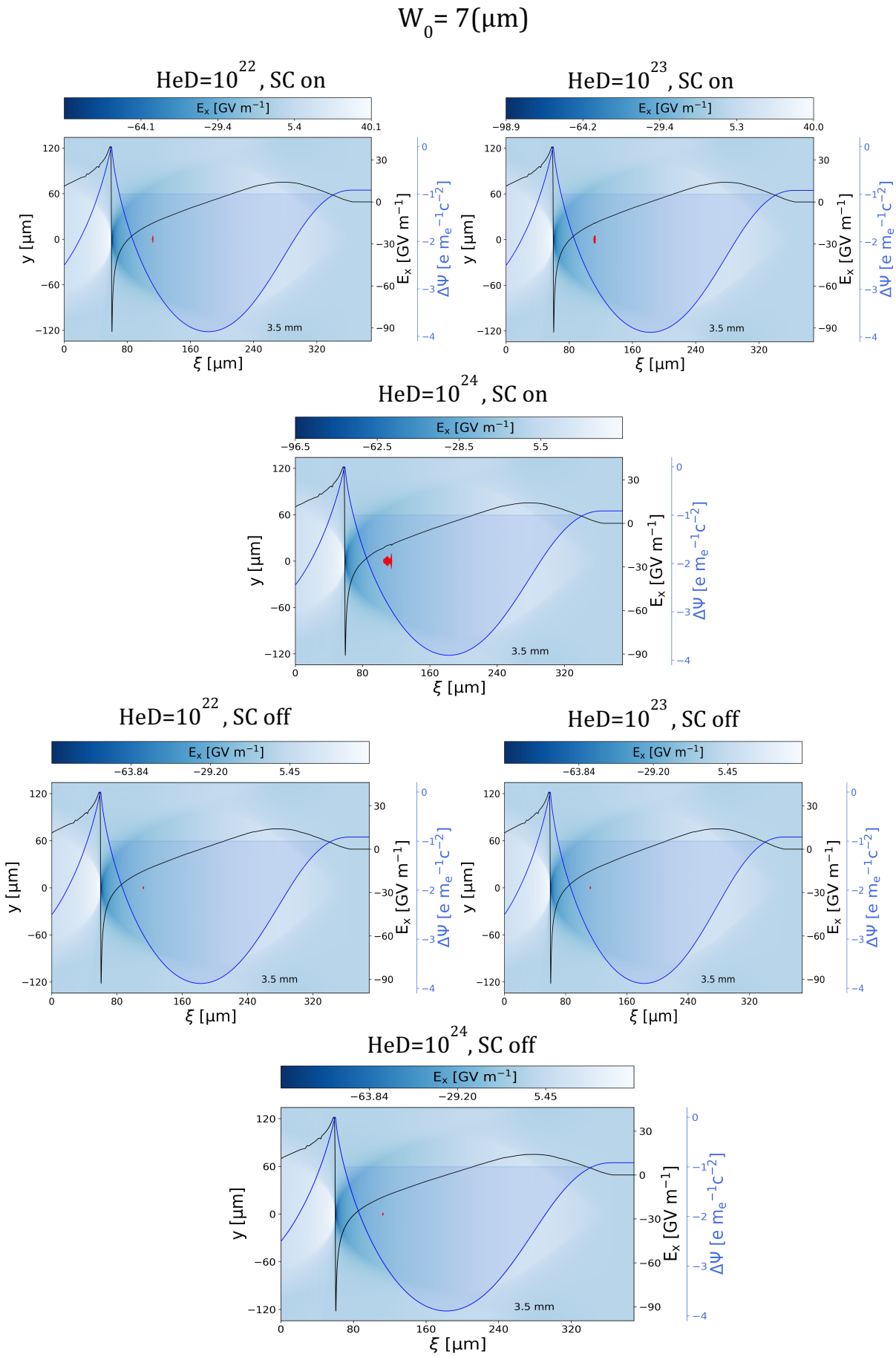

Figure 5.34: Plot of the accelerating longitudinal field (black line) in real space for w_0 = 7 μm at different He densities, when SC is on and off, the blue line shows electrostatic potential.

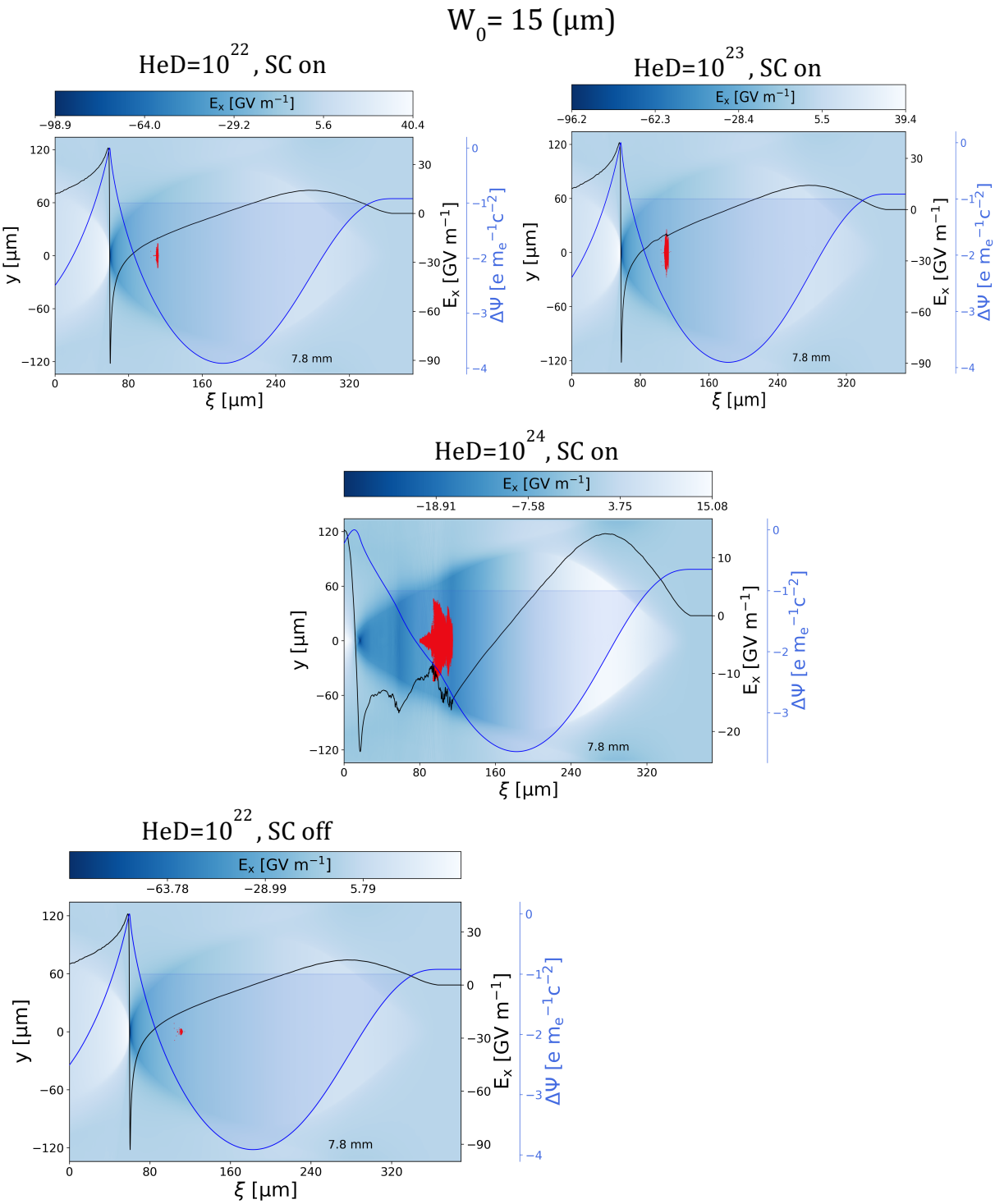

Figure 5.35: Plot of the accelerating longitudinal field (black line) in real space for w_0 = 15 µm at different He densities, when SC is on and off, the blue line shows electrostatic potential.

5.6 The Impact of Ionisation Front Movement

During focusing of the plasma photocathode laser pulse, at first, the laser intensity is not high enough to enable the associated electric fields to exceed the tunnel ionisation threshold of the HIT medium. This is desirable because, otherwise, the release volume would not be localized enough, which would be detrimental to the produced witness beam quality. During focusing [19], the laser intensity I increase, and for a Ti: sapphire laser pulse assumes values of:

$$I = a_0^2 \, 2\varepsilon_0 \, c \, (\frac{\pi m_e c^2}{e\lambda})^2 = \frac{a_0^2}{\lambda^2[\mu m^2]} \cdot 1.37 \cdot 10^{18} \, \mathrm{W/cm^2} \quad (5.3)$$

As in the simulations, we assume that a Ti: sapphire laser pulse with a central laser wavelength of $\lambda \approx 0.8$ μm is employed. For a Gaussian co-propagating laser pulse with a Rayleigh length of $Z_R = \pi w_0^2 / \lambda$, where w_0 is the laser spot size. The intensity envelope of the laser pulse along the propagation axis can be written as:

$$w(x) = w_0 \sqrt{1 + (\frac{x}{z_R})^2} \quad (5.4)$$

Depending on the laser intensity, $I \propto a_0^2 \propto E^2$, and given the peak laser intensity is set high enough. The focusing laser pulse will start to ionise the tunnel, reach the focus, and then diffract and reduce its intensity below the ionisation threshold. However, the laser pulse has a finite duration, and is represented by a Gaussian longitudinal intensity envelope. The corresponding electric laser field is always larger in the centre of the longitudinal laser pulse profile and lowers further outside. Figure (5.36) below shows the envelope of the laser pulse intensity (red dashed line) as a result of the laser spot size evolution w(x), and three snapshots of the laser pulse electric field, before reaching the focus, at focus, and after focus. In reality, the lase electric pulse-field oscillates and points in one (blue) and then the opposite (red) direction in one-half cycle, but of primary relevance to the tunnelling ionisation process is only the peak electric field amplitude, independent of the direction (and polarisation) of the laser electric field. In any case, the important point is that the laser pulse will ionise “earlier”, i.e., further ahead within the laser pulse when it has reached the focus than before or after the focus position. This simply results from the laser pulse having an overall larger peak intensity at the focus than outside the focus.

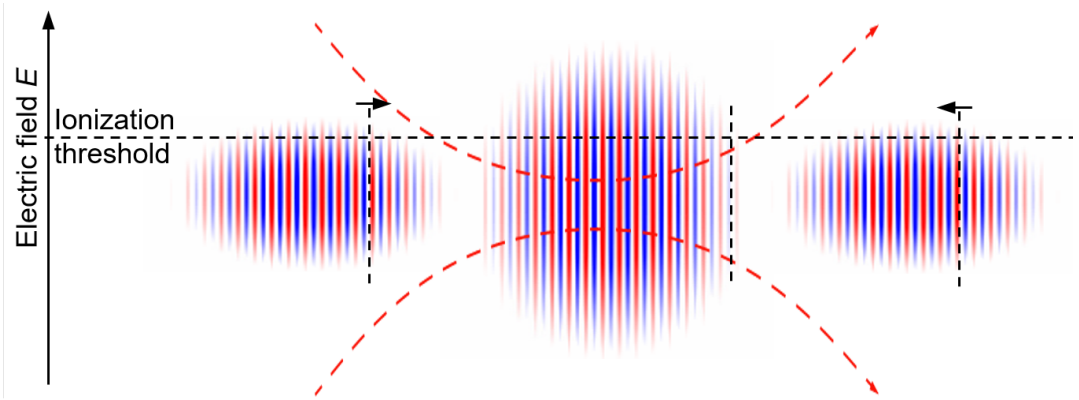

Figure 5.36: The sketch of the focusing and then diffracting plasma photocathode laser pulse. The laser pulse propagates from left to right thereby, and its transverse size is becoming smaller. At the same time, the peak electric field is becoming larger. The horizontal dashed line indicates the tunnelling ionisation threshold of the HIT medium. The vertical dashed lines indicate the localisation of the ionisation front, and the arrows indicate its forward motion in the focusing phase, and the backward movement in the diffracting phase.

For the plasma photocathode process, it is interesting how long the laser pulse is, as this is important for increasing the electric field along with the pulse envelope in the longitudinal direction in the co-moving frame. In this thesis, the laser pulse duration was set to $\tau = 30$ fs FWHM. As shown previously in Figure (5.4) and the discussion about ionisation yields, the actual section of the laser pulse where the bulk of the ionisation happens is much shorter than the laser pulse in this case. This 'ionisation front' is so sharp because of the exponential relation between tunnelling ionisation rates and the electric field that perturbs the electric potential of the HIT atoms.

In the Figure above, therefore, the HIT electric field ionisation threshold is indicated by the horizontal dashed black line, and the vertical dashed black lines indicate the position of the ionisation front in the three snapshots. The first ionisation sets in approximately the middle of the laser pulse when focusing. The laser intensity is always largest and, therefore, exceeds the ionisation threshold at the earliest. During further focusing, however, the ionisation front moves further ahead in the pulse in the co-moving frame because of further increasing electric field amplitude until it reaches the earliest position within the laser pulse when the laser pulse reaches the focus position in the laboratory frame. Afterwards, the laser pulse diffracts, and the ionisation front moves backwards again. This ionisation front movement is indicated by the arrows in the sketch Figure above.

The laser pulse oscillation is not resolved in the high-resolution PIC simulation, but the envelope approximation represents the laser pulse intensity for

numerical reasons. Nevertheless, the ionisation front position can be monitored [84]. This is shown in Figures (5.37) – (5.40), which is the sum of the electric field of the laser pulse and the wakefield, whereby the latter is a negligible contribution because the laser pulse is centred in the plasma blowout both longitudinally and transversally, as discussed earlier. First, the laser pulse electric field and the effect of the local tunnelling ionisation rates are given for the laser pulse in the focusing phase. The corresponding positions in the laboratory frame are shown below the snapshots. The released electrons have been tagged with unique identifiers, which are chronologically assigned. Therefore, lower tag numbers mean the electron macroparticles have been born earlier in the process by tunnelling ionisation, and higher tag numbers mean that electron macroparticles were born later. The tag numbers have been colour-coded to show this.

In Figures (5.37) and (5.38), the release process is shown for the case of laser spot size w_0=7 μm when space charge is switched on and off respectively, at a He density of $n_e = 3.3 \times 10^{22}$ m^{-3}. In this initial phase of the witness bunch production, there is no significant influence of the space charge interaction between the released electrons; both sets of snapshots representing the space charge on and space charge off situations are identical. One can see that as the laser pulse focuses, the peak electric field increases. The horizontal dashed line is a marker for the ionisation threshold and is set to a constant electric field level in all simulation snapshots. As a consequence of the increase of the laser electric field amplitude during focusing, the relative position where the ionisation threshold electric field amplitude is reached, also moving forward within the co-moving frame as the laser pulse is focused, and then moves back as the laser pulse diffracts, as shown in the later snapshots. The position of this 'ionisation front' in the co-moving frame is indicated by the dashed vertical line and the position label at the bottom. As defined here, the whole ionisation front moves only by approximately one micron in this configuration, which seems to be tiny compared to the plasma wavelength, or the laser pulse.

At the same time as the ionisation movement occurs, the overall momentary charge release rate and the laser pulse also increase and then decrease again, as can be deduced from the plotted macroparticle density. The colour coding shows that the green and yellowish macroparticles have already left the simulation box zoom-in as they are falling back and being captured in the wakefield, and only the newest electron macroparticles are shown in the displayed subset of the simulation box, e.g., in the two latest snapshots.

No difference can be seen between the case where space charge is switched on and off for these cases, indicating that the space charge effect at such low overall charge values released is subtle and/or is not yet pronounced enough, as these are the very early moments of the trapping process.

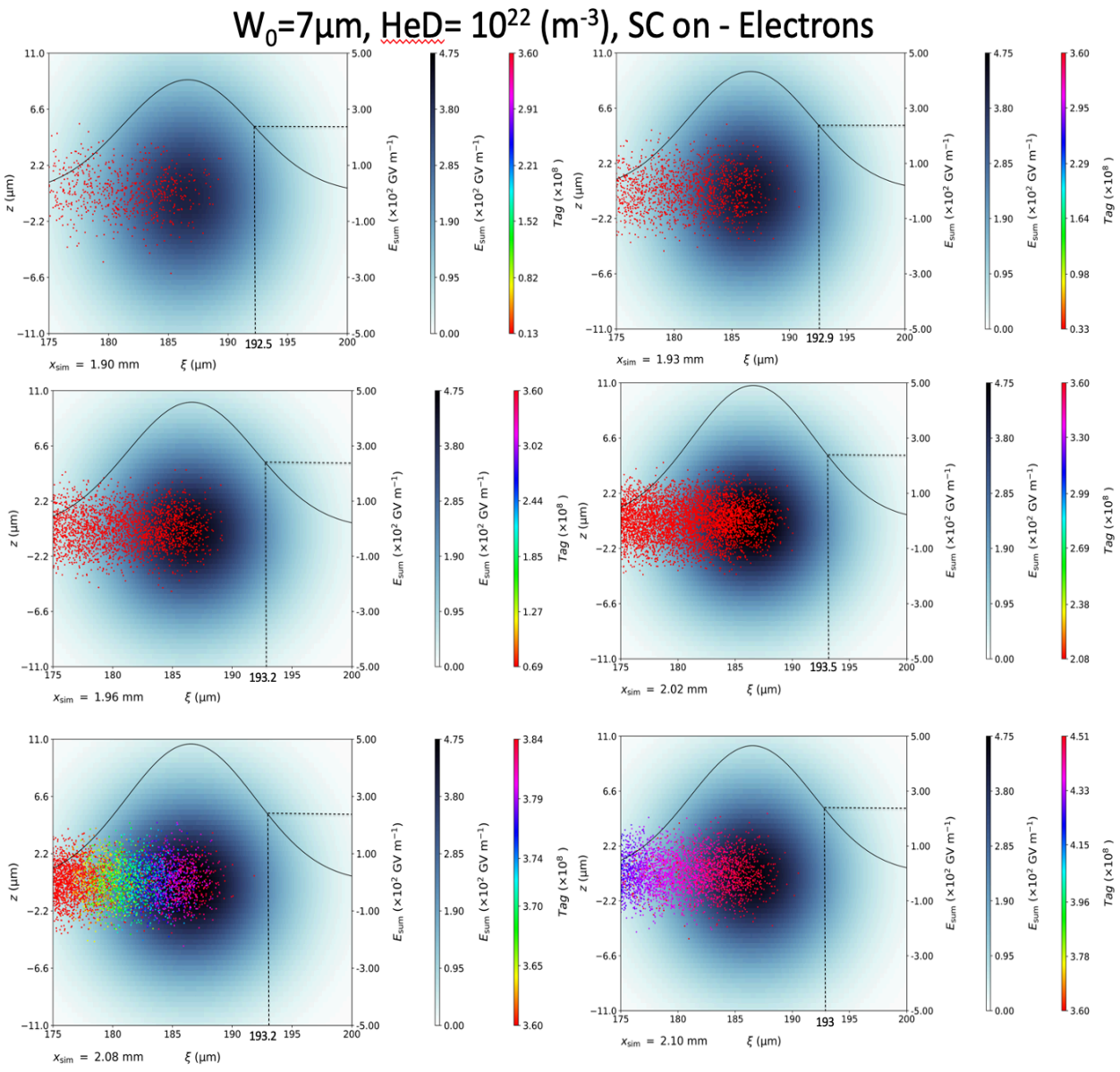

Figure 5.37: Plot of several snapshots of released electrons during the release process with colour coding according to their time of birth. The zoom-in shows the region of the simulation box and plasma wake where the laser pulse resides. A lineout of the electric field of the laser pulse allows monitoring of the position of the ionisation front in the co-moving frame. Here, the spot size is w_0=7 µm, and the He density = 3.3×10^{22} m^{-3}. Here, the space charge is switched on.

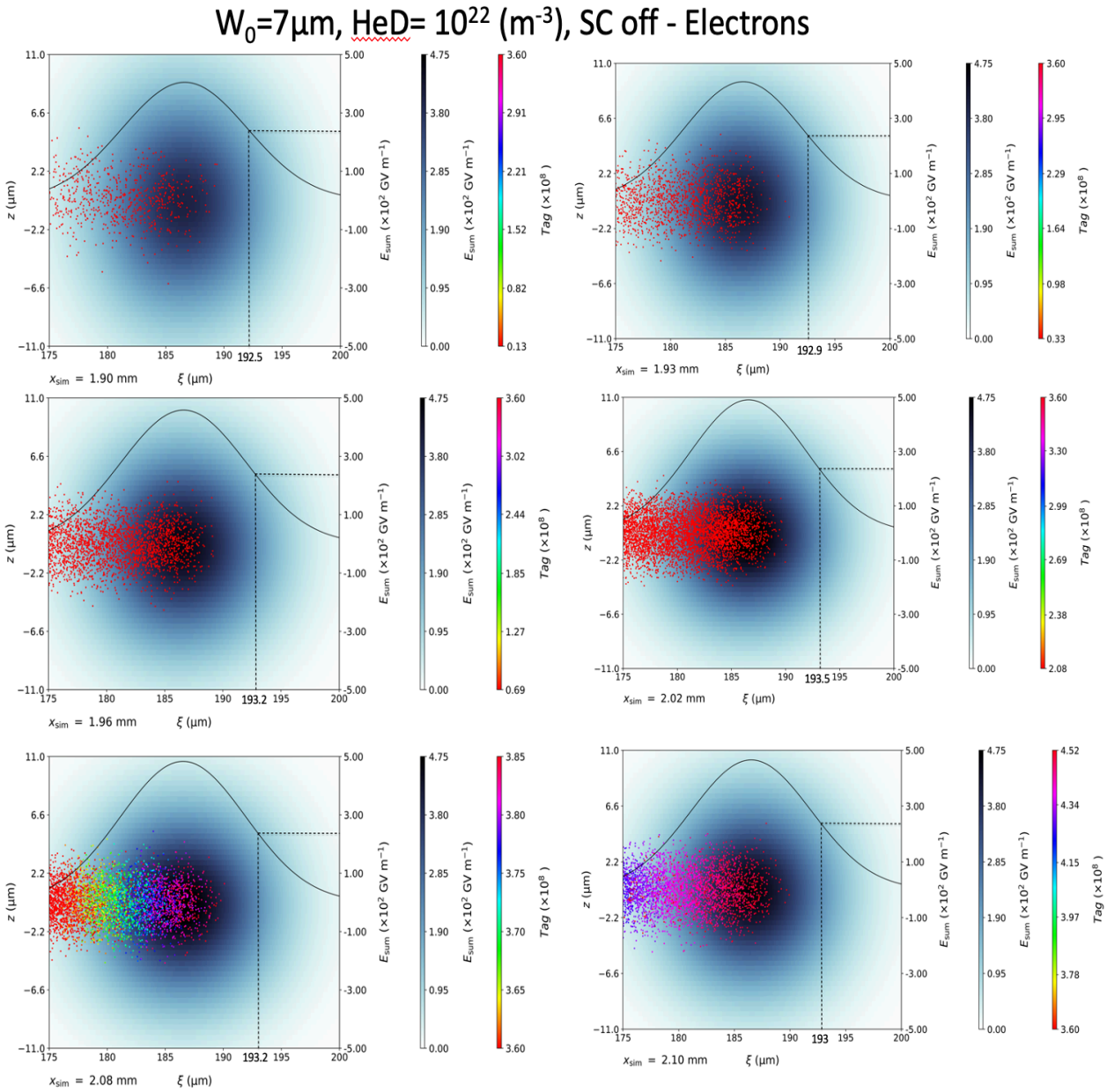

Figure 5.38: Plot of several snapshots of released electrons during the release process with colour coding according to their time of birth. The zoom-in shows the region of the simulation box and plasma wake where the laser pulse resides. A lineout of the electric field of the laser pulse allows monitoring of the position of the ionisation front in the co-moving frame. Here, the spot size is w_0=7 µm, and the He density = 3.3×10^{22} m^{-3}. Here, the space charge is switched off.

Next, Figures (5.39) and (5.40) show the release process for the case of w_0 = 15 µm when space charge is switched on and off, respectively, at He density of n_e = 3.3×10^{22} m^{-3}. Since a_0 is set to the same value as in the w_0 = 7 µm case, the peak intensity and electric field amplitude are the same. However, while the Rayleigh length

for the $w_0 = 7$ µm case is ≈ 192.3 µm, for the $w_0 = 15$ µm case, the Rayleigh length is longer, namely $Z_R \approx 883.1$ µm. This is reflected by a correspondingly larger ionisation front movement in this case, namely by nearly 3 µm. Again, the space charge cases are shown on and off; at these He densities and correspondingly low charge yields, there is again no significant difference between those cases visible here.

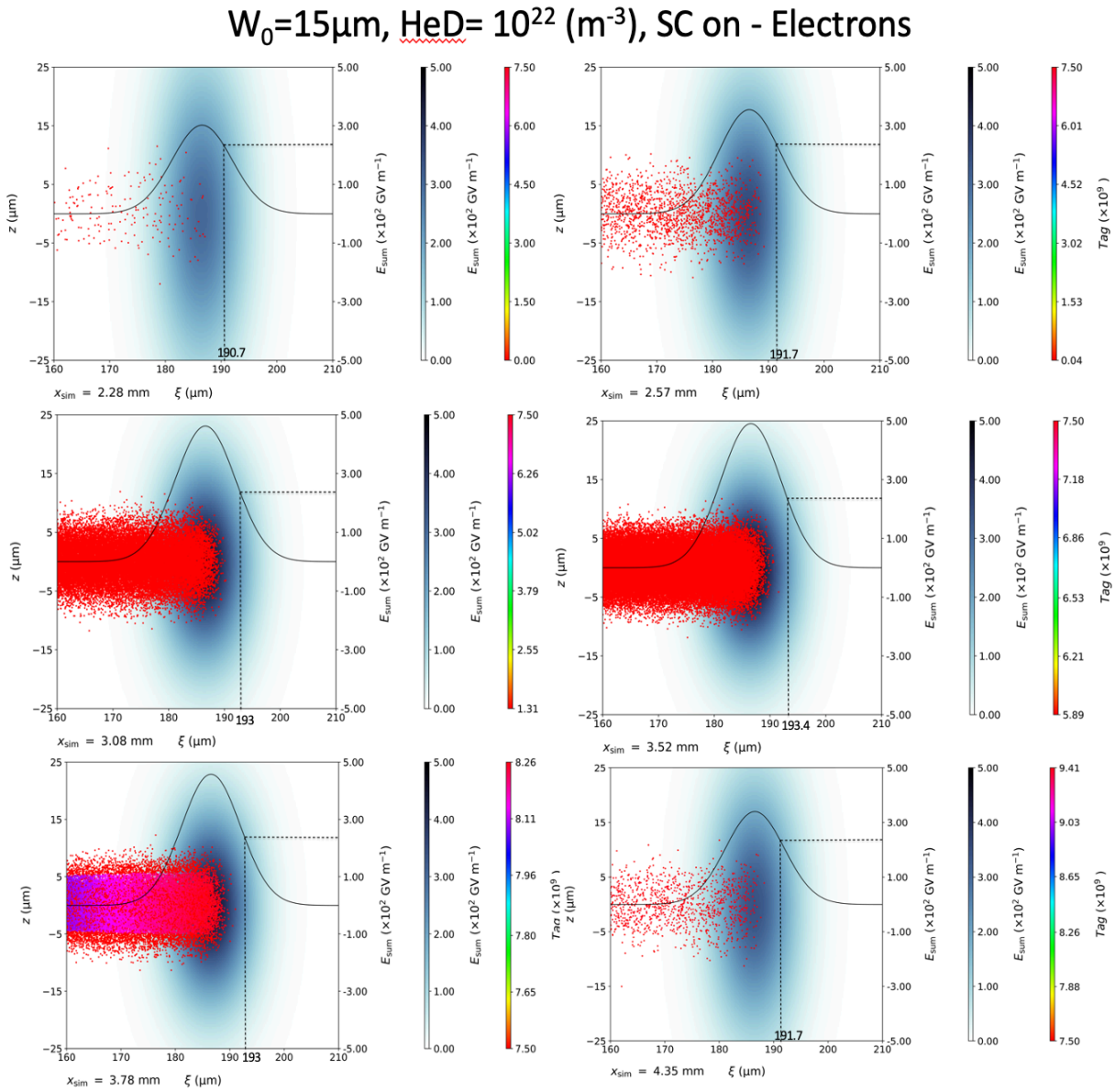

Figure 5.39: Plot of several snapshots of released electrons during the release process with colour coding according to their time of birth. The zoom-in shows the region of the simulation box and plasma wake where the laser pulse resides. A lineout of the electric field of the laser pulse allows monitoring of the position of the ionisation front in the co-moving frame. Here, the spot size is w_0=15 µm, and the He density = 3.3×10^{22} m^{-3}. Here, the space charge is switched on.

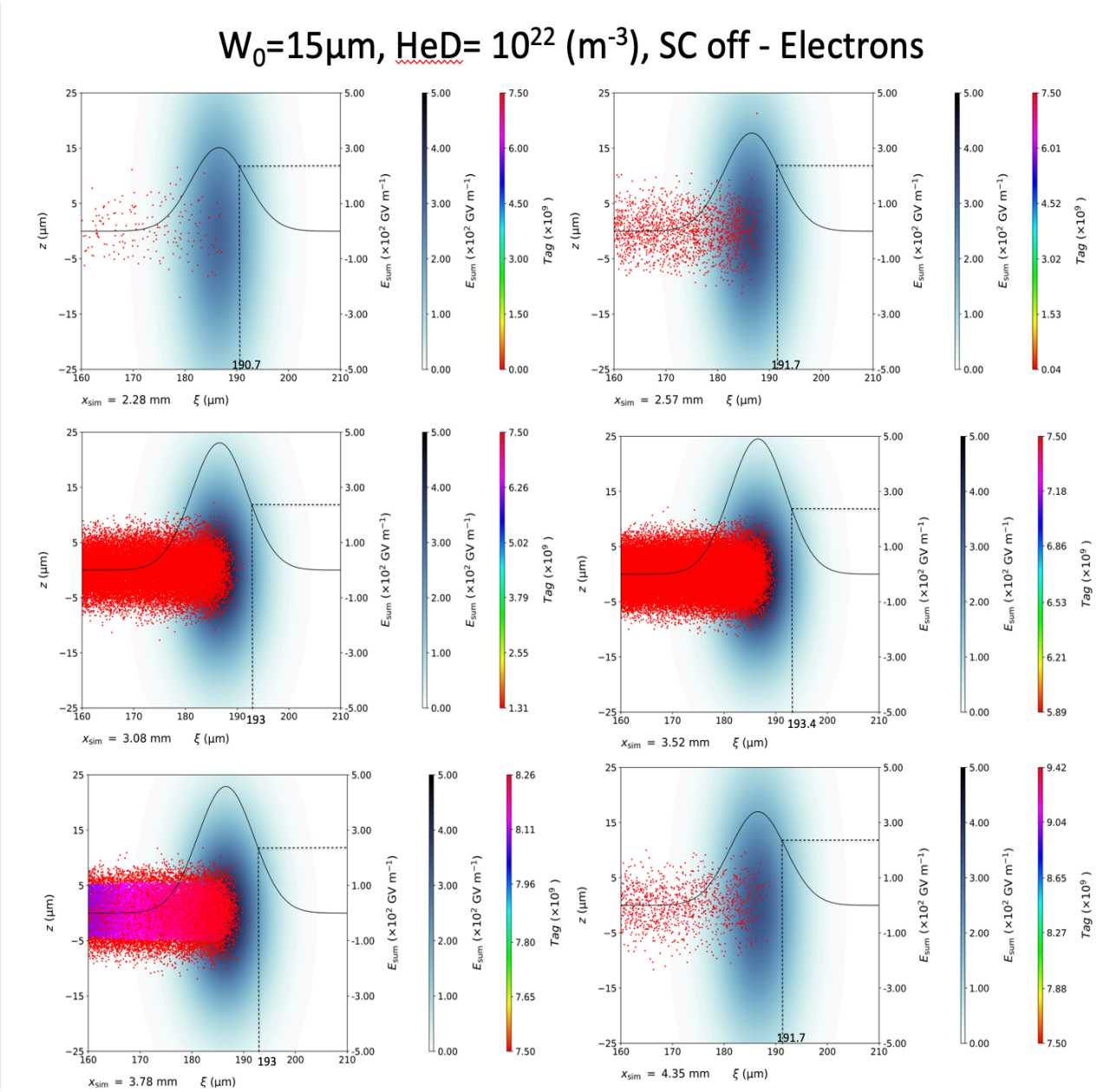

Figure 5.40: Plot of several snapshots of released electrons during the release process with colour coding according to their time of birth. The zoom-in shows the region of the simulation box and plasma wake where the laser pulse resides. A lineout of the electric field of the laser pulse allows monitoring of the position of the ionisation front in the co-moving frame. Here, the spot size is w_0=15 µm, and the He density = 3.3 × 10^{22} m^{-3}. Here, the space charge is switched off.

Without space charge, there is a simple relation between the release position of individual electrons and their trapping position. Hence, the position in the formed witness beam via the electrostatic potential, with space charge effects the impact of

ionisation front movement on the trapping position, is mixed with intra-bunch space charge dynamics.

5.7 In-Depth Study of Space Charge Effects on the Bunch Emittance

The visualisation of the release process for a HIT density of $3.3 \times 10^{22}\ m^{-3}$ has not revealed the impact of space charge on versus space charge off, previously we have seen, when plotting the slice parameters, e.g., parameters of emittance (see Figure 5.30 ff.), that there is a substantial difference in emittance values already at these low HIT densities, at least later during the bunch formation. Therefore, the bunch trapping process following the initial release process is now investigated in greater detail.

The following plots show the real space of released and trapped electrons. In addition, the corresponding ions, and the transverse phase space, both with colour-coded tags according to their birth times. For later times, starting from when the electron bunch is trapped, the slice emittance is added, showing both slice emittance plots for the space charge off versus space charge on cases. This enables another level of insight: first, plotting the colour-tagged beam in real space also during trapping, extends the previous analysis to later times, when space charge effects may begin to kick in. Second, plotting the HIT ions (black), which are generated as part of the plasma photocathode process, illuminates the dynamics where released HIT electrons are still overlapped and shielded by the HIT ions, and later phases where HIT ions are left behind since they are too heavy to be accelerated in the wake. Third, plotting the corresponding transverse phase spaces, also colour-coded, visualizes phase mixing and reveals where individual longitudinal slices sit in transverse phase space. The slice emittance plot then shows when and where space charge effects drive (slice) emittance growth within the bunch. In Figures (5.41) and (5.42), respectively, the situation without and with space charge effects switched on is shown.

The first snapshot in Figure (5.41) is still early times in the trapping process. The release process is still ongoing, and in fact, no released electron has reached the trapping position. Analysis of the transverse phase space plot in correlation with the longitudinal real space plot shows that the red macroparticles/electrons, released latest and have the highest tag numbers, form a distinct phase space ellipse. Therefore, the horizontal axis of the transverse phase space plot gives the transverse range over which electrons are released by the laser pulse, namely over a few micrometres. The transverse phase space plot's vertical axis gives these electrons momentary transverse momentum: electrons released on-axis (i.e., transverse coordinate z or $y \approx 0$) have negligible transverse momentum. This results from the transverse wakefields being approximately zero around the axis. Further outside the axis (i.e. where the absolute value of the transverse coordinate z or $y > 0$). In contrast, the transverse wakefield accelerates electrons towards the axis, which leads to transverse momentum gain. The

transverse wakefield focuses, which means that electrons released at transverse coordinate z or $y > 0$ will develop positive momentum z_p, whereas electrons released at transverse coordinate z or $y < 0$ will develop negative momentum z_p. This also means that the phase space ellipse will rotate clockwise in transverse phase space. The turquoise-coloured and blue-coloured electron macroparticles, which have lower tag numbers because they were released earlier, are already rotated in transverse phase space and have a different momentum-position composition.

The next snapshot is particularly interesting because the release process is still ongoing, but at the same time, the electrons born first have already reached their trapping position. The real space plot reveals that at a co-moving position of $\xi \approx 123$ μm, there is a crunch point during trapping. Here, electrons of a certain 'age' (blueish) are compressed to a very small transverse size, which is reflected by the small transverse size and a thin (blueish) horizontal phase space feature in the transverse phase space. It should be emphasized that there are already many more electrons released in this snapshot than in the previous snapshot. Therefore, there are many more tag numbers, and the colour bar has been re-normalised. Behind the crunch point, where electron trajectories cross, the transverse beam size increases again until nearly the same transverse size is reached during release. This is the result of transverse momentum conservation on short timescales.

In the fourth snapshot, the release process ceases, again leading to a characteristic "x"-shape in transverse phase space. As a result of the ceasing release process, the ion density is also decreased compared to the previous snapshot. This is interesting because the additional HIT ions provide an attractive Coulomb force on top of the LIT ions. They are, therefore, an important but only temporary factor in the balance between focusing transverse wakefields and de-focusing transverse intra-beam Coulomb forces.

In the fifth snapshot, nearly all released electrons have arrived at their trapping position, while the last HIT ions are left behind and leave the simulation box. It also makes sense to show the slice emittance, while the real longitudinal space and transverse phase plots represent the space charge off case. The slice emittance is shown for both the space charge off and on cases. This is an important analysis and finding because it shows that the emittance differences start to occur very early in the trapping process: the slice emittance in the backward region of the trapped bunch starts to diverge significantly (note that always the slice emittance is plotted logarithmically). At this point, the combined transverse phase space is an ellipse filled with all release electron phases.

In the sixth, seventh and eighth snapshot, the trapping process is completed, no new electrons (and corresponding tag numbers) are added, and phase-space rotation is slowed down, while electrons gain energy. One can see that while in real space, the bunch is ultrashort and pan-cake-like (i.e. much wider in size than long), in phase space, the individual phase space ellipses corresponding to different 'age cohorts' of the release process (i.e., colour-coded tag numbers), are distinct.

w_0=7(μm), HeD= 10^{22} (m^{-3}), SC off – Ions and Electrons

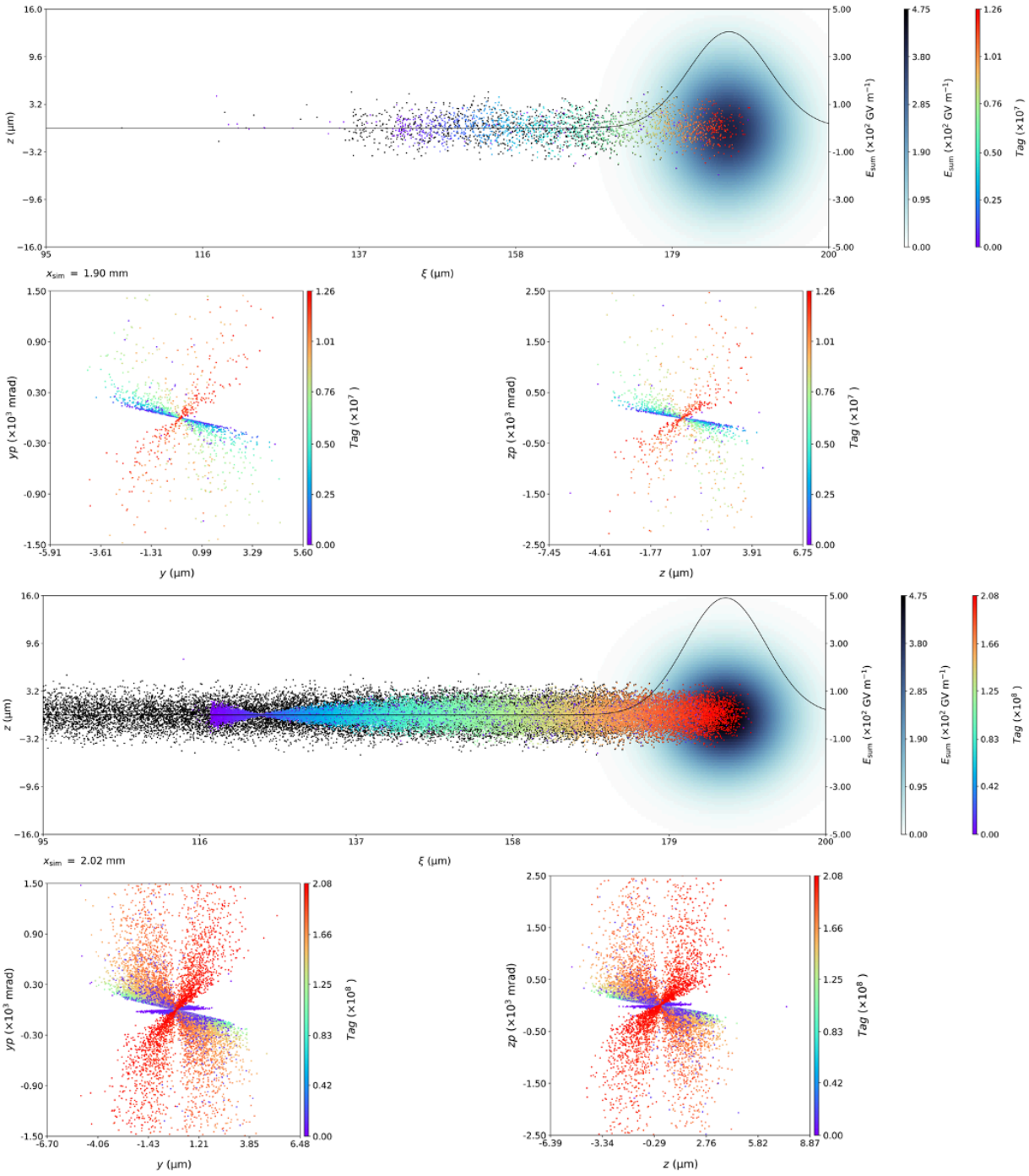

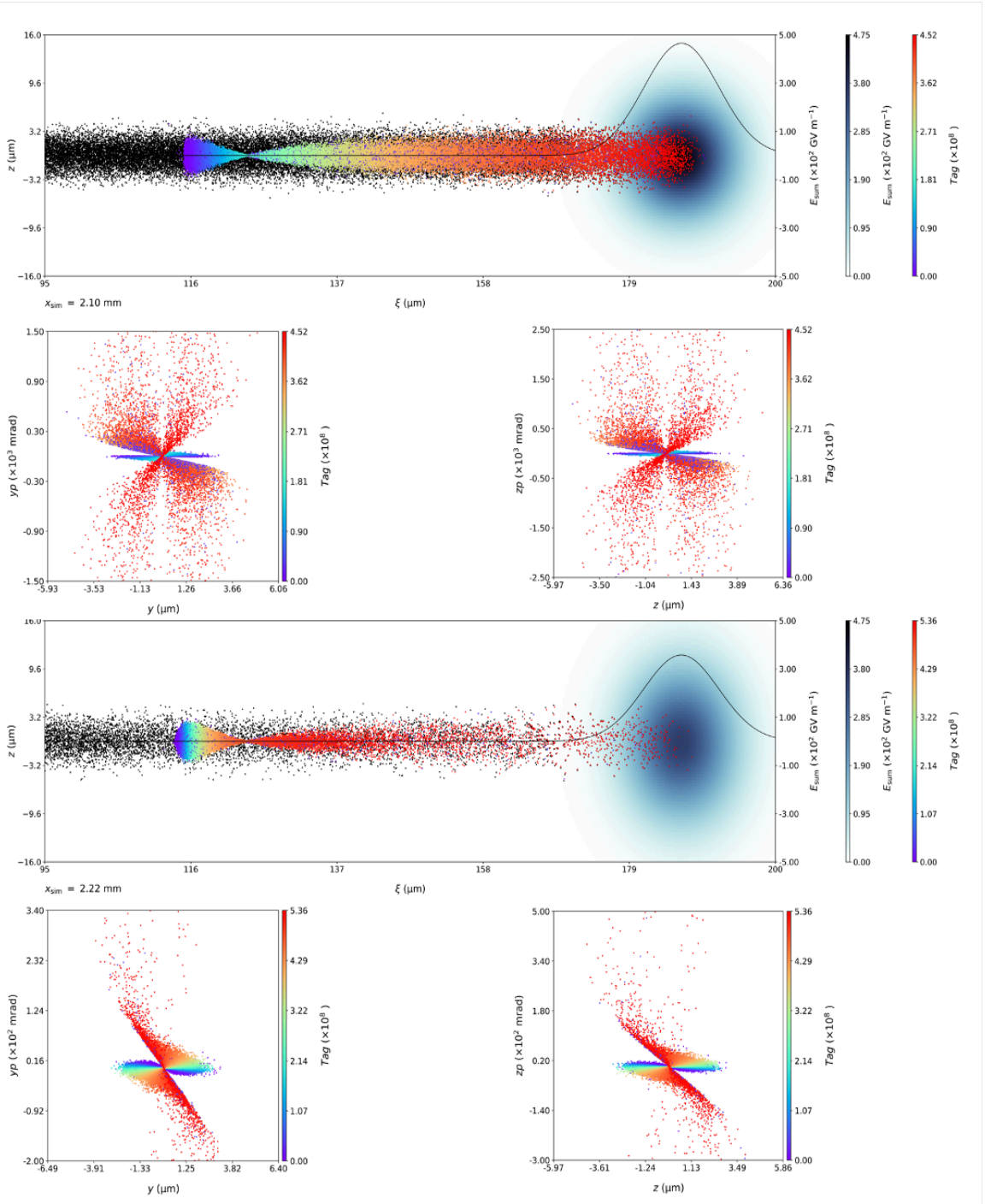
z (μm)
ξ (μm)
E_{sum} (×10² GV m⁻¹)
Tag (×10⁸)
x_{sim} = 2.10 mm
yp (×10³ mrad)
y (μm)
zp (×10³ mrad)
z (μm)
x_{sim} = 2.22 mm
yp (×10² mrad)
zp (×10² mrad)

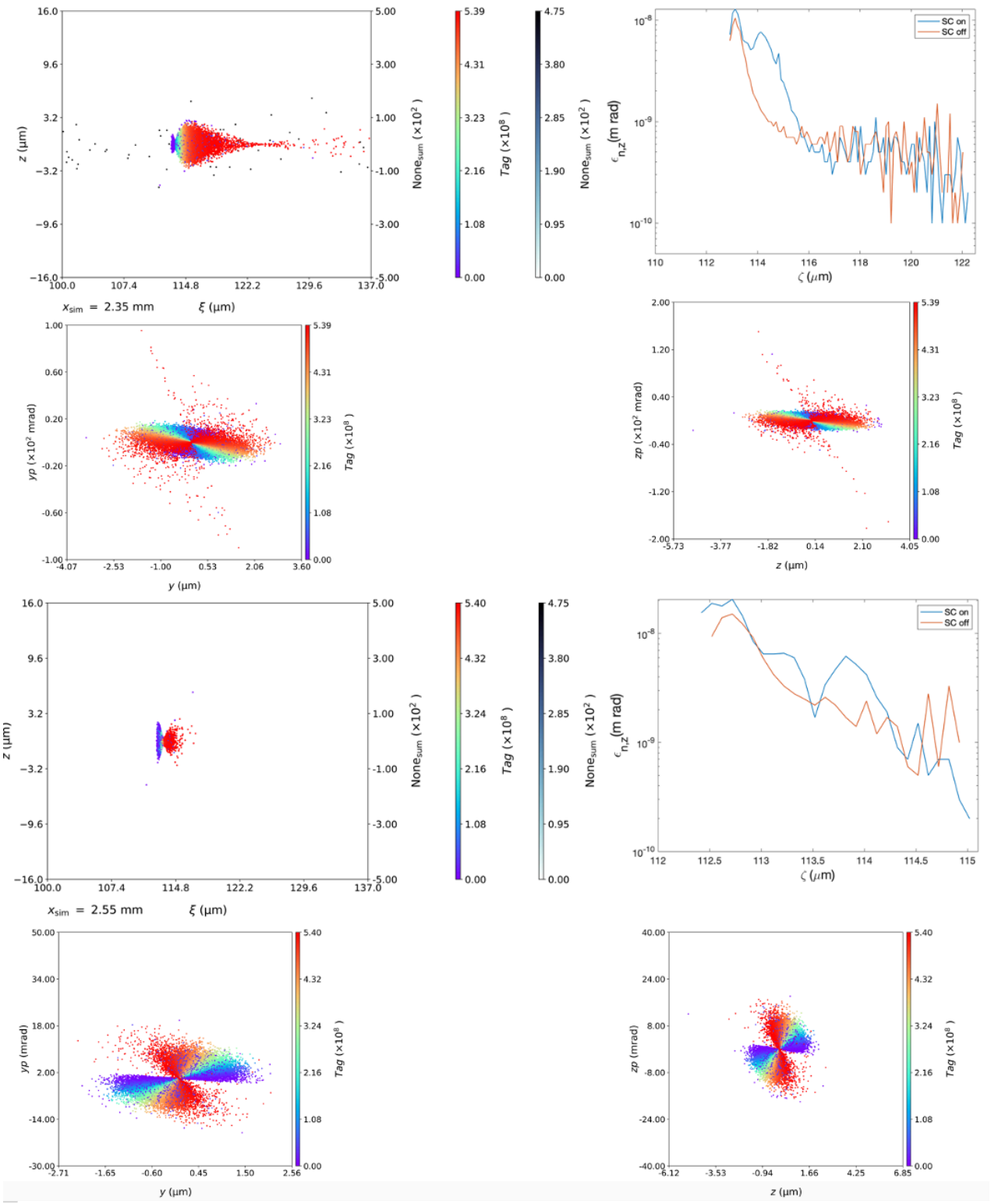
z (μm)
None_sum (×10^2)
Tag (×10^8)
x_sim = 2.35 mm
ξ (μm)
yp (×10^2 mrad)
y (μm)
SC on
SC off
ε_n,z (m rad)
ζ (μm)
zp (×10^2 mrad)
x_sim = 2.55 mm
yp (mrad)
zp (mrad)

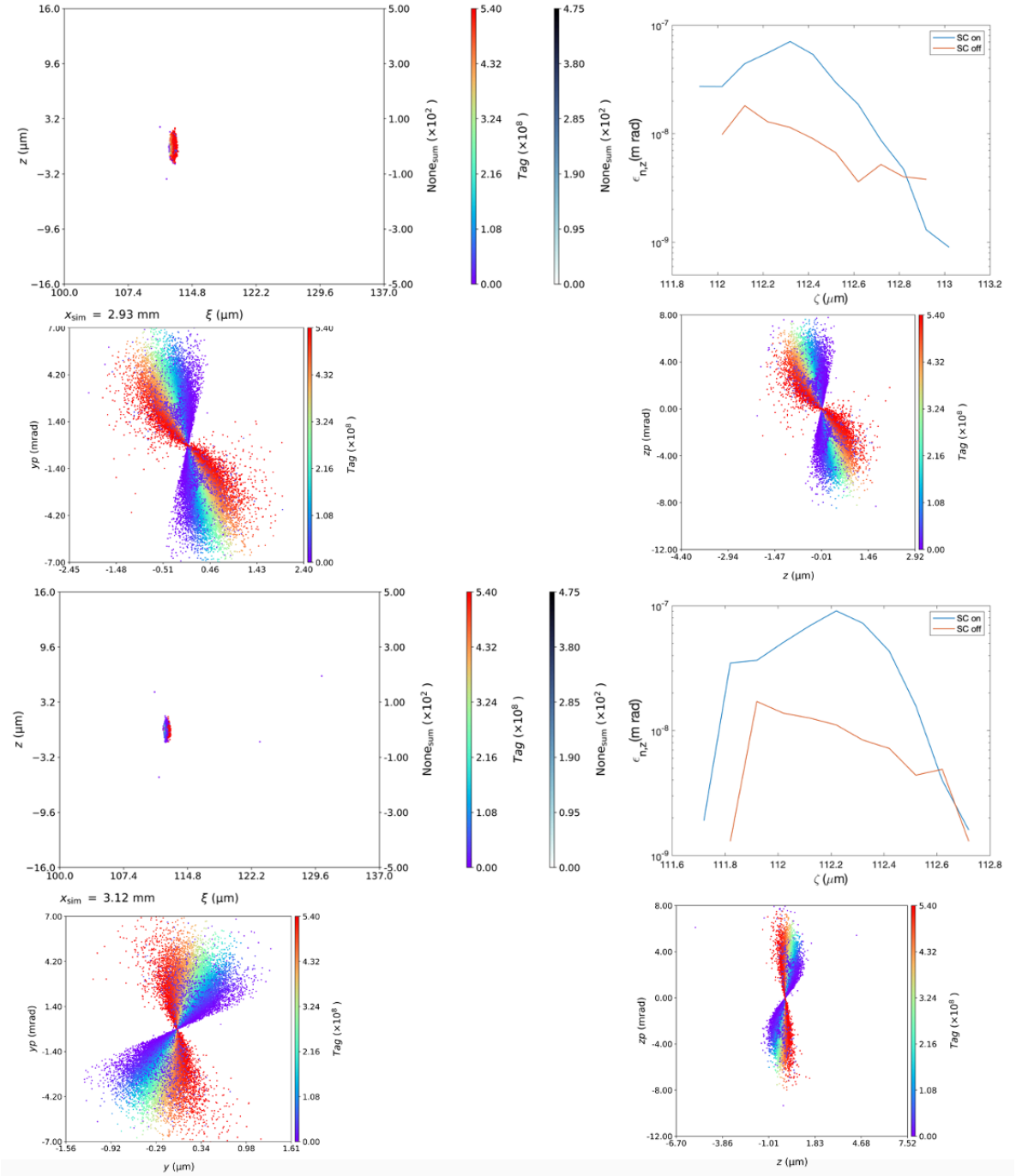

Figure 5.41: Eight snapshots during release and trapping, visualized by real space plot of HIT electrons (colour-coded according to their time of birth by tag numbers), HIT ions (black), colour-coded transverse phase space plots in both planes, and for snapshots 5-8 also the slice emittance. Here, the release laser pulse spot size is w_0=7 µm, and the He (HIT) density = 3.3×10^{22} m^{-3}. Space charge effects are switched off here.

When the space charge is switched on, the situation looks very similar for the first four snapshots in the space charge off case. In particular, also the transverse crunch point is at approximately the same longitudinal position as in the space charge

off scenario. Therefore, it can be concluded that the intra-beam space charge is not significantly relevant for the phase space dynamics up to this point. During the trapping and compression, the phase space ellipses (represented by the different colours) are increasingly distorted, and an additional, less systematic mixing process sets in. This is particularly pronounced and visible in snapshots seven and eight. Here, the colours are nearly fully mixed in transverse phase space, the transverse phase space volume and the transverse beam width are significantly larger than in the space charge off scenario, and the slice emittance becomes larger than the switched off space charge.

w_0=7(μm), HeD= 10^{22} (m^{-3}), SC on – Ions and Electrons

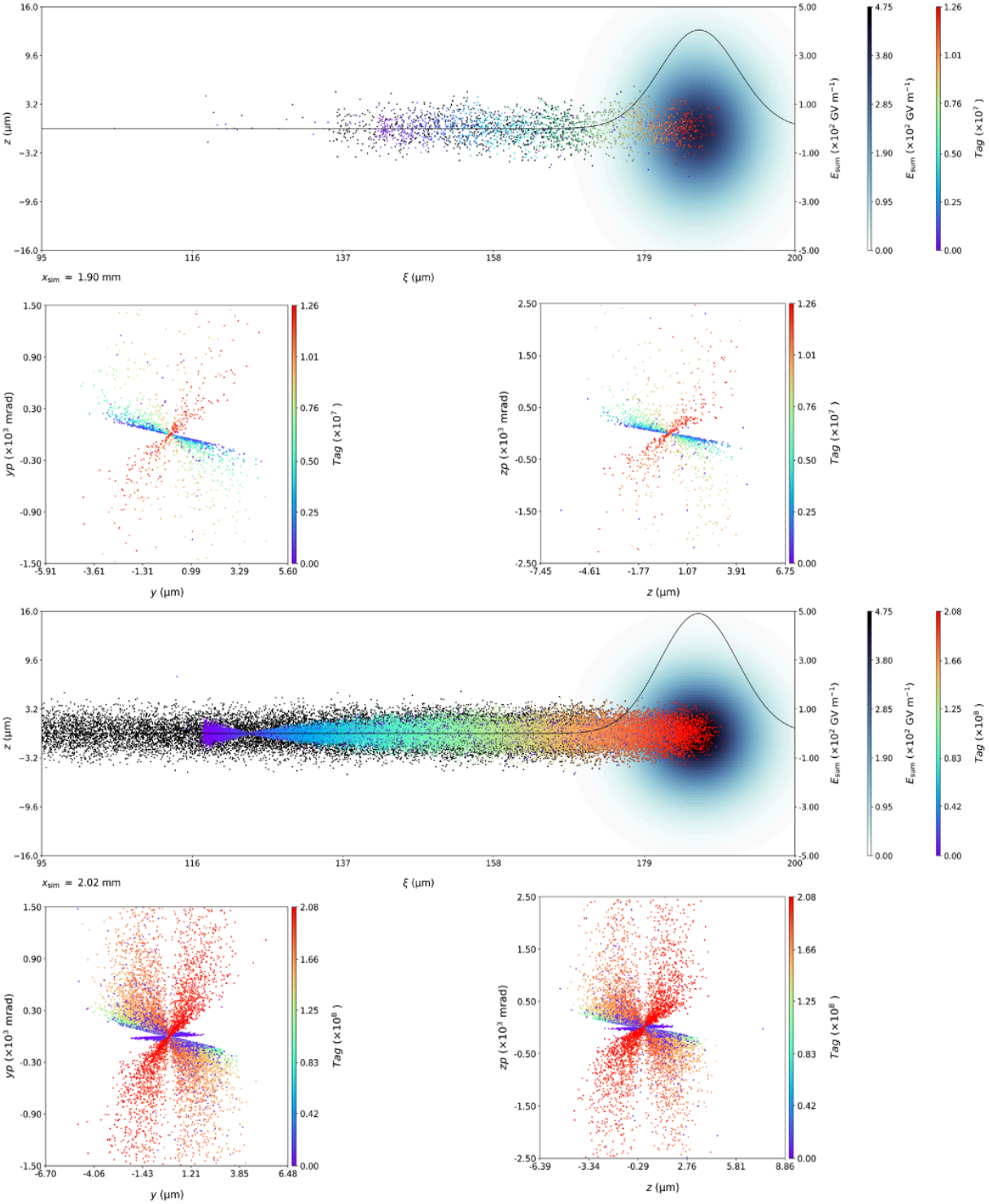

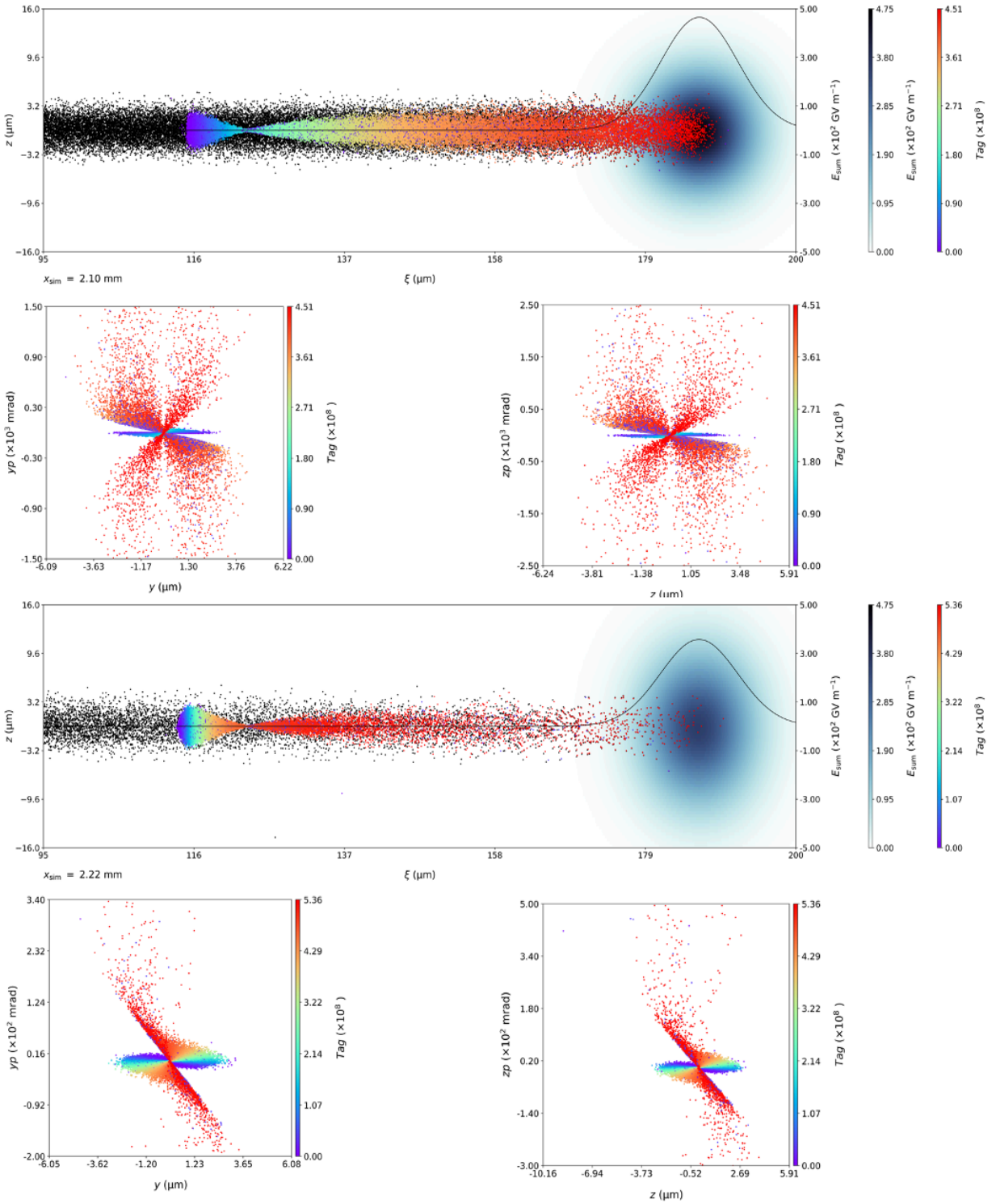
z (μm)
ξ (μm)
x_{sim} = 2.10 mm
E_{sum} (×10² GV m⁻¹)
Tag (×10⁸)
yp (×10³ mrad)
y (μm)
zp (×10³ mrad)
z (μm)
x_{sim} = 2.22 mm
yp (×10² mrad)
zp (×10² mrad)

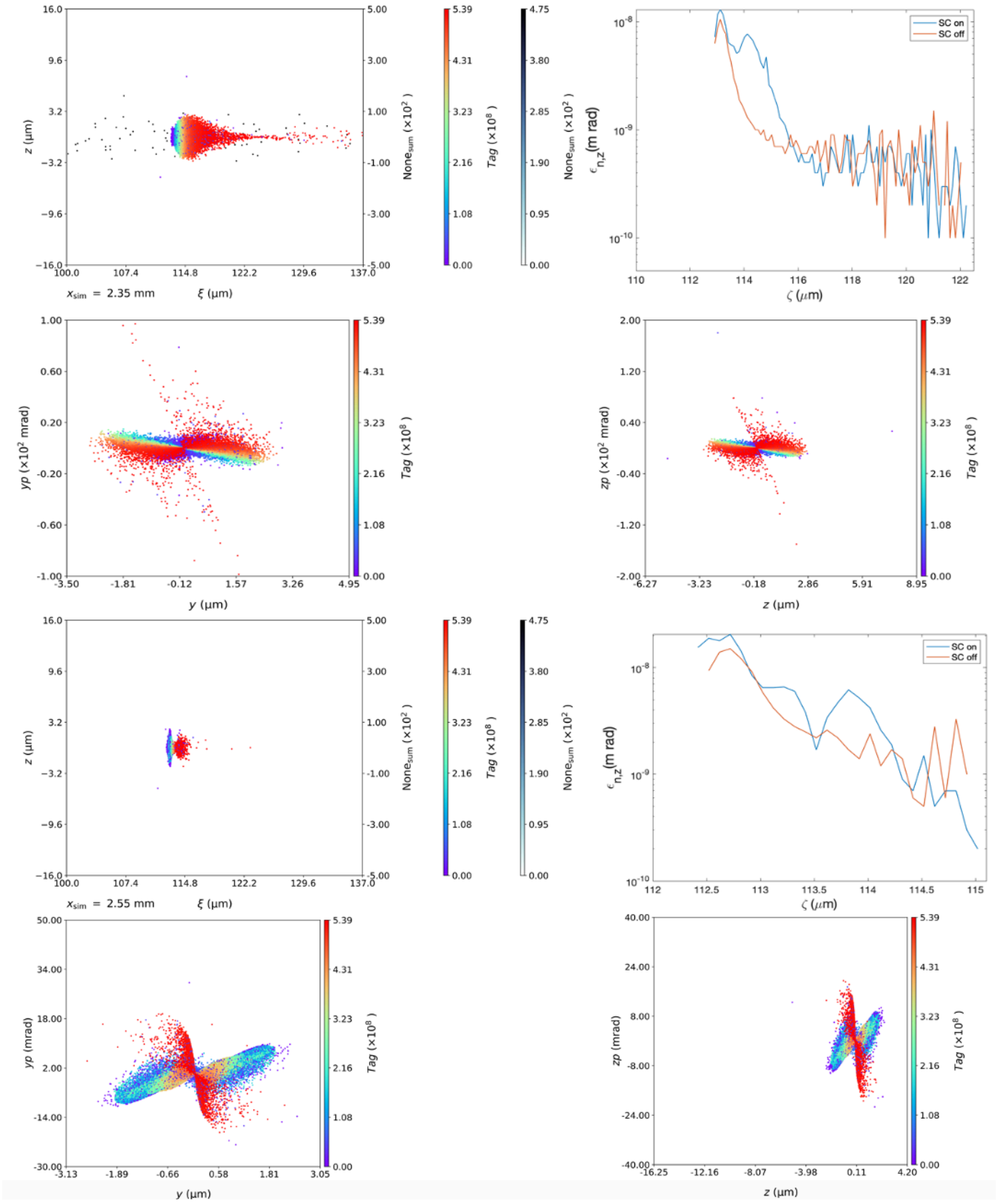
z (μm)
x_{sim} = 2.35 mm
ξ (μm)
None$_{sum}$ (×10^2)
Tag (×10^8)
SC on
SC off
$\epsilon_{n,z}$(m rad)
ζ (μm)
yp (×10^2 mrad)
y (μm)
zp (×10^2 mrad)
z (μm)
x_{sim} = 2.55 mm
yp (mrad)
zp (mrad)

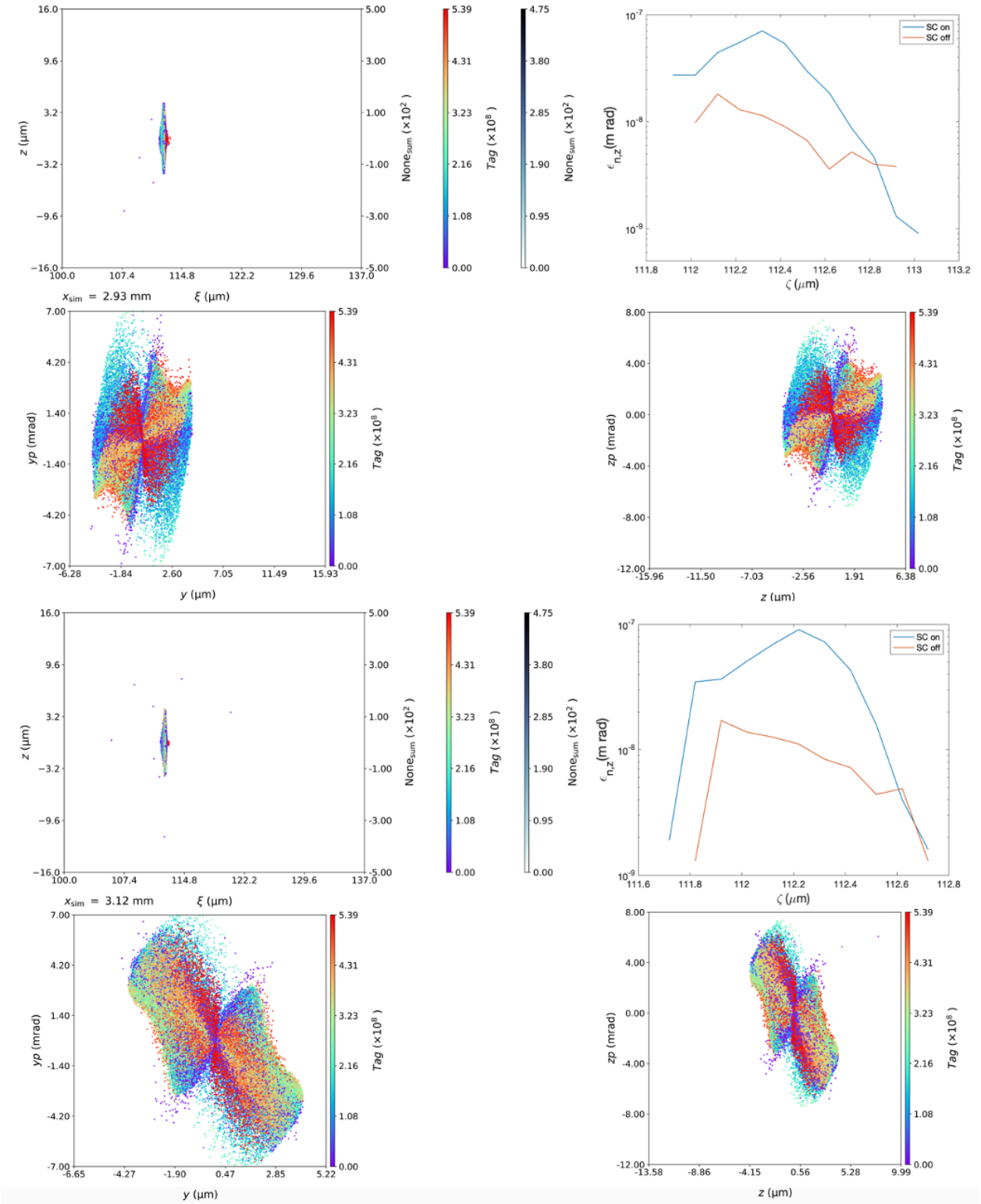

Figure 5.42: Eight snapshots during release and trapping, visualized by real space plot of HIT electrons (colour-coded according to their time of birth by tag numbers), HIT ions (black), colour-coded transverse phase space plots in both planes, and for snapshots 5-8 also the slice emittance. Here, the release laser pulse spot size is w_0=7 µm, and the He (HIT) density = 3.3×10^{22} m^{-3}. Space charge effects are switched on here.

The implemented feature of tagging released macroparticles will investigate the distribution along the formed witness bunch. Figure (5.43) shows the colour-coded real space of the formed witness beam for the case of $w_0 = 7$ μm at He density of $n_e = 3.3 \times 10^{22}$ m^{-3} for the cases of space charge off. The first panel shows all macroparticles. Here, one can see a trend with respect to the longitudinal trapping position in case of the space charge off case, which seems to indicate that electrons born later (higher tag numbers) are trapped more at the head of the bunch, but in the case of the space charge on case, the effect of ionisation front movement, temporal release time and space charge all overlap. In order to investigate this further, the range of macroparticles is broken down into three subsets. These electrons are born the earliest, those of middle age, and those born the latest. In total, four plots are shown per case: the one with all particles, and the three with the subsets.

Generally, in the case of space charge being switched off, the bunch is shorter and less wide when compared to the case of space charge switched on (Figure (5.44). This is the effect of beam loading and increased transverse momentum and emittance (see Figures (5.27) and (5.29)).

For the space charge off case, from the plots of the three cohorts of the electrons liberated during the plasma photocathode process in the space charge off case, one finds that electrons released earlier are particularly contributing to the formation of the transverse wings of the formed beam. This can be attributed to the fact that they have accumulated more transverse momentum during the trapping process. Also, it seems that the electrons released earlier (first third) and the particles that are released later (third third) actually overlap in the same position in the front of the bunch, and the intermediate particles (second third) are slipped further back and trap further at the back of the bunch. This behaviour may be explained as a result of ionisation front movement regarding the centre of the wakefield, which is shown in Figures (5.37) - (5.40).

When space charge effects are switched on see Figure (5.44), the formed bunch is much longer as we see the transverse phase space, and wider than without space charge effects. In the first third of electrons, one sees a particularly distinct trend: electrons born first (coloured in blue) are trapped earlier, while electrons born later (yellow) are trapped later. In principle, this can result from the exact position of the ionisation front within the electrostatic potential (as a reminder, when electrons are released at deeper electrostatic potential, they are trapped earlier, and vice versa), or space charge effects. However, in this case, one has the comparison with the space charge off case: there, one does not see such a clear distinction in the first third of electrons, which implies that space charge effects are the dominating factor for the observed effect. This is consistent with the significantly widened beam: space-charge forces of electrons released early, trapped on-axis, push electrons that are born and arrive later further to the outside. This means they receive larger transverse momentum, consistent with earlier observations, and due to the conservation of energy

and momentum, this means the forward momentum required for trapping will be reached later. Consequently, these electrons are trapped later.

If one looks at the second third of electrons, the most striking feature is that very few electrons born in this window contribute to the head of the formed witness bunch. Again, this can be interpreted by the space charge forces that push electrons further to the outside, beam loading that reduces the local electric accelerating field even if only slightly, and the ionisation front position. This cohort (the second third) is released when the laser pulse reaches its focus, hence the ionisation front is further ahead compared to the first and third third of electrons. The ionisation front position is the same for the case of space charge off, and hence, the comparison with this case enables us to isolate the effect of the space charge. It appears from this comparison that the space charge is not dominating the trapping position in this case: both with or without space charge. There are electrons trapped at similarly early positions. This is then consistent with the observation in the third third of electrons, which are trapped earlier and again contribute significantly to the head of the witness beam.

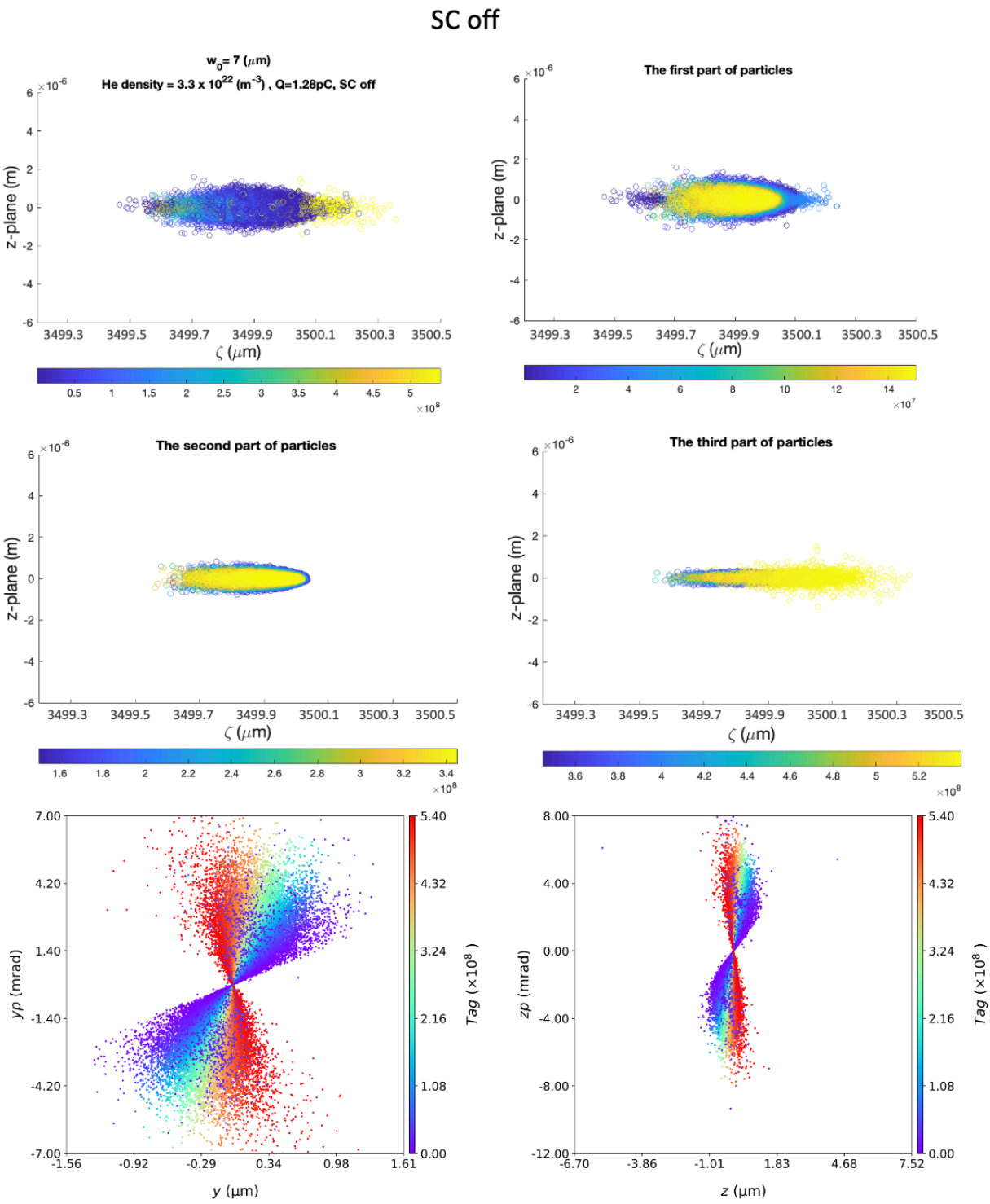

Figure 5.43: Plot the released electrons during the release process and transverse phase space using the colour coding according to their time of birth, for the case of w_0=7μm with the He density= 3.3x10^{22} m^{-3} when space charge is switched off.

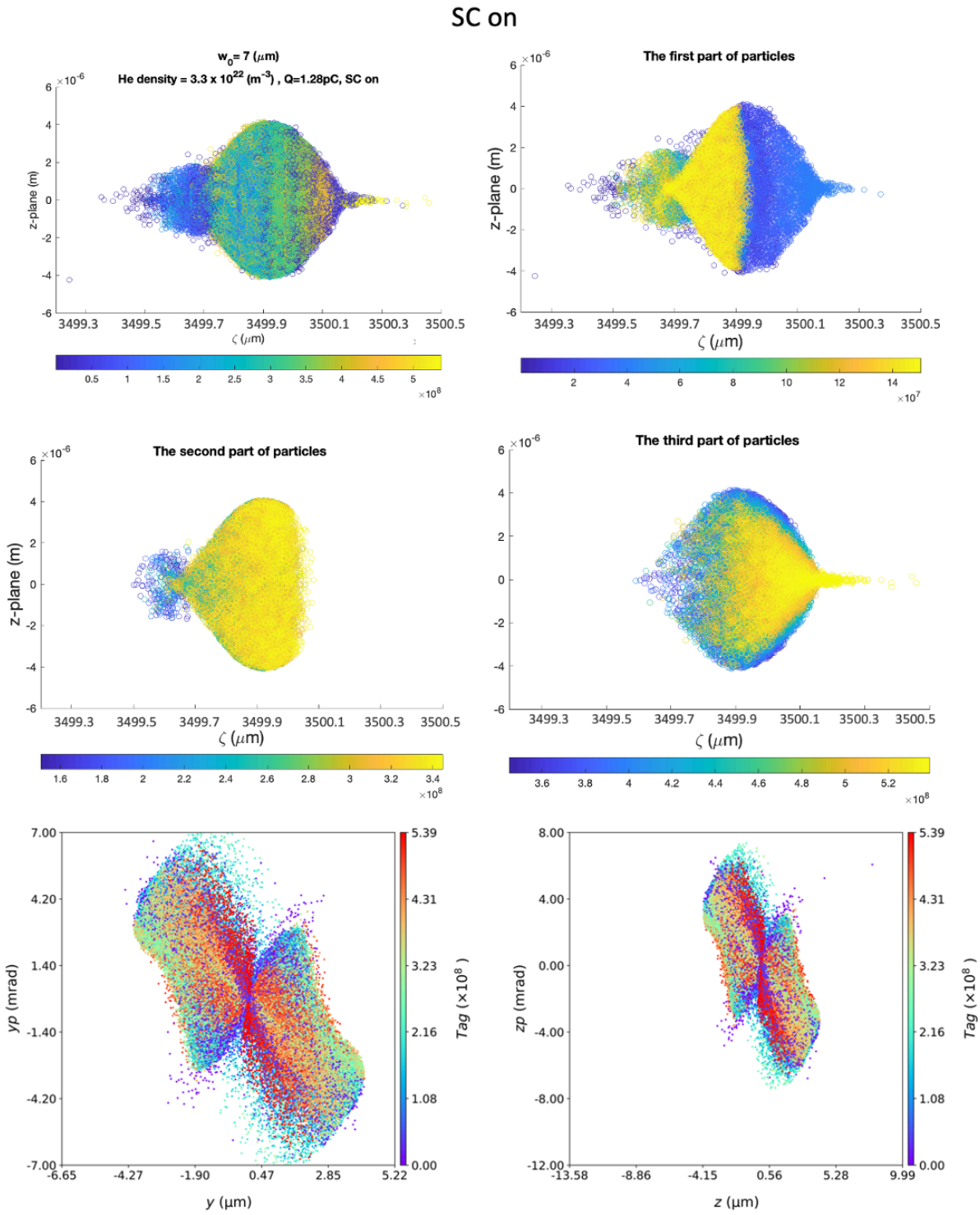

Figure 5.44: Plot the released electrons during the release process and transverse phase space using the colour coding according to their time of birth, for the case of w_0=7μm with the He density= 3.3×10^{22} m^{-3} when space charge is switched on.

These detailed observations, simulations with and without space charge is high resolution, tagged electrons and the above investigations of real and phase space dynamics, and analysis of the dynamics of projected and slice beam parameters, open the door to detailed understanding and optimization of witness beam formation and parameters. These tools have been exploited in simulations for free-electron-lasers as part of the STFC-funded PWFA-FEL project, and will be crucial for further plasma photocathode work, optimization towards high 5D and 6D brightness beams, different types of plasma photocathodes etc.

5.8 Summary

This study intends to create a compact plasma accelerator that can be built in the Middle East without a large infrastructure. To build an effective FEL, we would like to develop electron beams with exceptional emittance and brightness. Low beam emittance can be achieved by combining low transverse momentum with a smaller beam size. Several reasons result in greater transverse momentum and beam dimensions, the most important of which is "space charge," which is caused by higher charge densities when the beam is trapped and compressed. This reduces the brightness by increasing the transverse phase space and thus the emittance.

The impact of space charge on the witness beam and the dynamics that space charge causes throughout the release, trap, and initial accelerate processes were investigated in this study. We might not have to accelerate the beam to higher energy levels. Using modern, high-resolution PIC simulations, the influence of space charge is deeply analyzed. The laser pulse of w_0=7 μm and w_0=15 μm at artificially set ionisation potential values are for two spot sizes. We constructed three well-defined high-resolution simulations for low-charge, medium-charge, and high-charge witness bunches. We are working on and testing strategies for reducing numerical noise to focus on its physics. This entails first creating appropriate codes for analyzing simulation results. Second, we reduced the cell size in the simulation box and then used high dump rates in the simulation, which achieved 3064 dumps for the case of w_0=15 μm. For instance, making this simulation hugely expensive, requiring over 5 million core-hours and 400 TB of storage on the Shaheen supercomputer. This is the first time we have used high resimulation with a high dump rate in the TH approach.

On the other hand, the simulation is special because it allows us to investigate aspects that would otherwise be impossible to discover via experimentation. We intentionally raised the driver beam charge to capture and maintain a greater witness beam charge. Therefore, we put the ionisation potential of He gas at an artificially high amount. As a result, the maximum electric fields of the drive beam and wake-field rise, exceeding the helium tunnelling ionisation threshold, resulting in undesired hot spots and dark

current production. For this reason, we increased the ionisation potential to enable us to research space charge impacts and understand some concepts that are difficult to interpret experimentally.

We employed colour-coded tags numbers to monitor electrons and study the dispersion along the produced witness bunch. We employed a clever approach to turn off the witness beam self-field interaction in the simulation. This implies that the electron macroparticles in the witness beam will solely be affected by the plasma wakefields and does not repel each other. This enables the comparison of witness beam characteristics for simulations with and without space charge (SC), exploration of significant differences, hence isolation and understanding of the space charge processes.

The simulated scans indicated that there are three phases involved in enhancing emittance: First, the thermal emittance is caused by the laser kick's residual momentum, which is affected by laser parameters such as w_0, a_0, etc. When the laser pulse stops releasing electrons due to diffraction, its contribution is complete. Second, during the release and trapping processes, the phase mixing effect takes over and dominates the emittance increase for a period. Third, the space charge effect appears earlier in the trapping process, increasing charge densities when electrons are trapped and compressed. As a result, as we observed in this chapter, as space charge forces grow, space charge forces stretch the created witness bunch. At the same time, the research reveals that as the net released charge is increased, the estimated emittance increases significantly.

The relationship between emittance and space charge has attracted considerable attention in the exploration and study. The contributions of thermal emittance, phase mixing, and space charge to emittance could be used to design appropriate bunch production for various applications. The findings given in this thesis should serve as a solid foundation for developing and expanding a robust backdrop for a SAXFEL machine. Additionally, these findings could be utilized to develop plasma Wakefield accelerators and advance the UK XFEL and STFC programs and future initiatives.

Chapter 6

6.1 Conclusions and Outlook

The electron beam quality produced from an accelerator is crucial for any application. A high-profile application that epitomizes the need for extremely high electron beam quality is the free-electron laser. In an undulator, high phase-space density is required to develop the emission of coherent radiation and strong gain of the photon field intensity. Therefore, the conditions for lasing in a free-electron laser can be described by criteria that put the electron beam transverse emittance, energy, energy spread, and current into relation with the undulator parameters in terms of periodicity and magnetic field strength. These parameters and relations define the ability of the free-electron laser to develop lasing, the resonant wavelength, and the gain, i.e. the speed by which the photon field power is rising during the coherent emission process.

Conventional plasma-based accelerator approaches struggle to reach the required beam quality. Reasons for this are rather fundamental: while the ultrahigh electric field gradients in plasma waves offer many appealing features for the production of high-quality beams, the injection into the plasma wave is a challenging process, which is at the same time defining for the available electron beam quality. For example, electrons captured from the background plasma wave via what is typically called 'self-injection' usually carry much transverse momentum since they previously have received large transverse momentum by the driver beam as the fundamental mechanism of plasma wave excitation. The electric fields associated with the space charge of the driver beam point outwards in the laboratory frame due to Lorentz contraction; hence, plasma electrons primarily are ejected transversally. When they are re-attracted by the ions, it depends rather sensitively on the individual electron trajectories whether they may be captured in the accelerating field of the plasma wave or not. While some of those plasma electrons during this trapping process may lose transverse momentum previously imparted by the space charge of the driver beam, most of them retain significant residual transverse momentum, which in turn imposes limits for the obtainable transverse emittance of the electron beam. This limit of normalised emittance typically is around 1 μm rad. Also importantly, the rate and amount of charge injected by self-injection or similar processes dependent on individual plasma electron oscillations can vary strongly in the dependence of the driver beam or the plasma profile from shot to shot.

In contrast, the plasma photocathode injection process is largely decoupled from the driver beam and background plasma oscillation. Furthermore, in PWFA, the electric field associated with the space charge of the driver beam can be comparably modest, e.g., with peak amplitudes in the range of tens of GV/m. This can leave media with higher tunnelling ionisation thresholds intact, which is a key prerequisite for the

plasma photocathode process. For example, a gas mixture of hydrogen and helium can be used, where hydrogen plasma is used to support the plasma wakefield, and helium, thanks to its substantially larger ionisation threshold, remains in gaseous form until hit by the plasma photocathode laser pulse. Because the laser pulse naturally has rapidly oscillating electric fields, a laser pulse with an electric field amplitude exceeding the tunnelling ionisation threshold of the high ionisation threshold medium will not impart significant residual transverse momentum on the liberated electrons.

This is in stark contrast to the role of the driver beam: the driver electron beam transverse space-charge fields shall be large in order to impart large transverse momentum to plasma electrons in order to excite the collective plasma wave oscillation, whereas the witness electron release laser pulse shall impart negligible transverse momentum to the released witness electrons.

Low transverse momentum, and small beam size, are the desirable defining factors for achieving low beam emittance. This is reflected by the compactness of transverse phase space, and the large current density of the witness beam. Nevertheless, even if the initial residual transverse momentum imparted by the plasma photocathode laser pulse is negligible, factors subsequently increase the transverse momentum and beam size. Phase mixing sets in immediately during the release process, as the released slices of electrons, are captured, accelerated, longitudinally, and transversely compressed in the plasma wakefield. Then, some effects impact the witness beam quality due to its charge density being trapped and compressed to increase charge densities. The intra-beam interaction due to increasing collective repulsive Coulomb forces in the forming witness beam can become important. This may increase the transverse phase space and the emittance, in turn reducing the brightness. Additionally, space charge due to increased charge densities can become significant and no longer negligible from the plasma wave's perspective, manifest by reducing effective accelerating electric fields in the form of beam-loading.

These complex effects during beam formation are of paramount importance for the witness beam shape and quality in terms of emittance, current, energy spread and brightness. In this thesis, these effects are investigated in detail, using advanced, high-resolution particle-in-cell simulations. Generating witness beams at nm-rad emittance levels and studying the formative phase of witness beam production in detail, particularly when exploring the witness beam dynamics and subtle space charge effects at lower total charge levels. Significant effort has been put into developing and testing techniques that decrease numerical noise issues to concentrate on physics. This involved developing and testing suitable scripts to analyse the simulation outputs.

Furthermore, this requires not only high resolution in 3D, but also high dump rates. This puts high demands on computational resources, and is costly. Further significant effort has been made to make the simulations as efficient as possible, and the simulations' computational costs are very substantial. A careful down-selection of

the parameter range to be scanned was used. Furthermore, initial parameter regime sweeps have been carried out at reduced resolution and reduced computational costs. These studies have been useful to refine the required resolution for high-resolution runs, concerning the feasibility of requirements for suitable exploration of details of the witness beam formation dynamics. More than 5 million core-hours were required, and ~400 TB of storage. This would not have been possible on many high-performance computing clusters and allocations, but fortunately, in the context of this thesis, the Shaheen-II cluster at KAUST in Saudi Arabia could be used to facilitate the research presented.

On the other hand, simulations uniquely allow exploring details and dependencies that are not accessible by experiment. Several of these approaches that can be exclusively exploited in simulations have been used for this thesis. For example, the ionisation potential of the species from which electrons were liberated from set to arbitrary values to operate in extremely strong plasma waves was allowed to produce and capture witness beams with charges up to several nC. Also, released particles were tagged and tracked. This allowed the examination of relations between date (and location) of birth times with positions in the formed bunch in real and phase space, to investigate the movement of the ionisation front within the release laser pulse, and the exact moment space charge forces and their impact on the formed bunch emittance kick in.

Further, exploiting VSim's modular structure, a field splitting technique was implemented that allowed us to switch off/on intra-beam space-charge forces. If switched on, witness beam electron macroparticles will 'see' each other, and their electric field configuration was added on the top of the plasma wakefields to account, e.g., for beam loading, as is reality. If switched off, the released electron macroparticles would not repel each other but would merely be regarded as test particles inside the wakefield. These features have proven to be extremely important to investigate and understand the effect of space charge forces and their dynamics in detail.

Using these techniques, the studies revealed that thermal emittance resulted from the residual transverse momentum obtained during tunnelling ionisation and interaction with the remaining laser pulse, and phase mixing due to different times of birth of the electrons. Space charge forces dominate the overall emittance when the total released charge exceeds approximately a few pC. This is a rather general statement and depends on the specific scenario, e.g., if the wakefield driver is transversally matched to the wakefield or not, but very important to focus on the important effects and limitations going forward.

Both the projected and slice parameters of the formed witness bunches have been investigated in terms of analysis. There are two mechanisms by which the charge of the witness beam can be tuned. One is to tune the laser pulse, for example, in terms

of intensity or terms of spot size. The other is to tune the density of the high ionisation threshold species. Tuning the laser pulse spot size and/or the laser pulse intensity will vary the focus volume in which electrons are released. For example, a larger spot size means that more electrons are released off-axis, where they will develop more transverse momentum when being accelerated towards the axis by the transverse wakefields.

In contrast, tuning the high ionisation threshold component density will keep the release volume constant. This is particularly useful to investigate the emittance contributions and their dynamics. The analysis shows that at high released charge levels in the range of nC, space charge forces are so strong that they significantly elongate the formed witness bunch. This is an interesting form of dynamic beam loading, which is unique to the plasma photocathode process. The analysis at the same time also shows that the projected emittance increases strongly as the overall released charge is increased.

On the one hand, the simulation scans revealed that the temporal sequence of contributions to the emittance has three phases: first, the thermal emittance resulting from the residual momentum of the laser kick following the tunnelling ionisation occurs. This contribution is determined exclusively by the frequency and intensity in terms of a_0 of the laser pulse. Further factors are the duration of the laser pulse, its shape, and polarization. This contribution is finished when the laser pulse has stopped releasing electrons because of diffraction. Second, betatron phase mixing sets in, as the individual electrons are accelerated and their betatron frequency and amplitude increase, while the Lorentz factor γ associated with individual electrons increases due to the acceleration. This phase mixing, which has been visualized, e.g., by plotting the colour-coded transverse phase space slice ellipses, sets in immediately, but then may dominate the emittance growth for a while, particularly, in the period where the release process has stopped, but not all electrons are trapped and have reached their final position on the wakefield. In this period, phase mixing is rapid, but witness charge densities are not yet high because the beam is not yet compressed at the trapping position. An exception may be the transverse 'crunch points' of witness beam electrons during the trapping process, when LIT ions and still HIT ions provide focusing forces and produce transversally small electron beam sizes. In any case, dependent on the HIT density, ionisation front movement and the overall released witness beam charge, the dominating emittance growth mechanism may be space charge (third phase). As the witness electrons' space charge is Lorentz compressed, and the forming current produces as pinching magnetic field, the scale of the transverse forces as γ^{-2}, and this emittance growth mechanism is saturated after a while.

On the other hand, the simulations revealed the sequence of contributions and their relative magnitude. The thermal emittance contribution is extremely low. It has been ignored to model this correctly by resolving laser pulse oscillations instead of using the computationally much more efficient envelope approximation. The phase

mixing emittance contribution is typically much larger, and can be the overall contributing factor, but only at low released charge values, e.g., in the sub-pC range. For (much) larger charges, the dominating emittance growth contribution comes from the space charge.

Figure 6.1 below summarises the relative magnitude and sequence of emittance growth mechanisms due to the plasma photocathode witness beam formation conceptually (not to scale).

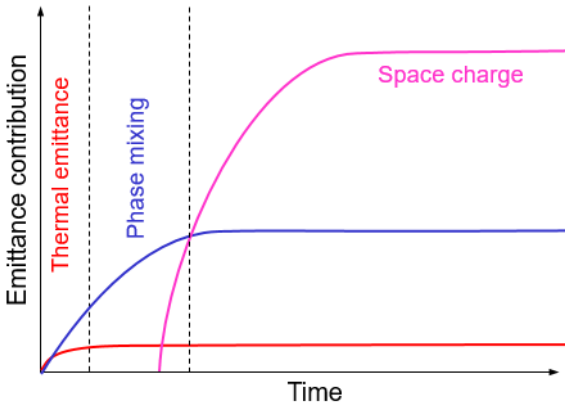

Figure 6.1: Schematic overview on the three different contributions and phases of emittance growth: i) thermal emittance due to laser pulse release, ii) betatron phase mixing, iii) space charge.

Chapter 4 investigated the influence of matched to unmatched driver beams, the influence of the laser pulse intensity, transverse, and longitudinal variation of the plasma photocathode position on the produced witness beam quality. This is useful for understanding parametric dependencies that are important for experiment design, analysis, and applications.

Chapter 3 investigated a key application for beams produced from the Trojan Horse mechanisms. This work was done collaboratively. The main contribution of this thesis has been the underlying PIC simulations that produced the beams that were then used for FEL simulations. One key simplification for this was that the electron beam had only been artificially dechirped to fulfil the energy spread criterion. There are several pathways to realise this practically. One method is the escort beam dechirper method [96], where the first electron beam is aiming at a relatively low charge to optimise emittance and brightness of the beam, and a second plasma photocathode process is then used to provide the high charge bunch to provide tailored beam-loading of the plasma wake, thus being able to reverse the accumulated chirp of the witness beam. Another way is direct beam loading, by which the witness beam (slice) current

is designed, for example, by increasing the HIT density or the laser pulse intensity of focusing, to beam load immediately in such a way that the accelerating electric field around the trapping position is flattened. A higher space charge is required to achieve suitable beam loading in both cases.

Chapter 5 used simulations highly resolved in space and time to explore what happens to beams from the plasma photocathode in terms of quality when the charge is ramped up. From the perspective of applications, this addressed both the direct beam loading approach by a single witness beam and the escort beam loading dechirper approach. It is a challenge to tailor the characteristics of these beams in such a way that they can serve both purposes, robust production of short beams with optimized, as low as possible (slice) emittance, and for the production of longer beams with high charge and current that strongly beam load. The relation between emittance (and other beam quality aspects) and space charge has received special attention in the exploration and analysis. Revealing the contributions and sequence of thermal emittance, phase mixing and space charge to emittance helps design suitable bunch production. Since space charge is the dominating emittance contribution, and has high charge and/or currents as possible are required for many applications. Hopefully, the techniques and insights presented and discussed will prove valuable for future plasma photo gun designs.

Linking emittance growth to space-charge fields in the balance between plasma ion background, HIT plasma ions and increasingly compressed and accelerated witness beam electrons via the transverse momentum growth as driving force allowed to pinpoint the phases during witness generation and acceleration in which the space charge forces and emittance growth kicks in. Then, the tagged transverse phase space evolution reflects this emittance growth in further detail.

Profiting from these results and insights, in the STFC PWFA-FEL project, start-to-end simulations have been carried through involve further improved, noise-optimised high-resolution PIC-simulations, beam transport simulations and sophisticated FEL simulations. These results are currently in preparation for publication and are expected to be a cornerstone for future experimental work and plasma-based (X)-FEL design. It is expected that the results produced as part of this thesis will be used to improve plasma wakefield accelerators to drive those plasma-based PWFA systems of the future.

The electron beams that drive suitable plasma photocathode-equipped PWFA systems can come either from linacs, such as those at SLAC FACET-II, or those potentially foreseen for the UK X-FEL, but also can come from LWFA systems. Such hybrid LWFA-PWFA systems have recently made tremendous progress experimentally [85]. The latter is particularly of interest for countries in which no advanced, larger accelerator infrastructure in the form of GeV-scale, km-scale linacs exists, because they offer access to PWFA-capable systems with a spatial footprint of a few metres.

In this context, plans and proposals have been developed towards a compact X-FEL system in Saudi Arabia with a working title acronym SAXFEL. As shown in Figure 6.2 below, such a system may be realised with a spatial footprint of only a few tens of metres, at dramatically reduced costs compared to existing hard X-FELs, and potentially with cutting edge capabilities as a result of electron beams from plasma photocathodes designed based on principles and insights described in this thesis.

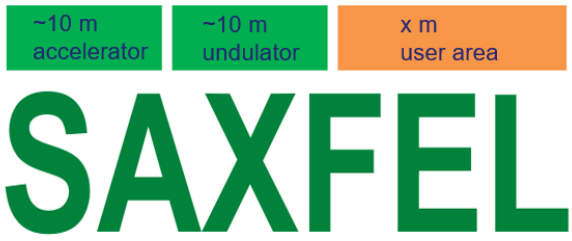

Figure 6.2: Conceptual, the basic layout of SAXFEL, a potential X-FEL in Saudi Arabia. The accelerator part would be based on a hybrid LWFA-PWFA-System, with a plasma photocathode based on principles and insights-driven forward as part of this thesis. Thanks to the ultrahigh brightness provided by such electron beams, an undulator of only ~10 m length may be sufficient to generate soft to hard x-ray pulses, which then could be used for experiments in the user area.

It is clear that much more knowledge needs to be developed locally, both theoretically and experimentally, to realise this vision. Hopefully, the results presented in this thesis will be a key fundament for this. World-leading computational resources at KAUST in Saudi Arabia, exploited in this thesis, have been proven to push this research further and build and expand the knowledge base for the know-how and skills required for a SAXFEL machine. A parallel aim is to explore synergistic R&D questions required to push forward the UK XFEL project, and further potential future X-FEL projects that may employ the plasma photocathode technology. In particular, the development of XFELs based on plasma photocathodes and compact hybrid LWFA-PWFA layouts require significantly more development in theory and simulation, but could be realised completely based on commercially available technology, and will be a focus of further work.

Bibliography

[1] T. Tajima and J. M. Dawson, "Laser electron accelerator," Phys. Rev. Lett. **43**, 267-270 (1979).

[2] L. Evans, "The Large Hadron Collider," 34th SLAC Summer Institute On Particle Physics (SSI 2006), July 17-28, 2006.

[3] https://www6.slac.stanford.edu.

[4] C. Joshi, W. B. Mori, T. Katsouleas, J. M. Dawson, J. M. Kindel, and D. W. Forslund, "Ultrahigh gradient particle acceleration by intense laser-driven plasma density waves," Nature **311**, 525–529 (1984).

[5] S. Takeda, K. AkAI, M. AkEMOTO ,H. AKIYAMA, et al., "Electron Linac of Test Accelerator Facility for Linear Collider," Part. Accel. **30,** 153–159 (1990).

[6] C. Joshi, "Plasma Accelerators," Scientific American **294**, 40-47 (2006).

[7] C. Nieter and J. R. Cary, "VORPAL: A Versatile Plasma Simulation Code," J. Comput. Phys. **196**, 448 (2004).

[8] I. Langmuir, "The Arrangement of Electrons in Atoms and Molecules," Journal of the American Chemical Society **41**, 868 (1919).

[9] H. M. Mott-Smith, "History of “Plasmas”," Nature **233**, 219 (1971).

[10] F. Chen, Introduction to Plasma Physics and Controlled Fusion (Plenum Press, 1974).

[11] R. Goldston and P. Rutherford, Introduction to Plasma Physics (Institute of Physics Publishing,1995).

[12] P. Debye and E. Hückel, "Zur Theorie der Elektrolyte," Physikal. Zeitschr. **24,** 185 (1923).

[13] N. Meyer-Vernet, "Aspects of Debye shielding," American Journal of Physics **61**, 249 (1993).

[14] L. Tonks and I. Langmuir, "Oscillations in ionized gases, " Phys. Rev. **33**, 195 (1929).

[15] J. Taylor, Classical Mechanics (University Science Books Publishing, 2005).

[16] L. Keldysh, " Ionization in the field of a strong electromagnetic wave," Sov. Phys. JETP **20**, 1307–1314 (1965).

[17] A. M. Perelomov, V. S. Popov and M. V. Terent’ev, "Ionization of atoms in an alternating electric field," Sov. Phys. JETP **23,** 924–934 (1966).

[18] F. H. M. Faisal, "Multiple absorption of laser photons by atoms, " Journal of Physics B **6,** L89 –L92 (1973).

[19] T. Heinemann, "On the Applications of Plasma Lenses towards Hybrid Plasma Wakefield Accelerators," MSc thesis, University of Hamburg (2015).

[20] D. Bauer, "Plasma formation through field ionization in intense laser matter interaction," Laser and Particle Beams **21**, 489–495 (2003).

[21] P. Scherkl, "High-Quality Radiation from Inverse Compton Scattering using Ultralow-Emittance Electron Bunches," Masters thesis, University of Hamburg (2015).

[22] J. Bakos, A. Kiss, L. Szabo, and M. Tendler., "Light intensity dependence of the multiphoton ionization probability in the resonance case," Physics Letters A **41**, 163–164 (1972).
[23] C. Z. Bisgaard and L. B. Madsen, "Tunneling ionization of atoms," Am. J. Phys. **72**, 249 (2004).
[24] M. Ammosov, N. Delone, and V. Krainov. "Tunnel ionization of complex atoms and atomic ions in an electromagnetic field, " In Proceedings of SPIE **0664**, 138–141 (1986).
[25] G. L. Yudin and M. Yu. Ivanov, "Nonadiabatic tunnel ionization: Looking inside a laser cycle, " Physical Review A **64,** 013409 (2001).
[26] S. Augst, D. D. Meyerhofer, D. Strickland, et al., "Laser ionization of noble gases by coulomb-barrier suppression, " J. Opt. Soc. Am. B **8 ,** 858–867 (1991).
[27] D. L. Bruhwiler, D. A. Dimitrov, et al., " Particle-in-cell simulations of tunneling ionization effects in plasma-based accelerators," Physics of Plasmas **10**, 2022 (2003).
[28] C. Joshi, W. B. Mori, T. Katsouleas, J. M. Dawson, J. M. Kindel, and D. W. Forslund, "Ultrahigh gradient particle acceleration by intense laser-driven plasma density waves," Nature **311**, 525 (1984).
[29] P. Chen, J. M. Dawson, R. Huff and T. Katsouleas, "Acceleration of electrons by the interaction of a bunched electron beam with a plasma, " Phys. Rev. Lett. **54**, 693 (1985).
[30] E. Esarey, C. B. Schroeder, and W. P. Leemans, "Physics of laser-driven plasma-based electron accelerators," Reviews of modern physics **81**, 1229 (2009).
[31] B. Hidding, G. Manahan, O. Karger, A. Knetsch, G. Wittig, D. Jaroszynski, Z. M. Sheng, Y.Xi, A. Deng, J.B. Rosenzweig, G. Andonian, A. Murokh,G.Pretzler, D.L. Bruhwiler and J. Smit, "Ultrahigh brightness bunches from hybrid plasma accelerators as drivers of 5th generation light sources," Journal of Physics B: Atomic,Molecular and Optical Physics **47,** 234010 (2014).
[32] E. Esarey, J. Krall, and P. Sprangle., "Envelope analysis of intense laser pulse self-modulation in plasmas," Phys. Rev. Lett. **72**, 2887 (1994).
[33] W. B. Mori, C. D. Decker, D. E. Hinkel, and T. Katsouleas. "Raman forward scattering of short-pulse high-intensity lasers, " Phys. Rev. Lett. **72**,1482 (1994).
[34] N. E. Andreev, L. M. Gorbunov, V. I. Kirsanov, A. A. Pogosova, and R. R. Ramaza- shvili, "The theory of laser self-resonant wakefield excitation, " Physica Scripta **49,** 101 (1994).
[35] E. Oz, T. Katsouleas, P. Muggli, et al. "Ionization-induced electron trapping in ultrarelativistic plasma wakes, " Physical Review Letters **98**, 084801 (2007).
[36] V. Malka, "Laser plasma accelerators," Physics of Plasmas **19**, 055501 (2012).
[37] S. Bulanov, F. Pegoraro, A. Pukhov, and A. Sakharov, "Transverse-wake wave breaking, " Phys. Rev. Lett. **78**, 4205–4208 (1997).
[38] C. B. Schroeder, E. Esarey, B. A. Shadwick, and W. P. Leemans, "Trapping, dark

current, and wave breaking in nonlinear plasma waves," Phys. Plasmas **13**, 033103 (2006).
[39] S. Y. Kalmykov, A. Beck, X. Davoine, E. Lefebvre, and B. A. Shadwick, "Laser plasma acceleration with a negatively chirped pulse: all-optical control over dark current in the blowout regime," New J. Phys. **14**, 033025 (2012).
[40] T. Katsouleas, S. wilks, P. Chen, et al., "Beam loading in plasma accelerators," Particle Accelerators **22**, 81–99 (1987).
[41] M. Tzoufras, W. Lu, F. S. Tsung, et al., "Beam loading in the nonlinear regime of plasma-based acceleration," Physical Review Letters **101**, 145002 (2008).
[42] S. Bulanov, N. Naumova, F. Pegoraro, and J. Sakai, "Particle injection into the wave acceleration phase due to nonlinear wake wave breaking," Phys. Rev. E **58**, R5257–R5260 (1998).
[43] H. Suk, N. Barov, and J. B. Rosenzweig, "Plasma electron trapping and acceleration in a plasma wake field using a density transition," Physical Review Letters **86**, 1011 (2001).
[44] A. Martinez de la Ossa,Z. Hu, et al., "Optimizing density down-ramp injection for beam-driven plasma wakefield accelerators," Physical Review Accelerators and Beams **20**, 091301 (2017).
[45] H. Ekerfelt, et al., "A tunable electron beam source using trapping of electrons in a density down-ramp in laser wakefield acceleration," Scientific Reports **7**, 12229 (2017).
[46] D. Umstadter, J-K Kim, and E. Dodd, "Method and apparatus for generating and accelerating ultrashort electron pulses," Phys. Rev. Lett. **76**, 2073 (1996).
[47] M. Chen, Z.-M. Sheng, Y.-Y. Ma, et al., "Electron injection and trapping in a laser wakefield by field ionization to high-charge states of gases," Journal of Applied Physics **99**, 056109 (2006).
[48] A. Pak, K. A. Marsh, S. F. Martins, W. Lu, W. B. Mori, and C. Joshi, "Injection and trapping of tunnel-ionized electrons into laser-produced wakes," Phys. Rev. Lett. **104**, 025003 (2010).
[49] B. Hidding, G. Pretzler, J. B. Rosenzweig, T. Königstein, D. Schiller, and D. L. Bruhwiler, "Ultracold electron bunch generation via plasma photocathode emission and acceleration in a beam-driven plasma blowout," Phys. Rev. Lett. **108**, 035001 (2012).
[50] B. Hidding, J. B. Rosenzweig, Y. Xi, et al., "Beyond injection: trojan horse underdense photocathode plasma wakefield acceleration," in "AIP Conference Proceedings," (2012), vol. **1507**, pp. 570–575.
[51] Y. Xi, B. Hidding, D. Bruhwiler, G. Pretzler, and J. B. Rosenzweig, "Hybrid modeling of relativistic underdense plasma photocathode injectors, "Phys. Rev. ST Accel. Beams **16**, 031-303 (2013).
[52] F. Harlow, "A Machine Calculation Method for Hydrodynamic Problems," Los Alamos Scientific Laboratory report LAMS-1956, (1955).
[53] C. Nieter and J. R. Cary, "Vorpal: a versatile plasma simulation code," Journal of

Computational Physics **196**, 448–473 (2004).
[54] T.Zh. Esirkepov. "Exact charge conservation scheme for particle-in-cell Simulation with an arbitrary form-factor, " Computer Physics Communications **135**,144–153 (2001).
[55] B. M. Cowan, D. L. Bruhwiler, et al., "Characteristics of an envelope model for laserplasma accelerator simulation, " Journal of Computational Physics **230**, 61 – 86 (2011).
[56] W. L Kruer, The Physics of Laser Plasma Interactions (CRC Press, 2003).
[57] B. Hidding, G. G. Manahan, etal., "FIRST MEASUREMENTS OF TROJAN HORSE INJECTION IN A PLASMA WAKEFIELD ACCELERATOR," In: Proceedings of the 8th International Particle Accelerator Conference. IPAC Proceedings . CERN Publishing, Geneva, pp. 1252-1257.
[58] P. M. Lapostolle, "Possible emittance increase through filamentation due to space charge in continuous beams," Nuclear Science, IEEE Transactions on Nuclear Science **18**, 1101-1104 (1971).
[59] F. J. Sacherer, "RMS envelope equations with space charge," Nuclear Science, IEEE Transactions on **18**, 1105-1107 (1971).
[60] K. Floettmann, "Some basic features of the beam emittance, " Physical Review Special Topics: Accelerators and Beams **6,** 034202 (2003).
[61] G. G. Manahan, "Studies of transverse properties of relativistic electrons from laser wakefield accelerator," Ph.D. thesis, University of Strathclyde (2013).
[62] M. Reiser, Theory and Design of Charged Particle Beams (Wiley-VCH Verlag GmbH & Co. KGaA, Weinheim , 2008).
[63] L. A. Gizzi, R. Assmann, et al., Laser-Driven Sources of High Energy Particles and Radiation, (Springer Nature Switzerland AG ,2019).
[64] M. Ferrario, M. Migliorati, and L. Palumbo, "Space Charge Effects," in Proceedings of the CAS-CERN Accelerator School (2013).
[65] B. Hidding, A. Beaton, etal., " Fundamentals and Applications of Hybrid LWFA-PWFA," Appl. Sci. **9**, 2626 (2019).
[66] T. P. Wangler, " Emittance Concept and Growth Mechanisms ," AIP Conference Proceedings **377,** 3 (1996).
[67] B. W. J. McNeil and N. R. Thompson, " X-ray free-electron lasers," Nat. Photon. **4**, 814-821 (2010).
[68] B. M. Alotaibi, R. Altuijri, A. F. Habib, A. Hala, B. Hidding, Sh. M. Khalil, B. W. J. McNeil, P. Traczykowski, "Plasma wakefield accelerator driven coherent spontaneous emission from an energy chirped electron pulse", New Journal of Physics **22**, 013037 (2020).
[69] A. F. Habib, "A fifth generation light source driven by advanced plasma wakefield a ccelerators," Master's thesis, University of Hamburg and University of Strathclyde (2017).
[70] L.T. Campbell and B.W.J. McNeil, "A Simple Model For The Generation Of Ultra-Short Radiation Pulses," in FEL2012: Proceedings of the 34th International Free-Electron Laser Conference (2012).

[71] B.M. Alotaibi, "Numerical studies of a plasma accelerator driven Free Electron Laser," Ph.D. thesis, University of Strathclyde (2019).
[72] CS Hwang, etal., "Development trends for insertion devices of future synchrotron light sources," Physical Review Special Topics Accelerators and Beams **14**, 044801 (2011).
[73] B. M. Alotaibi, Sh. M. Khalil, B.W.J. McNeil and P. Traczykowski, "Modelling a laser plasma accelerator driven free electron laser," J. Phys. Commun. **3**, 065007 (2019).
[74] L.T. Campbell and B.W.J. McNeil, "Puffin: A Three Dimensional Unaveraged Free Electron Laser Simulation Code," Phys. of Plasmas **19**,093119 (2012).
[75] B. M. Alotaibi, **R. Altuijri** et al., "Plasma Accelerator Driven Coherent Spontaneous Emission" in 39th Free Electron Laser conference, TUP051 (2019).
[76] https://github.com/UKFELs/Paraffin.
[77] G. G. Manahan, A. F. Habib, P. Scherkl, et al., "Single-stage plasma-based correleated energy spread compensation for ultrahigh 6D brightness electron beams," Nat. Commun. **8**, 15705 (2017).
[78] G. G. Manahan, A. F. Habib, P. Scherkl, D. Ullmann, A. Beaton, A. Sutherland, G. Kirwan, P. Delinikolas, T. Heinemann, R. Altuijri, et al., "Advanced schemes for underdense plasma photocathode wakefield accelerators: pathways towards ultrahigh brightness electron beams, "Philosophical Transactions of the Royal Society A: Mathematical, Physical and Engineering Sciences **377**, 0182 (2019).
[79] K. A. Marsh, C. E. Clayton, et al., "Beam matching to a plasma wakefield accelerator using a ramped desity profile at the plasma boundary," in "Proceedin of 2005 particle accelerator conference, EEE," (2005), pp. 2702- 2704.
[80] J. B. Rosenzweig, B. Brei, et al., "Acceleration and focusing of electrons in two-dimensional nonlinear plasma wake fields," Physical Review A **44**, R6189 (1991).
[81] C. B. Schroeder, J. L. Vay, E. Esaray, et al., "Thermal emittance from ionization induced trapping in plasma accelerators," Physical Review Special Topics:Accelerators and Beams **17**, 101301 (2014).
[82] B. M. Cowan, D. L. Bruhwiler, et al., " Generalized algorithm for control of numerical dispersion in explicit time-domain electromagnetic simulations" Phys. Rev. ST Accel. Beams **16,** 041303 (2013).
[83] R. Tarkeshian, J. L. Vay, R. Lehe, et al., "Transverse Space-Charge Field-Induced Plasma Dynamics for Ultraintense Electron-Beam Characterization," Physical Review X **8**, 021039 (2018).
[84] A. Knetsch. "Acceleration of laser-injected electron beams in an electronbeam driven plasma wakefield accelerator." PhD thesis. University of Hamburg, 2017.
[85] T. Kurs, T. Heinemann, et al., "Demonstration of a compact plasma accelerator powered by laser-accelerated electron beams," Nat. Commun. **12**, 2895 (2021).

Appendix

Appendix A
Paper 1

PHILOSOPHICAL TRANSACTIONS A

Phil. Trans. R. Soc. A.
doi:10.1098/not yet assigned

Advanced schemes for underdense plasma photocathode wakefield accelerators: Pathways towards ultrahigh brightness electron beams

GG Manahan[1,2,*], AF Habib[1,2], P Scherkl[1,2], D Ullmann[1,2], A Beaton[1,2], A Sutherland[1,2], G Kirwan[1,2,3], P Delinikolas[1,2], T Heinemann[1,2,3], R. Altuijri[1,2,4], A Knetsch[3], O Karger[5], N Cook[6], DL Bruhwiler[6], Z-M Sheng[1,2,7], JB Rosenzweig[8] and B Hidding[1,2]

[1]Scottish Universities Physics Alliance, Department of Physics, University of Strathclyde Glasgow G4 0NG, UK. [2]Cockcroft Institute, Sci-Tech Daresbury, Keckwick Lane, Daresbury, Cheshire WA4 4AD, UK. [3]Deutsches Elektronen-Synchrotron DESY, Hamburg, Germany. [4]Physics Department, Princess Nora Bint Abd Ulrahman University, Riyadh, Kingdom of Saudi Arabia. [5]Department of Experimental Physics, University of Hamburg, Hamburg, Germany. [6]RadiaSoft LLC, Boulder, Colorado, USA. [7]Laboratory for Laser Plasmas and School of Physics and Astronomy, Shanghai Jiao Tong University, China. [8]Particle Beam Physics Laboratory, University of California, Los Angeles, California, USA

Keywords: plasma wakefield acceleration, under-dense plasma photocathode, simultaneous spatial and temporal focusing, energy spread compensation

Summary

The "Trojan Horse" underdense plasma photocathode scheme applied to electron-beam driven plasma wakefield acceleration has opened up a path which promises high controllability and tunability and to reach extremely good quality as regards emittance and 5D beam brightness. This combination has the potential to improve the state-of-the-art in accelerator technology significantly. In this paper, we review the basic concepts of the Trojan Horse scheme and presents advanced methods for tailoring both the injector laser pulses and the witness electron bunches and combine them with the Trojan Horse scheme. These new approaches will further enhance the beam qualities, such as transverse emittance and longitudinal energy spread, and may allow, for the first time, to produce ultrahigh 6D brightness electron bunches, which is a necessary requirement for driving advanced radiation sources.

1. Introduction

Recently, plasma-based wakefield accelerators, driven by either highly intense laser pulse [1- 2] or relativistic electron beams [3-4], are globally seen as the next generation drivers for advanced radiation sources. Their potential applications for high energy physics are also recognised. This novel acceleration technique can harness high energy gains in laboratory scale (GV m^{-1}) because the generated plasma waves are capable of sustaining electric fields with amplitudes greater than E_0, the non-relativistic wave breaking field. Mathematically, E_0 can be expressed as $E_0\,\{\mathrm{V\,m^{-1}}\} \approx 96\sqrt{n_0\{\mathrm{cm^{-3}}\}}$, where n_0 is the background electron density of the plasma [5]. For instance, plasma with density of $n_0 = 10^{18}$ cm^{-3} can yield accelerating fields of ~ 96 GV m^{-1} – these are orders of magnitude greater than the achievable in conventional RF linacs. Hence, it is possible to realise cost-efficient and medium-scale accelerators. Today, production of quasi-monoenergetic, GeV-scale electron bunches within few cm accelerating length is routinely demonstrated worldwide [2, 4].

*Author for correspondence (grace.manahan@strath.ac.uk).

In the case of electron beam-driven plasma acceleration (PWFA), electron bunches can be accelerated with high efficiency through the blowout regime, a scenario of highly nonlinear plasma excitation [6-7]. The bunch density, n_b, of the electron beam driver with a bi-Gaussian distribution is described as $n_b = N_b/\left[(2\pi)^{3/2}\sigma_z\sigma_r^2\right]$, where N_b is total number of electrons, and σ_z and σ_r are the electron driver's bunch length and radial size. In this highly nonlinear regime, the electron driver bunch density is greater than the n_0 ($n_b/n_0 \gg 1$), such that the plasma electrons are completely expelled, creating a nearly spherical ion cavity, known as the blowout. Furthermore, high efficient excitation of the blowout is obtained when σ_z is smaller than the plasma wave number, k_p [8]. Inside the blowout, strong transverse focusing forces and GVm^{-1} level longitudinal fields are attainable. Hence, various electron injection schemes into this regime have been conceived and studied.

The process of electron injection into the plasma wakes plays a key role because the important beam parameters (such as normalised transverse emittance ϵ_n, energy spread $\Delta W/W$, total charge Q and bunch duration σ_z) are largely defined by the initial acceleration stage. The various electron bunch injections can be categorised into two: (i) via external injection [3-4] where an electron bunch with an initial energy and beam parameters are injected and further accelerated into a plasma blowout and (ii) via internal injection where the electrons accelerated are initially at rest and the residual transverse momentum is minimal. Example of these internal injection schemes are using plasma density transition [9-12] and those where additional electrons are release within trapping regions based on higher-level ionisation due to electron field or wakefield spikes [13-17]. One scheme, known as the underdense plasma photocathode (popularised as the Trojan Horse scheme) is based on ionisation injection triggered by a laser pulse. This scheme combines the long acceleration distances of electron-beam driven plasma wakes and limited peak electric fields of particle drivers with the controllability and tuneability of the laser pulses to release electrons directly inside the blowout [18-19]. In this method, electron bunches with transverse emittance as low as nm-rad is possible. Therefore, accelerators based on Trojan Horse scheme may lead to further step-change by increasing the tuneability and electron beam quality in terms of emittance and 5D brightness by orders of magnitude, where the B_{5D} is mathematically expressed as $B_{5D} = 2I_p/\epsilon_n^2$, where I_p is the peak current ($I_p = cQ/\sqrt{2\pi}\sigma_z$). Interestingly, the concept of laser-triggered ionisation has also been reported for application in laser wakefield acceleration, which can be found in these References [20-22] and have shown production of high quality electron beams.

In this article, we present an overview of the Trojan Horse scheme, its advantages, challenges and potential applications using the electron bunch generation. We also presents advanced and novel methods, which in combination with the Trojan Horse concept, aim to enhance the electron beam qualities and in consequence, will further boost the overall beam brightness.

2. Trojan Horse scheme: the underdense plasma photocathode wakefield acceleration

The Trojan Horse (TH) underdense plasma photocathode scheme requires underdense mixtures of low ionisation threshold (LIT) and high-ionisation threshold (HIT) species, such as Hydrogen and Helium (H/He). The high amplitude blowout based on the LIT component is driven by an electron beam, as in the conventional PWFA. Hydrogen, which have ionisation thresholds of $\xi_{i,H} = 13.6$ eV for atomic and $\xi_{i,H_2} = 15.4$ eV for molecular (H_2), is an ideal plasma source because it can be easily ionised either by a modest energy laser pulse or by the self-field of the electron beam driver.

The free electrons are released from the HIT component by a strongly focused, ultra-short laser pulse, which can be called as the TH injector laser. Helium is popularly used as HIT component because of its relatively high ionisation threshold ($\xi_{i,He} = 24.6$ eV). The peak amplitude of the normalised vector potential for the laser pulse used to ionise the HIT component can be as low as $a_0 \sim 0.01$. For a linearly polarised Gaussian beam, a_o is related to the laser peak intensity, I_L, as $a_0 \approx 0.85 \times 10^{-9}\, \lambda\,\{\mu m\}\sqrt{I_L\,\{W\ cm^{-2}\}}$, where λ is the laser central wavelength. Here, the laser pulse intensity can be as low as $I_L\{W\ cm^{-2}\} = 10^{15}/\lambda^2\{\mu m\}$ [5]. At these intensities, the oscillating electric fields are sufficient to induced tunnelling ionisation [23]. The injected electrons are then rapidly accelerated in the blowout. Because the HIT electrons can be selectively released at any point in the blowout (e.g. at the centre of the blowout, approximately the location of the minimum trapping potential [24]), thus the trapping requirements are substantially decreased.

Since the wakefield generation and electron bunch injection are completely decoupled in TH scheme, the electron beam production offers more tuneability. For instance, multibunches with high beam quality and controlled energies are obtainable with this method. By using synchronised TH injector lasers that are independently tuned, such as varying the

delays and having different foci, electrons are released at different positions inside the plasma blowout, and therefore with different energies [25].

One of the issues in PWFA, particularly in triggered ionisation injection schemes is the occurrence of dark current. Dark current is the result of uncontrollable self-injection of electrons ionised by electric field spikes or "hot-spots". These hot spots can be generated by either the (i) wake vertex due to the recombining plasma electrons and/or (ii) by the electron beam driver itself. Detailed studies for the optimisation of the electron and plasma dynamics have been carried through in Reference [26] and have obtained conditions for a dark-current free blowout suitable for the TH scheme. Using intensive 3D particle-in-cell simulations, it is found that to obtained a dark-current free scenario with TH scheme, a blowout radius must be at all times smaller than the fully pre-ionised plasma column width, otherwise the electrons near this blowout will overshoot and will not properly re-attracted; therefore the overall blowout dynamics collapses. These have been presented in details in Reference [26]. Recently, experimental breakthrough and signatures of the TH injection were obtained in the "E210: Trojan Horse PWFA" program of SLAC FACET-I [27].

In the following sections, we present methods of (i) tailoring the plasma photocathode laser to decrease the release volume of the HIT electrons, which might result in the reduction of the initial emittance of the electron bunches and (ii) modifying the accelerating fields of the blowout which can result in compensating the accumulated longitudinal energy spread and chirp of the injected electron bunches.

3. Simultaneous spatial and temporal focusing of plasma photocathode laser

In the TH scheme, the reduction in the transverse normalised emittance is a direct consequence of the extremely low residual transverse momentum, $p/m_e c \sim a_0/2$, from the underdense photocathode laser's ponderomotive force. Here, m_e is the electron mass and c is the speed of light. It is furthermore desirable to decrease the release volume of the HIT electrons to reduce both the initial phase space as well as the longitudinal phase mixing due to electrons being born off axis and at different betatron phases of the driving wake, [18, 28], which can both increase emittance.

One technique to reduce the longitudinal extension of the release region has been reported previously based on the collision of two ultra-short laser pulses in transverse geometry [20]. However, the collision of two lasers creates substantial experimental complexity and challenges in terms of alignment and timing. In this section, we propose the use of simultaneous spatial and temporal focusing (SSTF) of a single laser pulse, a technique known from material processing and microscopy [29-33], and study the applicability for the TH injector lasers. SSTF was first suggested in Ref. [34] for a related laser-driven two-pulse scheme. With SSTF combined with TH, it is capable of reducing the release length of the HIT electrons by more than an order of magnitude when compared with the Rayleigh length z_R of a pulse with the typical longitudinal Gaussian distribution.

In the SSTF method, a transverse spatial chirp of the pulse frequency components is generated before passing through a focusing element. This can be done, for example, by placing a single-pass grating pair (suggested by Ref. [35]) as sketched in Figure 1a, where the SSTF configuration is adapted for the TH accelerator. By carefully choosing the arrival time of the SSTF laser with respect to the electron beam driver, the axial peak intensity of the SSTF laser occurs at the centre of the blowout, indicated by the dashed ellipse in Figure1a.

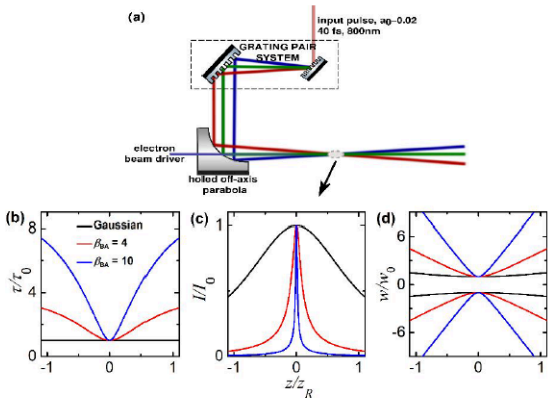

Figure 1: (a) Suggested set-up for the SSTF-TH scheme. A spatially chirped laser photocathode is focused at the location of the plasma blowout using an off-axis parabolic mirror. (b) Normalised pulse duration τ/τ_0, (c) the axial peak intensity I/I_0 and (d) transverse beam size w/w_0 of an SSTF pulse as a function of axial position z/z_R for different values of β_{BA}. The parameters are normalised to its corresponding non-spatially chirped pulse with axial Gaussian profile.

The following discussion of SSTF is mainly based on Ref. [35], where analytical study of SSTF is discussed. The spatially chirped laser can be considered analytically as a superposition of Gaussian beamlets, where each beamlet has a radius $(1/e^2)$ of w_{beamlet}, and is shifted from its central frequency ω_0. If the plasma photocathode laser has an initial spectral bandwidth of $\Delta\omega$, the position of each frequency component is $\alpha\,\Delta\omega$, where α is the chirp rate and can be expressed in dimensionless parameter as $\beta = \alpha\,\Delta\omega/w_{\text{beamlet}}$ [35]. At the entrance of the focusing element, the transverse profile is elongated along the axis where the chirp is applied due to the lateral stretching of the pulse. The amount of ellipticity can be characterized by a dimensionless parameter called beam aspect ratio, β_{BA}, which is defined as the beam radii $(1/e^2)$ ratio of the spatially chirped input pulses. It is expressed as: $\beta_{BA} = \sqrt{1+\beta^2}$ [35]. The frequency components recombine only at the focal region, where the smallest pulse duration is achieved (see Figure 1b). Away from the focus, the pulse is further stretched compared with an unchirped pulse, as shown in Figure 1b. An initial pulse with symmetric Gaussian distribution, $\lambda = 0.8$ µm, pulse length of $\tau_0 = 40$ fs, and a focus spot size of $w_0 = 4$ µm, is used for the calculation, giving a Rayleigh length of $z_R = 62$ µm. The structure of an SSTF pulse deviates from a typical Gaussian beam, in which the axial intensity strongly peaks at the focal position and drastically drops farther from the focus, as shown Figure 1c and Figure 2. For $\beta_{BA} = 4$, the FWHM of the axial intensity reduces to $z_{SSTF} \approx 13$ µm, more than 50% reduction compared to the z_R of the unchirped pulse. If the grating pair can produced spatial chirp with $\beta_{BA} = 14$, z_{SSTF} is further reduced down to 1 µm, more than an order of magnitude smaller than the z_R normally reached by conventional focusing.

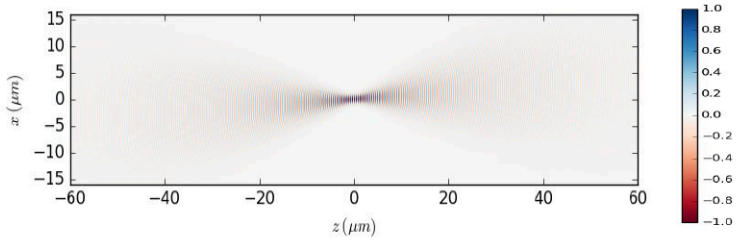

Figure 2: Field propagation of an SSTF pulse with beams aspect ratio of 4. Fields are normalised to 1.

It is important to note that the reduction on the FWHM of the axial intensity is primarily β_{BA} dependent, which can be changed by modifying the grating pair setup. On the other hand, the SSTF pulse maintains its transverse spot size, as

shown in Figure 1d. Here, it is shown that the beam diverges quickly with increasing β_{BA} value; this leads to lower intensities and longer pulse duration far from the focus. These analytical calculations show that with the SSTF method, the axial FWHM of the plasma photocathode laser can be compressed down to 1 μm without significantly changing the peak intensity and spot size. Figure 2 shows the field evolution of an SSTF pulse with beam aspect ratio of *4*, propagating in vacuum. Here, we can see that the fields are only at maximum within a small range of z near the focus location.

As an initial simulation, the SSTF-TH scheme is approximated with VSIM [36] particle-in-cell (PIC) simulations by artificially confining the HIT component in a very narrow region. These are carried through in 3D, which is necessary to catch the physics of the bunch generation and trapping process adequately. Simulation of longer acceleration distance and parameter scans are also required, which makes full resolution of the laser pulse resource-prohibitive. Instead, here we rely on analytical estimations of the release region volumes, and model the photocathode laser represented using an envelope approximation, propagating collinear and trailing 50 μm behind the electron beam driver. The HIT electron release is triggered by the laser pulse via advanced tunneling ionization implementation and geometrically fully resolved in transverse direction, but in the axial direction the release is artificially confined to the corresponding SSTF length as discussed above and plotted in Figures 1 and 2. For example, for an SSTF-TH laser with $\beta_{BA} = 14$, $w_0 = 4$ μm and a_0 0.02, the release length is confined to ~1 μm longitudinal length. A mixture of hydrogen and helium is used as LIT/HIT underdense medium. The electron beam driver has the following characteristics: energy $W = 23$ GeV, total charge $Q = 1$ nC, normalized rms emittance $\varepsilon_n = 2.25$ μm, rms width $\sigma_r = 20$ μm and rms length $\sigma_z = 30$ μm, corresponding to a bunch density $n_b \approx 2 \times 10^{17}$ cm^{-3}. The hydrogen component is preionized at a density of $n_H = 5 \times 10^{16}$ cm^{-3}, corresponding to a plasma wavelength $\lambda_p = \sqrt{\pi/n_H r_e} \approx 150$ μm, where r_e is the classical radius of an electron, while the He density is maintained to $n_H = 5 \times 10^{17}$ cm^{-3}.

Figures 3(a) and (b) show the wake driven by the electron beam immediately after when He electrons are (a) generated by a ~40 fs laser pulse inside the blowout at the focal region (equivalent to the longitudinal distance of $z = 400$ μm) and are (b) trapped and accelerated after 1 mm, where the bunch has gained a maximum energy of 10 MeV. In contrast to conventional TH, where the initial bunch distribution is rather cigar-like, since $z_R > w_0$, in SSTF-TH the initial bunch distribution is pancake-like, since $z_{SSTF} < w_0$. This can be seen in Figure 3a. From the initial results, the rms transverse emittance of the witness bunch using this SSTF approximation produces lower rms transverse emittance by an order of magnitude, as compared with the usual TH pulse that has Gaussian distribution. Note that the artificial confinement of the SSTF in these simulations is implemented because SSTF is a spatial chirp and thus the bandwidth of the laser pulse changes through propagation axis. Since we are using an envelope approximation in VSIM, the effect of the bandwidth on the dispersion of each frequency components of the laser in the plasma is not implemented. The consideration of the SSTF pulse dispersion in plasma is currently on going and will be discussed elsewhere.

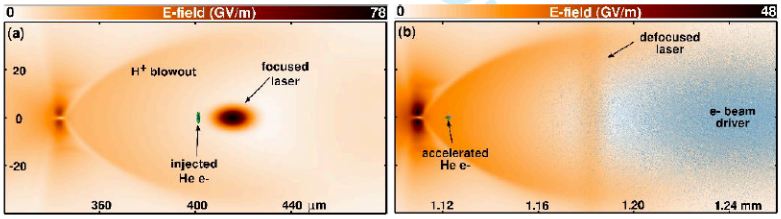

Figure 3: Snapshots from 3D PIC simulation immediately after (a) He generation and (b) after ~ 1 mm of acceleration.

4. Compact, plasma-based energy compensation technique

The high-energy acceleration in plasma inherently produces electron bunches with substantial longitudinal energy spread or chirp. This is well-known and is, currently, the central challenge in any plasma-based accelerators. The large energy spread is detrimental in several ways. Beam extraction and transport is difficult and leads to deterioration of the transverse emittance. It also limits the applications of these beams for advanced radiation sources. Therefore, the "energy spread and chirp problem" degrades the overall beam brightness and is a showstopper for fully harnessing the potentials of plasma-based accelerators.

Conventionally, 6D beam brightness is a figure of merit for comparing the quality of the radiation sources. High 6D brightness beams are characterised by high peak current, low transverse normalised emittance and narrow longitudinal energy spread. It is essential in many applications, such as to reach high-gain and shorter wavelengths in free-electron lasers [37] and for high-energy colliders, to enhance the focusability of the beam and increase its luminosity [38]. The 6D beam brightness can be expressed mathematically as $B_{6D} = B_{5D} \,/\, 0.1\%\ \Delta W_{\mathrm{rms}}/W \,\{\mathrm{Am}^{-1}/0.1\ \mathrm{BW}\}$.

In this section, a flexible scheme of tailoring the energy distribution of low-emittance electron beams inside a plasma-based accelerator is discussed, a concept which is initially introduced in Ref [39]. The tailoring process is based on beam-loading mechanism and can be tuned to achieve energy spread reduction without altering the electron beam emittance. In this concept, two moderate TH laser pulses are used to inject electrons to accelerating plasma wake and modify the field so that the accelerated low emittance electron beam of interest (called the witness bunch) will experience a longitudinal phase space rotation. This idea is one of the applications of the electron multibunch production as mentioned in Section 2. The loaded field reverses the effective accelerating gradient, and counter-rotates the accumulated longitudinal energy spread of the witness bunch. As a result, the energy spread is reduced, enabling the production of ultrahigh 6D brightness beams.

In this concept of plasma dechirper, the first TH laser releases the witness bunch at the beginning of the plasma stage. The parameters of the first TH laser is still the typical one used in any TH scheme, ie, $a_0 \ll 1$ and and strongly focus, e.g. spot size $w_0 < 5$ μm. This ensures that the injected electrons will obtained good beam qualities. After a period of acceleration, in which the witness bunch has gained sufficient energy and is stabilised, a second TH laser is introduced and this laser releases a second batch of electrons, which is called in Ref. [39] as the "escort bunch." The parameters (a_0, w_o and τ_0) of the second TH laser pulse are considerably higher than the first TH laser, such that the produced escort bunch will have a bunch charge density that is capable of overloading the wakefield. In Ref. [39], the escort bunch has gained a total charge of 100 pC in comparison to the witness bunch that is only 5 pC, and has shown that it significantly alters the longitudinal electric field. That means that the presence of the escort bunch strongly overloads the electric field. This results in the counter-clockwise rotation of the longitudinal phase space of the witness bunch while further accelerating. Consequently, the correlated energy spread is reduced reaching its minimum value, a position where extraction is ideal. The resulting energy compensation is shown in Figure 4, in which the phase space of the witness bunch at the position of the minimum energy spread is plotted. The extent of the overloaded field, known as the "dechirping region," must be much longer than the witness bunch such that the dechirping occurs from head to tail of the bunch. That means that the optimisation of the escort bunch must be focused on obtaining high charge and longer bunch duration than the witness bunch.

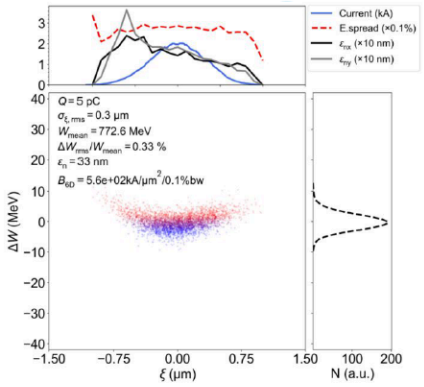

Figure 4: Longitudinal phase-space of the witness bunch during at the position of minimum energy spread from Ref [39].

The main challenges of this approach are the additional laser pulse to produce the escort bunch and the tuneability and spatiotemporal alignment accuracy of both laser pulses. To test how the alignment of the two TH laser pulses affect the plasma dechirping process, an initial jitter study is performed. For this initial analysis, the first TH laser is introduced with a transverse offset with respect to the blowout axis. The result is shown in Figure 5, where the dechirping distance, Δz, and the resulting uncorrelated energy spread is monitored. In this study, a comparable shorter plasma wavelength (λ_p

~ 100 μm) is used, corresponding to a blowout radius, $R_{b,max}$ is 40 μm. As shown in the plot, the dechirping distance and residual energy spread of the witness bunch is quite resilient to the jitter of the initial position of the first TH laser pulse, ie. the y-offset must be greater than $0.2*R_{b,max}$ to see a significant increase in the uncorrelated energy spread. Fortunately, the tolerance against spatiotemporal alignment jitters increases when considering longer plasma wavelengths (hence smaller plasma densities). This is because the plasma blowout increases both in longitudinal and transverse direction. The laser-to-electron drive beam jitter, however, is independent of the plasma wavelength, which means that at lower plasma densities it is easier to release the electrons consistently in the desired phase and at the right trapping position. Furthermore, the residual uncorrelated energy spread decreases when going to longer plasma wavelengths.

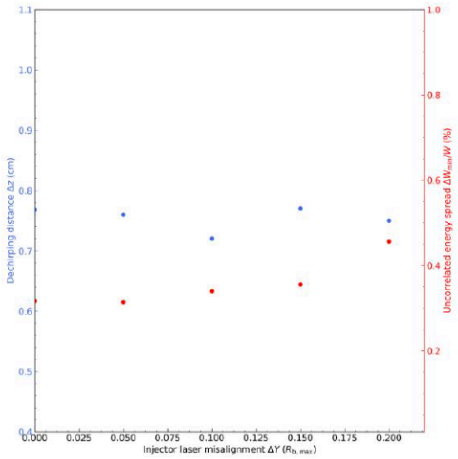

Figure 5: Effect of the first TH laser pulse offset to the plasma-based dechirping techniques. The initial position of TH laser is offset transversely with respect to the blowout axis. Here, the plasma wavelength is 100 μm, thereby the maximum blowout radius, $R_{b,max}$ is 40 μm.

5. Conclusions

In this paper, the Trojan Horse scheme is reviewed for the application in electron-beam driven plasma wakefield accelerator. The decoupling of the plasma blowout generation and electron injection allows greater tuneability and control of the acceleration process and witness bunch qualities, such as transverse emittance and 5D brightness. These developments in electron beam emittance and 5D-brightness may have transformative impact on key applications such as compact yet high performance free-electron lasers. Two advanced methods were presented and were proposed to integrate with the TH scheme. These combinations have the potential of further improving the witness bunch qualities and may pave the way of boosting the 6D beam brightness of the electron bunches.

Additional Information

Acknowledgement

We acknowledge the in-depth discussion of SSTF application to TH scheme with R. Lehe and S. Cook.

Funding Statement

This work used computational resources of the National Energy Research Scientific Computing Center, which is supported by DOE DE-AC02-05CH11231, and of JURECA (project hhh36), of HLRN, and Shaheen (project k1191), and the DFG Emmy-Noether program. This work was supported by a fellowship within the FIT worldwide programme of the

German Academic Exchange Service (DAAD), and by RadiaBeam Technologies. DLB would like to acknowledge DOE Office of Science award # DE-SC0013855.

Data Accessibility

Data are available upon request through the corresponding author.

Competing Interests

We have no competing interest.

Authors' Contributions

All authors contributed equally in this manuscript.

References

1. Wang X. et al. 2013. Quasi-monoenergetic laser-plasma acceleration of electrons to 2 GeV. *Nat. Commun.* **4**, 1988. (doi: 10.1038/ncomms2988)
2. Leemans WP. et al. 2014. Multi-GeV Electron Beams from Capillary-Discharge-Guided Subpetawatt Laser Pulses in the Self-Trapping Regime. *Phys. Rev. Lett.* **113**, 245002. (doi: 10.1103/PhysRevLett.113.245002)
3. Blumenfeld I. et al. 2007. Energy doubling of 42 GeV electrons in a metre-scale plasma wakefield accelerator. *Nature*. **445**, 741-4. (doi: 10.1038/nature05538)
4. Litos M. et al. 2014. High-efficiency acceleration of an electron beam in a plasma wakefield accelerator. *Nature*. **515**, 92-95. (doi: 10.1038/nature13882)
5. Esarey E., Schroeder CB and Leemans W. 2009. Physics of laser-driven plasma-based electron accelerators. *Rev. Mod. Physics.* **81**, 1229. (doi: 10.1103/RevModPhys.81.1229)
6. Rosenzweig J.B. et al. 1991. Acceleration and focusing of electrons in two-dimensional nonlinear plasma wakefields. *Phys. Rev. A.* **44**, R6189-R692. (doi: 10.1103/PhysRevA.44.R6189)
7. Lu W. et al. 2006. Nonlinear theory for relativistic plasam wakefields in the blowout regime. *Phys. Rev. Lett.* **96**, 165002. (doi: 10.1103/PhysRevLett.96.165002)
8. Barov N., Rosenzweig JB., Thompson MC., and Yoder RB. 2004. Energy loss of a high-charge bunched electron beam in plasma: Analysis. *Phys. Rev. Accel. Beams*. 7, 061301. (doi: 10.1103/PhysRevSTAB.7.061301)
9. Suk H., Barov N., Rosenzweig JB. and Esarey E. 2001. Plasma Electron Trapping and Acceleration in a Plasma Wake Field Using a Density Transition. *Phys. Rev. Lett.* **86**, 1011-1014. (doi: 0.1103/PhysRevLett.86.1011)
10. Geddes CGR. et al. Plasma-density gradient injection of low absolute momentum spread electron bunches. *Phys. Rev. Lett.* **100**, 215004. (doi: 10.1103/PhysRevLett.100.215004)
11. Bulanov S. et al. 1998.Particle injection into the wave acceleration phase due to nonlinear wave wake breaking. *Phys. Rev. E.* **58**, R5257-R5260. (doi:10.1103/PhysRevE.58.R5257)
12. Xu XL. et al. 2017. High quality electron bunch generation using a longitudinal density-tailored plasma-based accelerator in the three-dimensional blowout regime. *Phys. Rev. Accel. Beams.* **20**, 111303. (doi: 10.1103/PhysRevAccelBeams.20.111303)
13. Umstadter D., Kim JK. and Dodd E. 1995. Method and apparatus for generating and accelerating ultrashort pulses. US Patent Serial No. 5789876.
14. Chen M. et al. 2006. Electron injection and trapping in a laser wakefield by field ionization to high-charge states of gases. *Journ. Applied Phys.* **99**, 056109. (doi: 10.1063/1.2179194)
15. Oz E. et al. 2007. Ionization-induced electron trapping in ultrarelativistic plasma wakes. *Phys. Rev. Lett.* **98**, 084801. (doi: 10.1103/PhysRevLett.98.084801)
16. Pak A et al. 2010. Injection and trapping of tunnel-ionized electrons into laser-produced wakes. *Phys. Rev. Lett.* **104**, 025003. (doi: 10.1103/PhysRevLett.104.025003)
17. Martinez de la Ossa A. et al. 2013. High-quality electron beams from beam-driven plasma accelerators by wakefield-induced ionization injection. *Phys. Rev. Lett.* **111**, 245003. (doi: 10.1103/PhysRevLett.111.245003)
18. Hidding B. et al. 2012. Ultracold electron bunch generation via plasma photocathode emission and acceleration in a beam-driven plasma blowout. *Phys. Rev. Lett.* **108**, 035001. (doi:10.1103/PhysRevLett.108.035001)
19. Xi Y. et al. 2013. Hybrid modeling of relativistic underdense plasma photocathode injectors. *Phys. Rev. ST Accel. Beams.* **16**, 031303. (doi: 10.1103/PhysRevSTAB.16.031303)

20. Li F. et al. 2013. Generating high-brightness electron beams via ionization injection by transverse colliding lasers in plasma-wakefield accelerator. *Phys. Rev. Lett.* **111**, 015003. (doi: 10.1103/PhysRevLett.111.015003)
21. Yu LL. et al. 2014. Two-color laser ionization injection. *Phys. Rev. Lett.* **112**, 125001. (doi: 10.1103/PhysRevLett.112.125001)
22. Xu XL. et al. 2016. Nanoscale electron bunching in laser-triggered ionization injection in plasma accelerators. *Phys. Rev. Lett.* **117**, 034801. (doi:10.1103/PhysRevLett.117.034801)
23. Chen M. et al. 2013. Numerical modeling of laser tunnelling ionization in explicit particle-in-cell codes. *Journ. Comp. Phys.* **236**, 220-228. (doi:10.1016/j.jcp.2012.11.029)
24. Pak, A. et al. 2010. Injection and trapping of tunnel-ionized electrons into laser-produced wakes. *Phys. Rev. Lett.* **104**.025003. (doi: 10.1103/PhysRevLett.104.025003)
25. Hidding et al. 2014. Tunable electron multibunch production in plasma wakefield accelerators. arXiv:1403.1109
26. Manahan GG. et al. 2016. Hot spots and dark current in advanced plasma wakefield accelerators. *Phys. Rev. Accel. Beams.* **19**, 011303. (doi: 10.1103/PhysRevAccelBeams.19.011303)
27. Hidding B. et al. 2017. First measurements of Trojan Horse injection in a plasma wakefield accelerator. *Proc. Of IPAC 2017*. 1252-1257.
28. Xu, XL. et al. 2014. Phase-space dynamics of ionization injection in plasma-based accelerators. *Phys. Rev. Lett.* **112**, 035003. (doi: 10.1103/PhysRevLett.112.035003)
29. Oron D., Tal E. and Silberberg Y. 2005. Scanningless depth-resolved microscopy. *Opt. Exp.* **13**, 1468. (doi: 10.1364/OPEX.13.001468)
30. Durst ME., Zhu G. and Xu C. 2006. Simultaneous spatial and temporal focusing for axial scanning. *Opt. Exp.* **14**, 12243-12254 (doi: 10.1364/OE.14.012243)
31. Durst ME., Zhu G. and Xu C. 2007. Simultaneous spatial and temporal focusing in nonlinear microscopy. *Opt. Commun.* **281**, 1796-1805. (doi: 10.1016/j.optcom.2007.05.071)
32. Block E. et al. 2013. Simultaneous spatial and temporal focusing for tissue ablation. *Biomed. Opt. Exp.* **4**, 831-841. (doi: 10.1364/BOE.4.000831)
33. Kammel R. e al. 2014. Enhancing precision in fs-laser material processing by simultaneous spatial and temporal focusing. *Light: Science & Applications.* **3**, e169. (doi: 10.1038/lsa.2014.50)
34. Bourgeois N., Cowley J. and Hooker SM. 2013. Two-pulse ionization injection into quasilinear laser wakefields. *Phys. Rev. Lett.* **111**, 155004. (doi: 10.1103/PhysRevLett.111.155004)
35. Durfee CG. et al. 2012. Intuitive analysis of space-time focusing with double-ABCD calculation. *Opt. Exp.* **20**, 14244. (doi: 10.1364/OE.20.014244)
36. Nieter, C. and Cary, J.R. 2004. VORPAL: A versatile plasma simulation code. *J. Comp. Physics*. **196**. 448-478. (doi: 10.1016/j.jcp.2003.11.004)
37. Di Mitri S. 2015. On the importance of electron beam brightness in high gain free electron lasers. *Photonics*. **2**, 317-341. (doi: 10.3390/photonics2020317)
38. Emma P. and Raubenhemier T. 2001. Systematic approach to damping ring design. *Phys. Rev. Accel. Beams.* **4**, 021001. (doi: 0.1103/PhysRevSTAB.4.021001)
Manahan GG. et al. 2017. Single-stage plasma-based correlated energy spread compensation for ultrahigh 6D brightness electron beams. *Nat. Commun*. **8**, 15705. (doi: https://doi.org/10.1038/ncomms15705)

Appendix B
FPS2019/46 Plasma Physics Conference - Poster

Parametric Tolerance Study of Trojan Horse plasma wakefield acceleration scheme

R. Altuijri[1, 2, 3], P. Scherkl[2,3], T. Heinemann[2,3], A.F. Habib[2,3], A. Hala[4] and B. Hidding[2, 3]

1 Physics Department, Faculty of Science, Princess Nora Bint AbdUlrahman University, Riyadh, KSA.
2 Physics Department, Faculty of Science, Strathclyde University, Glasgow, UK.
3 Cockcroft Institute, Sci-Tech Daresbury, Keckwick Lane, Daresbury, Cheshire WA4 4AD, UK.
4 King Abdulaziz City for Science and Technology-KACST, Riyadh, KSA.

Introduction

A promising scheme for plasma wakefield acceleration is the hybrid plasma acceleration mechanism, which is experimentally connected to world-wide programs at various accelerator facilities. This scheme may lead to extremely high quality electron bunches, which can be used to drive ultrabright light sources such as free electron lasers. The big challenge for plasma acceleration is to produce electron bunches with high quality in terms of low emittance, energy spread and high brightness. To overcome this challenge, the Trojan Horse scheme [1,2,3,4] is used for production of designer electron beams.

Motivation

This work explores the Trojan Horse mechanism in a parametric study by variation of the injector laser pulse by intensity, spot size and relative spatiotemporal synchronization and alignment. These parameters define output electron witness beam parameters and its quality. This sensitivity study shows a high robustness of the scheme, which is promising for a wider key prospect of the approach, namely the development of compact plasma accelerators to produce electron beams with unprecedented emittance and brightness in order to power free electron lasers.

Methodology

The method used to produce the bunches is as follows:

- Change some parameters on the input file of Vsim code then do the simulation.
- Analysis of the output files through PicViz program to know the results of beam parameters such as charge, energy, energy spread, emittance, brightness and current.
- Plot the evolution of the parameters over simulation length via PicViz and Matlab.
- Discuss the quality of the bunch that is produced and its suitability for the application to build FEL's.

Results

The background of blowout was fixed and parameters related to the laser pulse was changed. Two parameters were changed, these are the spot size w_0 and intensity a_0 for laser pulse, before applied matching condition [5] ($r^2_{matched} = \varepsilon_n * \sqrt{2} / (\omega p/c) / \sqrt{\gamma p}$) and after applied, which is an important part on plasma wakefield accelerator is the stability of the driver beam propagation inside blowout by applied the beam matching through its propagated with a constant radius.

First, a_0 was fixed and the value of w_0 was changed many, where it affected on the quality of the witness beam as shown in Figure 1 when we plot the evolution of the transverse emittance, brightness and mean energy during propagation. From scans, the emittance growth with increasing spot size is observed in the both cases from w_0 = 7 μm to w_0 = 19 μm, but after matching through its propagated the values are close together. On the otherhand, the witness beam has high mean energy after matching.

After that, a_0 was changed and w_0 was fixed. It's clear how this change affects on the values of emittance and brightness. The brightness increases as the laser intensity increases from a_0 = 0.016 to a_0 = 0.019 due to a strongly increased current caused by higher charge being released as laser intensity increases. Nevertheless the emittance decreases as laser intensity increases, in addition the mean energy decrease. This is depicted in Figure 2 for both cases.

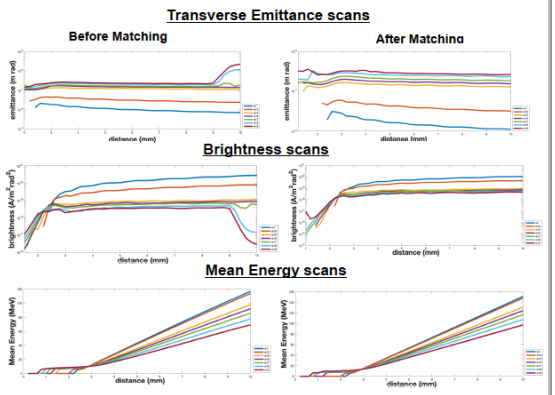

Figure 1: Parameters evolution of the witness bunch during propagation when we change w_0 and fixed a_0.

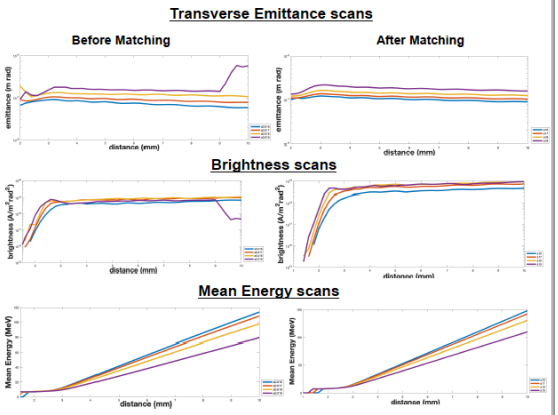

Figure 2: Parameters evolution of the witness bunch during propagation when we change a_0 and fixed w_0.

Conclusion

The laser pulse must be adjust accurately due to the quality of witness bunch strongly depends on the properties of laser pulse such as laser spot size and laser intensity. In addition, to power FEL via produced beams through Trojan Horse technique.

References

[1] Rosenzweig, T. Königstein, D. Schiller, and D. L. Bruhwiler, Phys. Rev. Lett. 108, 035 001(2012).
[2] Y. Xi, B. Hidding, D. Bruhwiler, G. Pretzler, and J. B. Rosenzweig, Phys. Rev. ST Accel. Beams 16, 031 303(2013).
[3] B. Hidding, G. Manahan, O. Karger, A. Knetsch, G. Wittig, D. Jaroszynski, et al., Journal of Physics B: Atomic,Molecular and Optical Physics 47, 234010 (2014).
[4] G.G. Manahan, A.F. Habib, P. Scherkl, et al., Nat. Commun. 8, 15705 (2017).
[5] K. A. Marsh, C. E. Clayton, et al., Proceedings of 2005 Particle Accelerator Conference, pages 2702-2704, IEEE, 2005.

Appendix C
Paper 2

Plasma Wakefield Accelerator Driven Coherent Spontaneous Emission from an Energy Chirped Electron Pulse

B.M. Alotaibi[1,2], R. Altuijri[1,2], A. F. Habib[1,3], A. Hala[6], B. Hidding[1,3], Sh.M. Khalil[5], B.W.J. M^{c}Neil[1,3], P. Traczykowski[1,3,4]

[1] SUPA, Department of Physics, University of Strathclyde, Glasgow, G4 0NG
[2] Physics Department, Faculty of Science, Princess Nourah Bint Abdulrahman University, Riyadh, KSA
[3] Cockcroft Institute, Warrington, WA4 4AD, UK
[4]ASTeC, STFC Daresbury Laboratory, Warrington, WA4 4AD, UK
[5] Plasma Physics and Nuclear Fusion Department, NRC, Atomic Energy Authority, Cairo, Egypt
[6] King Abdulaziz City for Science and Technology-KACST, Riyadh, KSA

Abstract. Plasma accelerators [1] are a potentially important source of high energy, low emittance electron beams with high peak currents generated within a relatively short distance. As such, they may have an important application in the driving of coherent light sources such as the Free Electron Laser (FEL) which operate into the X-ray region [2]. While novel plasma photocathodes [3] may offer orders of magnitude improvement to the normalized emittance and brightness of electron beams compared to Radio Frequency-driven accelerators, a substantial challenge is the energy spread and chirp of beams, which can make FEL operation impossible. In this paper it is shown that such an energy-chirped, ultrahigh brightness electron beam, with dynamically evolving current profile due to ballistic bunching at moderate energies, can generate significant coherent radiation output via the process of Coherent Spontaneous Emission (CSE) [4]. While this CSE is seen to cause some FEL-induced electron bunching at the radiation wavelength, the dynamic evolution of the energy chirped pulse dampens out any high-gain FEL interaction. This work may offer the prospect of a future plasma driven FEL operating in the high-gain Self Amplified CSE (SACSE) mode.

Keywords: Plasma Accelerator, Plasma Photocathode, Free Electron Laser, Coherent Spontaneous Emission
Submitted to: *New J. Phys.*

1. Introduction

Free electron lasers (FELs) are sources of high-power coherent radiation, tunable over a wide range of the electromagnetic spectrum from the far-infrared into the hard X-ray. FELs operating at the shorter wavelengths are unique sources, beyond the reach of current conventional lasers, that open up new areas of scientific exploration in diverse fields of study from the creation of warm dense matter to structural and functional biology [5].

Short wavelength FELs consists of a relativistic electron beam propagated through an oscillatory magnetic field called an undulator. The oscillating electron beam emits spontaneous synchrotron radiation at the resonant radiation wavelength given by:

$$\lambda_\mathrm{r} = \frac{\lambda_\mathrm{u}}{2\gamma^2}(1 + \bar{a}_\mathrm{u}^2), \tag{1}$$

where λ_u is the undulator period, γ is the Lorentz factor of the electron beam and $\bar{a}_\mathrm{u}$ is the RMS undulator parameter [2]. The oscillating electrons interact cooperatively via this common radiation field and begin to spatially bunch at the resonant radiation wavelength. This cooperative instability results in an exponential growth of the coherent emission process known as Self Amplified Spontaneous Emission (SASE) [2, 6, 7].

In this cooperative, high-gain regime of FEL operation, a simplified analysis shows that the radiation power increases as $P(z) \approx P_0 \exp(\sqrt{3}z/l_\mathrm{g})$ along the z-axis of the undulator, where $l_\mathrm{g} = \lambda_\mathrm{u}/4\pi\rho$ is the 1D gain length and ρ is the FEL or Pierce parameter [2, 6, 7]. Typically $\rho \sim 10^{-3} - 10^{-4}$ for short wavelength FELs. The FEL parameter also gives an estimate of the energy extraction efficiency from the electron beam to the radiation [2, 6, 7].

Short wavelength FELs are currently powered by up to kilometre size radio-frequency (RF) driven accelerators. These RF-based accelerators offer high quality electron beams necessary for operation with a typical normalised emittance of $\epsilon_\mathrm{n} \sim 0.1 - 1\pi\,\mathrm{mm\,mrad}$; bunch charges of $Q \sim 10\,\mathrm{pC} - 1\,\mathrm{nC}$ and with sufficiently small energy spreads σ_γ, which satisfy the energy spread criterion $\sigma_\gamma/\gamma < \rho$ required for FEL operation [2, 6, 7]. Further, the electron beam has to meet the emittance condition $\epsilon_\mathrm{n} \lesssim \gamma\lambda_\mathrm{r}/4\pi$ [8, 6]. Plasma wakefield-based acceleration technologies can sustain much larger accelerating gradients, of the order of tens of GV/m, compared to conventional RF-linacs [9]. This is a promising approach driven either by a highly intense laser pulse [10, 11, 12], a relativistic charged particle beam [13, 14, 15] or a combination of both [16], exciting large-amplitude non-linear plasma wave. The electric field inside the non-linear plasma wave is approximated by the non-relativistic wave breaking field $E_0(\mathrm{Vm^{-1}}) \approx 96\sqrt{n_\mathrm{e}(\mathrm{cm^{-3}})}$, where n_e is the electron density of the ambient plasma. For example, for typical plasma density of $n_\mathrm{e} = 10^{17}\,\mathrm{cm^{-3}}$ this will result in electric fields of the order of $30\,\mathrm{GVm^{-1}}$. This allows reducing the footprint of the accelerating structure from kilometre to few centimetre scale and, in principle, opens the prospect of university laboratory scale FELs.

In the past years, significant effort have been dedicated to demonstrate plasma-

based accelerators driven FEL [17, 18]. Recently, the demonstration of spontaneous undulator radiation in the soft X-ray regime driven by a plasma-based accelerator are shown in [19]. However, next to stability challenges, the inherent by-product of plasma-based accelerators is a comparably large energy spread as result of correlated energy spread ('chirp'), slice energy spread ($\sigma_\gamma/\gamma > \rho$), and similar emittance limits as in state-of-the-art linacs. While plasma-based accelerators inherently produce short bunches of the few femtosecond scale and large, kA-scale currents, in combination, the energy spread and emittance limits impose limits on the 5D and 6D brightness, and hence the x-ray wavelength and gain obtainable from such accelerators. While several methods have been proposed for mitigating the limitations of plasma wakefield accelerators [20, 21, 22, 23], some of which utilise energy chirped beams [24, 25], ultimately it would be desirable to produce electron beams with emittance and energy spread improved substantially.

The plasma photocathode approach [3, 29, 28] is a method which has been developed to address and overcome these limitations. It is based on tunneling ionization of a higher ionization threshold gas or component in the plasma by a focused laser pulse directly within the plasma wave. This 'plasma photocathode' can be realized within electron-beam driven plasma wakefield accelerators (PWFA) as well as, in principle, in laser-driven plasma wakefield accelerators (LWFA). PWFA-based plasma photocathodes combine intrinsic advantages of PWFA such as dark-current-free and phase-constant operation and long acceleration lengths with far-reaching decoupling between the plasma medium which supports the wakefield (e.g. hydrogen) and the one supporting the plasma photocathode medium (e.g. helium). In this approach, an electron driver beam sets up a hydrogen-based plasma wave and its characteristic and co-moving 'bubble'-like structure, while a spatiotemporally synchronized laser pulse is focused inside the bubble structure. The laser intensity is tuned such that it exceeds the tunneling ionization threshold of helium only around its focus, which is facilitated by the strongly nonlinear scaling ionization rates. This way, the laser pulse releases electrons locally confined directly within the hydrogen plasma bubble, and with negligible transverse residual momentum due to the relatively low intensities and ponderomotive potential of the plasma photocathode laser pulse. This leads to a dramatically confined initial transverse phase space and thus low emittance of the produced electron bunches. The multi-GV/m electric plasma wakefields then rapidly accelerate and compress the released helium electrons and mitigate space charge-related emittance growth. This allows production of electron bunches with ultralow normalised emittance ϵ_n and high-current I and thus ultrahigh 5D-brightness $B_{5D} = I_p/\epsilon_{n,x}\epsilon_{n,y}$, exceeding those obtainable from conventional accelerators by many orders of magnitude. In addition, methods are under development [26] which can further reduce the energy spread of bunches produced by plasma photocathodes via tailored beam-loading in phase-constant PWFA's, which promise to decrease the energy chirp substantially, thus nurturing prospects for ultrahigh 6D-brightness electron beam production as drivers for next-generation light sources.

The driver electron beam employed to excite the hydrogen PWFA based accelerator

structure in which the central plasma photocathode mechanism can be realized may come from a linac, but also may come from a compact laser wakefield accelerator, as many characteristics of LWFA electron beam output such as high current and charge density and modest energy spread and emittance are very favourable or at least not prohibitive for driving a PWFA stage [27, 29]. The intrinsic synchronization of the plasma photocathode laser pulse with the laser pulse-generated electron beam drive beam is an explicit advantage of this compact, all-optical solution [27, 29].

In this paper, the dynamics of a fs-scale and nm-Rad normalised emittance electron bunch from a plasma photocathode with natural negative energy chirp and at 250 MeV electron energies is explored. Such a bunch combines ultrahigh (slice) brightness, which implies strong gain characteristics, with dispersive compression due to a rotation in longitudinal phase space, which gives rise to a current spike. Previous studies have shown that an electron beam energy chirp can have both detrimental and beneficial effects upon the FEL interaction depending upon the gradient of the chirp [30, 31].

One effect, which to the authors' knowledge has not been modelled before with a PWFA plasma photocathode-generated energy chirped beam, is to induce the generation of Coherent Spontaneous Emission [4, 31]. CSE arises when the electron pulse has significant *current* gradients over a resonant radiation wavelength. It is shown that for the electron beam parameters used here, such current gradients can be realised when the energy chirped beam undergoes spatial dispersive compression in its propagation direction due to the correlated energy spread [4, 31]. CSE can have radiation power output orders of magnitude above normal spontaneous emission, and can therefore be a useful radiation source in its own right. By dominating any normal spontaneous emission, CSE can also self-seed the FEL interaction [32]. It has also been shown that CSE can help mitigate the effects of a homogeneous electron energy spread in beams without an energy chirp, significantly reducing the start-up time and enhancing the generation of high intensity, short, superradiant radiation pulses from a poor-quality electron pulse [33] .

2. Electron beam generation and acceleration PIC modelling

The PWFA stage and the subsequent controlled electron beam injection via the plasma photocathode method are modeled with the fully explicit 3D Particle-In-Cell (PIC) code VSim [34]. The simulation box, moving with the speed of light, consists of $109 \times 65 \times 65$ cells with one macroparticle per cell this leads to approximately 450 k of macroparticles modelling the background plasma. The size of the co-moving box is set to $345\,\mu\text{m} \times 205\,\mu\text{m} \times 205\,\mu\text{m}$ to accommodate the blowout structure. The PIC simulation runs for $t_{\text{sim}} = 4.6\,\text{ps}$ corresponding to $z_{\text{sim}} = t_{\text{sim}}c = 14\,\text{mm}$ of propagation distance. A bi-gaussian charge distribution driver beam of ultra-relativistic energy $W_{\text{d}} = 10\,\text{GeV}$ and relative energy spread of $\Delta W_{\text{rms,d}}/W_{\text{d}} = 2\,\%$ is shot into an uniformly distributed preionized hydrogen plasma of density $n_{\text{p}} = 4.95 \times 10^{16}\,\text{cm}^{-3}$ corresponding to a plasma wavelength of $\lambda_{\text{p}} = 2\pi c(m_{\text{e}}\varepsilon_0/n_{\text{p}}e^2)^{1/2} = 150\,\mu\text{m}$, where

c is the speed of light, m_e is the electron mass, e and ε_0 represent the electron charge and the vacuum permittivity, respectively. Driver beam charge is optimized to $Q_d = 800\,\mathrm{pC}$, and its longitudinal and transverse dimensions are matched to the plasma density with $\sigma_{z,d} = 20\,\mu\mathrm{m}$ and $\sigma_{(x,y),d} = 3.5\,\mu\mathrm{m}$, respectively, resulting in "cigar"-like electron beam of peak density $n_d = 1.3 \times 10^{18}\,\mathrm{cm}^{-3}$. This driver beam parameters are tailored to meet the blowout condition $n_d/n_p \gg 1$ and to excite a large amplitude plasma wave by expelling plasma electrons by means of its unipolar radial electric fields $E_r(r) = Q_d/(2\pi)^{3/2}\varepsilon_0\sigma_z r[1 - \exp(-r^2/2\sigma_r)]$ while keeping the heavy ions immobile. At the same time, the parameters are balanced towards dark-current-free PWFA operation such that the maximum radial electric field $E_{r,max} = 28\,\mathrm{GVm}^{-1}$ is below the tunnel-ionization threshold of the background helium gas of density $n_{He} = 1.5 \times 10^{17}\,\mathrm{cm}^{-3}$ [35]. A moderate intensity laser pulse trailing the driver beam at the distance $\Delta\xi = 115\,\mu\mathrm{m}$ with the normalized amplitude $a_0 = 0.018$, FWHM pulse duration $\tau_0 = 30\,\mathrm{fs}$, and rms spot size $w_0 = 7\,\mu\mathrm{m}$, reaches its focal position at $z_i = 2\,\mathrm{mm}$ where the laser pulse intensity is just above the tunnel-ionization threshold of the neutral helium. This results in localized ionization of helium gas directly inside the blowout cavity. The tunnel-ionized helium electrons are quickly accelerated to relativistic energies and are trapped inside the blowout structure. Note, that due to the moderate laser intensity the residual transverse momentum of the electrons is very small and combined with the confined ionization volume of the laser pulse the normalized emittances can be as low as nm rad.

Table 1: 3D PIC simulation PWFA driver beam and plasma photocathode laser parameters.

Driver parameters			**Photocathode laser parameters**		
Name	Symbol	Values	Name	Symbol	Values
Energy	W_d	10 GeV	Wavelength	λ_l	800 nm
Rel. energy spread	$\Delta W_{rms,d}/W$	2 %	Laser amplitude	a_0	0.018
RMS bunch length	$\sigma_{z,d}$	20 μm	Pulse duration	τ_0	30 fs
RMS bunch width	$\sigma_{x,y,d}$	3.5 μm	RMS spot size	w_0	7 μm
Norm. emittance	$\epsilon_{n,d}$	50 μm	Laser position	ξ_i	200 μm
Charge	Q_d	800 pC	Focal position	z_i	2 mm

Fig. 1 shows PIC results of a dephasing-free plasma wakefield excited by an ultra-relativistic driver beam (green dots) with a peak current $I_{pk,d} \approx 4.5\,\mathrm{kA}$. The solid black line represents the on-axis accelerating electric field with maximum accelerating field $E_{z,max} = -24\,\mathrm{GVm}^{-1}$ at the rare of the blowout. The solid blue line is the corresponding electrostatic wake potential in units of electronic rest energy ($em_e^{-1}c^{-2}$). The transparent blue filling indicates the trapping potential which has to satisfy the trapping condition $\Delta\Psi < -1$ to support trapping of the released electrons inside the blowout structure. In (left) the laser pulse (not shown here) just released helium electrons via the plasma photocathode method at the co-moving position ξ_i =200 μm at the trapping potential

minimum $\Delta\Psi_{\min}$. This is a preferable position to obtain highest trapping efficiency due to the deep potential. The electrons are velocity bunching and are in the process of forming an electron bunch ("witness beam"). In (right) the witness beam of charge $Q_{\rm w} = 3.6\,{\rm pC}$ is accelerated to mean energy of $W_{\rm w} \approx 247\,{\rm MeV}$ after an acceleration distance of $\Delta z = 12\,{\rm mm}$. The projected normalized emittance of the witness beam is $\epsilon_n = 21\,{\rm nm\,rad}$ combined with the peak current of $I_{\rm pk,w} \approx 1.5\,{\rm kA}$ this results in 5D brightness of $B_{\rm 5D} \approx 6.8\times10^{18}\,{\rm A/m^2/rad^2}$. The driver beam and injector laser parameters are summarize in Table 1 and output witness beam characteristics are highlighted in Table 2.

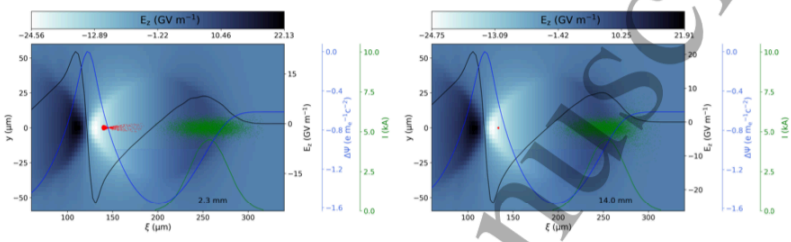

Figure 1: 3D PIC simulation of the plasma photocathode beam-driven wakefield acceleration. The green and red dots show drive and witness beam, respectively. The color map represents the accelerating gradient E_z while the solid black line is the electric field on-axis and the solid blue line represents the electrostatic trapping potential $\Delta\Psi$. In (left) witness beam tapping process is shown at $z = 2.3\,{\rm mm}$ while in (right) the witness beam is trapped and already accelerated to the final energy.

Table 2: Projected witness beam parameters from the 3D PIC simulation at the end of the acceleration $z = 14\,{\rm mm}$.

Name	Symbol	Values
Energy	$W_{\rm w}$	247.3 MeV
Lorentz factor	γ	483.9
Total energy spread	$\Delta\gamma/\gamma$	3 %
Slice energy spread	σ_γ/γ	0.3 %
Normalised emittance	$\epsilon_{\rm n,w}$	21 nm rad
RMS bunch length	$\sigma_{\rm w}$	0.26 μm
Bunch charge	$Q_{\rm w}$	3.6 pC
Peak current	$I_{\rm pk,w}$	1.5 kA
5D Brightness	$B_{\rm 5D}$	$6.8 \times 10^{18}\,{\rm A/m^2/rad^2}$

The macroparticle distribution from the VSim PWFA simulation has too sparse a phase-space distribution for accurate FEL simulation (it does not have enough

macroparticles per resonant wavelength and it has unknown shot-noise statistics) e.g. with Puffin. It also has different format and units, and must hence be converted into suitable format and units of microparticles, for which the conversion script of [36] was used. The beam of macroparticles from VSim is 'up-sampled' to create a beam with a greater number of microparticles which have the correct shot-noise statistics as an equivalent beam of real electrons. The method of [37] uses cumulative distribution function approach together with an optional smoothing function to obtain such a beam of microparticles. The relevant parameters of the beam of microparticles are compared to the original beam of macroparticles from the VSim simulation in Fig. 2 (dashed). Here, key bunch characteristics such as normalised emittance ϵ_{n}, Lorentz factor γ, slice energy spread σ_γ and current I are plotted versus the co-moving coordinate $z_2 = ct - z$, such that the electron beam head is on the left and the electron beam tail is on the right in this figure. The microparticle distribution has also had the correct shot-noise statistics applied as described in [39]. This beam of microparticles can now be used to simulate longitudinal phase space rotation, self-seeding and radiation output via CSE using the Puffin simulation code.

A particularly prominent signature of the plasma photocathode-generated electron bunch are its very low normalized slice emittance ϵ_{n} around 10 nm rad throughout the electron beam (top panel). The beam further has a slice current exceeding 1 kA (bottom panel), and an average RMS slice energy width of $\sigma_\gamma \approx 1.5$ (third panel), and a corresponding relative slice energy spread of $\sigma_\gamma/\gamma \approx 0.3\%$. As can be seen in the second panel of Fig. 2, the electron beam exhibits a negative longitudinal energy chirp, which is the natural result of the beam being accelerated in the linear electric field of the strongly nonlinear plasma wave.

While the benefits of ultralow emittance and ultrahigh brightness electron beams for radiation generation are huge, such beams constitute a particularly demanding challenge for extraction of beams from the plasma stage without emittance degradation and the transport line towards applications such as an undulator. A concept to remove the energy chirp of beams from the plasma photocathode mechanism in one and the same plasma stage via beam loading with a second electron beam population and further acceleration has recently been proposed [26], and experimental efforts to demonstrate the feasibility of this approach, as well as suitable beam extraction and transport designs are under development and corresponding start-to-end simulations are subject of a different work. Nevertheless, the energy chirp may artificially removed and the FEL energy spread condition for lasing, $\sigma_\gamma/\gamma \lesssim \rho$ is satisfied providing estimates of suitable undulator parameters, enabling calculation of saturation length and power using the 3D analytic approximation of Ming Xie [40, 41]. Fig. 3 shows the result of such artificial dechirping assuming no resultant increase in the slice energy spread.

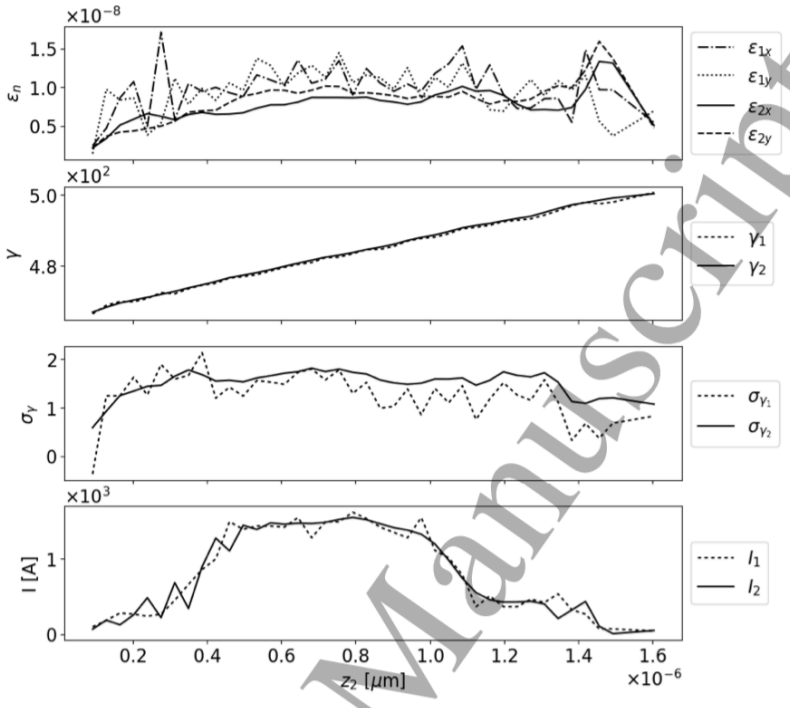

Figure 2: From top, the electron beam normalised emittance ϵ_n, localised Lorentz factor γ, RMS energy spread σ_γ and current I, as a function of window position $z_2 = (ct - z)$ of the beam. In this window, travelling at speed c along the z-axis of the undulator, the head of the electron bunch is on the right, the tail on the left, and the beam will propagate to larger values of z_2 as the beam propagates through the undulator. The dashed plots (index 1) show the original macroparticle beam from the VSim simulation and the solid plots (index 2) show the beam following smoothing and up-sampling to a greater number of microparticles with the correct shot-noise statistics.

3. Unaveraged FEL simulation

There are many codes available to design and simulate FEL operation [42, 43, 44, 45]. Here, the unaveraged 3D FEL simulation code Puffin is used [46, 47]. In addition to the FEL interaction, Puffin is able to model the effects of the macroscopic electron beam changes due to (correlated) electron beam energy and any CSE and Self Amplified CSE (SACSE) that may arise. First, suitable undulator parameters are chosen and FEL saturated power and undulator length estimates are also made for an electron

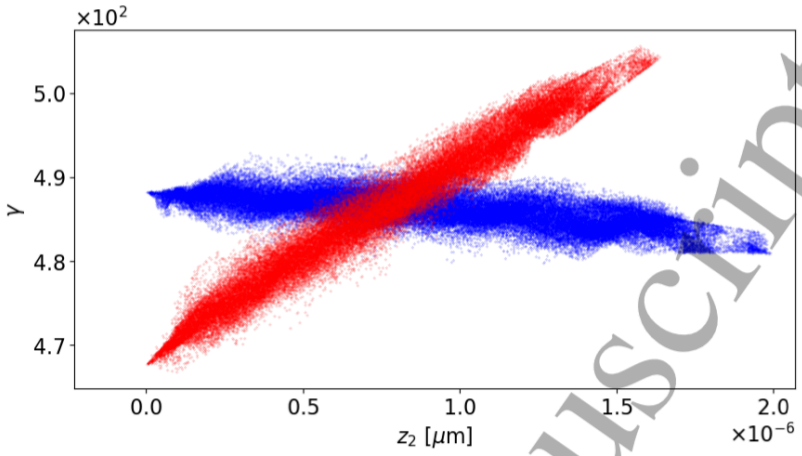

Figure 3: Shown in red is the accelerator electron beam phase-space output: Lorentz factor γ as a function of position z_2 within the beam. The beam propagates along the positive z-axis. Also shown (blue) is the electron beam with the energy chirp artificially removed.

beam with no energy chirp in the steady state regime using the analytical Ming Xie formalism [40, 41].

3.1. Analytical parameter study without beam energy chirp

In order to choose a suitable set of undulator parameters before any full simulation using Puffin and to estimate FEL performance from a hypothetical beam without an energy chirp for steady state (no pulse effects) FEL operation, the Ming Xie formalism of [40, 41] was used to vary the planar undulator period λ_u and undulator parameter a_u. The parameters of Table 3 were used as estimates of the unchirped parameters of Fig. 2. The estimated FEL saturation power and length in this steady state regime are plotted in Fig. 4.

The undulator parameters chosen for the full simulations were $\lambda_u = 0.015$m and $a_u = 1.0$. With these values, the radiation wavelength is $\lambda_r \approx 67$nm and the FEL parameter at peak current is $\rho = 0.021$. Given that the average RMS slice energy spread is $\sigma_\gamma/\gamma \approx 3 \times 10^{-3}$ the energy spread condition for FEL lasing of $\sigma_\gamma/\gamma \lesssim \rho$ is well satisfied in the absence of an energy chirp. The steady state, Self Amplified Spontaneous Emission (SASE) saturation length is then approximated as $L_{sat} \approx 1.4$m and saturation power $P_{sat} \approx 2.2$GW.

The electron bunch does not, however, conform to the steady-state approximation as it is only ~ 6 cooperation lengths long, where the cooperation length $l_c = \lambda_r/4\pi\rho$ [48].

This relatively short electron pulse length will result in the output of short, single pulses, at saturation. This type of short pulse operation is in the weak superradiant regime of FEL operation [48] and also results in reduced saturation powers from that of the steady-state, Ming Xie approximation above.

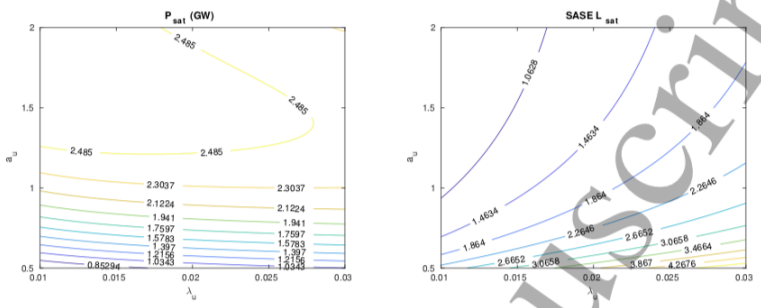

Figure 4: Contour plots of the saturated power P_{sat} (left) and the saturation length L_{sat} (right) as a function of λ_u and a_u using the electron beam parameters of Table 3

.

3.2. Numerical simulation with an energy chirped beam

The Puffin simulation uses the energy chirped electron bunch distribution output from the PWFA as shown in Fig. 3. As discussed above, the macroparticle output from the VSim accelerator modelling was first up-sampled to generate an equivalent distribution of a greater number of microparticles with the correct shot-noise statistics. The beam of microparticles was matched to the natural focusing channel of the undulator lattice chosen for the simulation as above using the method of [38].

It is seen from the parameters of the chirped pulse, plotted in Fig. 2, that the electron pulse generated by the PWFA has a length of $l_e \approx 24\lambda_r \approx 6l_c$ and has a negative energy chirp in z (positive energy chirp in z_2). During propagation through

Table 3: The approximate output parameters from the PWFA used for the Ming Xie formalism parameter estimates.

Parameter	Value
Peak current I_{pk}	1500 A
Normalised emittance	0.01 mm mrad
Bunch Lorentz factor (γ)	486
RMS energy spread	0.3%
Bunch charge	3.6 pC

the undulator, dispersion will cause this short, energy chirped electron bunch to self-compress longitudinally due to rotation in longitudinal phase space, which is significant at these comparatively low energies, and it may even 'flip over' in longitudinal phase space [4]. During this process, the electron bunch length may approach that of the resonant wavelength ($l_e \sim \lambda_r$) and consequently would be expected to radiate significant CSE. Note that this CSE is not due to the FEL interaction and can only be modelled using un-averaged FEL simulation codes such as Puffin.

In what follows the CSE generation due to energy chirped bunch shortening and any FEL processes were modelled self-consistently. It should be noted that the FEL interaction may also amplify CSE in addition to the spontaneous emission due to electron beam shot-noise in a process called Self Amplified Coherent Spontaneous Emission (SACSE) [32]. As with SASE, given the large energy chirp here, any SACSE process would be expected to be significantly affected.

The electron longitudinal phase space evolution and the corresponding transverse radiation intensities are plotted for different positions through the undulator in Figs. 5,6. The energy of the radiation pulse as a function of distance through the undulator is shown in Fig. 7. Also shown is the spontaneous radiation emitted by the electron bunch without any FEL interaction – i.e. the radiation from both shot-noise and CSE, for both the chirped and un-chirped bunches of Fig. 3. The corresponding average bunching parameters $|\bar{b}|$, for both the chirped and un-chirped electron pulses are shown in Fig. 8. The radiation pulse 'instantaneous' power (i.e. unaveraged over a radiation wavelength [46]) and electron bunching parameter $|b|$ at saturation, is shown in Fig. 9 as a function of local position z_2.

It is seen from the electron phase space of Figs. 5,6 that the electron energy chirp causes the electron bunch to longitudinally compress in phase space and shorten as it propagates through the undulator. At saturation, $z = 1.95$m, the electron bunch is only ~ 9 resonant radiation wavelengths long.

In what follows, the FEL interaction can be 'switched off' in the Puffin simulation by artificially de-coupling the electrons from the radiation field. The electrons then only emit spontaneous emission due to both shot-noise and CSE.

The radiation energy growth from the chirped electron pulse, both with and without the FEL interaction, is shown in Fig. 7. The growth is not exponential but has a growth which is proportional to $\sim z^2$, more consistent with CSE [4]. That the radiation energy emitted in the absence of the FEL interaction is similar to that with the FEL interaction, confirms that the emission in both cases arises mainly from CSE. Also plotted is the radiation energy emitted from the electron pulse in the absence of any energy chirp. Here, there is no shortening of the electron pulse and the CSE emission is greatly reduced. In fact, the energy growth is quasi-linear with distance z through the undulator, consistent with incoherent spontaneous emission due to shot-noise only.

The evolution of the mean electron bunching parameter $|\bar{b}|$ of Fig. 8 increases quasi-linearly with distance through the undulator until $z \approx 1.2$. This is in broad agreement with the increased bunching due to the dispersive shortening of the electron pulse which

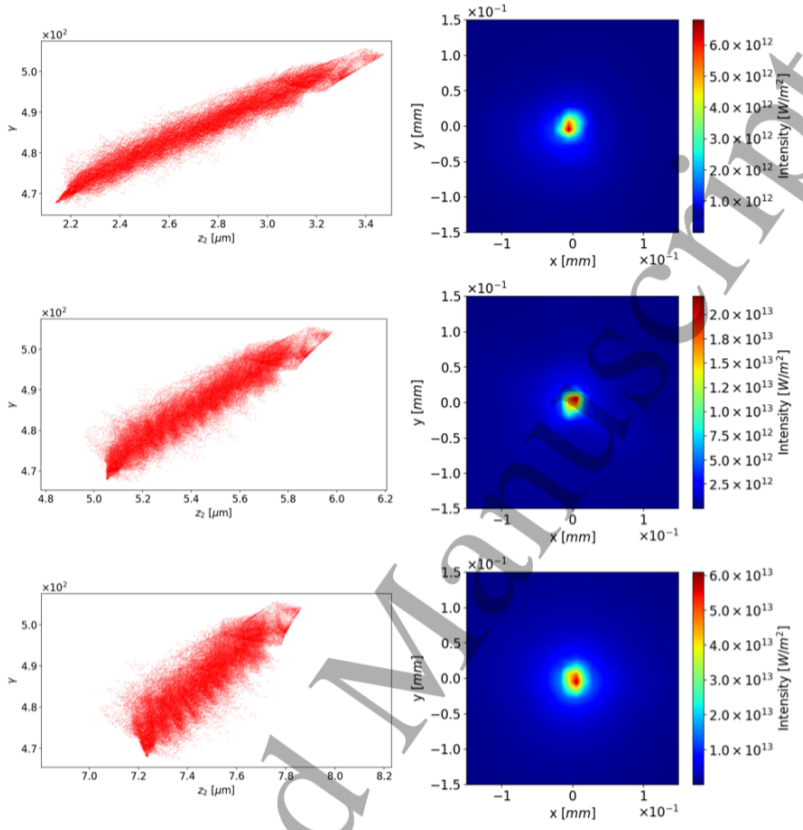

Figure 5: The electron beam longitudinal phase space (γ, z_2) and the corresponding transverse intensity, averaged over the pulse length, at 5 different positions along the undulator: $z = 0.45$, $z = 1.05$ and $z = 1.50$. The initial energy chirp at $z = 0$ is seen to cause the electron pulse to compress and then will decompress longitudinally.

causes significant current gradients with respect to the radiation wavelength. It is this type of bunching which drives the Coherent Spontaneous Emission [4] and which may act as a self-generated seed field which can be amplified as SACSE [32, 33]. Also plotted is the electron bunching of the electron pulse in the absence of any energy chirp. As described above, there is no shortening of the electron pulse and the bunching remains approximately constant and at a much smaller value, mainly due to shot-noise, than when the pulse shortens and significant current gradients occur at the radiation wavelength scale.

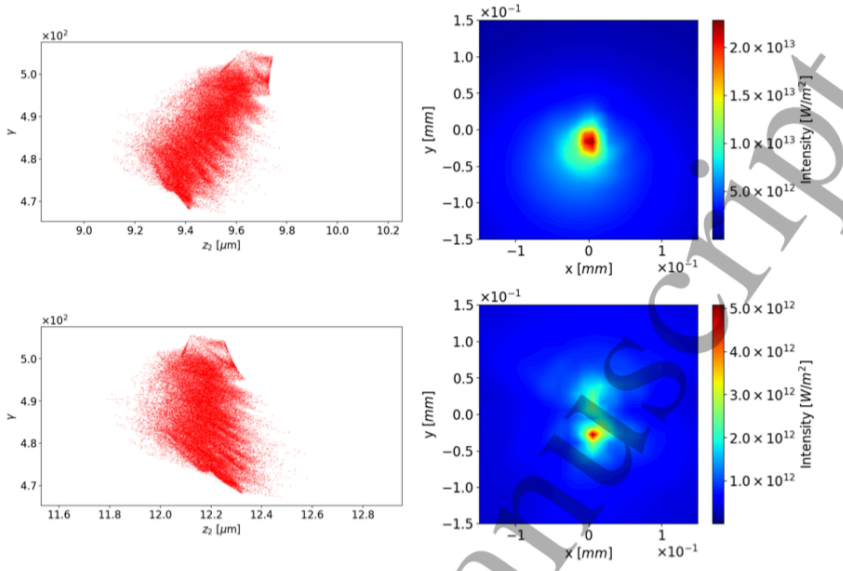

Figure 6: The electron beam longitudinal phase space (γ, z_2) and the corresponding transverse intensity, averaged over the pulse length, at 5 different positions along the undulator: $z = z_{sat} = 1.95$ and $z = 2.55$ m. The initial energy chirp at $z = 0$ is seen to cause the electron pulse to compress and then will decompress longitudinally.

The differences of the radiation emission and electron bunching, between the spontaneous-only case, when the FEL interaction is switched off, and that where the FEL interaction is included in the simulation, can be attributed to a small additional bunching due to SACSE. Some small periodic bunching about the radiation wavelength $\lambda_r \approx 67$nm due to SACSE, can be seen from Figs. 5,6 in the evolution of the electron phase-space through the undulator. The lack of any significant FEL gain is consistent with the work of [30] where for negative values of their chirp parameter $\hat{\alpha}$, here $\hat{\alpha} \approx -2$ at $z = 0$, FEL power output is greatly reduced from that expected from an un-chirped beam. So while some increased bunching is evident due to the FEL interaction between radiation and electrons, it is not operating in the collective, high-gain mode, significantly reducing the power emitted. Following the minimum of its length, the electron bunch continues to disperse as it propagates through the undulator, flipping over in phase space and indeed re-absorbing some of the emitted radiation and is consistent with that of previous simplified models [4].

Fig. 9 plots both the radiation power and electron bunching as a function of local position at saturation. It is seen that the electron pulse bunching, corresponding to the electron pulse at saturation of Figs. 5,6, is within a small local interval around

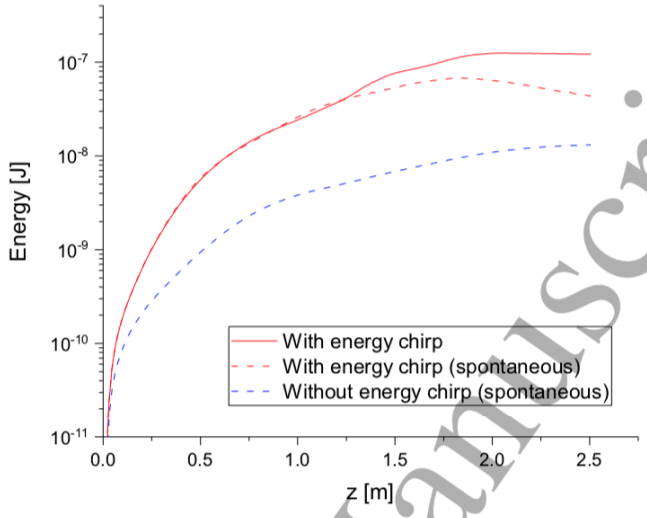

Figure 7: Radiation energy as a function of distance z through the undulator. Two of the plots (red) are for the chirped pulse including (solid) the FEL interaction and (dashed) without the FEL interaction. The case without energy chirp or FEL interaction demonstrates an energy growth with a quasi-linear dependence with z, corresponding to shot-noise spontaneous emission without significant CSE contribution.

$z \sim 9.5\mu$m. The radiation pulse power for $z_2 < 9.5\mu$m has propagated ahead of the electron bunch and is propagating in vacuum.

Fig. 10 is the same simulation as for Fig.9, but with the FEL interaction switched off. The radiation is then that due to spontaneous radiation from shot-noise and CSE only. The difference in the power emitted between the two is then due to the FEL interaction as observed from the additional electron bunching of Figs. 8 and 5,6. The modest increase in output power demonstrates that the FEL is not, however, operating the in the high-gain regime.

4. Conclusion

Using a start-to-end approach, but without a detailed modelling of beam extraction and transport lattice modelled between PWFA and FEL input, PWFA driven FEL interaction was studied numerically using a 3D model. The PWFA electron pulse output had a significant quasi-linear energy chirp. For the beam energy used here,

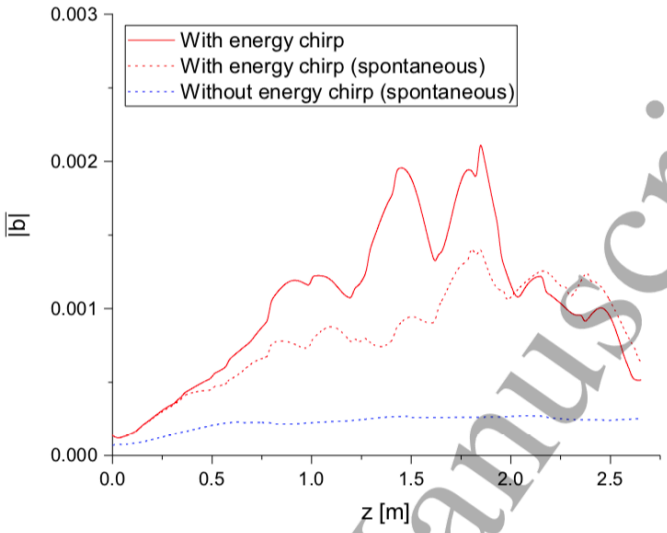

Figure 8: Average bunching parameter evolution for the electron pulse as a function of distance through the undulator both with (solid red) and without (dashed red) the FEL interaction. Also shown is the average bunching for the case of no energy chirp (dashed blue).

this chirp causes the electron pulse to shorten as it propagates through the undulator and emit significant CSE power. This CSE was seen to drive the electrons to give some weak periodic bunching at the resonant radiation wavelength, but not to enter into a collective, high-gain regime where analysis in the steady-state regime (no pulse effects) predicts output powers approximately two orders of magnitude greater.

The dynamic shortening of the electron pulse and subsequent emission of CSE as it propagates through the undulator is an effect that has not previously been modelled in plasma accelerator driven FEL simulations. The resultant CSE seeding of the high gain FEL interaction (SACSE) is a mechanism that may prove useful to future plasma accelerator driven FEL designs. Methods to remove the electron beam energy chirp that would allow a PWFA FEL, are the subject of on-going research and, if possible, are expected to allow the high gain FEL interaction to develop, possibly in a SACSE mode of operation, and generate output of short coherent pulses of high power radiation.

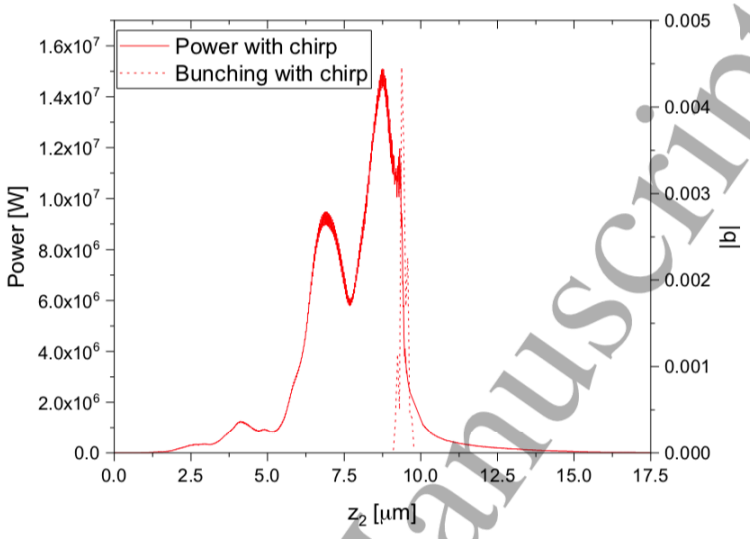

Figure 9: The radiation power profile (solid red) and the electron bunching parameter (dashed red) as a function of $z_2 = (ct - z)$ at $z = z_{sat} = 1.95$m through the undulator for the energy chirped case.

Acknowledgments

The authors wish to thanks to (i) King Abdullah University of Science and Technology (KAUST), http://kaust.edu.sa, and (ii) KAUST Supercomputing Laboratory (KSL) Thuwal, Saudi Arabia, for their help in offering access to SHAHEEN HPC facilities.
We gratefully acknowledge the support of STFC's ASTeC department for HPC access, using the STFC Hartree Centre; The Science and Technology Facilities Council Agreement Number 4163192 Release #3; and the John von Neumann Institute for Computing (NIC) on JUROPA at Jülich Supercomputing Centre (JSC), under project HHH20. This work used computational resources of the National Energy Research Scientific Computing Center (NERSC), which is supported by DOE DE-AC02-05CH11231.

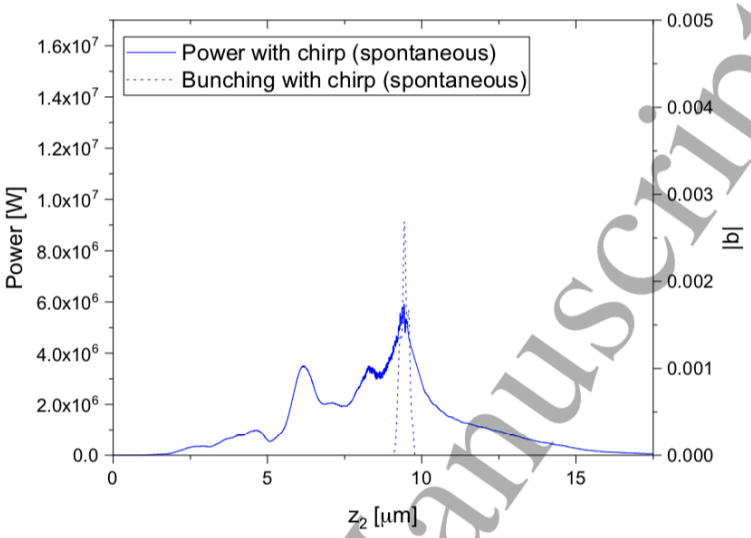

Figure 10: As Fig. 9, but with no FEL interaction (spontaneous only.) The radiation power profile (solid blue) and the electron bunching parameter (dashed blue) as a function of $z_2 = (ct - z)$ at $z = z_{sat} = 1.95$m through the undulator for the energy chirped case.

References

[1] Esary E et al 2009 *Rev. Mod. Phys.* **81** 1229
[2] McNeil B W J and Thompson N R 2010 *Nat. Photon.***4** 814-21
[3] Hidding B, et al 2012 *Phys. Rev. Lett.* **108** 035001
[4] Campbell L T and McNeil B W J 2012 *Proc. FEL2012 (Nara, Japan)*
[5] Seddon E A, Clarke J A, Dunning D J,Masciovecchio C, Milne C J, Parmigiani F, Rugg D, Spence J C H, Thompson N R, Ueda K 2017 *Rep. Prog. Phys.* **80** 115901
[6] Huang Z et al 2007 *Phys. Rev. ST Accel. Beams.* **10** 034801
[7] Bonifacio R et al 1984 *Opt. commun.* **50** 373
[8] Murphy J B and Pellegrini C et al 1985 *J. Opt. Soc. Am. B* **2** 259
[9] Tajima T and Dawson T M 1979 *Phys. Rev. Lett.* **43** 267
[10] Wang X et al 2013 *Nat. Commun.* **4** 1988
[11] Leemans WP et al 2014 *Phys. Rev. Lett.* **113** 245002
[12] Gonsalves AJ et al 2019 *Phys. Rev. Lett.* **122** 084801
[13] Rosenzweig J B, Breizman B, Katsouleas T, Su J J 1991 *Phys. Rev. A* **44** R6189R6192
[14] Blumenfeld I et al 2007 *Nature* **445** 741744
[15] Litos M et al 2014 *Nature* **515** 9295
[16] Walker PA et al 2017 *J. Phys.: Conf. Ser.* **874** 012029

[17] Huang Z et al 2012 *Phys. Rev. Lett.* **109** 204801.
[18] Schlenvoigt H P et al 2008 *Nat. Phys.* **4** 130133
[19] Pittman M et al 2002 *Appl. Phys. B* **74** 529
[20] Maier A R et al 2012 *Phys. Rev.* X **2** 031019.
[21] Seggebrock T, Maier A R, Dornmair I, and Grner F 2013 *Phys. Rev. ST Accel. Beams.* **16** 070703
[22] Couprie M E et al 2014 *J. Phys. B: At. Mol. Opt. Phys.* **47** 234001
[23] Loulergue A et al 2015 *New J. Phys.* **17** 023028.
[24] Campbell L T and Maier A R 2017 *New. J. Phys.* **19**, 033037
[25] Schroeder C B et al 2002 *Nucl. Instrum. Methods Phys. Res. A* **483** 89.
[26] Manahan G G, Habib A F and et al 2017 *Nat. Commun.* **8** 15705
[27] Hidding B et al 2010 *Phys. Rev. Lett.* **104** 195002
[28] Deng A, Karger O and et al 2019 *Nat.Phys.* accepted, arXiv:1907.00875v1
[29] Hidding B et al 2014 *J. Phys. B: At. Mol. Opt. Phys.***47** 234010
[30] Saldin E L et al 2006 *Phys. Rev. Special Topics Accel. Beams.* **9(5)** 050702.
[31] Henderson J R , Campbell L T, McNeil B W J 2014 *Proc. FEL2014 (Basel, Switzerland)* MOC04, 303-309
[32] McNeil B W J, Robb G R M and Jaroszynski D A 1999 *Opt. Commun.* **165** 65
[33] McNeil B W J, Robb G R M and Jaroszynski D A 2000 *Nucl. Inst .Meth. Phys. Res. A***445** 72–76
[34] Chet N and John R C 2004 *J. Comp. Phys.* **196** 448
[35] Manahan G G et al 2016 *Phys. Rev. Accel. Beams* **19** 011303
[36] https://github.com/UKFELs/FXFEL/
[37] https://github.com/UKFELs/JDF
[38] https://github.com/UKFELs/Paraffin
[39] McNeil B W J, Poole M W, and Robb G R M, 2003 *Phys. Rev. ST Accel. Beams.* **6** 070701.
[40] Xie M 1995 *Proc. the Particle Accelerator Conference 1995 (Geneva)*
[41] Xie M 2000 *Nucl. Instrum. and Methods Phys. Res. A* **445** 59
[42] Reiche S 1999 *Nucl. Instrum. Methods Phys. Res. A* **429** 243-8.
[43] Freund H P et al 2017 *New. J. Phys.* **19** 023020.
[44] Saldin E L et al 1999 *Nucl. Insrtum. Meth. Phys. Res. A* **429** 233.
[45] Fawley W M 2006 *Proc. FEL 2006(BESSY, Berlin, Germany)* pp 218-221
[46] Campbell L T and McNeil B W J 2012 *Phy. Plasmas.***19** 093119
[47] Campbell L T et al 2018 *Proc. IPAC2018 (Vancouver, BC, Canada)* THPMK112
[48] Bonifacio R, McNeil B W J and Pierini P 1989 *Phys. Rev. A* **40** 4467–4475

Appendix D
Paper 3

ISBN: 978-3-95450-210-3 doi:10.18429/JACoW-FEL2019-TUP051

PLASMA ACCELERATOR DRIVEN COHERENT SPONTANEOUS EMISSION

B.M. Alotaibi[1,2], R. Altuijri[1,2], A. F. Habib[2,3], B. Hidding[2,3], B.W.J. M^{c}Neil[2,3], P. Traczykowski[2,3]
[1]Physics Department, Faculty of Science,
Princess Nourah Bint Abdulrahman University, Riyadh, KSA
[2]SUPA, Department of Physics, University of Strathclyde, Glasgow, UK
[3]Cockcroft Institute, Warrington, UK

Abstract

Plasma accelerators [1] are a potentially important source of high energy, low emittance electron beams with high peak currents and generated within a relatively short distance. While novel plasma photocathodes [2] may offer improvement to the normalised emittance and brightness of electron beams compared to Radio Frequency-driven accelerators, a challenge is the energy spread and chirp of the beams, which can make FEL operation impossible. In this paper it is shown that such an energy-chirped beam, with a dynamically evolving current profile due to ballistic bunching, can generate significant coherent radiation output via the process of Coherent Spontaneous Emission (CSE) [3]. While this CSE is seen to cause some FEL-induced electron bunching at the radiation wavelength, the dynamic evolution of the energy chirped pulse dampens out any high-gain FEL interaction.

INTRODUCTION

Significant effort have been dedicated to demonstrating a plasma-based accelerator driven FEL [4–6]. However, next to stability challenges, the inherent by-product of plasma-based accelerators is a relatively large slice energy spread ($\sigma_\gamma/\gamma > \rho$) and a correlated energy spread ('chirp') when compared with RF linacs. In this paper, the dynamics of the electron bunch from a plasma photocathode [2], which can have an inherent negative energy chirp, is explored. One effect, which to the authors knowledge has not been modelled before with such a PWFA plasma photocathode-generated energy chirped beam, is to induce the generation of Coherent Spontaneous Emission (CSE) [3,7]. CSE arises when the electron pulse has significant *current* gradients over a resonant radiation wavelength. It is shown that for the electron beam parameters used here, such current gradients can be realised when the energy chirped beam undergoes spatial dispersive compression in its propagation direction due to the correlated energy spread [3,7]. By dominating any normal spontaneous emission, it has been shown in 1D simulations that CSE can also self-seed the FEL interaction in a process called Self Amplified Coherent Spontaneous Emission (SACSE) [8]. The CSE was also shown in 1D to help mitigate the effects of a homogeneous electron energy spread in beams without an energy chirp, significantly reducing the start-up time and enhancing the generation of high intensity, short, superradiant radiation pulses from a poor-quality electron pulse [9].

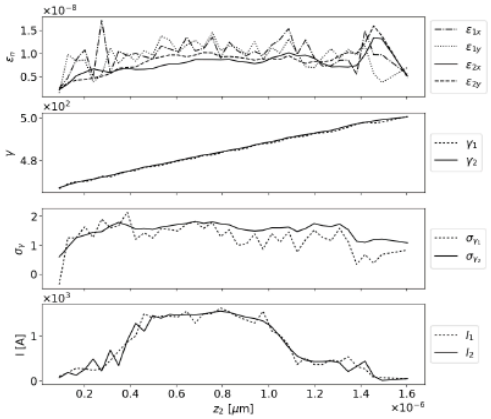

Figure 1: From top, the electron beam normalised emittance ϵ_n, localised Lorentz factor γ, RMS energy spread σ_γ and current I, as a function of window position $z_2 = (ct - z)$ of the beam. In this window, travelling at speed c along the z-axis of the undulator, the head of the electron bunch is on the left, the tail on the right, and the beam will propagate to larger values of z_2 as the beam propagates through the undulator. The dashed plots (index 1) show the original macroparticle beam from the VSim simulation and the solid plots (index 2) show the beam following smoothing and up-sampling to a greater number of microparticles with the correct shot-noise statistics.

ELECTRON BUNCH SIMULATION

A macroparticle distribution is taken from a VSim simulation of a PWFA. These macroparticles have too sparse a phase-space distribution for an accurate FEL simulation as there are too few macroparticles per resonant wavelength and they have unrealistic shot-noise statistics. These macroparticles are converted into a suitable distribution of *microparticles* using the scripts [10] and [11]. The relevant bunch parameters of a microparticle beam are compared to the original beam of macroparticles in Fig. 1. The microparticle distribution has had the correct shot-noise statistics applied as described in [12]. It is seen that the electron beam has a negative longitudinal energy chirp, which is the result of the beam acceleration in the electric field of the nonlinear plasma wave.

ISBN: 978-3-95450-210-3 doi:10.18429/JACoW-FEL2019-TUP051

UNAVERAGED FEL SIMULATION

The unaveraged 3D FEL simulation code Puffin was used [13,14] as it is able to model both macroscopic electron beam changes due to the electron beam energy chirp and any CSE and SACSE that may arise. The Ming Xie formalism of [15, 16] was used to chose the planar undulator period λ_u and undulator parameter a_u. The estimated beam parameters of the unchirped beam of Fig. 1 are: $I_{pk} = 1500\,\mathrm{A}$, $\epsilon_{xy} = 0.01\,\mathrm{mm\,mrad}$, $\gamma = 486$, $\sigma_\gamma = 0.3\,\%$, $Q = 3.6\,\mathrm{pC}$.

The undulator parameters selected for simulations were $\lambda_u = 0.015\,\mathrm{m}$ and $a_u = 1.0$. The resulting radiation wavelength is $\lambda_r \approx 67\,\mathrm{nm}$ and the FEL parameter at peak current is $\rho = 0.021$. Given that the average slice energy spread is $\sigma_\gamma/\gamma \approx 3 \times 10^{-3}$ the energy spread condition for FEL lasing of $\sigma_\gamma/\gamma \lesssim \rho$ is well satisfied in the absence of an energy chirp. The steady state, Self Amplified Spontaneous Emission (SASE) saturation length is then approximated as $L_{sat} \approx 1.4\,\mathrm{m}$ and saturation power $P_{sat} \approx 2.2\,\mathrm{GW}$. The electron bunch does not, however, conform to the steady-state approximation as it is only ~ 6 cooperation lengths long, where the cooperation length $l_c = \lambda_r/4\pi\rho$ [17]. This relatively short electron pulse length will result in the output of short, single pulses, at saturation. This type of short pulse operation is in the weak superradiant regime of FEL operation [17] and also results in reduced saturation powers from that of the steady-state, Ming Xie approximation above. The Puffin simulation uses the energy chirped electron bunch distribution output from the PWFA as shown in Fig. 1. The beam of microparticles was matched to the natural focusing channel of the undulator lattice chosen for the simulation as above using the method of [18]. It is seen from the parameters of the chirped pulse, plotted in Fig. 1, that the electron pulse generated by the PWFA has a length of $l_e \approx 24\lambda_r \approx 6l_c$ and has a negative energy chirp in z (positive energy chirp in z_2). During propagation through the undulator, dispersion will cause this short, energy chirped electron bunch to self-compress longitudinally due to rotation in longitudinal phase space, which is significant at these relatively low energies, and it may even 'flip over' in longitudinal phase space [3]. During this process, the electron bunch length may approach that of the resonant wavelength ($l_e \sim \lambda_r$) and consequently would be expected to radiate significant CSE. In what follows the CSE generation due to energy chirped bunch shortening and any FEL processes were modelled self-consistently. The FEL interaction may also amplify CSE in addition to the spontaneous emission due to electron beam shot-noise in the SACSE [8]. As with SASE, given the large energy chirp here, any SACSE process would be expected to be significantly affected. The electron bunch length is plotted as a function of position through the undulator in Fig. 2, and is seen to shorten and flip over before lengthening again.

The energy of the radiation pulse as a function of distance through the undulator emitted by the chirped bunch is shown in Fig. 3 both with and without the FEL interaction included in the simulation. The FEL interaction is 'switched off' in the Puffin simulation by artificially de-coupling the electrons from the radiation field. Also shown is the sponteneous emission with the energy chirp artificially removed from the electron bunch. The corresponding average bunching parameters $|\bar{b}|$, for both the chirped and un-chirped electron pulses are shown in Fig. 4.

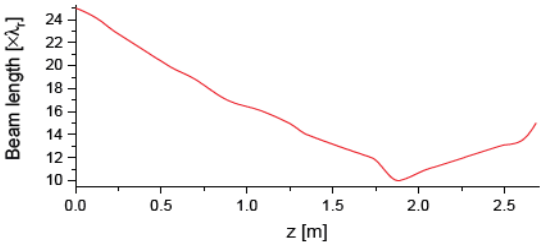

Figure 2: The full electron bunch length in units of resonant wavelentgh. The initial energy chirp at $z = 0\,\mathrm{m}$ is seen to cause the electron pulse to compress and then will decompress longitudinally.

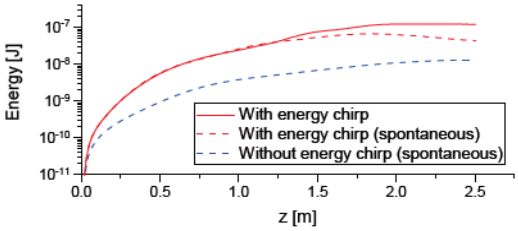

Figure 3: Radiation energy as a function of distance z through the undulator. Two of the plots (red) are for the chirped pulse including (solid) the FEL interaction and (dashed) without the FEL interaction. The case without energy chirp or FEL interaction (blue dashed) gives an energy growth with a quasi-linear dependence with z, corresponding to shot-noise spontaneous emission without significant CSE contribution.

The radiation pulse 'instantaneous' power (i.e. unaveraged over a radiation wavelength [13]) and electron bunching parameter $|b|$ at saturation, is shown in Fig. 5 as a function of local position z_2. It is seen from the Fig. 2 that the elec-

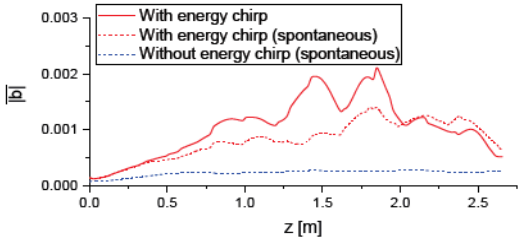

Figure 4: Average bunching parameter evolution for the electron pulse as a function of distance through the undulator both with (solid red) and without (dashed red) the FEL interaction. Also shown is the average bunching for the case of no energy chirp (dashed blue).

ISBN: 978-3-95450-210-3 doi:10.18429/JACoW-FEL2019-TUP051

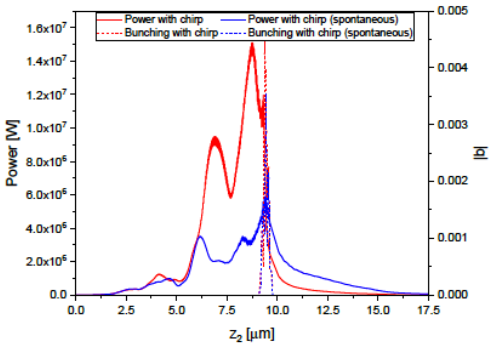

Figure 5: The radiation power profile (solid red) and the electron bunching parameter (dashed red) as a function of $z_2 = (ct - z)$ at $z = z_{sat} = 1.95$ m through the undulator for the energy chirped case and corresponding case for the FEL interaction 'switched off' (solid blue and dashed blue).

tron energy chirp causes the electron bunch to longitudinally compress in phase space and shorten as it propagates through the undulator. At saturation, $z = 1.95$ m, the electron bunch is only $\sim$ 10 resonant radiation wavelengths long. When the FEL interaction is switched off, the electrons then only emit spontaneous emission due to both shot-noise and CSE. Figure 3 shows that the energy growth is not exponential but is proportional to $\sim z^2$, more consistent with CSE [3]. That the radiation energy emitted in the absence of the FEL interaction is similar to that with the FEL interaction, confirms that the emission in both cases arise mainly from CSE. In the absence of any energy chirp or FEL interaction, there is no shortening of the electron pulse and the CSE emission is greatly reduced. The energy growth is then quasi-linear with distance z through the undulator, consistent with incoherent spontaneous emission due to shot-noise only.

The evolution of the mean electron bunching parameter $|\bar{b}|$ of Fig. 4 increases quasi-linearly with distance through the undulator until $z \approx 1.2$ m. This is in broad agreement with the increased bunching due to the dispersive shortening of the electron pulse which causes significant current gradients with respect to the radiation wavelength. It is this type of bunching which drives the Coherent Spontaneous Emission [3] and which may act as a self-generated seed field which can be amplified as SACSE [8, 9]. Also plotted is the electron bunching of the electron pulse in the absence of any energy chirp. As described above, there is no shortening of the electron pulse and the bunching remains approximately constant and at a much smaller value, mainly due to shot-noise, than when the pulse shortens and significant current gradients occur at the radiation wavelength scale. The differences of the radiation emission and electron bunching, between the spontaneous-only case, when the FEL interaction is switched off, and that where the FEL interaction is included in the simulation, can be attributed to a small additional bunching due to SACSE. Some small periodic bunching about the radiation wavelength $\lambda_r \approx 67\,nm$ due to SACSE, can be seen in the evolution of the electron phase-space through the undulator. The lack of any significant FEL gain is consistent with the work of [19] where for negative values of their chirp parameter $\hat{a}$, here $\hat{a} \approx -2$ at $z = 0$ m, FEL power output is greatly reduced from that expected from an un-chirped beam. So while some increased bunching is evident due to the FEL interaction between radiation and electrons, it is not operating in the collective, high-gain mode, significantly reducing the power emitted. Following the minimum of its length, the electron bunch continues to disperse as it propagates through the undulator, flipping over in phase space and indeed re-absorbing some of the emitted radiation and is consistent with that of previous simplified models [3]. Figure 5 (red) plots both the radiation power and electron bunching as a function of local position at saturation. It is seen that the electron pulse bunching, corresponding to the electron pulse at saturation of Fig. 2, is within a small local interval around $z \sim 9.5$ μm. The radiation pulse power for $z_2 < 9.5$ μm has propagated ahead of the electron bunch and is propagating in vacuum.

Figure 5 show results for both simulations with the FEL interaction switched on (red) and off (blue). The radiation is then that due to spontaneous radiation from shot-noise and CSE only. The difference in the power emitted between the two is then due to the FEL interaction as observed from the additional electron bunching of Figs. 4 and 2. The modest increase in output power demonstrates that the FEL is not, however, operating the in the high-gain regime.

CONCLUSION

Using a start-to-end approach, PWFA driven FEL operation was studied numerically using an unaveraged 3D model. The PWFA electron pulse output had a significant quasi-linear energy chirp. This chirp causes the electron pulse to shorten as it propagates through the undulator and emit significant CSE power. This CSE was seen to drive the electrons to give some weak periodic bunching at the resonant radiation wavelength, but not to enter into a collective, high-gain regime where analysis in the steady-state regime (no pulse effects) predicts output powers approximately two orders of magnitude greater. The dynamic shortening of the electron pulse and subsequent emission of CSE as it propagates through the undulator is an effect that is not normally modelled in FEL simulations. Methods to remove the electron beam energy chirp are the subject of on-going research and, if possible, are expected to allow the high gain FEL interaction to develop and output short coherent pulses of high power radiation.

ACKNOWLEDGMENTS

The authors wish to thank (i) KAUST Supercomputing Laboratory (KSL) Thuwal, Saudi Arabia, (ii) STFC's ASTeC, using the STFC HPC Hartree Centre, (iii) The Science and Technology Facilities Council Agreement Number 4163192 Release #3, (iv) and the John von Neumann Institute for Computing on JUROPA at Jülich Supercomputing Centre, under project HHH20.

ISBN: 978-3-95450-210-3 doi:10.18429/JACoW-FEL2019-TUP051

REFERENCES

[1] E. Esary *et al.*, "Physics of laser-driven plasma-based electron accelerators", *Rev. Mod. Phys.*, vol. 81, pp. 1229, 2009. doi:10.1103/RevModPhys.81.1229

[2] B. Hidding *et al.*, "Ultracold Electron Bunch Generation via Plasma Photocathode Emission and Acceleration in a Beam-Driven Plasma Blowout", *Phys. Rev. Lett.*, vol. 108, pp. 035001, 2012. doi:10.1103/PhysRevLett.108.035001

[3] L. T. Campbell and B. W. J. McNeil, "Puffin: A Three Dimensional, Unaveraged Free Electron Laser Simulation Code", in *Proc. FEL'12*, Nara, Japan, Aug. 2012, paper MOPD12, pp. 73–76.

[4] M. Pittman, S. Ferré, J.P. Rousseau, L. Notebaert, J.P. Chambaret, and G. Chériaux, "Design and characterization of a near-diffraction-limited femtosecond 100-TW 10-Hz high-intensity laser system", *Appl. Phys. B*, vol. 74, pp. 529-535, Apr. 2002. doi:10.1007/s003400200838

[5] Z. Huang, Y. Ding, and C.B. Schroeder, "Compact X-ray Free-Electron Laser from a Laser-Plasma Accelerator Using a Transverse-Gradient Undulator", *Phys. Rev. Lett.*, vol. 109, pp. 204801, Nov. 2012. doi:10.1103/PhysRevLett.109.204801

[6] H.P. Schlenvoigt *et al.*, "A compact synchrotron radiation source driven by a laser-plasma wakefield accelerator", *Nat. Phys.*, vol. 4, pp. 130-133, 2008. doi:10.1038/nphys811

[7] J. Henderson, L.T. Campbell, and B.W.J. McNeil, "Chirped and Modulated Electron Pulse Free Electron Laser Techniques", in *Proc. FEL'14*, Basel, Switzerland, Aug. 2014, paper MOC04, pp. 303–309.

[8] B.W.J. McNeil,, G.R.M. Robb, D.A. Jaroszynski, "Self-amplification of coherent spontaneous emission in the free electron laser", *Opt. Commun.*, vol. 165, pp. 65-70, 1999. doi:10.1016/S0030-4018(99)00222-9

[9] B.W.J. McNeil, G.R.M. Robb, D.A. Jaroszynski, "SACSE in a FEL amplifier with energy spread", *Nucl. Inst .Meth. Phys. Res. A*, vol. 445, pp. 72-76, 2000. doi:10.1016/S0168-9002(00)00116-9

[10] https://github.com/UKFELs/FXFEL

[11] https://github.com/UKFELs/JDF

[12] B.W.J. McNeil, M.W. Poole, G.R.M. Robb, "Unified model of electron beam shot noise and coherent spontaneous emission in the helical wiggler free electron laser", *Phys. Rev. ST Accel. Beams.*, vol. 6, pp. 070701, 2003. doi:10.1103/PhysRevSTAB.6.070701

[13] L.T. Campbell and B.W.J. McNeil, "Puffin: A three dimensional, unaveraged free electron laser simulation code", *Phy. Plasmas.*, vol. 19, pp. 093119, 2012. doi:10.1063/1.4752743

[14] L.T. Campbell, B.W.J. McNeil,, P.T. Traczykowski, and J.D.A. Smith, "An Updated Description of the FEL Simulation Code Puffin", in *Proc. IPAC'18*, Vancouver, Canada, Apr.-May 2018, pp. 4579–4582. doi:10.18429/JACoW-IPAC2018-THPMK112

[15] M. Xie, "Design Optimization for an X-Ray Free Electron Laser Driven by SLAC Linac", *Proc. the Particle Accelerator Conference 1995 (Geneva)* in *Proc. PAC'95*, Dallas, TX, USA, May 1995, paper TPG10, pp. 183-185.

[16] M. Xie, "Exact and variational solutions of 3D eigenmodes in high gain FELs", *Nucl. Instrum. and Methods Phys. Res. A*, vol. 445, pp. 59-66, 2000. doi:10.1016/S0168-9002(00)00114-5

[17] R. Bonifacio, B.W.J. McNeil,, and P. Pierini, "Superradiance in the high-gain free-electron laser", *Phys. Rev. A*, vol. 40, pp. 4467-4475, 1989. doi:10.1103/PhysRevA.40.4467

[18] https://github.com/UKFELs/Paraffin

[19] E.L. Saldin, E.A. Schneidmiller, and M.V. Yurkov, "Self-amplified spontaneous emission FEL with energy-chirped electron beam and its application for generation of attosecond x-ray pulses", *Phys. Rev. Special Topics Accel. Beams.*, vol. 9, pp. 050702, 2006. doi:10.1103/PhysRevSTAB.9.050702